Microstructural Characterisation and Mechanical Properties of an Extruded Nanoquasicrystalline Aluminium Alloy

Asad Hameed

Saint Cross College

A thesis submitted for the degree of

Doctor of Philosophy

Department of Materials, University of Oxford

Trinity, 2016

Table of Contents

Acknowledgments

I thank God Almighty for watching and guiding me every moment. It is hard to find words to thank my wife who has been selflessly supportive for allowing me to pursue the DPhil degree, while she waited for me at the home country. Without her assured backing, this pursuit would have been impossible and I am so very grateful to her. I am thankful to my five year old whose innocent skype conversations have been refreshing, invigorating and sanity restoring. I am grateful to my mother, siblings and other family members who have been praying for the successful completion of my degree.

I would like to heartily thank my supervisors Prof. Marina Galano and Prof. Fernando Audebert for their guidance and support throughout the duration of my DPhil. They confided in me and allowed me to work with a sense of great independence. They have been very critical as well as appreciative of new ideas and plans which not only motivated me but also helped me to correct mistakes and make amends. I am also thankful to Prof. Angus Wilkinson and Dr John Mason for their support in conducting the ultrasonic fatigue tests. I am grateful to Prof. Richard Todd for the training on the Grindosonic equipment and density measuring kit in his lab. I especially thank (retired) technician Bob Lloyd for helping me in extrusions and heat treatments, and also Laurie Walton for patiently bearing my hundreds of hours of presence in the mechanical workshop during machining of samples. I would like to thank Gabriella chapman for my SEM/EBSD training and Neil Young for arranging my TEM training.

Finally, I would like to thank my friends and colleagues in the department, especially Weiyue Xu, Stella Pedrazzini, Kumar Sundaram, Rashid Bhatti, Nur Azhani, Khushbu Dash and others for extending their help and support and making the department worthy place to work and enjoy. I am also thankful to my friend Wajahat Kazmi for our cooking ventures and thoughtful discussions at the weekends.

Abstract

Conventional aluminium alloys rapidly lose mechanical strength above 150°C, limiting their elevated temperature usage in engineering applications. The rapidly solidified (RS) nanoquasicrystalline (NQX) $Al_{93}Fe_3Cr_2Ti_2$ alloy has the potential to be used at elevated temperatures (250-350°C) as it retains high strength at those temperatures. There have been some microstructural studies and limited work on the mechanical properties of the alloy. However, a detailed study of both the microstructure and the mechanical properties (elastic constants, tensile behaviour, and fatigue behaviour) has not been carried out for the bulk alloy.

RS NQX $Al_{93}Fe_3Cr_2Ti_2$ alloy powder in 25-50μm fraction size was consolidated using extrusion to produce bars. The microstructure of the extruded bars was characterised using X-ray diffraction, differential scanning calorimetry, scanning electron microscopy, transmission electron microscopy, energy dispersive X-ray spectroscopy, scanning transmission electron microscopy, and electron backscattered diffraction. The microstructure was observed to contain approximately 44% volume fraction of nano size quasicrystalline icosahedral (I-phase) particles embedded in submicron size aluminium grains.

The alloy bar samples were annealed at elevated temperatures (250, 300, 350, 400, and, 450°C) for long hours (100h) and the microstructural evolution was studied using aforementioned characterisation techniques. As a result of the annealing at 350°C for 100h, the I-phase starts to transform into other stable and metastable intermetallics which grow with the increase in the annealing temperature. Room temperature mechanical properties such as hardness, Young's modulus, and shear modulus were measured, and tensile tests for the alloy samples were carried out in

the ‘as extruded’ and ‘annealed’ conditions. The alloy retains its microstructure and mechanical properties after annealing at 300^{o}C for 100hrs. The alloy results are exceptional, as conventional Al alloys suffer >45% strength loss after the same heat treatment. Orowan and Hall-Petch mechanisms were found the dominant strengthening mechanism in the alloy at room temperature.

Tensile tests were performed at 23°C as well as elevated temperature (150-500°C) at four strain rates (10^{-2}-$10^{-5}s^{-1}$). Tensile strength values at ambient temperature are comparable to the high strength conventional Al alloys; however, elevated temperatures (~300°C) tensile strength of the NQX $Al_{93}Fe_3Cr_2Ti_2$ alloy is 3 to 8 times higher than conventional Al alloys. High values of the apparent stress exponent and the apparent activation energy of plastic flow were observed for all test temperatures. At intermediate temperatures (150-250°C), several manifestations of dynamic strain ageing were observed in the alloy. Plastic flow models were used to explain the elevated temperature behaviour, and it was deduced that 250-350°C temperature range experienced a transition from power law break down to power law creep, whereas a climb controlled mechanism was operative at 425-500°C temperature range.

Fatigue testing was carried out using conventional and ultrasonic frequencies at room temperature and only conventional frequency at 300^{o}C. The alloy exhibits type II fatigue behaviour. The room temperature fatigue performance is comparable with the high strength conventional alloys, and far superior to any conventional Al alloy at 300^{o}C.

The following figures in this thesis were reprinted with permission from the respective publisher.

Figure No.	**Publisher**	**License no**
Figure 2.2 (b) pistons	Springer	3985550989567
Figure 2.4 (a)	Elsevier	3985561272273
Figure 2. 4 (b)	Springer	3985570014611
Figure 2.5	American Physical Society	3985570483529
Figure 2.6 and 2.8	Elsevier	3985571226682
Figure 2.7	Elsevier	3985571475954
Figure 2.10 and 2.11	Springer	3985580164421

1. Introduction

Traditionally, aerospace and automotive (industrial) sectors have been driving the engineering initiatives for the development of high strength, lightweight, and cost-effective materials (Polmear, 2006). Conventional Al alloys have found extensive usage in these sectors in the form of cheap and lightweight engineering application up to ~200°C. The strength of these conventional Al alloys rapidly degrades above ~150°C (Inoue and Kimura, 2000, ASM, 1990) and costly Ti is deemed a material solution above ~250°C.

The developments in the rapid solidification (RS) technique have led to the production of Al-based alloys with superior mechanical properties in comparison to alloys produced through conventional metallurgy techniques (Audebert et al., 2002). These RS alloys sometimes contain the metastable icosahedral quasicrystalline phase (I-phase). The I-phase drew much scientific attention since its discovery by Shechtman et al. (1984), as it exhibits conventionally forbidden 5-fold symmetry (Dubois and Wei, 2005). These rapidly solidified Al-based, I-phase containing alloys exhibit high hardness, high strength and superior thermal stability as compared to the conventional alloys (Inoue, 1998). One such novel RS Al-based nano-quasicrystalline (NQX) alloy is $Al_{93}Fe_3Cr_2Ti_2$ which was developed more than a decade ago by Inoue and coworkers (Inoue, 1998). The RS $Al_{93}Fe_3Cr_2Ti_2$ (NQX alloy from here on) contains very small (<~200nm) I-phase reinforcement particles in ultrafine size (<1μm) grains of α-Al. It can be potentially used at high temperatures (up to 350^{o}C) as a cheaper alternative to costly Ti or other conventional Al alloys in engineering applications (Inoue and Kimura, 2001). Many researchers (Inoue, 1998, Audebert et al., 2002, Galano et al., 2004, Yamasaki et al., 2007, Galano et al., 2009) have reported excellent mechanical properties of the alloy at ambient and elevated temperatures. A significant research effort on the alloy has been dedicated to the ribbons produced through melt spinning, and whilst studies on the bulk samples do exist,

the detailed expositions on the mechanical properties of the bulk NQX alloy vis-à-vis the microstructural study is still lacking. There have been some works on the mechanical behaviour of the bulk extruded alloys; however, those have been either limited to small temperature ranges (Rounthwaite, 2012, Pedrazzini, 2014)[A] or a single strain rate (Inoue, 1998, Yamasaki et al., 2007, Chlupová et al., 2011). As a result, understanding of high temperature plastic deformation mechanisms in the bulk NQX alloy is underdeveloped. Furthermore, the fatigue behaviour of the alloy at very high number of cycles and elevated temperatures is not known. If the NQX alloy has to compete with the high strength and/or high temperature conventional aluminium alloys in the industry, a better understanding of the mechanical behaviour of the bulk alloy is required.

In this thesis, the microstructure and corresponding mechanical properties of the alloy were studied for the 'as extruded' NQX alloy, and also after annealing heat treatments at high enough temperatures resulting in the metastable I-phase transformation. The effect of the heat treatments on the α-Al grain growth as well as on the transformation and subsequent coarsening of the metastable I-phase particle was analysed. The corresponding changes in the mechanical properties were also measured. The study of the microstructure also led to the estimation of the contributions of various strengthening mechanisms to the overall yield strength of the NQX alloy.

In this work, the mechanical properties were measured at a wide temperature (23^{o}C-500^{o}C) and strain rate range (10^{-2} to$10^{-5}s^{-1}$). This enabled to investigate the possible deformation mechanisms in the NQX alloy at elevated temperatures (250^{o}C-500^{o}C) and also confirmed the presence of dynamic strain ageing at the intermediate temperatures (~150^{o}C-250^{o}C). The fatigue behaviour of the alloy was investigated at the high cycle and

[A] Work done previously in our research group.

very high cycle high cycle fatigue regimes, as well as at elevated temperatures and it was compared with conventional Al alloys.

Young's modulus, shear modulus and Poisson's ratio are considered important material elastic properties in engineering component design which were measured and analysed for the NQX alloy for the first time in the 'as extruded' and 'annealed' conditions. Overall, this is a novel study on the bulk NQX alloy which provides the information and analysis about its microstructure and mechanical behaviour. This will help to draw the NQX alloy another step closer towards its practical engineering application[B].

The outline of the thesis is as follows: chapter two contains the literature review and chapter three describes the experimental methods employed in this research. Chapter four provides the details of consolidation and characterisation of the extruded bars, whereas chapter five discusses the thermal stability and the phase transformations in the extruded NQX alloy after prolong annealing at high temperatures. Chapter six reports the mechanical properties of the NQX alloy measured at room temperature in the 'as produced' and 'annealed' conditions. Chapter seven contains the elevated temperature mechanical properties. Chapter eight relates the observations and findings from the previous chapters and holds a general discussion about the behaviour of the NQX alloy. Chapter nine concludes the thesis and proposes avenues for the future work.

[B] In addition to the mechanical properties, a few thermo-physical properties such as coefficient of thermal expansion, thermal diffusivity and thermal conductivity of the alloy were also measured (for the first time) which are deemed important for a high temperature engineering application. These have been included as 'appendix 5'.

References

ASM (1990) *Nonferrous Alloys and Special-Purpose Materials, vol. 2. ASM International, Materials Handbook*: ASM International.

Audebert, F., Prima, F., Galano, M., Tomut, M., Warren, P. J., Stone, I. C. and Cantor, B. (2002) 'Structural characterisation and mechanical properties of nanocomposite Al-based alloys', *Materials transactions,* 43(8), pp. 2017-2025.

Chlupová, A., Chlup, Z., Kruml, T., Kuběna, I. and Roupcová, P. 'Microstructure, tensile properties and fatigue behaviour of bulk nano-quasicrystalline al alloy $AL_{93}FE_3CR_2TI_2$', *Nano Con*, Brno, Czech Republic, 21-23 September 2011.

Dubois, J.-M. and Wei, T. K. (2005) *Useful quasicrystals.* World Scientific.

Galano, M., Audebert, F., Cantor, B. and Stone, I. (2004) 'Structural characterisation and stability of new nanoquasicrystalline Al-based alloys', *Materials Science and Engineering: A*, 375, pp. 1206-1211.

Galano, M., Audebert, F., Escorial, A. G., Stone, I. and Cantor, B. (2009) 'Nanoquasicrystalline Al–Fe–Cr-based alloys. Part II: Mechanical properties', *Acta materialia,* 57(17), pp. 5120-5130.

Inoue, A. (1998) 'Amorphous, nanoquasicrystalline and nanocrystalline alloys in Al-based systems', *Progress in Materials Science,* 43(5), pp. 365-520.

Inoue, A. and Kimura, H. (2000) 'High-strength aluminum alloys containing nanoquasicrystalline particles', *Materials Science and Engineering: A,* 286(1), pp. 1-10.

Inoue, A. and Kimura, H. (2001) 'Fabrications and mechanical properties of bulk amorphous, nanocrystalline, nanoquasicrystalline alloys in aluminum-based system', *Journal of light metals,* 1(1), pp. 31-41.

Pedrazzini, S. (2014) *Characterisation and Mechanical Properties of Bulk Nanostructured Al-based Composites for High Temperature Applications.* DPhil Thesis, University of Oxford, Oxford.

Polmear, I. (2006) *Light metals: from traditional alloys to nanocrystals.* Oxford: Elsevier.

Rounthwaite, N. J. (2012) *Development of Bulk Nanoquasicrystalline Alloys for High Strength Elevated Temperature Applications.* DPhil Thesis, University of Oxford.

Shechtman, D., Blech, I., Gratias, D. and Cahn, J. W. (1984) 'Metallic phase with long-range orientational order and no translational symmetry', *Physical Review Letters,* 53(20), pp. 1951.

Yamasaki, M., Nagaishi, Y. and Kawamura, Y. (2007) 'Inhibition of Al grain coarsening by quasicrystalline icosahedral phase in the rapidly solidified powder metallurgy Al–Fe–Ti–Cr alloy', *Scripta materialia,* 56(9), pp. 785-788.

2. Literature Review

2.1 Introduction

The development of high strength, light-weight, and cost effective materials has been driven by the engineering requirements mainly from the aerospace and automotive industries (Polmear, 2006). Aluminium and its alloys are classified as the 'light-weight' materials and have been extensively used for room temperature applications (Totten and MacKenzie, 2003). Aluminium has a low density of 2.7g/cm^3 and its price is 1.6 $US/kg. In comparison, the density of Ti is 4.5g/cm^3, and its price is about 11.7 $US/kg[A] which is more than seven times higher.

High strength is one of the primary performance criteria at room temperature, whereas thermal stability and strength retention are vital for elevated temperature applications (Robinson et al., 2003). Commercial aluminium alloys rapidly lose strength above ~150-200°C which limits their use in a strength based high temperature engineering application (Inoue and Kimura, 2000); therefore, titanium alloys are mostly used in lightweight elevated temperature applications (Polmear, 2006).

A considerable research effort has been put in developing manufacturing methods to produce cheap and lightweight aluminium alloys capable of sustaining higher temperatures (Belov et al., 2002). 'Rapid solidification' is one such technique which has provided a variety of opportunities to develop aluminium alloys with complex microstructures (Inoue, 1998). These alloys can maintain service properties (strength, modulus, hardness) over a wide temperature range and may potentially replace costly Ti, up to 350°C in engineering applications (Krainikov and Neikov, 2012). The goal if materialised, will

[A] Commercially pure grade 1 ingot price of Ti is from www.metalprices.com.
Aluminium price is from London metal exchange www.lme.com as of Aug 2016.

significantly lower the component cost (due to low Al price) as well as improve fuel economy (due to weight reduction).

This chapter provides the background literature for rapidly solidified Al alloys which can be used in elevated temperature applications, with a special focus on nanoquasicrystalline $Al_{93}Fe_3Cr_2Ti_2$ alloy.

2.2 Commercial Aluminium Alloys Produced Through Conventional Methods

Aluminium is soft and ductile in pure form, and in order to impart strength it is commonly alloyed with Mn (3xxx series), Mg (5xxx series), Cu (2xxx series), Mg, and Si (6xxx series) and Zn (7xxx series), to provide a wide variety of commercial alloys (ASM, 1990). The commercial Al alloys can be divided into two categories: (i) heat treatable alloys, and (ii) non-heat-treatable alloys. The former respond to thermal treatments (e.g. quenching, precipitation or age hardening) and form precipitates which provide strengthening by impeding dislocation motion. The non-heat treatable alloys rely on work hardening in a combination with annealing procedure, thus increasing dislocation densities and subsequently the strength of the alloy (ASM, 1990, Polmear, 2006).

7xxx series, precipitation hardened Al alloys have the highest tensile strengths in conventional aluminium alloys, such as 7075-T6 (570MPa) or 7178-T6 (610MPa) (ASM, 1990). The precipitation hardened 2xxx series Al alloys retain the high temperature strength better, despite having a moderate room temperature strength, such as 2014-T6 (480MPa), 2024-T4 (470MPa), and 2618-T361(440MPa) (ASM, 1990).

2.2.1 Applications

Aluminium alloys are also one of the most abundantly used materials in aerospace and automotive applications (Robinson et al., 2003).

2.2.1.1 Aerospace

7xxx series Al alloys are used in upper wing, skin, internal ribs/frames and landing gears of aircraft (Cantor et al., 2001). Hidumimium RR.58 (a precursor to 2618 alloy) had been used in pistons and gas turbines of aero-engines. It also met the high skin temperature requirements of sustained supersonic flight at Mach~2 (Robinson et al., 2003). 2024 alloy has been used in the aircraft wheels in which high temperatures are achieved for short durations (Robinson et al., 2003). However, if the component temperature exceeds 150-200°C Titanium is used instead of aluminium (Cantor et al., 2001).

A noticeable example for the requirement of 'high temperature' lightweight material in the aerospace applications is that of a jet engine. A schematic of an axial flow jet engine alongside the important airflow parameters such as temperature, velocity, pressure and metals used in each section of the engine is shown in Figure 2.1 (Rolls-Royce, 1986).

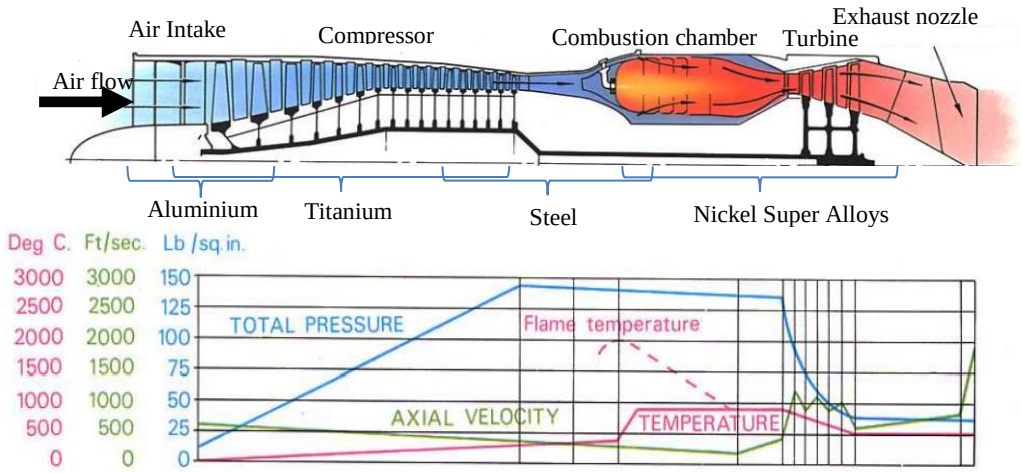

Figure 2.1 Schematic of a single spool axial flow turbojet engine with approximate airflow parameters (temperature, velocity, and total pressure), adapted from Rolls-Royce (1986).

Airflow temperature inside the compressor gradually increases after each stage and at the compressor outlet section may reach ~350-400°C as seen in the schematic. Aluminium alloys are used in small quantities in low temperature (<150^{o}C) areas such as intake

casing area, engine components and accessories (Rolls-Royce, 1986). Titanium alloys are predominantly used in the compressor section at temperatures up to ~500^{o}C (Lütjering and Williams, 2003), which are unusable for the aluminium alloys. Consequently, the development of cost-effective Al alloys which can sustain higher temperatures (Fine, 1986) and replace Ti up to 340/350^{o}C, is desirable.

2.2.1.2 Automotive

Eutectic or hypereutectic Al-Si alloys are extensively used for engine blocks and piston applications in automotive gasoline engines (Ye, 2003, ASM, 1990). Mg, Cu, and Ni additions are made in order to improve the strength, whereas Fe, Mn and Pb are added to modify die sticking, to improve ductility and to improve machinability respectively (Ye, 2003). In piston applications, M124 is an extensively used Al-Si-Cu alloy which has a 350°C strength of 35-55MPa, whereas M174 is a modified Al-Si-Cu alloy having a strength of 45-65MPa at the same temperature[B] (Mahle, 2012). A low thermal expansion, good corrosion, wear resistance, machinability, and a good high temperature strength are desired properties in alloys for automotive engine application (Mahle, 2012, Ye, 2003).

The temperature on the piston face increases with the engine revolutions per minute (RPM). Pistons face temperature for typical RPMs in gasoline engines is close to 150-200^{o}C. The effect of engine RPM on the temperature of various components of an automotive gasoline engine are shown in Figure 2.2 (a) (Pulkrabek, 2004). Temperature distribution in a piston of a gasoline engine at a high RPM is shown in Figure 2.2 (b) (Mahle, 2012). The present Al alloys in heavily loaded turbocharged gasoline engines reach their limit around ~250^{o}C (Mahle, 2012).

[B] M124: Wt% Si (11-13), Cu (0.8-1.5), Mg (0.8-1.3), Ni (0.8-1.3), Fe (0.7 max), Mn (0.3 max), and Al (remainder)
M174: Wt% Si (11-13), Cu (3-5), Mg (0.5-1.2), Ni (1-3), Fe (0.7 max), Mn (0.3 max), and Al (remainder).

The work output of a thermodynamic cycle can be improved by increasing the temperature inside the combustion chamber, on the other hand, sustained exposure to high temperature can overage the alloys and cause creep and/or thermomechanical fatigue failures (Ye, 2003). Costly Ti or heavy Fe are the material solutions for such sustained higher temperature requirements, but using heavier masses in piston can cause large undesirable inertial forces and torques (Mahle, 2012). Lightweight aluminium alloys which can maintain strength at high temperature are therefore required.

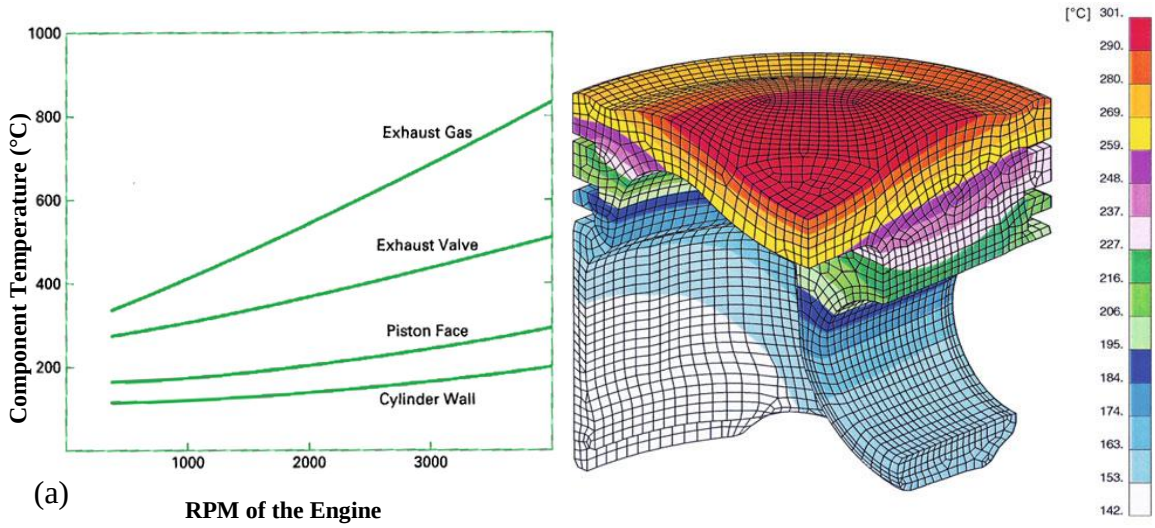

(a)

(b)

Figure 2.2 (a) Effect of engine RPM on the component temperature in a gasoline engine after Pulkrabek (2004), (b) finite element model of temperature distribution on a piston of a gasoline engine (Mahle, 2012).

2.3 Strengthening Mechanisms in Al alloys

The knowledge of strengthening mechanisms is necessary to understand and exploit the mechanical properties for the design of alloys in engineering applications.

The interactions of dislocations with the lattice, solute atoms, other defects (vacancies, dislocations, stacking faults, voids etc.), boundaries and precipitates contribute to the strength of engineering materials. Based on these interactions, several strengthening

mechanisms in alloys are reported in the literature. These mechanisms include: lattice friction, solid solution strengthening, dislocation strengthening, grain boundary strengthening and particle dispersion strengthening (Abbaschian and Reed-Hill, 2008, Dieter and Bacon, 1986). Some of the important mechanisms in the Al alloys are discussed in this section.

2.3.1 Dislocation strengthening or work hardening

Dislocations interact with each other to produce new dislocations of low mobility (sessile dislocations) (Dieter and Bacon, 1986). The sessile dislocations act as barriers to the moving dislocations and stress must be increased to overcome the barrier, assuming no thermal activation. If the dislocations are assumed to be distributed in a random pattern then the contribution to the flow stress due to the dislocation density per unit area (ρ_{dis}) can be estimated by Taylor's equation given below (Totten and MacKenzie, 2003).

$$\Delta\sigma_{w.h} = \alpha_{w.h} M G b \sqrt{\rho_{dis}} \qquad \textbf{Eqn. 2.1}$$

Where $\Delta\sigma_{w.h}$ is the contribution to flow stress due to work hardening, $\alpha_{w.h}$ is a pre-factor generally ~0.2 for Al, G_{Al} is the shear modulus of Al, b is the Burgers vector, ρ_{dis} is the dislocation density. M is Taylor's factor.

2.3.2 Grain boundary (GB) strengthening

Grain boundaries also contribute to the strengthening of the material by impeding dislocation motion. A material with fine grain size has, therefore, a higher strength in comparison to its coarse-grained counterparts. It was presented by Hall (1951) and Petch (1953) in the form of the famous Hall-Petch equation (Dieter and Bacon, 1986).

$$\Delta\sigma_{g.b} = \frac{K_{H.P}}{D^{x}} \qquad \textbf{Eqn. 2.2}$$

Where $\Delta\sigma_{g.b}$ is strength contribution due to grain boundaries, D is the grain diameter, x is the exponent used as 0.5 in the original Hall-Petch model. $K_{H.P}$ is microstructure stress intensity parameter.

It was experimentally shown by Hall and Petch that the yield (and the flow) stress has an inverse proportional relationship with $\sqrt{(D)}$, where D is the grain diameter. The grain boundary effect was explained using the dislocation pile-up model by Hall (1951), Petch (1953) and Cottrell (1958). The model assumes that in a polycrystalline material, dislocations are stopped by the grain boundaries which act as barriers to slip propagation and dislocation movement. On increasing the grain size and/or the applied stress, the number of dislocations inside the grain also increases in the form of the pile up(s). The dislocation pile up exerts a stress in a neighbouring grain and on reaching a critical value, a slip source is activated in that grain; the process is then repeated. The magnitude of the stress exerted by the pile up relates to the dislocation density which is inversely proportional to grain size as $\rho=1/D$ (Conrad, 1963). Substitution of the dislocation density value in the original Taylor's relation (Eqn. 2.1) results in the Hall-Petch relation of $K_{H.P}/\sqrt{(D)}$ (Conrad, 1963). The grains are assumed to be equiaxed in the models, in reality, the grains have a size distribution which may cause yielding of the larger grains before the smaller ones. Moreover, the grains favourably oriented for the slip also start undergoing plastic deformation while remaining grain are still undergoing elastic deformation (Chateau, 2011).

Li and Chou (1970) proposed that as a result of deformation, grain boundary ledges act as sources of dislocations which propagate in the undeformed grains. Smaller grain sizes have increasing difficulties in the dislocation emission which relates to the original Hall-Petch relation. Ashby (1970) refined this concept and proposed that during plastic deformation, the neighbouring grain must accommodate geometric incompatibilities by

emitting dislocations near grain boundaries where the deforming grain interior region changed to the undeforming grain boundary region. These dislocations were called as geometrically necessary dislocations (GNDs)[C]. The density of GNDs is dependent on inverse grain size and the treatment also causes yield stress increase as per $1/\sqrt{(D)}$ or the Hall-Petch relation. Meyersm and Ashworth (1982) further built on Ashby's model and experimentally showed that the highest dislocation densities are observed near grain boundaries. In their model, it was hypothesised that a polycrystalline material can be assumed to be a composite which contains a work hardened grain boundary region (called mantle) and relatively soft grain interior (called the core). The strength of such a materials in this model was considered to be dependent on the inverse square root of grain diameter $1/\sqrt{(D)}$ using appropriate substitutions . The grain boundary area fraction is very large in materials with a nano-sized grain (D<100nm) structure so the core/mantle model becomes relevant in such cases. Benson and coworkers (Fu et al., 2001, Benson et al., 2001) extended the core and mantle model and performed numerical computations to successfully explain the mechanical behaviour of nanocrystalline materials.

It was found that all the aforementioned models result in the equations of the form of the original Hall-Petch equation. The models use an average grain size and assume constant values of $K_{H.P}$ and exponent 'x', whereas the rate-controlling deformation mechanisms may change with the grain size (Yu et al., 2005)[D] which may also change the $K_{H.P}$ or 'x' values . Continuum plasticity approaches have been used to account for the various plastic flow barriers and the influence of GNDs, to model the constitutive response of a material with a range of grain sizes (Pineau et al., 2016). The simulations help to find the

[C] The dislocations emitted to accommodate plastically deforming grains are called GNDs. The dislocations emitted inside the grains as a result of the macroscopic applied stress, are called statistically stored dislocations.

[D] Rate controlling mechanism and grain diameter: For D>1μm, dislocation intersection mechanisms. For 1μm >D>10nm, dislocation emission from GBs or GB shear by dislocation pile up mechanism. For D<10nm, GB processes.

effect of grain size on the strain hardening in addition to the yield strength (Balint et al., 2008) with mixed success (Pineau et al., 2016).

2.3.3 Particle dispersion strengthening

A distribution of small particles can hinder the dislocation glide and an increased stress is required for the dislocation propagation in its slip plane. The increase in stress is inversely dependent on the interparticle spacing (L or λ) (Dieter and Bacon, 1986). If the distributed particles are hard (non-shearable), the dislocations can only pass by bowing between those (assuming no thermal activation), as shown in Figure 2.3. After the main dislocation line completely glides past the particles, a dislocation loop structure is left around the particles (Ashby and Jones, 2005). The incoming dislocations have to accommodate both particles and the dislocation loop structure.

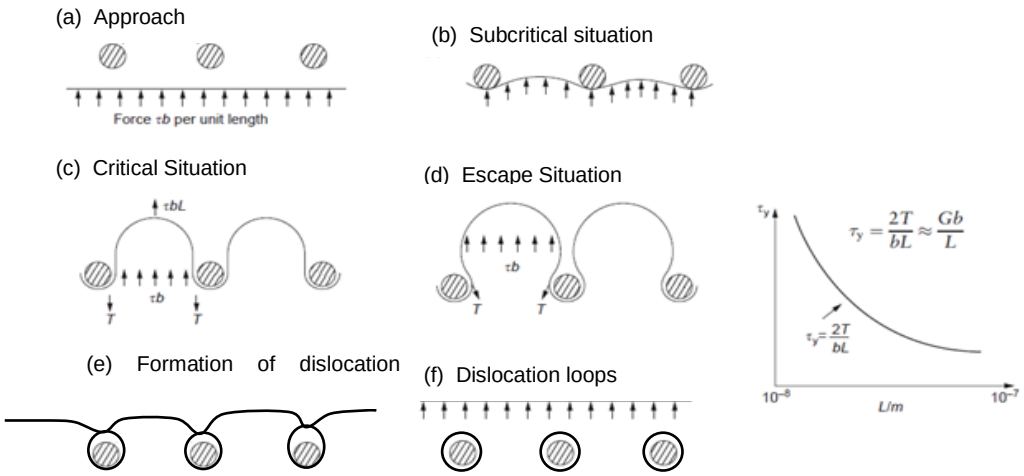

Figure 2.3 A schematic view of the particle strengthening by Orowan's mechanism after (Ashby and Jones, 2005).

The dispersion strengthening contribution in a polycrystalline material is provided by the Orowan equation given below (Orowan, 1948).

$$\Delta\sigma_p = M\frac{Gb}{\lambda_s} \qquad \textbf{Eqn. 2.3}$$

Where $\Delta\sigma_p$ is the strengthening contribution due to the hard particles, M is Taylor's factor, and G is the shear modulus. λ_s (or L) is the edge to edge planar interparticle spacing for the spherical particles and it has been calculated using several approaches in literature (Corti et al., 1974). One simple form of the relation to calculation the mean random interparticle (edge to edge) planar spacing is given by Eqn. 2.4 .

$$\lambda_s = \frac{2D_{p,s}}{3f_v}(1-f_v) \qquad \textbf{Eqn. 2.4}$$

Where $D_{p,s}$ is mean planar particle diameter and f_v is volume fraction.

Particle diameter in a volume is measured experimentally using TEM, whereas planar diameter is measured from polished samples (using SEM or optical microscopy) (Corti et al., 1974). particle planar diameter ($D_{p,s}$) is related to the particle diameter in volume (D_p) as Eqn. 2.5 (Brown and Ham, 1971).

$$D_{p,s} = D_p\sqrt{\frac{2}{3}} \qquad \textbf{Eqn. 2.5}$$

The dislocation particle interaction and subsequent dispersion strengthening assumed a dislocation line with a constant tension between two isolated impenetrable spherical obstacles of equal strength (Orowan, 1948). However, Foreman and Makin (1966) and separately Kocks (1967) treated the problem to include a random array of obstacles instead of an isolated pair of obstacles which was originally considered by Orowan. They used computations and produced empirical equations which modified the original Orowan equation and provided better theoretical foundations. Later, arguments were presented that force due to the obstacles was dependent on the energy of dislocation per unit length and included a logarithmic dependency term of the form $\ln(D_{p,s}/b)$, where $D_{p,s}$ is the mean particle planar diameter (Brown and Ham, 1971). The original Orowan equation was thus modified and called the Ashby–Orowan equation given below (Ashby, 1968).

$$\Delta\sigma_{Or} = 0.13M\frac{\ln\left(\frac{D_{p,s}}{b}\right)}{\lambda_s} \qquad \textbf{Eqn. 2.6}$$

Hirsch et al. then further modified the equation (Brown and Ham, 1971), and later (Bacon et al., 1973) considered the effect of self-intersection of the dislocation. The modification results in Eqn. 2.7 which has been extensively used in literature (Brown and Ham, 1971, Han and Dunand, 2000, Han et al., 2003, Bacon et al., 1973).

$$\Delta\sigma_{Or} = M\frac{0.4Gb}{\pi(1-\upsilon)^{1/2}}\frac{\ln\left(\frac{D_{p,s}}{b}\right)}{\lambda_s} \qquad \textbf{Eqn. 2.7}$$

Where υ is the Poisson's ratio, (other parameters have been defined in equations above). Accurate quantitative prediction using Orowan's equation is somewhat difficult, especially if the particles exist in a large size range. However, it serves well to qualitatively estimate the particle strengthening contribution both in alloys (Inoue and Kimura, 2001, Topping et al., 2012) and composites[E] (Tong and Fang, 1998). Dislocation dynamic simulations have also been carried out on more realistic microstructures such as carbide dispersions in steels, and the calculations have been observed to be comparable with the various versions of Orowan's equations (Queyreau et al., 2010).

2.3.4 Solid solution strengthening

Strain fields of substitutional or interstitial solute atoms in the solvent lattice can interact with the mobile dislocations to give rise to solid solution strengthening. Mott and Nabarro (1948) showed that the strengthening is caused by the size effect of solute atoms which was later modified by Fleischer (1963) to include the modulus term, and a general form is given by Eqn. 2.8.

$$\Delta\sigma_{ss} \propto \left|\frac{1}{G}\left(\frac{dG}{dc}\right) - (\beta)\frac{1}{a}\left(\frac{da}{dc}\right)\right| \qquad \textbf{Eqn. 2.8}$$

[E] Alloys example : (Topping et al.) Ultrafine grain Al-Mg-Mn forged alloy; (Inoue et al.) : Al-Ni-Mm (Mm=mischmetal); Composite example: (Tong and Fang) Al-TiC insitu composite

Where a is the lattice parameter, c is the solute concentration, $\Delta\sigma_{ss}$ is the strengthening due to presence of solute, G is the shear modulus, da/dc is the change in the lattice parameter with respect to the solute concentration, dG/dc is the change in the shear modulus of the solution with respect to the solute concentration and β is a material dependent constant.

Solute concentration and atomic size factor[F] are important parameters in solid solution strengthening and for a smaller concentration of solute in Al matrix the contribution due to this strengthening is negligible (Campbell, 2008). When the temperature is increased the solid solution strengthening becomes less effective due to increased diffusion also if the annealing treatment reduces the solute in the matrix the solid solution strengthening effect is reduced (Totten and MacKenzie, 2003).

A general form of the solid solution strengthening equation has been used in literature, as shown in Eqn. 2.9 (Ryen et al., 2006, Chateau, 2011).

$$\Delta\sigma_{ss} \approx K_{ss} c^{n_{ss}} \qquad \textbf{Eqn. 2.9}$$

Where n_{ss} and K_{ss} are the material dependent constants, c is the solute concentration.

2.4 Rapidly Solidified (RS) Al Alloys

Rapid solidification is a novel method of producing high-performance aluminium alloy for potential use in aerospace and automotive applications. It increases the strength of the alloy by (i) retaining a high quantity of foreign elements in solid solution than the equilibrium, (ii) refining the grain size (iii) reducing segregation, and (iv) producing

[F] Atomic size factor (δ_{sf}) $\delta_{sf} = \left(\frac{r_{solute} - r_{Al}}{r_{Al}} \right)$, where r is the atomic radii.

submicron size strengthening phases (Grant, 1983, Krainikov and Neikov, 2012, Otooni, 2013).

Many RS systems with superior temperature properties have been developed and studied over the years, and a few examples of some prominent Al-based RS alloys are provided in Table 2.1. The solid solubility of foreign elements in aluminium increases as a result of rapid solidification as seen in Table 2.1.

Table 2.1 Some examples of popular, high strength RS Al alloy systems and compositions (at%) (Mondolfo, 1976), (Knipling et al., 2006), (Krainikov and Neikov, 2012).

System	Fe	Cr	Ce	V	Si	Mn	Zr	Mo
Al-Fe-Ce	3.2-5.3		0.8-1.7					
Al-Cr-Mn/Zr		0.8-3.3				2.6	1	
Al-Fe-V/Mo-Si	2.0-6.3			0.3-0.8	1.1-2.5			1
Maximum solubility of elements in Al								
Equilibrium State	0.025	0.4	0.01	0.21	1.6	0.9	0.08	0.056
RS alloys	6	6	1.9	2	16	9	1.5	1.5

Most of the aforementioned RS alloys are mainly Al-Fe alloys which produce a high volume fraction of the 2nd phase particles/dispersoids. The addition of slow diffusing transition metals in RS Al-Fe alloys improves the coarsening resistance of the dispersoids and stabilise the microstructure at high temperature (Skinner et al., 1986, Krainikov and Neikov, 2012, Belov et al., 2002). Dislocations-dispersoids interaction provides particle strengthening. These dispersoids also cause grain boundary pinning and thus providing Hall-Petch strengthening at elevated temperatures (Mitra, 1992, Belov et al., 2002). The dispersoids may ultimately coarsen/transform/dissolve at higher temperatures, however, they widen the 'useable temperature' window of the alloy.

2.4.1 Production of RS Al alloys

Several prominent companies have been leading the research effort on the rapidly solidified (RS) alloys including: Lockheed, Pratt & Whitney, allied signal, Alcoa, Pechiney,

VILS, etc. (Belov et al., 2002). The RS alloys can be produced by several methods. A widely used method is melt spinning in which the melt is squirted on rapidly rotating Cu disc to obtain ribbons at a very high cooling rate of 10^4-10^7 K/s (Grant, 1983). Another popular method is gas atomisation where the liquid metal is atomised with the help of gas or ultrasonic oscillations through which a powder is obtained (Krainikov and Neikov, 2012, Grant, 1983). The atomised powder or the comminuted ribbons can be consolidated using hot isostatic pressing and/or extrusion to form the bulk material.

2.4.2 Microstructure and properties of RS Al alloys

Al-Fe-V-Si and Al-Cr-Zr are amongst promising RS Al alloys. The strengthening contribution in these alloys is provided by coarsening resistant nano size $Al_{13}(Fe, V)_3Si$, and $Al_{13}Cr_2$+Al_3Zr dispersoids respectively. The microstructure of these alloys is shown in Figure 2.4, the Al-Fe-V-Si alloy contains <100nm precipitates whereas Al-Zn-Cr alloys have ~200nm size precipitates in Al matrix.

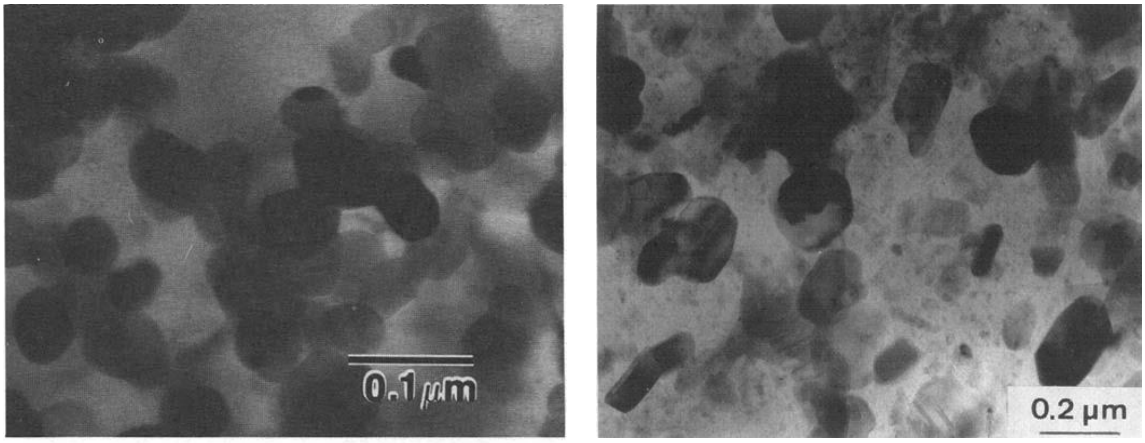

(a) Al-Fe-V-Si **(b) Al-Zn-Cr**

Figure 2.4 (a) $Al_{13}(Fe, V)_3Si$ dispersoids in Al-Fe7.9-V1.5-Si1.5 (wt%) (Skinner et al., 1986), (b) Al_3Zr dispersiods in Al-Cr5-Zr2 (wt%) (Bouchaud et al., 1991).

These RS alloys show fairly high elevated temperature strength. For example Prakash et al. (1999) measured the strengths of atomised/extruded Al-Fe8-V-Si2 (wt%) and Al-Fe8-

Ce4 (wt%) at 300°C to be ~208MPa. Bouchaud et al. (1991) measured the strength of atomised/extruded Al-Cr5-Zr2 (wt%) at 300°C to be ~130MPa. In comparison, the strength of conventional Al alloys 2024-T6 and 2618-T351 at 300°C is ~60-70MPa. Traditionally Al-Si alloys have been used in piston application. A company 'RSP Technology' produces RS Al-Fe-Si alloys by melt-spinning followed by bulk processing[G]. These RS alloys have been reported to have excellent elevated temperature properties, which are much better than conventional Al alloys. The company offers to use these alloys in pistons, pump housing, impellers, and valves replacing conventional Al alloys, Ti and steel between 150°C-450°C. A few examples of the properties of its alloys for high temperature application are provided in Table 2.2.

Table 2.2 Properties of RS Al alloys produced by 'RSP Technology'.

Alloy	Composition (wt%)	UTS (MPa)			E (GPa)
		20°C	150C°C	300°C	23°C
RSA-905	AlFe2.5Ni5Cu2.5Mn1Mo0.8Zr0.8	600	500	180	90
RSA-4019	AlSi20Fe5Ni2	400	380	175	
RSA-461	AlSi21Cu4Mg1.2Fe2.5Ni1.5	550	440	180	

2.4.3 Quasicrystalline phase in Al alloys

Inoue and coworkers produced an RS $Al_{93}Fe_3Cr_2Ti_2$ alloy which had elevated temperature properties better than other conventional and RS alloys (Inoue, 1998). In this alloy, icosahedral quasicrystalline particles were observed.

The quasicrystalline phase is a complex intermetallic phase, which is aperiodic and lacks translational symmetry; however, it exhibits rotational symmetries. Shechtman et al.

[G] www.rsp-technology.com

(1984) were the first to report the formation of icosahedral[H] quasiperiodic crystals (or quasicrystals in short) in an RS $Al_{86}Mn_{14}$ alloy which exhibited a five-fold diffraction pattern as shown in Figure 2.5. Five-fold symmetry is prohibited in conventional crystallography, and for this reason, quasicrystals had been one of the most debated entities in the realm of complex intermetallics. However, the debate has been settled in favour of the quasicrystals, with their existence being unequivocally proven and accepted by the scientific community (Dubois and Wei, 2005).

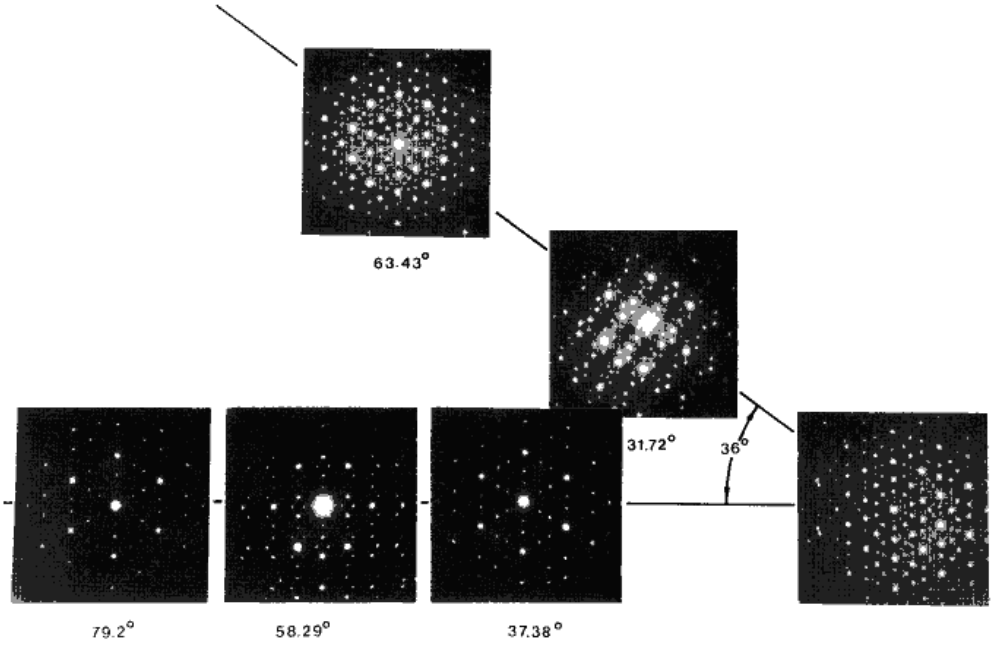

Figure 2.5 The diffraction patterns produced from icosahedral quasicrystals in an $Al_{84}Mn_{14}$ (at.%) alloy showing 2, 3 and 5 fold symmetries (Shechtman et al., 1984).

Soon after the first discovery, decagonal, octagonal and dodecagonal phases were discovered with the axes of ten, eight or twelve-fold symmetry respectively (Dubois and Wei, 2005). Initially the quasicrystalline phase was discovered in rapidly solidified alloys and it was believed that only such phase could only exist in a metastable state; however, a thermodynamically stable icosahedral quasicrystal was soon found in Al-Cu-Li alloy

[H] The rotational symmetries are similar to icosahedral point group therefore it was called 'icosahedral phase'.

(Dubost et al., 1986). Quasicrystals are known to have high hardness, high modulus, low coefficient of friction and low toughness (Dubois and Wei, 2005).

This review focuses on a metastable, icosahedral quasicrystalline alloy produced by rapid solidification.

2.5 A Quasicrystalline Al alloy for elevated temperature applications

Hard icosahedral quasicrystalline phase (I-phase) in a ductile Al matrix is a good combination to compensate for the brittleness of the I-phase and low strength of Al matrix and this draws a great technological interest. I-phase has been known to form in Al-TM (transition metal) alloys. It has been observed in binary alloys e.g. Al-Mn (Shechtman et al., 1984) , Al-V (Inoue et al., 1986), Al-Cr (Inoue et al., 1987); ternary alloys e.g. Al-Fe-Cr (Manaila et al., 1989), Al-Fe-Nb (Audebert et al., 1997); and quaternary alloys e.g. Al-Fe-Cr/V-Ti (Inoue, 1998), and Al-Fe-Cr-Ti/V/Ta/Nb (Galano et al., 2009b).The focus of this review is a high temperature $Al_{93}Fe_3Cr_2Ti_2$ alloy which was first produced by Inoue and coworkers through rapid solidification, and it contained nano size I-phase particles (Inoue, 1998).

Nanoquasicrystalline $Al_{93}Fe_3Cr_2Ti_2$ alloy contains a high volume fraction >40% of the spherical I-phase particles in Al matrix. The microstructure of a melt spun nanoquasicrystalline $Al_{93}Fe_3Cr_2Ti_2$ alloy by Galano et al. (2009b) is shown in Figure 2.6.

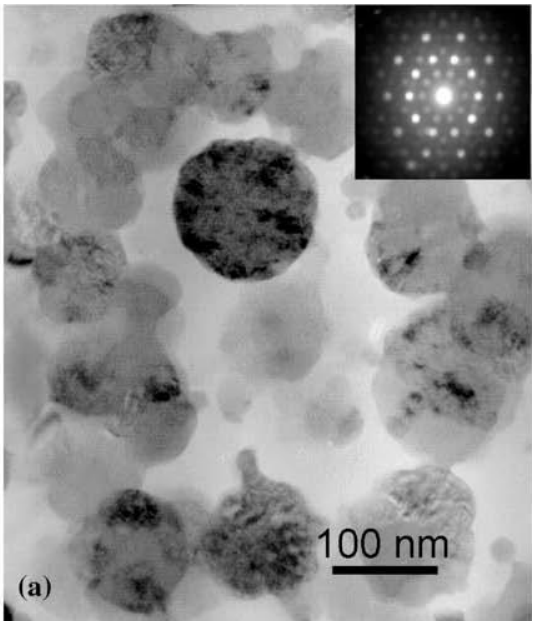

Figure 2.6 Microstructure of a melt spun Al-Fe-Cr-Ti alloy in 'as spun' state (Galano et al., 2009b).

Each element present in the Al-Fe-Cr-Ti system may possibly have an effect on the properties of the alloy. For example, Al is an important quasicrystalline forming element, and the Al matrix imparts ductility to the alloy; therefore, the ratio of matrix to quasicrystals is important in determining the dominant fracture mechanism (Audebert et al., 2002). Fe additions in the Al-Fe-Cr-Ti system contribute to the thermal stability of the alloy (Kimura et al., 2000). Cr has been observed to promote the quasicrystalline formation and decrease the size of the quasicrystals (Kimura et al., 2000). Ti has a high melting point and a low diffusivity and it provides thermal stability to the quasicrystals such as Al-Fe-Cr (Galano et al., 2009b).

2.5.1 Mechanical properties at room temperature

Two methods have been widely employed to successfully produce the I-phase containing alloys in Al-Fe-Cr-Ti system, which are : (i) melt spinning (Audebert et al., 2002, Galano et al., 2004, Galano et al., 2009b), and (ii) gas atomisation (Inoue, 1998, Todd et al.,

2004, Yamasaki et al., 2007, Vojtěch et al., 2012, Rounthwaite, 2012) (details in Table 2.3).

The powders obtained from the gas atomization process are sieved in various powder fractions and consolidated in the form of bars. The powder fraction size affects the hardness and strength of the bulk extruded alloy, whereby smaller the powder fraction size greater the alloy strength (Todd et al., 2004, Rounthwaite, 2012). This is due to the presence of finer microstructure present in the smaller powder particle size.

The bulk alloy in Al-Fe-Cr-Ti system displays excellent room temperature tensile strength which is of the order of high strength Al alloy (7075-T6), and the elastic modulus higher than any commercial Al alloy (e.g. 7xxx series). Some examples of the room temperature mechanical properties of the bulk extruded alloys in Al-Fe-Cr-Ti system are provided in Table 2.3 alongside the alloy composition and processing method used.

The excellent strength was thought to be provided by various strengthening mechanisms in these alloys such as: (i) Orowan's mechanism (Audebert et al., 2002, Vojtěch et al., 2007, Galano et al., 2009b) (ii) internal strains (Audebert et al., 2002), (iii) solid solution strengthening (Galano et al., 2009b), and (iv) Hall-Petch effect (Vojtěch et al., 2007, Inoue and Kimura, 2001).

Table 2.3 Composition, powder fraction size, processing conditions and room temperature mechanical properties of extruded RS Al-Fe-Cr-Ti alloy.

Composition (at%)	Powder size(μm)	Processing	UTS	σ_{yield}	$\varepsilon_{failure}$	E	HV	$\dot{\varepsilon}$	Reference
			MPa	MPa	%	GPa		s^{-1}	
$Al_{93}Fe_3Cr_2Ti_2$	~26	Atomisation, Extrusion (400°C)	658	545	4.4	85	192	5.00E-04	(Inoue, 1998)
	125	Atomisation, Extrusion (400°C)	537	464	5.4	90	165	5.00E-04	
$Al_{93}Fe_3Cr_2Ti_2$	25-50	Atomisation, Extrusion (400°C)	596	520	5.9	80	162-169	3.00E-04	(Todd et al., 2004)
$Al_{93.1}Fe_{2.3}Cr_{2.3}Ti_{2.3}$	<38	Atomisation, Extrusion (400°C)		490	4			5.00E-04	(Nagaishi et al., 2007)
$Al_{92.5}Fe_{2.5}Cr_{2.5}Ti_{2.5}$	<38	Atomisation, Extrusion (350°C)		540	4			5.00E-04	(Yamasaki et al., 2007)
$Al_{95}Fe_{1.1}Cr_3Ti_{0.8}$	<100	Atomisation, Extrusion (480°C)	380	166	15		132	1mm/min	(Vojtěch et al., 2012)
$Al_{93}Fe_3Cr_2Ti_2$	25-50	Atomisation, Extrusion (375°C)	545	462	6.8	82	174	4.00E-04	(Rounthwaite, 2012)

UTS = Ultimate tensile strength, σ_{Yeild} = Yield strength, $\varepsilon_{failure}$, failure strain, HV = Microhardness, E = Young's Modulus, $\dot{\varepsilon}$= Strain rate

2.5.2 Thermal stability

In the Al-Fe-Cr-Ti system, a high volume fraction of I-phase is present in the Al matrix. However, the I-phase in this system is metastable and it transforms at elevated temperatures. Todd et al. (2004) studied various powder fraction sizes of atomised powders of a nanoquasicrystalline $Al_{93}Fe_3Cr_2Ti_2$ using differential scanning calorimetry. The main exothermic peak at ~820K was found to be related to the decomposition of metastable I-phase. The peak height increased with the decrease in powder particle size, and it was associated with the increasing degree of metastability in smaller powder particles due to a higher cooling rate during atomisation (Todd et al., 2004)

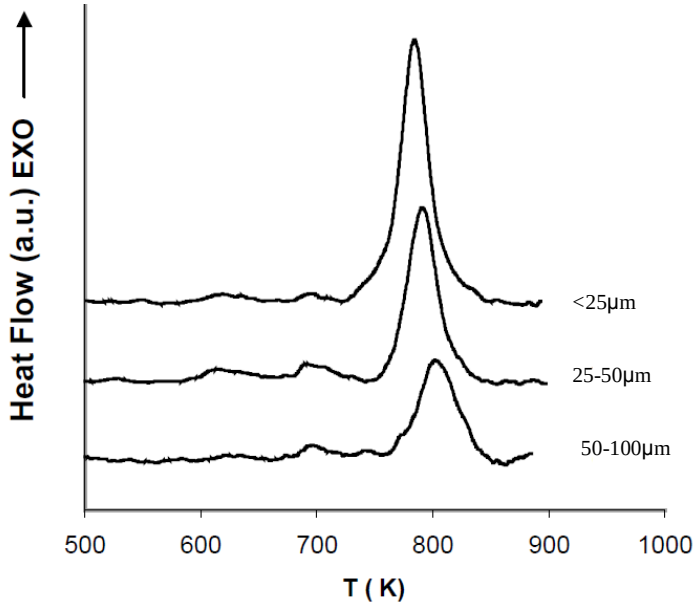

Figure 2.7 Differential scanning calorimetry of I-phase containing $Al_{93}Fe_3Cr_2Ti_2$ atomised alloy of various powder fraction sizes. The scans were carried out at a heating rate of 20K/min. (Todd et al., 2004).

Galano et al. (2009b) performed short duration 30min heat treatments at 450°C and 550°C in the melt spun nanoquasicrystalline $Al_{93}Fe_3Cr_2Ti_2$ alloy and the microstructure is shown in Figure 2.8. The alloy exhibited very good thermal stability as the microstructure contained a majority of the I-phase after treatment at 450°C. However, after 550°C heat

treatment, it transformed into stable (Al_3Ti, $Al_{13}Cr_2$, $Al_{13}Fe_4$) and metastable ($Al_{13}(Fe, Cr)_{2-4}$) intermetallics.

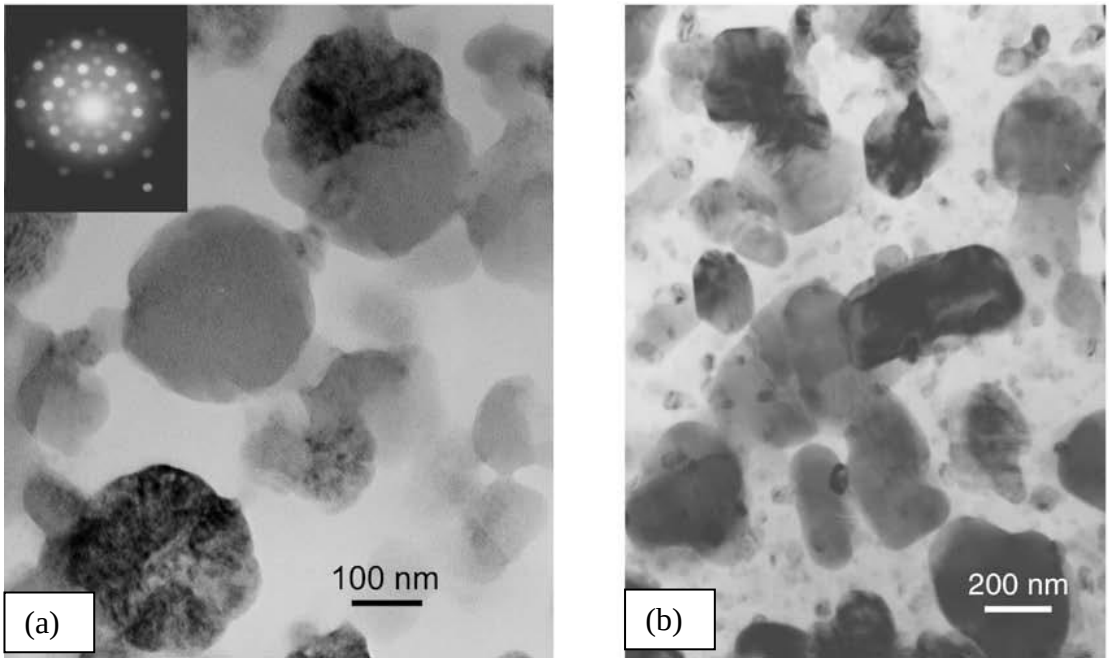

Figure 2.8 Melt spun nanoquasicrystalline $Al_{93}Fe_3Cr_2Ti_2$ alloy after 30min heat treatment at: (a) 450°C, (b) 550°C (Galano et al., 2009b).

Recently, García-Escorial et al. (2015) performed a study on long duration (1 to 1000hrs) heat treatments at 400°C on the bulk extruded nanoquasicrystalline $Al_{93}Fe_3Cr_2Ti_2$ alloy. The I-phase transformation into various stable (Al_3Ti, $Al_{23}Ti_9$, $Al_{13}Fe_4$, $Al_{13}Cr_2$) and metastable (Al_6Fe) intermetallics was reported, using XRD.

The I-phase transformation at elevated temperatures can have a detrimental effect on the mechanical properties of the alloy. However, in general, the thermal stability studies of nanoquasicrystalline $Al_{93}Fe_3Cr_2Ti_2$ alloy lack the evaluation of the effects of I-phase transformation on the mechanical properties (except microhardness). The effect of I-phase transformation on the tensile strength, elastic moduli and fracture behaviour of the alloy has never been studied in the bulk $Al_{93}Fe_3Cr_2Ti_2$ alloy. Consequently, the understanding of corresponding changes in the strengthening mechanisms due to the I-phase transformation is also deficient.

2.5.3 Elevated temperature mechanical properties of $Al_{93}Fe_3Cr_2Ti_2$ alloy

Room temperature mechanical properties are important; however, it is the high temperature performance which sets the RS $Al_{93}Fe_3Cr_2Ti_2$ alloy apart from the conventional Al alloys. Inoue (1998) claimed that the $Al_{93}Fe_3Cr_2Ti_2$ alloy exceeded the US Airforce performance goals for the development of an elevated temperature alloy. Figure 2.9 shows the effect of temperature on the tensile strength of the bulk extruded nanoquasicrystalline $Al_{93}Fe_3Cr_2Ti_2$ alloys, as observed in a few studies. Additionally, the approximate behaviour of a high strength conventional Al alloy is also shown with a dotted line for comparison. The strength decreases as a function of temperature; however, in comparison with high strength conventional Al alloys the $Al_{93}Fe_3Cr_2Ti_2$ alloy maintains a very high strength at elevated temperatures.

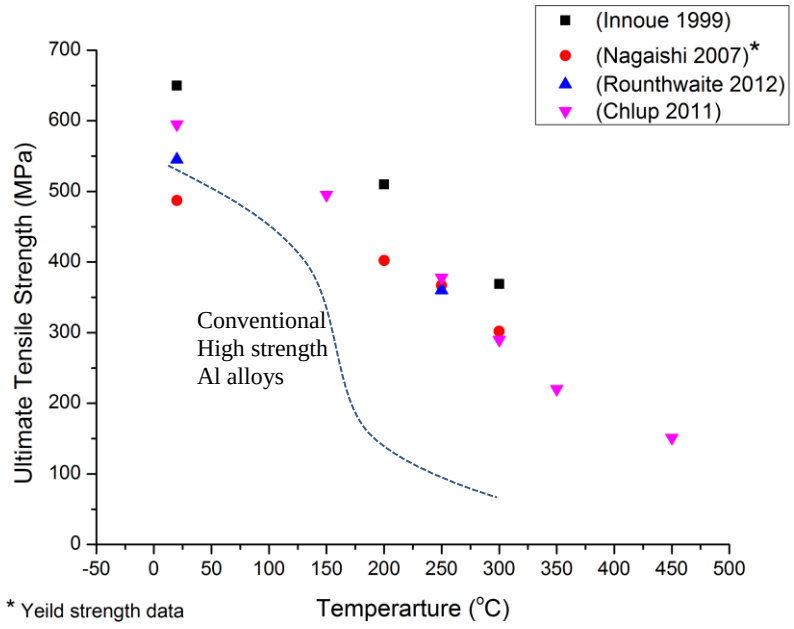

Figure 2.9 Elevated temperature tensile strength of RS $Al_{93}Fe_3Cr_2Ti_2$ quasicrystalline alloy (Nagaishi et al., 2007, Rounthwaite, 2012, Inoue, 1998, Chlupová et al., 2011). The approximate trend of the strength of high strength conventional Al alloys with temperature is marked with dotted lines, adapted from (ASM, 1990) and (Rice, 2003).

Mostly, the studies in the nanoquasicrystalline (NQX) $Al_{93}Fe_3Cr_2Ti_2$ alloys have been limited to small temperature ranges or a single strain rate. Therefore; flow stress

behaviour and plasticity parameters (and consequently the mechanisms) in the bulk NQX $Al_{93}Fe_3Cr_2Ti_2$ alloy are not well known e.g. strain hardening, strain rate hardening, stress exponent, the activation energy of deformation, to name a few. Similarly, the effect of temperature on the behaviour of elastic constants is also not known. There have been some hints of the occurrence of dynamic strain ageing (DSA) in the alloy in a few previous studies (section 2.6); however, no exclusive study is available. The fatigue behaviour of the alloy also needs to be investigated.

What follows is a brief literature review of the DSA, creep and fatigue in the RS Al alloys with a special focus on Al-Fe-Cr-Ti alloys.

2.6 Dynamic Strain Ageing

The jerky or serrated flow is a plastic instability which was first observed in the 1920s and named as the Portevin Le Chatelier (PLC) effect after it's discoverers (Robinson, 1994). In the 1950s, Cottrell successfully explained the yield point phenomena[I] in mild steels by proposing that given a long enough time, solute atoms diffuse towards a dislocation and form a solute cloud or atmosphere which anchors the dislocation to increase its strength (Abbaschian and Reed-Hill, 2008). The unlocking requires an extra force which causes the upper yield point, and after breaking free, the dislocation moves relatively freely which results in a lower yield point. The yield point does not appear if the test is unloaded and restarted but reappears if the material is aged for some time (known as strain ageing). During a mechanical test (tensile, compression, torsion), under a high enough temperature and low enough strain rate, the solute (interstitial or substitutional) atoms are able to diffuse towards the moving dislocations and 'pin' those

[I] Instead of smooth elastic to plastic transition, a sharp upper yield point and a low yield point were observed to occur in iron and low carbon steels. If the tensile test was interrupted during the plastic flow and immediately restarted again the two separate yield points do not appear. However, if the material was aged for some time and retested, the upper and lower yield points would again reappear.

dynamically, which is referred to as dynamic strain ageing or DSA (Abbaschian and Reed-Hill, 2008). The solute atoms 'age' the dislocation to increase the flow stress and once a dislocation breaks free from the solute under the action of increased flow stress a jerk in the stress-strain flow curve appears. Repeated pinning and unpinning during the test gives rise to a 'serrated flow'. PLC is one of the manifestations of DSA (Robinson and Shaw, 1994).

2.6.1 DSA manifestations

With the increase in temperature, the DSA has been observed to cause one or more of the following effects in stress-strain curves: (i) increase (or a plateau) in the yield strength referred to as 'yield strength anomaly', (ii) increase in work hardening rate, (iii) increase in Hall-Petch slope, (iv) reduction in ductility, (v) reduction (and often negative value) of strain rate sensitivity (SRS), and (vi) serrated flow (Rodriguez, 1984). A schematic of these anomalous behaviours is shown in Figure 2.10.

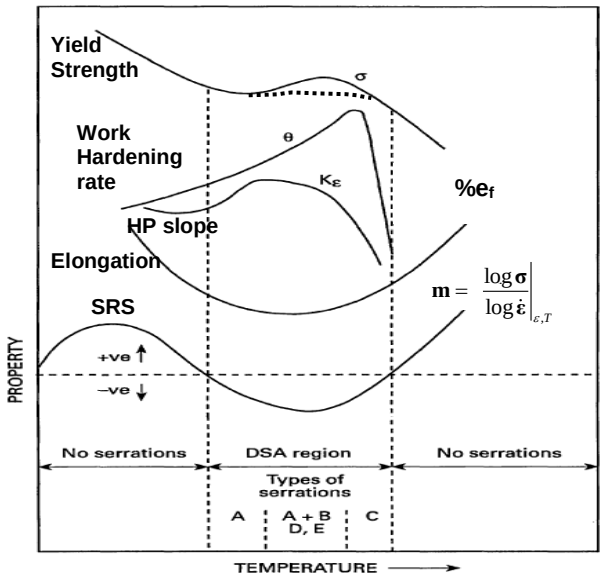

Figure 2.10 Schematic illustration of various DSA manifestations (Rodriguez, 1984).

In fact, all of these anomalies are a manifestation of DSA. Further, a presence of one or more of these anomalies in a specific temperature-strain rate range, hints towards the occurrence of DSA. The 'yield strength anomaly' is the situation whereby the flow stress becomes independent of temperature. A 'hump' or a plateau in the yield (or flow) stress vs temperature curve is dependent on the intensity or severity of DSA and its balance by the recovery rate (Morris, 1974).

2.6.2 Serrated flow conditions and types of serrations

The serrations in a flow curve can also possibly occur due to reasons other than the DSA, such as adiabatic heating or phase transformation during the test (Rodriguez, 1984) . Therefore, it becomes imperative to unambiguously confirm of the occurrence of the DSA with the presence of some other manifestation(s) in addition to the serrated flow. There are various types of serrations identified in DSA, a summary is provided in Table 2.4 and shape of these serrations can be observed in Figure 2.11.

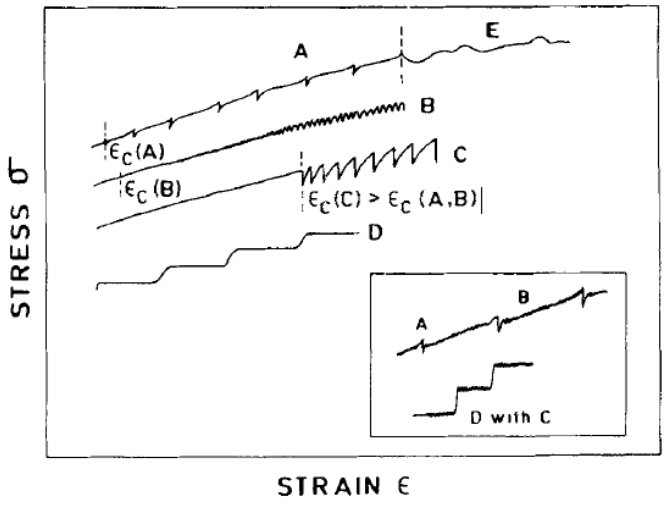

Figure 2.11 Examples of various types of serrations during DSA (Hall, 1970),(Rodriguez, 1984).

Table 2.4 A summary of various types of serrations during DSA (Hall, 1970),(Rodriguez, 1984).

Type	Shape	Condition
Type A	Serrations with abrupt load rise followed by drop below general level of σ-ε curve	
Type B	Load oscillations in quick succession, around a general level of σ-ε curve	Observed at high strain rates
Type C	Load drops below general level of σ-ε curve	Occurrence at high temperature, lower strain rates and higher strain values
Type D	Serrations are similar to plateaus in σ-ε curve but devoid of any work hardening	
Type E	Similar to type A	Observed at higher strains

2.6.3 DSA in RS Al alloys

The presence of substitutional (e.g. Mg, Fe) or interstitial (e.g. Si, Li) solutes in an Al matrix can cause DSA (Antolovich and Armstrong, 2014) and Al-Mg alloys are the most widely studied for DSA.

There are only a limited number of studies exclusively focused on DSA in the RS Al alloys. Table 2.5 summarises the studies on some RS Al alloys displaying DSA. Skinner et al. (1989) worked on the bulk RS alloys of Al with Fe, Ti, Zr and Si to study the DSA behaviour (compositions and details in Table 2.5). They concluded that Si was mainly responsible for the DSA at room temperature, and Fe was responsible for DSA between ~150-250^{o}C whereas Ti was speculated to be responsible for DSA at ~275^{o}C in the RS Al alloys under study. Bouchaud et al. (1991) worked along similar lines and found Fe to be responsible for DSA in RS Al-Fe-V-Si alloys at ~150^{o}C or similar temperatures whereas Cr was expected to be responsible for DSA in Al-Cr-Zr based alloy. Li and Bakker (1995) worked on a multi-component alloy Al-Si-Cu-Zn-Fe-Mn-Mg-Cr-Ni-Ti and found DSA occurring at ambient and low temperatures due to Mg (details in Table 2.5).

In RS $Al_{93}Fe_3Cr_2Ti_2$ alloys, there has been no exclusive attempt to unequivocally prove the presence of DSA. Rounthwaite (2012) and Pedrazzini (2014) worked on the same alloy and separately found indications which could be attributed to the DSA. Rounthwaite (2012) observed a lower ductility at 250°C and $10^{-4}s^{-1}$, whereas separately Pedrazzini (2014) observed the serrations (at high strain rate tests) at 350°C; however, the other manifestations of DSA were not found or discussed. The mechanical behaviour of the NQX $Al_{93}Fe_3Cr_2Ti_2$ alloy can be understood by investigating the occurrence of DSA. In the present work, it was carried out by finding its various manifestations, using a range of temperatures and strain rates in tensile tests.

Table 2.5 DSA in the rapidly solidified Al alloys tested under uniaxial tensile loading.

Alloy Composition (wt%)	Synthesis Method	DSA Related Parameters						Reference
		Strain Rate	Approximate. Temperature (in ^{o}C) related to			Serrations	Responsible Solute	
			Minima in SRS exponent	Minima in Ductility	Yield Strength Anomaly			
Al-8.5Fe-1.3V-1.7Si	Melt Spinning , Comminution ,Compaction and Extrusion	8.9E-2 to 8.9E-5	~150	150 to 225	RT to 325		Fe	(Skinner et al., 1989)
Al-6Fe-1V-1Si		5.56E-2 to 5.56E-5	~80	100 to 200	RT to 325		Fe	
Al-8.5Ti-3Si		1.11E-2 to 5.56E-5 (Jump)	~225	~250			Ti	
Al-10Fe-5Si			RT	~170 and at ~275			Si at RT, and Fe at high T	
Al-9.9Zr-6.1Si , Al-11.5Fe-1.5Zr			~RT and at ~200	~RT and at ~225			Si at RT, and Zr at high T	
Al-8.5Fe-1.3V-1.7Si		5E-5, 3.7E-6 (jump)	~125	~175			Fe	(Bouchaud et al., 1991)
Al-5Cr-2Zr		2.22E-5 , 4.44E-6	~150	150 to 250			Cr	
Al-11.7Fe-1.2V-2.4Si		6.56E-5 , 6.56E-6	150 & 250	~ 200	~100		Fe	(Mitra, 1992)
Al-7.1Si-2.7Cu-1.5Zn-1.1Fe-0.3Mn-0.3Mg-0.1Cr-0.1Ni-0.04Ti		1E-2, 1E-3	-40 to 60	~RT to 60		Type A and C	Mg	(Li and Bakker, 1995)

SRS is strain rate sensitivity

2.7 Creep

Rate dependent plasticity or creep is the elevated temperature ($T>\sim 0.3T_{melting}$) deformation of materials when stress levels are generally low (Frost and Ashby, 1982). The steady state creep strain rate can be approximated using power law creep Eqn. 2.10 (Evans and Wilshire, 1985).

$$\dot{\varepsilon} = C\sigma^{n_{se}} e^{\left(-\frac{Q}{RT}\right)} \qquad \textbf{Eqn. 2.10}$$

Where $\dot{\varepsilon}$ is the steady state strain rate in stage II of creep, n_{se} is the stress exponent, Q is the activation energy, T is temperature in K, σ is the constant applied stress, C is a constant. The apparent activation energy of creep can be obtained by using Eqn. 2.11.

$$Q = -R\frac{\delta \ln \dot{\varepsilon}}{\delta\left(1/T\right)}\bigg|_{\sigma} \qquad \textbf{Eqn. 2.11}$$

2.7.1 Creep deformation mechanisms

The stress exponent (n_{se}) provides a great deal of information about the deformation mechanisms in the materials under study. Generally, the conventional metallic materials can be divided into two classes ('M' and 'A'). Pure metals (class 'M') have the stress exponent close to 5 and the activation energy similar to that of lattice self-diffusion (Evans and Wilshire, 1985, Tjong and Mai, 2003). Solid solution strengthened alloys (class 'A') have the stress exponent close to 3 and the activation energy values matching the solute diffusion in the lattice. The rate controlling mechanisms are 'dislocation glide and climb' for the class 'M' and 'viscous solute drag to dislocation glide' for class 'A' materials (Evans and Wilshire, 1985). In superplastic materials, the grain boundary (GB) sliding is the dominant creep mechanism, with n_{se} values around 2 or lower (Chateau, 2011). The dispersion

strengthened (DS) metallic materials show very high n and Q values, with dislocation creep being the dominant mechanism at intermediate and high temperatures (Mukherjee, 2002). The summary of temperature/strain rate related plasticity parameters (n, Q) and the rate-controlling deformation mechanism(s) of the above mentioned material classes is provided in Table 2.6.

Table 2.6 Deformation mechanism, stress exponent and activation energy for different classes of materials (Tjong and Mai, 2003).

Material	(Approximate) n_{se}	Activation Energy (Q)	Rate Controlling Mechanism
Superplastic	~2 <	Related to GB diffusion	GB sliding
Class A	~3	Related to solute diffusion	Viscous drag during dislocation glide
Class M	~5	Related lattice self-diffusion	Dislocation climb and glide
Dispersion Strengthen	~(5.5-30)	Very high values of Q may be observed	Dislocation creep

A modified form of the creep equation can be written as a Mukherjee-Bird-Dorn relation in Eqn. 2.12 (Mukherjee, 2002). The various plastic flow mechanisms during the creep are defined under a 'steady state condition' of the flow rate in the power law creep equation.

$$\dot{\varepsilon} = C_1 \frac{Gb}{kT} D_o \left(\frac{\sigma}{G}\right)^{n_{se}} \left(\frac{b}{d}\right)^{p} e^{\left(-\frac{Q}{RT}\right)} \qquad \textbf{Eqn. 2.12}$$

Where $\dot{\varepsilon}$ is the steady state strain rate, C_1 is a constant, G is the shear modulus, b is the Burgers vector. k is the Boltzmann constant, D_o is a pre-exponential factor for diffusion, d is the grain diameter, and p is grain size exponent, T is temperature and Q is activation energy.

2.7.2 Creep in dispersion strengthened Al alloys

Pure aluminium exhibits class M behaviour with n_{se}~4.4 (between 370 to 593^{o}C) and Q~142kJ/mol which is the activation energy for Al self-diffusion (Frost and Ashby, 1982). Abnormally high values for n_{se} and Q are observed in dispersion strengthened Al materials; those include various composites and alloys (both conventional and RS), a summary of a few such alloys is provided in Table 2.7.

Table 2.7 n_{se} and Q of a few dispersion strengthen aluminium alloys.

Alloy	Processing	Test	Temp (T^{o}C)	n_{se}	Q (kJ/mol)	Reference
Al-Fe-Ce	Casting	Compres-sion	250-300	22	~229	(Yaney and Nix, 1987)
			450-500	8.2	~538	
(RS) Al-Cr-Zr	Atomisation, extrusion	Tensile	Up to 250	>21	~77	(Brahmi et al., 1996)
			300-600	7-10	Up to 300	
(RS) Al-Fe-X-Si (X=Cr,Mo,Mn)	Melt spinning , Communition, Extrusion	Tensile	300-554	~17-11	~250-700	(Carreño et al., 1997)
(RS) Al-Fe-V-Si	Jet casting, Communition, Extrusion	Tensile	350-554	~25	400	(Carreño and Ruano, 1998)
(RS) Al-Fe-V-Si	Powder metallurgy	Compres-sion	300-450	17-14	296	(Peng et al., 1999)
Al-Cu-Mg-Ti	Osprey Forming, Extrusion	Tensile (jump and quasi-static)	300	17	200-135	(Eddahbi et al., 2007)
			400	7		
			520	4.5-3		

Galano et al. (2009a) studied the plastic temperature-strain rate behaviour of the melt spun $Al_{93}Fe_3Cr_3Ti_2$ alloy ribbons in the temperature range of 300-350^{o}C using tensile testing and found high values (~7) of the stress exponent. However, the study was carried out on ribbons which showed little or no plasticity due to porosity so their results cannot be compared to the bulk alloys. A study of the plastic behaviour of the bulk I-phase containing $Al_{93}Fe_3Cr_3Ti_2$

alloy comprising a wider range of temperatures and quasi-static strain rates has not been undertaken. Such a study should help to explain the elevated temperature plastic flow mechanisms in the alloy.

2.8 Fatigue

In engineering applications, fatigue causes premature component failure. Generally, the fluctuating loads are well below the yield strength of the materials, so negligible plastic deformation is involved during the fatigue process giving little warning prior to failure (Lee, 2005).

2.8.1 Fatigue in RS Al alloys

Owing to their inherent high strength, the RS Al alloys show a better high cycle fatigue (HCF, failure cycles $>10^5$) performance, as compared to the conventional Al alloys as found in studies by Ohtera et al. (1992) and Haas et al. (1999) [J]. There has been only one very recent study of the fatigue testing of bulk extruded NQX $Al_{93}Fe_3Cr_2Ti_2$ alloy by Chlupova et al. (2016) at room temperature. They used various alloy powder sizes (0-25μm, 25-50μm and 50-100μm) and conducted tests at five stress levels using 5Hz frequency at a load ratio of 0.1, the SN curves are shown in Figure 2.12. Fatigue performance at 10^6 cycles for the alloy was observed to be better than the conventional alloys (Al2024, Al7075, Al5083). The study did not incorporate a very high cycle fatigue (VHCF) regime, and it did not discuss the role or nature of defects/inclusion causing fatigue failures and it was limited to room temperature.

[J] Othera et. al. worked on (atomised+extruded) $Al_{88.5}Ni_8Mm_{2.5}$ (Mm = mischmetal).
Hass et. al. worked on (atomised+extruded) $Al_{94}CrMn_3Cu_2$ I-phase containing alloy.

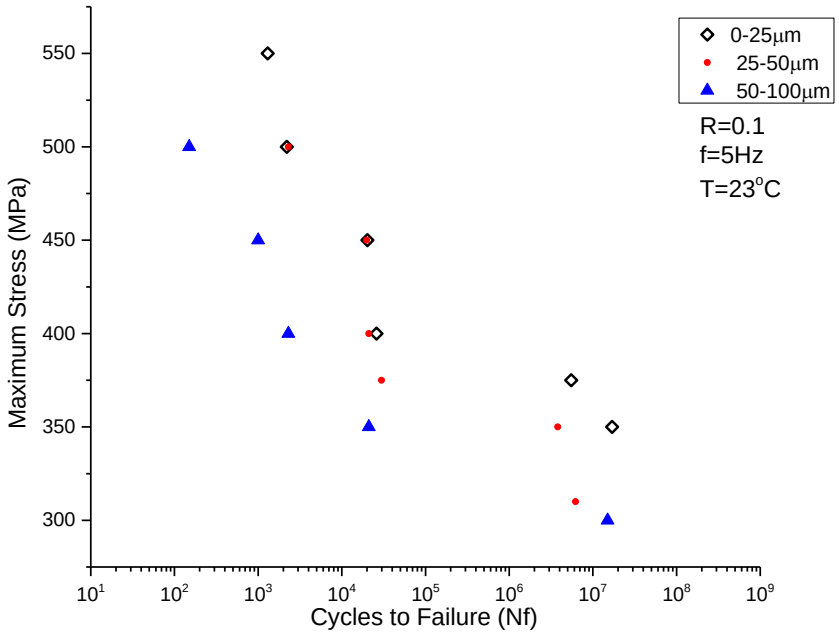

Figure 2.12 Room temperature SN curves for $Al_{93}Fe_3Cr_2Ti_2$ alloy for three powder sizes (Chlupova et al., 2016).

2.8.2 Very high cycle fatigue (VHCF) testing

The materials in the engineering applications such as automobiles, locomotives, and rotating parts in the jet engine may reach cycles in ranges of 10^8,10^9 and even 10^{10} respectively, so the concept of determining the fatigue limit at ~10^7 cycles may not hold (Marines, 2003). Using a conventional frequency of 60Hz, 10^8 cycles can be achieved in nineteen days, 10^9 in over six months and 10^{10} in over five years. Such long times are economically unfeasible and unrealistic in terms of material testing and development. In the 1950s, Mason (1956) showed that the ultrasound waves can be used to fracture the material. During the next three decades, the evolution of the technique continued as it developed and matured (Stanzl-Tschegg and Mayer, 2001) to incorporate a broad range of measurement and testing including crack growth studies, multiaxial loading, high/ low temperature testing and corrosive environment testing (Bathias and Paris, 2004). Ultrasonic testing is recognised as an efficient technique to

study the material fatigue, within reasonable time durations, even for a very high number of cycles (~>10^8) (Bathias and Paris, 2004). A commonly used 20kHz ultrasonic fatigue machine takes only about 14hrs to reach 10^9 cycles and six days to reach 10^{10} cycles which makes it very efficient in conducting such tests.

2.8.3 VHCF in Al alloys[K]

The alloys may be divided into type I and type II alloys from a fatigue fracture standpoint as studied in the HCF and VHCF regimes (Mughrabi, 2006). The former are inclusion free materials, and the latter has internal inhomogeneities to cause fracture initiations.

Some Al alloys show type II behaviour (e.g: Al-Si-Cu (Zhu et al., 2006), and Al-Mg-Si (Mayer et al., 1999)), whereas many others have been observed to show type I behaviour (e.g: Al6061 (Takahashi et al., 2014), Al2024 (Mayer et al., 2013) and AA6082 (Höppel et al., 2011)). Prediction of fatigue behaviour in Al alloys is, therefore, difficult. However, it can be studied reliably through experimentation.

There has been no account of a VHCF study or any high temperature fatigue study in the NQX $Al_{93}Fe_3Cr_2Ti_2$ alloy and corresponding fatigue fracture behaviour of this alloy is not known. These factors necessitate a fatigue study, on the NQX alloy, incorporating a higher number of cycles and/or elevated temperature.

[K] Only conventional alloys are mentioned in this section as VHCF studies on RS Al alloys are not available in open scientific literature.

2.9 Summary

Conventional Al alloys suffer huge strength drop off at elevated temperatures which restrict their use in elevated temperature engineering applications. Rapid solidification allows the formation of a new class of Al alloys which exploits various strengthening mechanisms and maintain elevated temperature strength fairly well. Quasicrystalline phase has a high hardness and high modulus and it is sometimes present in the rapidly solidified alloys. A promising rapidly solidified alloy is $Al_{93}Fe_3Cr_2Ti_2$ which contains a metastable nano size quasicrystalline phase. The alloy has a high thermal stability and it maintains elevated strength much better in comparison with the conventional Al alloys. Several mechanical properties and deformation mechanisms are unknown for the alloy and the following areas were identified for in-depth study.

- There have been some phase transformation studies on the melt spun and bulk alloys; however, the effect of the phase transformation on any changes in the strengthening mechanisms of the alloy is not known.
- The effect of prolonged temperature exposure on the I-phase transformation and on the corresponding mechanical properties of the bulk alloy is also unknown.
- The knowledge of the behaviour of elastic constants of the alloy at elevated temperatures is also lacking.
- Room temperature strain rate hardening behaviour is not available. Similarly, the effect of multiple quasi-static strain rates at a wide range of elevated temperatures (e.g. 150 to 500^{o}C) has never been studied in bulk samples. As a result, the knowledge of the deformation mechanisms at elevated temperatures is

underdeveloped. Strain hardening behaviour of the alloy over the wide temperature range has never been studied in the open literature.

- Dynamic strain ageing in the alloy has never been unambiguously confirmed, although some studies have hinted towards its occurrence.
- Fatigue behaviour of the alloy is not well known in high cycle regime, and has never been studied in a very high cycle regime (VHCF). The high temperature fatigue testing has also never been carried out in open scientific literature.

References

Abbaschian, R. and Reed-Hill, R. (2008) *Physical metallurgy principles.* Cengage Learning.

Antolovich, S. D. and Armstrong, R. W. (2014) 'Plastic strain localization in metals: origins and consequences', *Progress in Materials Science*, 59, pp. 1-160.

Ashby, M. 'Oxide dispersion strengthening'. *Proc. 2nd Bolton Landing Conf., GS Ansell, ed., Gordon and Breach, New York, NY*, 143.

Ashby, M. (1970) 'The deformation of plastically non-homogeneous materials', *Philosophical Magazine*, 21(170), pp. 399-424.

Ashby, M. F. and Jones, D. (2005) *Engineering materials 1: an introduction to properties, application, and design. Elsevier Butterworth-Heinemann, Amsterdam, Boston*.

ASM (1990) *Nonferrous Alloys and Special-Purpose Materials, vol. 2. ASM International, Materials Handbook*: ASM International.

Audebert, F., Prima, F., Galano, M., Tomut, M., Warren, P. J., Stone, I. C. and Cantor, B. (2002) 'Structural characterisation and mechanical properties of nanocomposite Al-based alloys', *Materials transactions*, 43(8), pp. 2017-2025.

Audebert, F., Sirkin, H. and Escorial, A. G. (1997) 'Aluminum-base Al-Fe-Nb amorphous and nanostructured alloys', *Scripta materialia*, 36(4), pp. 405-410.

Bacon, D., Kocks, U. and Scattergood, R. (1973) 'The effect of dislocation self-interaction on the Orowan stress', *Philosophical Magazine*, 28(6), pp. 1241-1263.

Balint, D., Deshpande, V., Needleman, A. and Van der Giessen, E. (2008) 'Discrete dislocation plasticity analysis of the grain size dependence of the flow strength of polycrystals', *International Journal of Plasticity*, 24(12), pp. 2149-2172.

Bathias, C. and Paris, P. C. (2004) *Gigacycle fatigue in mechanical practice.* CRC Press.

Belov, N. A., Aksenov, A. A. and Eskin, D. G. (2002) *Iron in aluminium alloys: impurity and alloying element.* CRC Press.

Benson, D. J., Fu, H.-H. and Meyers, M. A. (2001) 'On the effect of grain size on yield stress: extension into nanocrystalline domain', *Materials Science and Engineering: A*, 319, pp. 854-861.

Bouchaud, E., Kubin, L. and Octor, H. (1991) 'Ductility and dynamic strain aging in rapidly solidified aluminum alloys', *Metallurgical Transactions A*, 22(5), pp. 1021-1028.

Brahmi, A., Gerique, T., Lieblich, M. and Torralba, M. (1996) 'Creep behaviour of a rapidly solidified Al-5Cr-2Zr alloy between room temperature and 823 K', *Scripta materialia*, 35(12), pp. 1449-1454.

Brown, L. M. and Ham, R. K. (1971) 'Dislocation-Particle Interactions', in Kelly, A. & Nicholson , R.B. (eds.) *Strengthening methods in crystals*: Elsevier Publishing Company.

Campbell, F. C. (2008) *Elements of metallurgy and engineering alloys.* ASM International.

Cantor, B., Assender, H. and Grant, P. (eds.) (2001) *Aerospace materials*: CRC Press.

Carreño, F. and Ruano, O. A. (1998) 'Separated contribution of particles and matrix on the creep behavior of dispersion strengthened materials', *Acta materialia*, 46(1), pp. 159-167.

Carreño, F., Torralba, M., Eddahbi, M. and Ruano, O. A. (1997) 'Elevated temperature creep behavior of three rapidly solidified Al-Fe-Si materials containing Cr, Mn, or Mo', *Materials Science and Engineering: A*, 230(1), pp. 116-123.

Chateau, J. P. (2011) 'Basics of Mechanical Properties of Metals', in Belin-Ferré, E. (ed.) *Mechanical Properties of Complex Intermetallics Complex Metallic Alloys*: World Scientific.

Chlupova, A., Chlup, Z. and Kruml, T. (2016) 'Fatigue properties and microstructure of quasicrystalline AlFeCrTi alloy', *International Journal of Fatigue,* 91 (1), pp. 251–256.

Chlupová, A., Chlup, Z., Kruml, T., Kuběna, I. and Roupcová, P. 'Microstructure, tensile properties and fatigue behaviour of bulk nano-quasicrystalline al alloy $AL_{93}FE_3CR_2TI_2$', *Nano Con,* Brno, Czech Republic, 21-23 September 2011.

Conrad, H. (1963) 'Effect of grain size on the lower yield and flow stress of iron and steel', *Acta metallurgica,* 11(1), pp. 75-77.

Corti, C., Cotterill, P. and Fitzpatrick, G. (1974) 'The evaluation of the interparticle spacing in dispersion alloys', *International Metallurgical Reviews,* 19(1), pp. 77-88.

Cottrell, A. H. (1958) 'Theory of brittle fracture in steel and similar metals', *Trans. Met. Soc. AIME,* 212.

Dieter, G. E. and Bacon, D. (1986) *Mechanical metallurgy.* McGraw-Hill New York.

Dubois, J.-M. and Wei, T. K. (2005) *Useful quasicrystals.* World Scientific.

Dubost, B., Lang, J., Tanaka, M., Sainfort, P. and Audier, M. (1986) 'Large AlCuLi single quasicrystals with triacontahedral solidification morphology'.

Eddahbi, M., Jiménez, J. A. and Ruano, O. A. (2007) 'Microstructure and creep behaviour of an Osprey processed and extruded Al–Cu–Mg–Ti–Ag alloy', *Journal of alloys and Compounds,* 433(1), pp. 97-107.

Evans, R. W. and Wilshire, B. (1985) 'Creep of metals and alloys'.

Fine, M. E. (1986) *Rapidly Solidified Powder Aluminum Alloys: A Symposium.* Astm International.

Fleischer, R. (1963) 'Substitutional solution hardening', *Acta metallurgica,* 11(3), pp. 203-209.

Foreman, A. and Makin, M. (1966) 'Dislocation movement through random arrays of obstacles', *Philosophical magazine,* 14(131), pp. 911-924.

Frost, H. J. and Ashby, M. F. (1982) 'Deformation mechanism maps: the plasticity and creep of metals and ceramics'.

Fu, H.-H., Benson, D. J. and Meyers, M. A. (2001) 'Analytical and computational description of effect of grain size on yield stress of metals', *Acta Materialia,* 49(13), pp. 2567-2582.

Galano, M., Audebert, F., Cantor, B. and Stone, I. (2004) 'Structural characterisation and stability of new nanoquasicrystalline Al-based alloys', *Materials Science and Engineering: A,* 375, pp. 1206-1211.

Galano, M., Audebert, F., Escorial, A. G., Stone, I. and Cantor, B. (2009a) 'Nanoquasicrystalline Al–Fe–Cr-based alloys. Part II: Mechanical properties', *Acta materialia,* 57(17), pp. 5120-5130.

Galano, M., Audebert, F., Stone, I. and Cantor, B. (2009b) 'Nanoquasicrystalline Al–Fe–Cr-based alloys. Part I: Phase transformations', *Acta Materialia,* 57(17), pp. 5107-5119.

García-Escorial, A., Natale, E., Cremaschi, V. J., Todd, I. and Lieblich, M. (2015) 'Quasicrystalline Al93Fe3Cr2Ti2 alloys', *Revista de Metalurgia,* 51(4), pp. 10.3989/revmetalm. 054.

Grant, N. J. (1983) 'Rapid solidification of metallic particulates', *JOM,* 35(1), pp. 20-27.

Haas, V., Cho, M. I., Ishii, H. and Inoue, A. (1999) 'Behavior of quasicrystal-reinforced AL 94 CR 1 MN 3 CU 2 under fatigue conditions', *Nanostructured Materials,* 12(5), pp. 829-834.

Hall, E. (1951) 'The deformation and ageing of mild steel: III discussion of results', *Proceedings of the Physical Society. Section B,* 64(9), pp. 747.

Hall, E. (1970) *Yield point phenomena in metals and alloys.* Plenum Press.

Han, B. and Dunand, D. (2000) 'Microstructure and mechanical properties of magnesium containing high volume fractions of yttria dispersoids', *Materials Science and Engineering: A,* 277(1), pp. 297-304.

Han, B., Mohamed, F., Lee, Z., Nutt, S. and Lavernia, E. (2003) 'Mechanical properties of an ultrafine-grained Al-7.5 Pct Mg alloy', *Metallurgical and Materials Transactions A,* 34(3), pp. 603-613.

Höppel, H. W., May, L., Prell, M. and Göken, M. (2011) 'Influence of grain size and precipitation state on the fatigue lives and deformation mechanisms of CP aluminium and AA6082 in the VHCF-regime', *International Journal of Fatigue,* 33(1), pp. 10-18.

Inoue, A. (1998) 'Amorphous, nanoquasicrystalline and nanocrystalline alloys in Al-based systems', *Progress in Materials Science,* 43(5), pp. 365-520.

Inoue, A., Arnberg, L., Lehtinen, B., Oguchi, M. and Masumoto, T. (1986) 'Compositional analysis of the icosahedral phase in rapidly quenched Al-Mn and Al-V alloys', *Metallurgical and Materials Transactions A,* 17(10), pp. 1657-1664.

Inoue, A. and Kimura, H. (2000) 'High-strength aluminum alloys containing nanoquasicrystalline particles', *Materials Science and Engineering: A,* 286(1), pp. 1-10.

Inoue, A. and Kimura, H. (2001) 'Fabrications and mechanical properties of bulk amorphous, nanocrystalline, nanoquasicrystalline alloys in aluminum-based system', *Journal of light metals,* 1(1), pp. 31-41.

Inoue, A., Kimura, H. and Masumoto, T. (1987) 'Formation, thermal stability and electrical resistivity of quasicrystalline phase in rapidly quenched Al-Cr alloys', *Journal of materials science,* 22(5), pp. 1758-1768.

Kimura, H. M., Sasamori, K. and Inoue, A. (2000) 'Al–Fe-based bulk quasicrystalline alloys with high elevated temperature strength', *Journal of Materials Research,* 15(12), pp. 2737-2744.

Knipling, K. E., Dunand, D. C. and Seidman, D. N. (2006) 'Criteria for developing castable, creep-resistant aluminum-based alloys–A review', *Zeitschrift für Metallkunde,* 97(3), pp. 246-265.

Kocks, U. (1967) 'Statistical treatment of penetrable obstacles', *Canadian Journal of Physics,* 45(2), pp. 737-755.

Krainikov, A. and Neikov, O. (2012) 'Rapidly solidified high-temperature aluminum alloys. I. Structure', *Powder Metallurgy and Metal Ceramics,* 51(7-8), pp. 399-411.

Lee, Y.-L. (2005) *Fatigue testing and analysis: theory and practice.* Butterworth-Heinemann.

Li, D. and Bakker, A. (1995) 'Temperature and strain rate dependence of the portevin-le chatelier effect in a rapidly solidified Al alloy', *Metallurgical and Materials Transactions A,* 26(11), pp. 2873-2879.

Li, J. and Chou, Y. (1970) 'The role of dislocations in the flow stress grain size relationships', *Metallurgical and Materials Transactions,* 1(5), pp. 1145-1159.
Lütjering, G. and Williams, J. C. (2003) *Titanium.* Springer.
Mahle (2012) *Pistons and engine testing.* 1st edn. Stuttgart: Plenum Press.
Manaila, R., Florescu, V., Jianu, A. and Radulescu, O. (1989) 'On the transition-metal quasisublattice in icosahedral Al-Cr-Fe phases', *Philosophical Magazine B,* 60(5), pp. 589-599.
Marines, I. (2003) 'An understanding of very high cycle fatigue of metals', *International Journal of Fatigue,* 25(9-11), pp. 1101-1107.
Mason, W. (1956) 'Internal friction and fatigue in metals at large strain amplitudes', *The Journal of the Acoustical Society of America,* 28(6), pp. 1207-1218.
Mayer, H., Lipowsky, H., Papakyriacou, M., Rösch, R., Stich, A. and Stanzl-Tschegg, S. (1999) 'Application of ultrasound for fatigue testing of lightweight alloys', *Fatigue & fracture of engineering materials & structures,* 22(7), pp. 591-599.
Mayer, H., Schuller, R. and Fitzka, M. (2013) 'Fatigue of 2024-T351 aluminium alloy at different load ratios up to 1010 cycles', *International Journal of Fatigue,* 57, pp. 113-119.
Meyersm, M. A. and Ashworth, E. (1982) 'A model for the effect of grain size on the yield stress of metals', *Philosophical Magazine A,* 46(5), pp. 737-759.
Mitra, S. (1992) 'Elevated temperature mechanical properties of a rapidly solidified Al-Fe-V-Si alloy', *Scripta metallurgica et materialia,* 27(5), pp. 521-526.
Mondolfo, L. F. (1976) *Aluminum alloys: structure and properties'; 1976. London-Boston: Butter Worths & Co Ltd*.
Morris, J. (1974) 'Dynamic strain aging in aluminum alloys', *Materials Science and Engineering,* 13(2), pp. 101-108.
Mott, N. and Nabarro, F. (1948) 'Dislocation theory and transient creep'.
Mughrabi, H. (2006) 'Specific features and mechanisms of fatigue in the ultrahigh-cycle regime', *International Journal of Fatigue,* 28(11), pp. 1501-1508.
Mukherjee, A. K. (2002) 'An examination of the constitutive equation for elevated temperature plasticity', *Materials Science and Engineering: A,* 322(1), pp. 1-22.
Nagaishi, Y., Yamasaki, M. and Kawamura, Y. (2007) 'Effect of process atmosphere on the mechanical properties of rapidly solidified powder metallurgy Al–Ti–Fe–Cr alloys', *Materials Science and Engineering: A,* 449, pp. 794-798.
Ohtera, K., Inoue, A., Terabayashi, T., Nagahama, H. and Masumoto, T. (1992) 'Mechanical Properties of an Al 88.5 Ni 8 Mm 3.5 (Mm: Misch Metal) Alloy Produced by Extrusion of Atomized Amorphous plus fcc-Al Phase Powders', *Materials Transactions, JIM,* 33(8), pp. 775-781.
Orowan, E. (1948) 'Discussion in The Symposium on Internal Stresses in Metals and Alloys, Inst', *Metals, London,* 451.
Otooni, M. A. (2013) *Elements of rapid solidification: fundamentals and applications.* Springer Science & Business Media.
Pedrazzini, S. (2014) *Characterisation and Mechanical Properties of Bulk Nanostructured Al-based Composites for High Temperature Applications.* DPhil Thesis, University of Oxford.

Peng, L., Zhu, S., Ma, Z., Bi, J., Chen, H. and Wang, F. (1999) 'High temperature creep deformation of an Al–Fe–V–Si alloy', *Materials Science and Engineering: A*, 259(1), pp. 25-33.

Petch, N. (1953) 'The cleavage strength of polycrystals', *J. Iron Steel Inst.*, 174, pp. 25-28.

Pineau, A., Benzerga, A. A. and Pardoen, T. (2016) 'Failure of metals III: Fracture and fatigue of nanostructured metallic materials', *Acta Materialia*, 107, pp. 508-544.

Polmear, I. (2006) *Light metals: from traditional alloys to nanocrystals.* Oxford: Elsevier.

Prakash, U., Raghu, T., Gokhale, A. and Kamat, S. (1999) 'Microstructure and mechanical properties of RSP/M Al-Fe-V-Si and Al-Fe-Ce alloys', *Journal of materials science*, 34(20), pp. 5061-5065.

Pulkrabek, W. W. (2004) *Engineering fundamentals of the internal combustion engine.* Prentice Hall.

Queyreau, S., Monnet, G. and Devincre, B. (2010) 'Orowan strengthening and forest hardening superposition examined by dislocation dynamics simulations', *Acta Materialia*, 58(17), pp. 5586-5595.

Rice, R. C. (2003) *Metallic Materials Properties Development and Standardization (MMPDS): Chapters 1-4.* National Technical Information Service.

Robinson, J. (1994) 'Serrated flow in aluminium base alloys', *International Materials Reviews*, 39(6), pp. 217-227.

Robinson, J., Cudd, R. and Evans, J. (2003) 'Creep resistant aluminium alloys and their applications', *Materials science and technology*, 19(2), pp. 143-155.

Robinson, J. and Shaw, M. (1994) 'Microstructural and mechanical influences on dynamic strain aging phenomena', *International materials reviews*, 39(3), pp. 113-122.

Rodriguez, P. (1984) 'Serrated plastic flow', *Bulletin of Materials Science*, 6(4), pp. 653-663.

Rolls-Royce (1986) *The Jet Engine.* Birmingham, England.

Rounthwaite, N. J. (2012) *Development of Bulk Nanoquasicrystalline Alloys for High Strength Elevated Temperature Applications.* DPhil Thesis, University of Oxford.

Ryen, Ø., Holmedal, B., Nijs, O., Nes, E., Sjölander, E. and Ekström, H.-E. (2006) 'Strengthening mechanisms in solid solution aluminum alloys', *Metallurgical and Materials Transactions A*, 37(6), pp. 1999-2006.

Shechtman, D., Blech, I., Gratias, D. and Cahn, J. W. (1984) 'Metallic phase with long-range orientational order and no translational symmetry', *Physical Review Letters*, 53(20), pp. 1951.

Skinner, D., Bye, R., Raybould, D. and Brown, A. (1986) 'Dispersion strengthened Al□ Fe□ V□ Si alloys', *Scripta Metallurgica*, 20(6), pp. 867-872.

Skinner, D., Zedalis, M. and Gilman, P. (1989) 'Effect of strain rate on tensile ductility for a series of dispersion-strengthened aluminum-based alloys', *Materials Science and Engineering: A*, 119, pp. 81-86.

Stanzl-Tschegg, S. and Mayer, H. (2001) 'Fatigue and fatigue crack growth of aluminium alloys at very high numbers of cycles', *International Journal of Fatigue*, 23, pp. 231-237.

Takahashi, Y., Yoshitake, H., Nakamichi, R., Wada, T., Takuma, M., Shikama, T. and Noguchi, H. (2014) 'Fatigue limit investigation of 6061-T6 aluminum alloy in giga-cycle regime', *Materials Science and Engineering: A*, 614, pp. 243-249.

Tjong, S. C. and Mai, Y.-W. (2003) 'Failure of Metal-Matrix Composites', in Karihaloo, B.L. & Knauss, W.G. (eds.) *Fundamental Theories and Mechanisms of*

Failure Comprehensive structural integrity: Elsevier.
Todd, I., Chlup, Z., O'Dwyer, J., Lieblich, M. and García-Escorial, A. (2004) 'The influence of processing variables on the structure and mechanical properties of nano-quasicrystalline reinforced aluminium alloys', *Materials Science and Engineering: A,* 375, pp. 1235-1238.
Tong, X. and Fang, H. (1998) 'Al-TiC composites in situ-processed by ingot metallurgy and rapid solidification technology: Part II. Mechanical behavior', *Metallurgical and Materials Transactions A,* 29(3), pp. 893-902.
Topping, T. D., Ahn, B., Li, Y., Nutt, S. R. and Lavernia, E. J. (2012) 'Influence of process parameters on the mechanical behavior of an ultrafine-grained Al alloy', *Metallurgical and Materials Transactions A,* 43(2), pp. 505-519.
Totten, G. E. and MacKenzie, D. S. (2003) *Handbook of Aluminum: Vol. 1: Physical Metallurgy and Processes.* CRC Press.
Vojtěch, D., Michalcová, A., Průša, F., Dám, K. and Šedá, P. (2012) 'Properties of the thermally stable Al 95 Cr 3.1 Fe 1.1 Ti 0.8 alloy prepared by cold-compression at ultra-high pressure and by hot-extrusion', *Materials Characterization,* 66, pp. 83-92.
Vojtěch, D., Verner, J., Šerák, J., Šimančík, F., Balog, M. and Nagy, J. (2007) 'Properties of thermally stable PM Al–Cr based alloy', *Materials Science and Engineering: A,* 458(1), pp. 371-380.
Yamasaki, M., Nagaishi, Y. and Kawamura, Y. (2007) 'Inhibition of Al grain coarsening by quasicrystalline icosahedral phase in the rapidly solidified powder metallurgy Al–Fe–Ti–Cr alloy', *Scripta materialia,* 56(9), pp. 785-788.
Yaney, D. and Nix, W. (1987) 'Elevated temperature deformation behavior of an Al-8.4 wt pct Fe-3.6 wt pct Ce alloy', *Metallurgical Transactions A,* 18(6), pp. 893-902.
Ye, H. (2003) 'An overview of the development of Al-Si-alloy based material for engine applications', *Journal of Materials Engineering and Performance,* 12(3), pp. 288-297.
Yu, C., Kao, P. and Chang, C. (2005) 'Transition of tensile deformation behaviors in ultrafine-grained aluminum', *Acta Materialia,* 53(15), pp. 4019-4028.
Zhu, X., Shyam, A., Jones, J., Mayer, H., Lasecki, J. and Allison, J. (2006) 'Effects of microstructure and temperature on fatigue behavior of E319-T7 cast aluminum alloy in very long life cycles', *International Journal of Fatigue,* 28(11), pp. 1566-1571.

3. Experimental Methods

3.1 Powder Production and Consolidation

3.1.1 Gas atomisation of powders

NQX $Al_{93}Fe_3Cr_2Ti_2$ powder was produced by the industrial collaborator Alpoco Ltd. using the gas atomisation technique, in a unit that required at least 70kg of material to operate. A previous DPhil student in our research group Rounthwaite (2012) analysed the atomisation conditions of the powders produced at Alpoco. The master alloys (Al, Al-80Fe, Al-20Cr and Al-10Ti all in wt%) were melted in a crucible, a ceramic straw was used to suck the molten mixture and pass the melt through a nozzle at 1200^{o}C. The melt was sprayed in the form a jet, high-velocity gas from both sides of melt spraying nozzle broke up the jet into atomised powder. The gas was a mixture of Nitrogen with 3% Oxygen; the latter caused the formation of a thin oxide layer on the powder particles to make powder handling potentially safer. The powder was then collected and sieved to remove large size (>200μm) particles.

3.1.2 Sieving of powders

The sieving process was carried out by Henry Begg at our group. A stack of four Retsch sieves (Φ~200mm, L~50mm) was used for the powder sieving. The sieves supposedly separated the powders in size fractions of sub 25μm, 25-50μm, 50-75μm, 75-100μm, and 100-125-μm. About 40g powder was placed on the top of the sieve stack, and a Retsch A200 automatic sieve shaker was used to sieve the powder in approximately 8 min. The process was repeated for the sieved powder fractions to ensure the separation of the unwanted powder fraction. The metallic sieves were cleaned with the help of hard brush between the sieving runs and with distilled water after every ten runs to remove any

potential blockage. Each powder fraction size was weighed and stored in air tight jars. 25-50μm powder size was used for this project.

3.1.3 Extrusion of powder into solid bar

Aluminium cans were machined (Φ~50 mm, L~102mm) from 6082 alloy tube followed by cleaning with acetone and isopropanol. The bottom of the can was sealed with a proper size circular aluminium lid using aluminium foil and after loading the sieved powder the top lid was placed; a filled can is shown in Figure 3.1(a). A breather hole was already drilled on the top lid to help the removal of air during the compaction phase of the extrusion run. The can was sprayed with a lubricant 'Hexagonal Boron Nitride' (HBN) and placed in a separate box furnace for 15 min at 400^{o}C followed by 15 min at 415^{o}C to compensate for the heat loss during the transfer of the can from the furnace to the extruder. As shown in Figure 3.1(b), a 400 US ton (3.52MN) extruder was used to extrude the cans at 400^{o}C into 14mm diameter bars at an extrusion ratio (ER) of 12.75, using an extrusion speed of 0.9±0.1mm/s. Bar 1 was extruded at a speed of 8.3mm/s which proved helpful in understanding the effect of speed on the NQX alloy microstructure. The extrusion pressures were observed in a range of 1015-1240MPa during the extrusions of all the bars (except for bar B1). At the start of the extrusion run, the powder is initially compacted as a result of the ram pushing into the back of can whose front side rests against the die, after reaching a breakthrough pressure the extrusion of the compact takes place through the die and results in the extruded rod having a 14mm diameter.

(a)

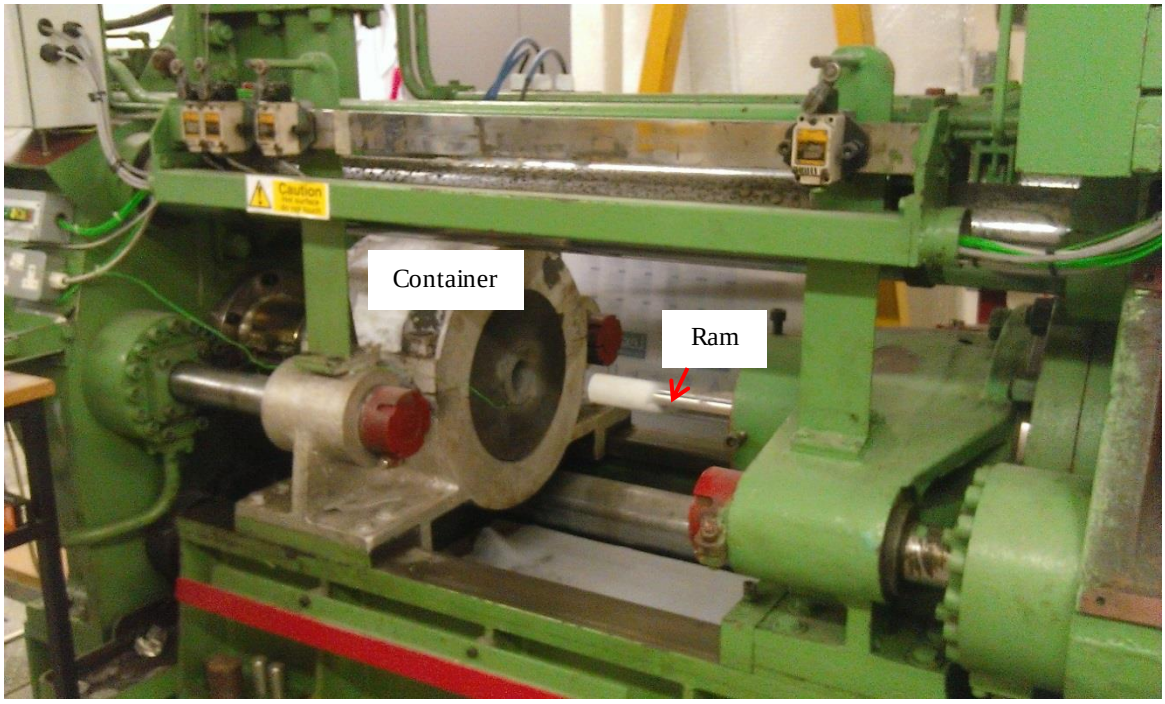

(b)

Figure 3.1 (a) An aluminium can filled with the alloy powder, (b) 3.52 MN extruder used for the extrusions.

3.2 Characterisation and Microstructural Analysis

3.2.1 Machining and sample cutting

Extruded bars were cut in pieces of small lengths (L~ 20 to 100mm) with a hand saw. Cylindrical samples with smooth uniform surface were obtained by removing the external ~0.5mm outer layer of the bar which was comprised of the 'can' material. Samples of required dimensions were cut with an Isomet 5000 precision cutter in longitudinal and cross-section directions for characterisation.

3.2.2 Polishing

3.2.2.1 Mechanical polishing

All the samples for polishing were either glued on an Al stub (with super glue) or mounted using conducting epoxy; the samples were ground using 1200, 2500 and 4000 grit silicon carbide papers. The samples were then polished using 3μm, 1μm, and 0.25μm diamond suspensions followed by a 3-4min polishing using a mixture of 90 vol % colloidal silica and 10 vol% hydrogen peroxide. Ultrasonic cleaning was carried out after each polishing step.

3.2.2.2 Ion polishing

Precision Ion Polishing System (Gatan, PIPS II, model 695) was used to achieve a flat surface, in the mechanically polished bulk samples, for the EBSD analysis. PIPS II uses Argon ions for the ion polishing. The polishing was carried out at room temperature for 90-120min at an energy of 4-5keV and gun(s) angle of 4^{o}.

3.2.3 X-ray diffraction (XRD)

XRD was carried out to find out the phases present in the specimens under study. A Philips 1810 or a Rigaku miniflex θ-2θ diffractometer using $Cu_{k-\alpha}$ radiation was used.

XRD scans were carried out using a voltage of 35 or 40kV, a current of 40 or 50mA, a two theta range of 10-100°, a step size of 0.02° and a dwell time of 1 or 0.2 sec. A combination of X'pert high score (software), the international standard for diffraction data (ICDD) with the database as PDF cards, national chemical database website (ICSD, 2016), and published literature were used to identify the peaks and phases in the diffractograms. XRD runs were carried out for the cross section, longitudinal, powder fillings (collected by sawing the bar) and sieved powder samples. The powder samples were sprinkled on a glass side, mildly coated with vacuum grease. Bulk samples were ensured to be flat and smoothened by grinding up to 4000 SiC paper.

3.2.4 Differential scanning calorimetry (DSC)

TA Instruments 2010 DSC was used for the measurements. Measured in a five-digit balance, the weight of each DSC sample was less than 10mg. Each sample was loaded in a Cu pan and sandwiched between two Molybdenum sheets to avoid a direct contact with Cu surface. DSC was performed under Argon flux, from 80^{o}C to 630^{o}C at a heating rate of 40^{o}C/min unless otherwise specified. A baseline subtraction was performed by (i) subtracting a DSC curve for a Cu Pan only containing Mo sheets from the original run and (ii) by subtracting a second or reheat run of the actual alloy sample. Figure 3.2 shows the original run for an alloy powder sample, the reheat run on the same sample, the DSC trace for empty Cu pan, a curve showing reheat subtracted run and a Cu pan subtracted run. It was observed that the subtraction of reheat run was a more effective method to remove the common fluctuations in the DSC curves of the alloy which could be present due to the effect of the equipment. It was possible to apply this method as the main transformation involved was not reversible.

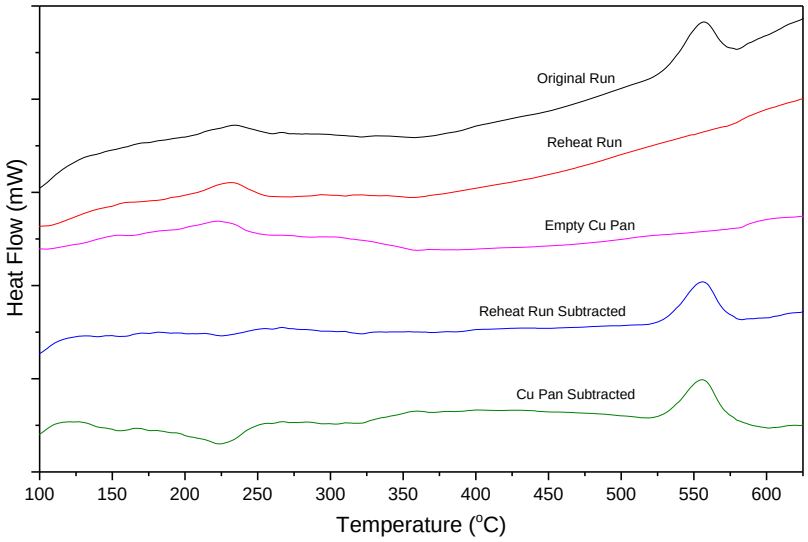

Figure 3.2 DSC curves showing the DSC trace of original (first) run and the effect of subtracting a reheat run or an empty Cu pan.

3.2.5 Scanning electron microscopy

A low vacuum tungsten filament Jeol 5510 scanning electron microscope (SEM) was used for the most of the fractographic analysis and low-resolution work. For imaging work, Voltage (V) of 10-15kV, spot size 20-30 and a working distance of 10-15mm were used. For energy dispersive x-ray spectroscopic (EDS) analysis V=20kV, spot size 50-60, and a working distance of 20mm were used. All high-resolution imaging work was carried out in a field emission gun equipped (FE) Jeol 6500F SEM. The working conditions were V=5-10kV, spot size : medium/(6-10) and working distance ~8-12mm. Oxford Instrument 'Aztech' software was used for the EDS analysis.

3.2.6 Electron backscattered diffraction

FESEM Jeol 6500F with an Oxford Instruments detector was used at V=15kV, working distance of 15mm and tilt angle of 70°. A TSL OIM software was used and an average area of 10x10 mm^2 ± (2x2mm^2) was scanned, a step size of 60-65nm, a long dwell time of 0.75s and 1x1 binning were used to improve detection. The average confidence index was

more than 0.1 which means 95% probability of correct indexation. The extensive mechanical polishing steps mostly thinned the spherical particles into thin circular plates. Quasicrystalline particles should have appeared 'blank' as EBSD software was supposed to detect only fcc aluminium grains; however, it was observed that even pointing the beam on a (thinned) particle detected weak Kikuchi pattern of fcc aluminium having a low confidence index. It was considered to be coming from the surface below the particle due to the interaction volume of the electron beam. In some cases, no signal could be picked up by the detector using the same conditions. The EBSD of the ultrafine sized alloy with nano size dispersed particles is a rudimentary attempt to estimate the grain size in this complex material containing a high volume fraction of nano size reinforcements, several difficulties were faced in the attempt to meausre the grain size[A]. Due to the uncertainty associated with the accurate measurement of the relevant data from the EBSD (in this material) care must be excercised while accepting the data. Other support techniques such as TEM (for grain size) and XRD (for texture) were therefore used for the confirmation. TEM micrographs exhibited similar sizes of the grains (as of EBSD) whereas texture from XRD supported EBSD texture analysis. Even in the TEM, accurate grain size measurements were sometimes difficult as the particles mask the grain boundaries. TSL OIM analysis software was used to analyse the data, a 'grain tolerance angle' of 15^{o} was used to define a 'grain' and minimum grain size cut-off was chosen to be

[A] **Difficulties**: (i) A good sample preparation for EBSD is not trivial as particles are hard in comparison with matrix so maintaining a uniform material removal rate is difficult during polishing. (ii) The nano size grains seem to reach the limit of the resolution of the microscope despite using a small step size. (iii) The presence of large number of I-phase particles block the beam from reaching the Al grains and results in low detection and subsequently an overall low confidence index as compared to single phase alloys. (iv) Low probe current and voltage were unable to provide proper detection. Under high voltage/probe current the specimen would charge up as the I-phase is known to have low electrical conductivity. Also high voltage/probe current results in larger interaction volume sometimes picking up signals from other (nano grains) in the vicinity of the target grain (v) Small step size and increased dwell time were used to improve detection but this slowed the scan speed significantly.

200nm [B]. The data was 'cleaned' once, using nearest neighbour orientation[C] to remove noise. The EBSD IPF maps have been shown in section 4.3.5 and 5.2.5 and these provide useful information about the texture; however, these may not be a true depiction of the grain size distribution. 'Unique grain colour map' is the best way to represent a 'grain' in the TSL OIM software (see details in Appendix 3). The grain diameter distributions observed in this work are obtained from the 'unique grain colour maps' provided in Appendix 3.

3.2.7 Transmission electron microscope sample preparation

Focused ion beam lift out specimen were prepared for 'as sieved' powder samples by a student in our research group Weiyue Xu. For the TEM sample preparation from bulk extruded bars, ~400µm thin slices were cut on slow speed saw from cylindrical bars, which were then thinned to ~85µm using 4000 grit SiC paper. 3mm diameter discs were cut using a punch and were dimpled on one side and polished on both sides using diamond suspensions of 3, 1 and 0.25µm sizes. The approximate thickness in the centre part of the 3mm disc was ~20µm. The final TEM samples were prepared using precision ion polisher system (Gatan, PIPS I, model 691) at Energy= 3.5-4keV, gun angles 6^{o}/-4^{o}, using dual beam modulation, till a pin hole was obtained.

3.2.8 TEM, EDS and scanning TEM (STEM)

A tungsten filament Jeol 2000fx TEM was used at a voltage of 200kV and spot sizes of 3 to 4. Selected area diffraction patterns (SADP) could not be acquired for most of the

[B] TSL:OIM software utilises user defined 'grain tolerance angle' for the definition of a 'grain'. The grain diameter distribution corresponds to the 'unique grain colour map'. A minimum grain size of 200nm was used for all EBSD work based on TEM observations as no grains smaller than 200nm were observed in this material using TEM.

[C] A method called 'grain dilation' was used which works as following. "If the majority of neighbours of a particular point belong to the same grain then the orientation of the particular point is changed to match that of the majority grain, otherwise the orientation is randomly changed to match any of the neighboring points, which belong to grains". (Source: Help file TSL OIM software).

quasicrystalline particles due to their small size; convergent beam diffraction was used instead. A beryllium double tilt holder was used to cause minimum interference in the EDS analysis. Samples were tilted at ~20^{o} towards Oxford Instrument EDS detector, and the EDS data was acquired in INCA software. Oxford Instrument Aztech software was used for the EDS analysis.

TEM images, diffraction patterns (DPs), EDS spectra and STEM images were also acquired in Jeol 2100 microscope. The microscope was operated by Mr. Weiye Xu at V=200kV.

3.3 Annealing of the Extruded Bars

Carbolite furnaces equipped with Eurotherm temperature controllers were used to anneal the samples under normal atmosphere. The furnace was heated to the desired temperature and after loading the sample, the controller was manually adjusted to prevent any temperature overshoot. The samples were air cooled at the end of the heat treatment. Nomenclature of the annealed samples used in the thesis is provided in Table 3.1 at the end of this chapter.

3.4 Mechanical Properties and Density Measurements

3.4.1 Density

Archimedes immersion method was used for density measurement, utilising distilled water as the immersion liquid. A UKAS calibrated BDH 250 modified electronic balance[D] was employed, measuring to the nearest 0.0001 g. A sequence of dry and immersed measurements of the mass was carried out at least three times until stable results were obtained. The temperature of the water was measured with a digital thermometer to the

[D] The balance was modified such that the weight of a sample immersed in a liquid placed in a beaker could be measured.

nearest 0.1°C, and the density was determined from specific gravity tables and density formula. To verify the results, two bars were additionally measured at National Physical Laboratory (NPL)[E]. A negligible density difference of 0.002g/cm^3 was noted in the measurements of NPL and those measured indigenously.

3.4.2 Microhardness

Wilson-Wolpert Instruments micro indenter coupled with Minuteman software was used to measure the microhardness of the bulk samples. A load of 500g and dwell time of 20 seconds was used on polished samples for measurement of microhardness, as per guide-lines provided in ASTM E384 standard (ASTM, 2011). A total of at least 20 indents were made and measured on each sample, the distance between consecutive indents or distance between an indent and the outer edge of the sample was at least three times the diagonal length of the indent to avert any effects of plasticity.

3.4.3 Measurement of dynamic elastic constants

Moduli measurements using dynamic and static methods may not necessarily coincide (Hatch, 1984). The dynamic method has inherent advantages over the quasi static methods as: (i) it is a nondestructive method, and the same sample can be used multiple times (ii) the load levels are far below the elastic limit and do not contain any complex anelastic effects or elastic hysteresis (Horst et al., 2006). In addition, the dynamic Young's modulus was required in the finite element computations used for designing the very high cycle fatigue (VHCF) specimen in the present work.

The dynamic Young's modulus (E), the shear modulus (G) were measured using the impulse excitation of vibration method provided in the ASTM standard E-1876 (ASTM, 2001). The Young's modulus (E) is related to the fundamental through-thickness flexural mode

[E] Measurements at NPL were performed by Dr Roger Morrell and his team.

frequency. The shear modulus (G) is related to the fundamental torsional mode frequency. Assuming homogeneous isotropic elastic material, the Poisson's ratio (ν) can be determined from E and G using the relation $E/2G = 1+\nu$. The weight of the sample bars was measured by using a calibrated five digit Westco R1602 balance. The geometry of the beams was measured to the accuracy of ±0.01mm in the length and ±0.001mm in the thickness or the width at multiple places using a digital Vernier calliper and a digital micrometre gauge.

3.4.3.1 Elastic constants measured at room temperature

Five beam-shaped samples with nearly parallel sides of dimensions~32x7x7 mm^3 ± 3x2x2 mm^3 were cut from an extruded bar using a precision Isomet 5000 cutter. The parallelism was improved to 0.1% accuracy by milling the samples on a mechanical flatbed precision grinder. The beams were placed on a polyurethane sheet, and the nodal points were marked at 0.5L and 0.223L from each end. In order to excite either the flexural or the torsional mode, the beams were struck with a steel ball attached to a polymeric stick. The corresponding flexural or the torsional frequencies were noted using dynamic frequency measuring equipment (Grindosonic system) in non-contact mode. The frequency readings were noted such that the difference between the consecutive readings was within 0.1%. The flexural or torsional frequency readings were then inputted in the related empirical formulae provided by the ASTM standard and given at the end of the section. As a starting point, the value of the Poisson's ratio (υ) was assumed as the same as of pure Al that is 0.33 and initial values for both the E and G were acquired. The value of Poisson's ratio was then modified during subsequent iterations such that the E and the G value obtained from the empirical formulae for the flexural mode matched (within 0.1%) the G and E values obtained from the empirical formulae for the torsional mode. The empirical formulae from the ASTM standard are provided below.

$$\frac{E}{2G} = 1 + \nu \qquad \textbf{Eqn. 3.1}$$

$$E = 0.9465\left(\frac{L}{t}\right)^3 (m\, f_{flex}^2 / b) T_1 \qquad \textbf{Eqn. 3.2}$$

$$T_1 = 1 + 6.585(1 + 0.0752\nu + 0.8109\nu^2)\left(\frac{t}{L}\right)^2 - 0.0.868\left(\frac{t}{L}\right)^4 - \left[\frac{8.34(1 + 0.2023\nu + 2.173\nu^2)(t/L)^4}{1 + 6.338(1 + 0.1408\nu + 1.536\nu^2)(t/L)^2}\right] \qquad \textbf{Eqn. 3.3}$$

$$G = \frac{4Lmf_{tor}^2}{bt}\left(\frac{B}{1 + A}\right) \qquad \textbf{Eqn. 3.4}$$

$$B = \left[\frac{b/t + t/b}{4(t/b) - 2.52(t/b)^2 + 0.21(t/b)^6}\right] \qquad \textbf{Eqn. 3.5}$$

$$A = \left[\frac{0.5062 + 0.8776(b/t) + 0.3504(b/t)^2 - 0.0078(b/t)^3}{12.03(b/t) + 9.892(b/t)^2}\right] \qquad \textbf{Eqn. 3.6}$$

E is the Young's modulus, G is the shear modulus, υ is the Poisson's ratio, L is the sample length, t is the sample thickness, b is the sample width, m is sample mass, f_{flex} is the fundamental flexural mode frequency, f_{tor} is fundamental torsional mode frequency, T_1 is a correction factor for fundamental flexural mode, and A is the empirical correction factor.

The results were further confirmed by modelling each beam-shaped bar in a finite element analysis (FEA) software (Abaqus 6.13) which used a linear perturbation procedure for finding the frequencies of first modes of vibrations. A hexahedron shaped mesh and a structured meshing technique were used. The flexural frequency (F1) and the torsional frequency (T1) for the first mode(s) of vibration for the given geometry were obtained by modelling and (initially) using experimentally obtained values of elastic constants. E,G

and υ values were then modified in the software such that the resulting modelled and experimental F1 and T1 were within 0.1% of the experimental average values.

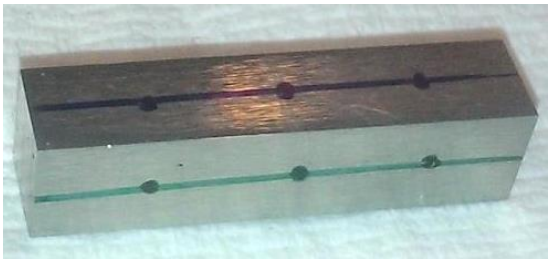

(a) Sample

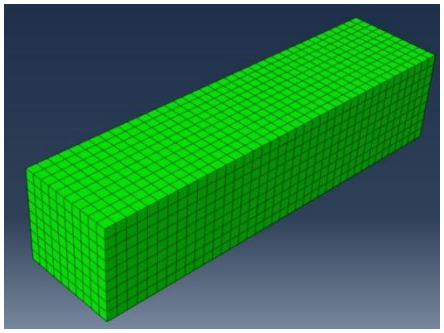

(b) FE model

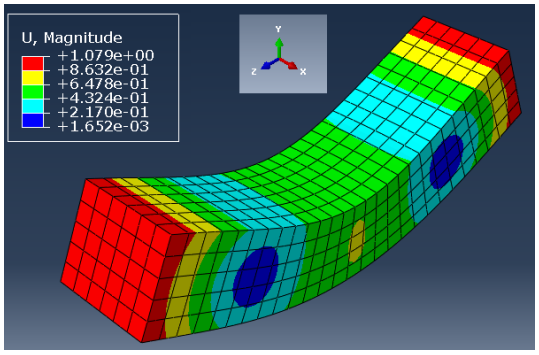

(c) 1st flexural mode

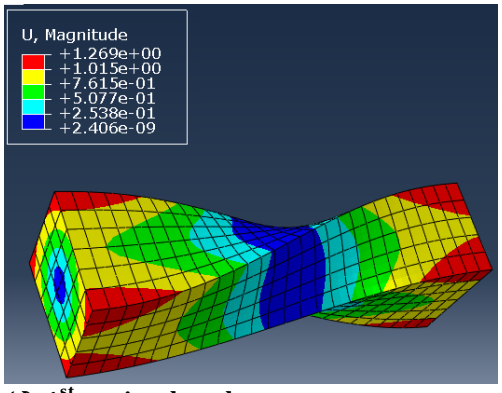

(d) 1st torsional mode

Figure 3.3 (a) One of the beam-shaped sample used for measuring elastic constants, nodal points and centre lines are marked, (b) finite element model in Abaqus 6.13, (c) first flexural mode of vibration in FE model, (d) First torsional mode of vibration in FE model.

3.4.3.2 Elastic constants at elevated temperature

Elevated temperatures elastic constant measurements were subcontracted to NPL. ASTM 1876 (ASTM, 2001) and the same impulse excitation concept employed for the room temperature measurements was also used for the elevated temperature measurements. An HTVP1250 instrument from IMCE BV, Belgium was used. A 12mm diameter piece of the alloy rod was provided from which a rectangular bar test piece 100x10x2.5 mm was machined using electro-discharge machining (EDM), followed by fine grinding to improve the face parallelism and remove EDM damage. The test-piece was suspended from a ceramic frame by winding fine nichrome wire at nodal points. The frame was located at such a position inside

the furnace system that the location of impact was central to the length of the test-piece, but offset to one side. Thus, the odd-numbered flexural modes F1, F3, F5, and the second torsional mode T2, were excited. The ratio of the frequencies of modes T2 and T1 determined at room temperature was then use to convert the detected T2 to the appropriate value of T1 in order to use the standard equation. This ratio stays constant with temperature (Morrell et al., 2015).

Thermal cycles were made using continuous ramps at a heating rate of 2°C/min to the required maximum temperature, which was held for 10 minutes, followed by cooling at the same rate. The temperature was measured using a Type S thermocouple with its bare tip in proximity (but not touching) of the test-piece. Impacts from beneath the test-piece were made automatically every minute during the ramps by a ceramic impactor fired from a magnetic pulser, and the impact sound was transmitted along a ceramic waveguide with its mouth positioned about 10mm above the centre of the test-piece to a microphone above the furnace. The Poisson's ratio was calculated from each detected pair of moduli values from Fl and T2. In order to smooth the data, the Young's modulus from F1 and F5, and shear modulus from T2 were curve-fitted as functions of temperature with fifth-order polynomials, separately for heating and cooling curves. These polynomials were then evaluated at 50 °C intervals to provide the data.

The uncertainties in the measurements are due to (i) imperfect thickness/face parallelism (ii) effect of the parasitic mass of the suspension, and (iii) fundamental accuracy of the correction functions within the calculation equations. Overall, keeping variations in test-piece thickness to below 0.01 mm it is usually possible to achieved modulus accuracy of better than 0.5%.

3.4.4 Tensile tests

A servo-hydraulic computer controlled universal test machine (ESH), operated by Zwick/Roel cubus software was used to carry out tensile tests. Cylindrical samples were

machined as per ASTM E8 (ASTM, 2009a) such that the gauge length (G_L) was ~16mm and gauge diameter was 4±0.1mm, a machined sample is shown in Figure 3.4(a). Three K-type thermocouples were used, one attached to just above each shoulder portion and one at the centre of the gauge section of the sample as shown in Figure 3.4 (b). All the tests were conducted in a 'displacement control' mode; therefore, all the reported strain rates are the 'nominal' strain rates at the start of the test. However; since the total strains are small, thus, the difference in nominal and actual strain rates is also small. Yield strength was measured using 0.2% offset method.

A carbolite furnace equipped with a Eurotherm controller was used to heat samples during elevated temperature tests as per ASTM E21 standard (ASTM, 2009b). All the samples were soaked at elevated temperature for ~1.25hr prior to the start of the test and tests were carried out within ±3°C of the intended test temperature. The load cell zero reading was affected by the increase in the chamber temperature, the load cell 'zero position' was separately calibrated at 50°C interval from 100 to 400°C and 25°C interval from 400-500°C. These 'temperature calibration' values were then subsequently used for the correction of the 'load cell reading' at all elevated temperature tests.

An epsilon 3542 type extensometer (up to 200°C) and epsilon 3555 type extensometer (up to 540°C) were used for strain measurements. In the case of unavailability of extensometer, the machine compliance and sample displacement outside the straight section can be subtracted from the load-displacement curve (Huerta et al., 2010). A straight cylinder of the same material (gauge length ~10mm, Dia 7.23mm) was used, and its (compliance) load-displacement curve at each testing temperature was obtained. The corresponding compliance curve(s) at respective temperatures were then subtracted from the load-displacement curves of the actual sample(s). The method resulted in similar tensile / yield strength values, but a small (up to ~0.5%) difference in elongation was

noted in comparison with the load-elongation curve obtained using the extensometer. A comparison of stress-strain curves in 'as tested', after subtraction of calibration curve and 'measured by extensometer' is provided in Figure 3.4(c).

Strain rate jump tests were carried out at 425°C, 450°C, 475°C, and 500°C. The tests were conducted such that the nominal strain rates were varied during the tensile tests. The tests were started at a nominal strain rate of $10^{-5}s^{-1}$, after achieving a quasi-steady state flow stress the crosshead speed was increased to result in a nominal strain rate of $10^{-4}s^{-1}$, The process was repeated to achieve 10^{-3} and $10^{-2}s^{-1}$ nominal strain rates.

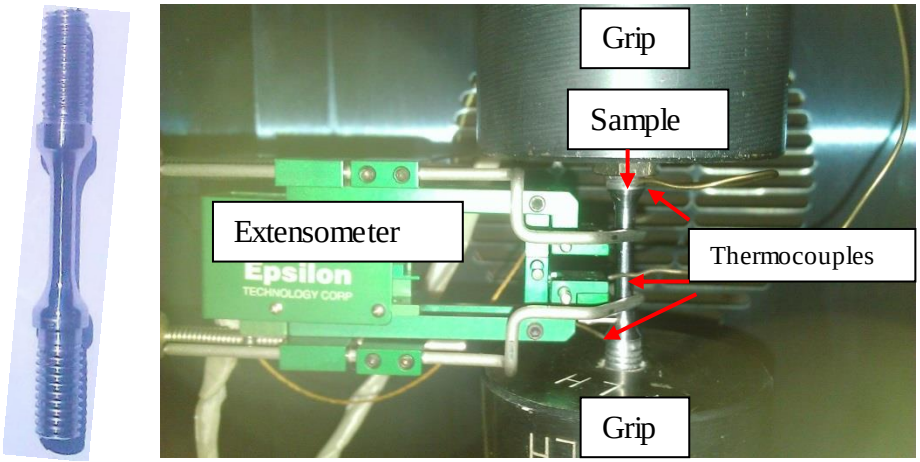

(a) **(b)**

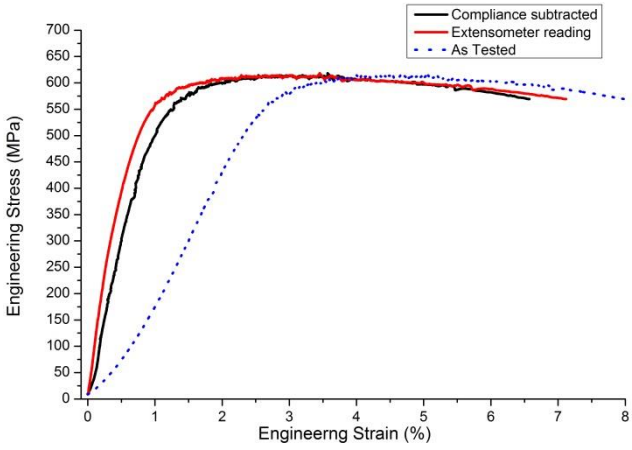

(c)

Figure 3.4 (a) A tensile sample of Φ=4±0.1 and gauge length~16mm, (b) tensile sample loaded in the grips, with three thermocouples and extensometer, (c) tensile curves in 'as tested' condition in comparison with tensile curve obtained from extensometer and after subtracting the compliance.

3.4.5 Fatigue tests

The schematics of the samples used for fatigue testing are shown in Figure 3.5. Load ratio ($R=\sigma_{min}/\sigma_{max}$) of 0.1 was used, so the samples were in tension-tension mode during the test. Conventional high cycle fatigue (HCF) tests were carried out as per guidelines provided in ASTM E466 standard (ASTM, 2015). Very high cycle fatigue tests were carried out using the guidelines from the works of Bathias and Paris (2004) and Mayer et al. (1999).

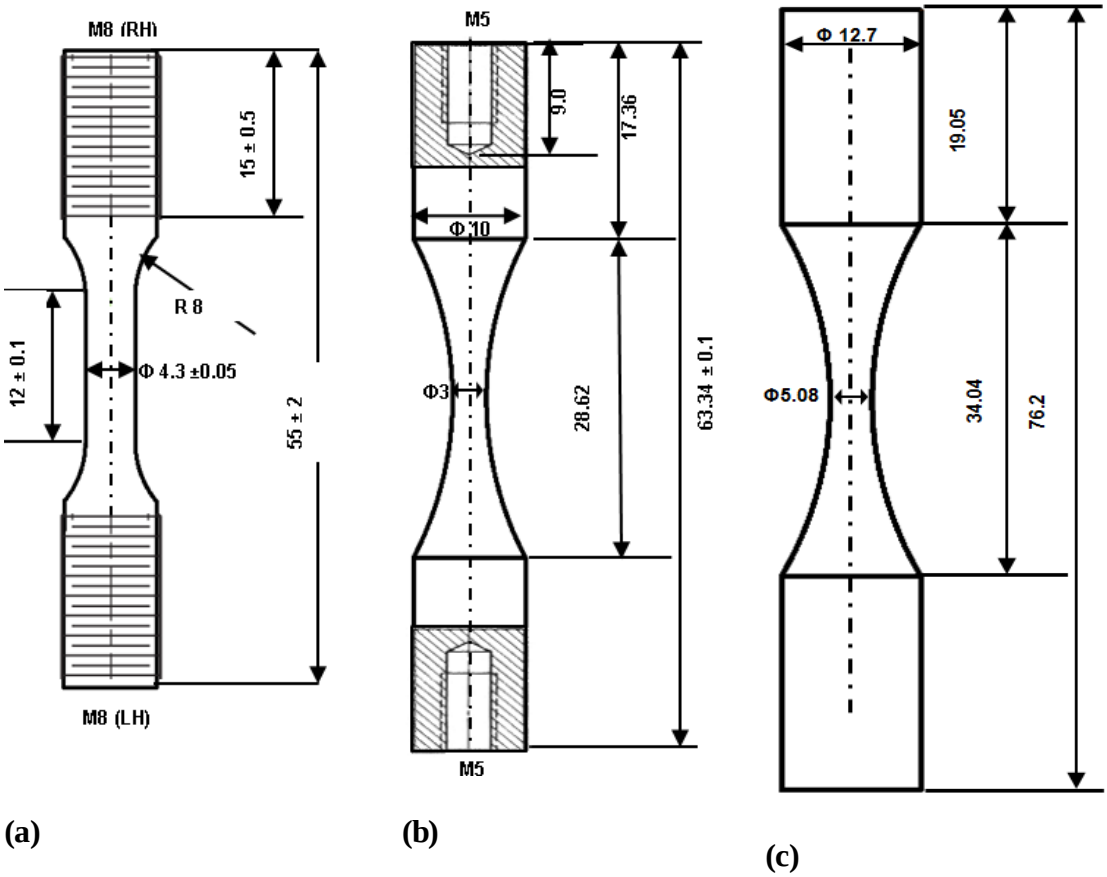

Figure 3.5 Schematic of fatigue samples: (a) 60Hz HCF, 23°C sample, (b) 20000Hz VHCF, 23°C sample, (c) 40Hz HCF, 300°C sample.

3.4.5.1 60Hz HCF, 23°C tests

A servo-hydraulic computer controlled universal test machine (ESH), operated by Zwick/Roel cubus software was used to conduct the 60Hz fatigue tests at room tempera-

ture. The tests were conducted in 'load control' mode, after optimising the proportional, integral, differential (PID) and signal gains at 60Hz to get the desired output load signal. The diameter of the gauge section was used to calculate the stress in the cross section area of the gauge length (Figure 3.5 (a)). Tests were carried out until failure in the straight section.

3.4.5.2 40Hz HCF, 300°C tests

300°C HCF tests for NQX alloy were subcontracted to Westmoreland Mechanical Testing and Co. A 100KN servo-hydraulic, computer controlled fatigue machine was used to conduct the HCF tests at 300°C till the fracture. PID and signal gains could only be adjusted till 40Hz on this machine. Three K-type thermocouples were used to measure the temperature on the centre section of the sample which was soaked at 300°C for 30min prior to the start of the test.

Ideally, the HCF tests at room temperature (60Hz) and 300°C (40Hz) tests should have been conducted at the same frequency. However, since a dynamic application of piston is envisaged for the NQX alloy, and generally the RPMs range from~2500-4500 for gasoline engines which correspond to the frequency range of ~40-70Hz (Mahle, 2012). Therefore, the fatigue testing at a frequency range of ~ 40-70Hz was considered to be more appropriate. However, the PID of high-temperature fatigue machine could not accurately control the output at 60Hz, so a slightly lower but suitable frequency (40Hz) was chosen. There is no difference in the fatigue tests conducted at different frequencies up to 200Hz (Stephens et al., 2000). It is also reported by Marines et al. (2003) that SN curve remain unaffected at conventional frequencies over 10Hz. It can, therefore, be assumed that 40 or 60 Hz would have no different effect on the fatigue performance of the alloy.

3.4.5.3 20kHz VHCF, 23°C tests

For VHCF tests, an ultrasonic frequency generator converts the 50/60Hz signal into 20kHz (ultrasonic) electrical signal. A piezoelectric transducer transforms the electrical signal into mechanical (displacement) output of the same frequency. An amplifier (horn) is used to amplify the incoming signal and provide the required displacement amplitude in the central section of the specimen. The sample must resonate at a frequency of 20±0.5kHz (in this case), in this way the sample reaches a maximum displacement at the end points and the maximum stress in the centre section. If a superimposed loading is required, then another horn is used at the bottom end of the sample, and a preload is achieved with the help of a universal testing machine frame.

A universal testing machine (Instron 1195) was used to apply the superimposed loading during the ultrasonic fatigue test. The NQX sample design was initially approximated using the analytical equations by Bathias and Paris (2004), it was further refined by modelling in 'Abaqus 6.13' using dynamic E, ν and ρ values measured in chapter 6, and the sample was designed to resonate at exactly 20.0±0.5kHz. The Intron frame was calibrated for the load values using strain gauges, and FEA calculations were used for converting the micro-displacement amplitude into corresponding load /stress. The actual sample and FE model are shown in Figure 3.6 (a, b) whereas a complete set up of an actual sample during the test, and its schematic are illustrated in Figure 3.7 (c). The centre section of the specimen was cooled by compressed air at 6 bars, the specimen surface temperatures were measured using a non-contact IR thermometer (during long tests only).

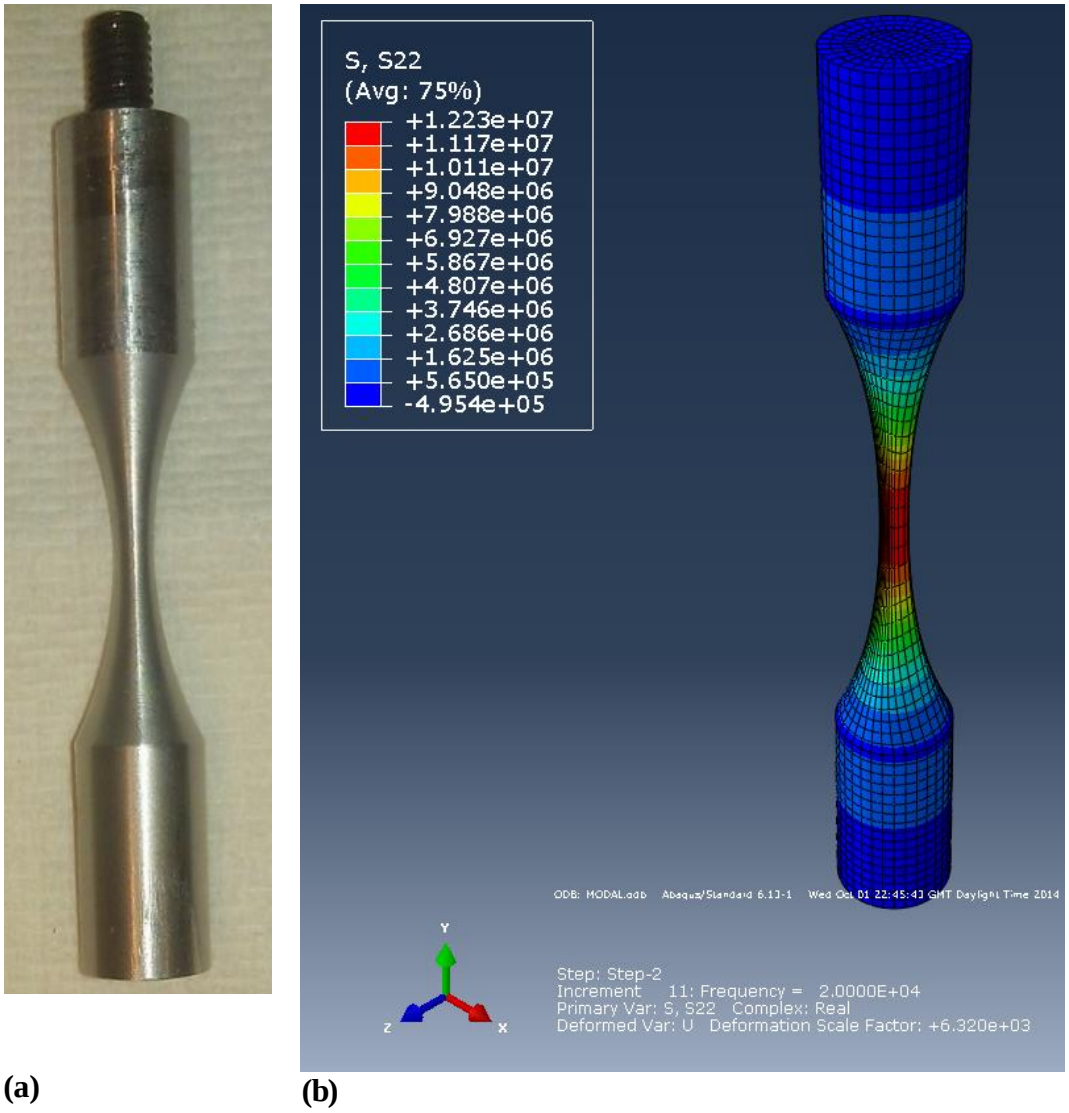

Figure 3.6 (a) A 20kHz, VHCF sample, (b) FE design used to calculate the stress due to 1µm displacement amplitude.

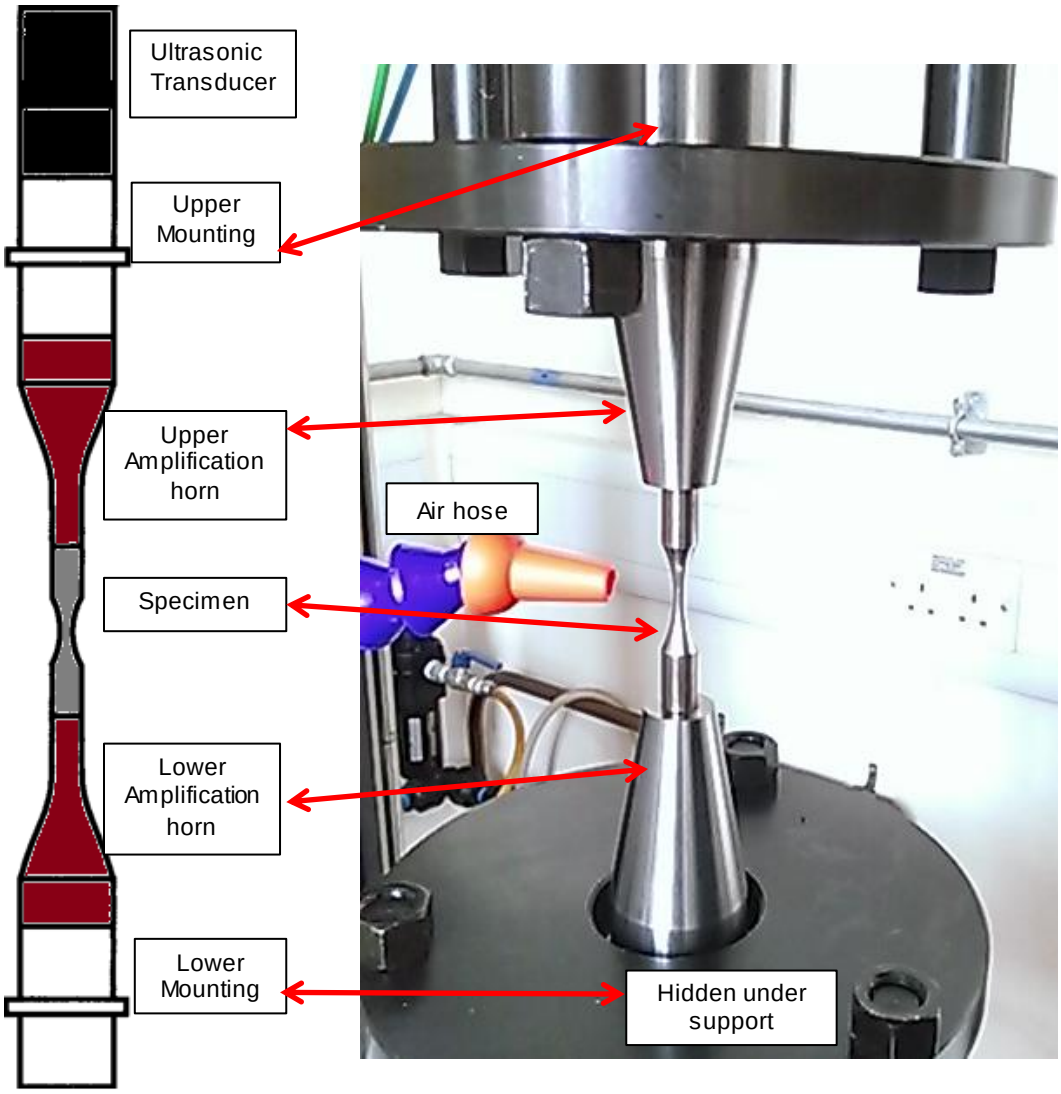

(c)

Figure 3.7 A schematic (left) and actual set up (right) of the ultrasonic fatigue.

Table 3.1 Nomenclature of the annealed samples used in the thesis.

<table>
<tr><th>Annealing Temperature (°C)</th><th>Annealing Time (hrs)</th><th>Sample Nomenclature</th><th colspan="4">Measurement / Test (location in the thesis)</th></tr>
<tr><td>250</td><td>100</td><td>250°C/100h</td><td rowspan="6">Microstructural Characterisation (Chapter 5)</td><td rowspan="5">Elastic constant measurements at 23°C (section 6.2)</td><td rowspan="5">Microhardness at 23°C (section 6.3)</td><td rowspan="5">Tensile tests at 23°C (section 6.4)</td></tr>
<tr><td>300</td><td>100</td><td>300°C/100h</td></tr>
<tr><td>350</td><td>100</td><td>350°C/100h</td></tr>
<tr><td>400</td><td>100</td><td>400°C/100h</td></tr>
<tr><td>450</td><td>100</td><td>450°C/100h</td></tr>
<tr><td>650</td><td>1</td><td>650°C /1h</td></tr>
<tr><th>Test* Temperature (°C)</th><th>Test Type</th><th>Sample Nomenclature Used</th><th colspan="4">Measurement / Test (location in the thesis)</th></tr>
<tr><td>350</td><td>Tensile</td><td>350°C/Tensile</td><td colspan="4" rowspan="6">Characterisation after tensile tests at elevated temperatures (section 7.2.2)</td></tr>
<tr><td>400</td><td>Tensile</td><td>400°C/Tensile</td></tr>
<tr><td>425</td><td>Strain rate jump tensile</td><td>425°C/ Tensile</td></tr>
<tr><td>450</td><td>As above</td><td>450°C/ Tensile</td></tr>
<tr><td>475</td><td>As above</td><td>475°C/ Tensile</td></tr>
<tr><td>500</td><td>As above</td><td>500°C/ Tensile</td></tr>
<tr><td>500</td><td>Elastic constant</td><td>500°C/Elastic</td><td colspan="4">As above</td></tr>
</table>

* Tensile tests, jump tensile tests or elastic constant measurements were carried out at elevated temperatures. Total exposure time at a temperature includes the sample soaking time (~1.25h) and the test time.

References

Author (2001)*: ASTM E1876 - 01 Standard Test Method for Dynamic Young's Modulus, Shear Modulus, and Poisson's Ratio by Impulse Excitation of Vibration*. Philadelphia PA: American Society for Testing and Materials.

Author (2009a)*: E8-09 Standard Test Methods for Tension Testing of Metallic Materials*. Philadelphia PA: American Society for Testing and Materials.

Author (2009b)*: E21-09 Standard Test Methods for Elevated Temperature Tension Tests of Metallic Materials*. Philadelphia PA: American Society for Testing and Materials.

Author (2011)*: ASTM E384 - 11e1 Standard Test Method for Knoop and Vickers Hardness of Materials*. Philadelphia PA: American Society for Testing and Materials.

Author (2015)*: ASTM E466 Standard Practice for Conducting Force Controlled Constant Amplitude Axial Fatigue Tests of Metallic Materials*. Philadelphia PA: American Society for Testing and Materials.

Bathias, C. and Paris, P. C. (2004) *Gigacycle fatigue in mechanical practice*. CRC Press.

Hatch, J. E. (1984) *Aluminum: properties and physical metallurgy*. ASM International.

Horst, C., Tetsuya, S. and Leslie, S. 2006. Handbook of Materials Measurement Methods. Springer, Berlin.

Huerta, E., Corona, J., Oliva, A., Avilés, F. and González-Hernández, J. (2010) 'Universal testing machine for mechanical properties of thin materials', *Revista mexicana de física*, 56(4), pp. 317-322.

ICSD (2016) *http://icsd.cds.rsc.org/*.

Mahle (2012) *Pistons and engine testing*. Stuttgart: Springer Fachmedien.

Marines, I., Dominguez, G., Baudry, G., Vittori, J.-F., Rathery, S., Doucet, J.-P. and Bathias, C. (2003) 'Ultrasonic fatigue tests on bearing steel AISI-SAE 52100 at frequency of 20 and 30 kHz', *International Journal of Fatigue*, 25(9), pp. 1037-1046.

Mayer, H., Lipowsky, H., Papakyriacou, M., Rösch, R., Stich, A. and Stanzl-Tschegg, S. (1999) 'Application of ultrasound for fatigue testing of lightweight alloys', *Fatigue & fracture of engineering materials & structures*, 22(7), pp. 591-599.

Morrell, R., Mildeova, P., Chapman, L., P N Quested and Gisby, J. (2015) *Thermal Expansion, Specific Heat, Thermal Diffusivity and Thermal Conductivity Estimation of an Aluminium Alloy*, Teddington, UK: National Physical Laboratory2015090077/1).

Rounthwaite, N. J. (2012) *Development of Bulk Nanoquasicrystalline Alloys for High Strength Elevated Temperature Applications*. DPhil Thesis, University of Oxford.

Stephens, R. I., Fatemi, A., Stephens, R. R. and Fuchs, H. O. (2000) *Metal fatigue in engineering*. John Wiley & Sons.

4. Consolidation and Characterisation of the NQX Alloy Bars

The chapter deals with the characterisation of 25-50μm size NQX alloy powder. Theoretical estimates of the pressure required for extrusion were performed, and the pressures during the extrusion runs were observed to be in a similar range. Detailed characterisation of the extruded bars is also included in this chapter.

4.1 Powder Characterisation

4.0 kg of 25-50μm size fraction of the sieved nanoquasicrystalline alloy powder (NQX-P alloy[A] from here on) was used during the study. Various characterization techniques were employed for the study of the alloy powders.

4.1.1 Optical emission spectroscopy

Inductive charged plasma coupled optical emission spectroscopy (ICP-OES) was carried out by industrial collaborator Alpoco, and the measured chemical composition of the NQX-P alloy is provided in Table 4.1. Impurities can be present in the master alloys in small quantities, and may also arise from the industrial scale gas atomisation process despite equipment cleaning. Oxygen can also be considered as an impurity as it was present in a small quantity during the atomisation process; however, it was excluded in the chemical analysis.

Table 4.1 Composition of the atomised powder measured by OES analysis.

Element	Al	Fe	Cr	Ti	Zn	Mg	Ni
Atomic %	93.001	2.897	1.934	1.979	0.021	0.017	0.012
Element	Si	Mn	Co	Cu	Ga	Zr	Pb
Atomic %	0.114	0.01	0.006	0.004	0.003	0.001	0.001

[A] Nomenclature of the 'NQX-P alloy' is used for the powder $Al_{93}Fe_3Cr_2Ti_2$ alloy, and the term 'NQX alloy' is used for the extruded $Al_{93}Fe_3Cr_2Ti_2$ alloy.

4.1.2 X-ray diffraction (XRD)

XRD studies were carried out on the NQX alloy powder. Aluminium peaks are observed at 38.5°, 44.7°, 65.1°, 78.2°, 82.4° and 99.1° corresponding to the (111), (200), (220), (311), (222) and (400) planes respectively (ICSD, 2016), as shown in Figure 4.1. Amongst the intermetallics, the icosahedral quasicrystalline phase (I-phase) has the most prominent peaks observed at ~22.7°, 41.0°, 43.2°, 61.1°, and 73.2°. The I-phase peaks were indexed by Galano and coworkers (Galano et al., 2004, Galano et al., 2009, Galano et al., 2014) using Cahn's indexation method (Cahn et al., 1986) for an I-phase containing alloy of the same composition. Using aforementioned works (by Galano et. al.), the main I-phase peaks of the NQX-P alloy were identified at 41.0° and 43.2°. Very small peaks for some other intermetallics such as θ_D-$Al_{13}(Fe, Cr)_{2-4}$ (~26.3°, 36.8°, and 75.5°) and Al_3Ti (39.3°, 100% intensity) were also identified in the XRD.

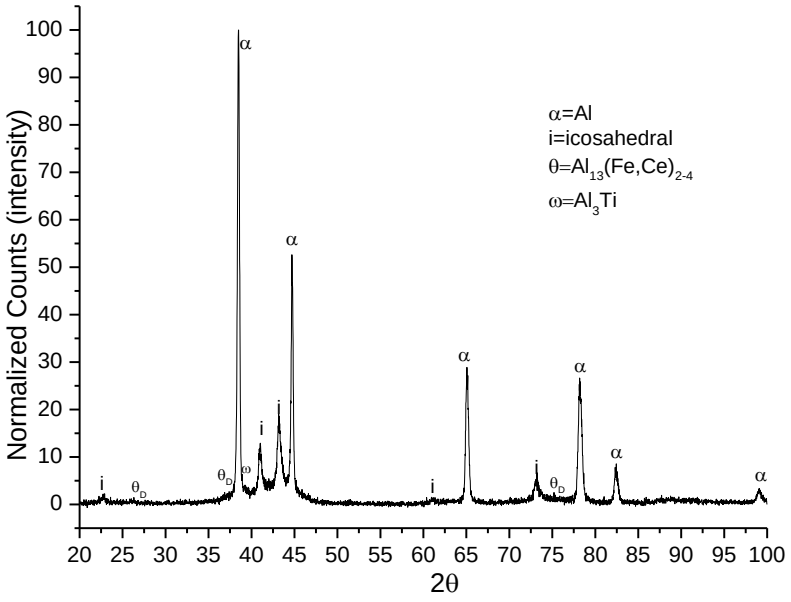

Figure 4.1 XRD of 25-50µm size fraction NQX alloy powder (NQX-P alloy). α-Al and I-phase peaks are marked.

$Al_{13}Fe_4$ (θ_{Fe}) and $Al_{13}Cr_2$ (θ_{Cr}) are stable intermetallic phases found in Al-Fe-Cr alloys having monoclinic structures, and these phases can dissolve significant amounts of Cr and Fe respectively (Mondolfo, 1976). The rapid solidification enhances the solid solubility

and induces large distortions by twinning. A metastable phase with a distorted monoclinic structure is sometimes obtained in the vicinity of the I-phase peaks and is referred to as a distorted θ phase (θ_D-$Al_{13}(Fe, Cr)_{2-4}$) by several authors (Manaila et al., 1989, Kim et al., 2007, Galano et al., 2009, Audebert et al., 2002, Sahoo and Stone, 2005).

4.1.3 Differential scanning calorimetry (DSC)

The I-phase in the NQX alloy is a metastable phase which transforms to stable phases on heating to a sufficiently high temperature. DSC was carried out on the NQX-P alloy samples to confirm the presence of the metastable phase. The baseline subtraction method was explained in section 3.2.4. One of the representative reheat subtracted DSC run is shown in Figure 4.2. The main exothermic transformation peak in NQX-P alloy samples was identified at 555°C±2°C, and the onset of the transformation was found at ~532±3°C. The transformation completes at ~580°C. The area under the peak provides the enthalpy of the transformation, which is found to be ~15±3J/g. It is comparable to the value reported by Rounthwaite (2012) on an alloy of similar composition and size fraction.

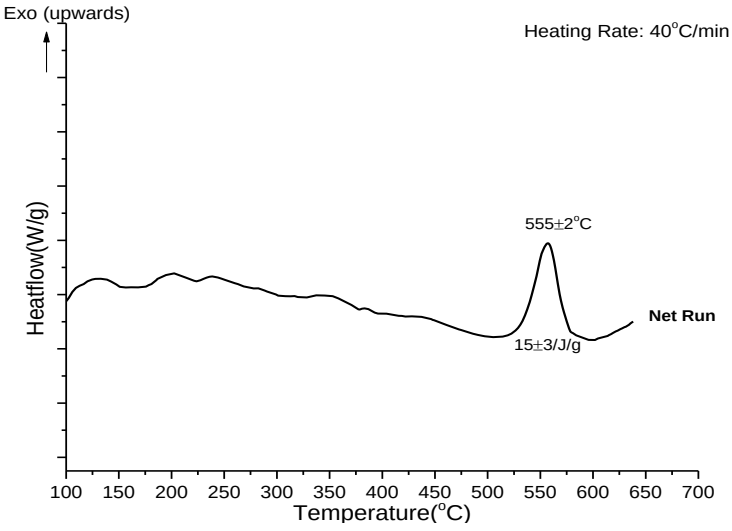

Figure 4.2 DSC run of the NQX-P alloy carried out at 40°C/min. The upward peak shows an exothermic reaction.

4.1.4 Scanning electron microscopy (SEM)

The morphology, size, and shape of the powder were studied by SEM. The larger size powder particles were elongated, and nodular, whereas smaller size powder particles were more spherical, as observed in Figure 4.3. Fine size particles (<5µm) were also present and comprised only a small volume fraction of total powder particles. As seen in Figure 4.3 (a-inset), a few finer particles (satellite particles) were observed to be fused with coarser particles. Satellite particles are undesirable as they have a different micro-structure than the host particle and result in poor packing density on consolidation (Grant, 1983). The complete or partial coalescence of the particles occurs due to the difference in the cooling rate of individual particles during their solidification in the gas atomisation process (Otooni, 2013). A few examples of such particles are highlighted by the dotted circles in Figure 4.3 (a). As observed in Figure 4.3 (b), higher magnification and closer inspection revealed that the surface of the powder particles was not smooth.

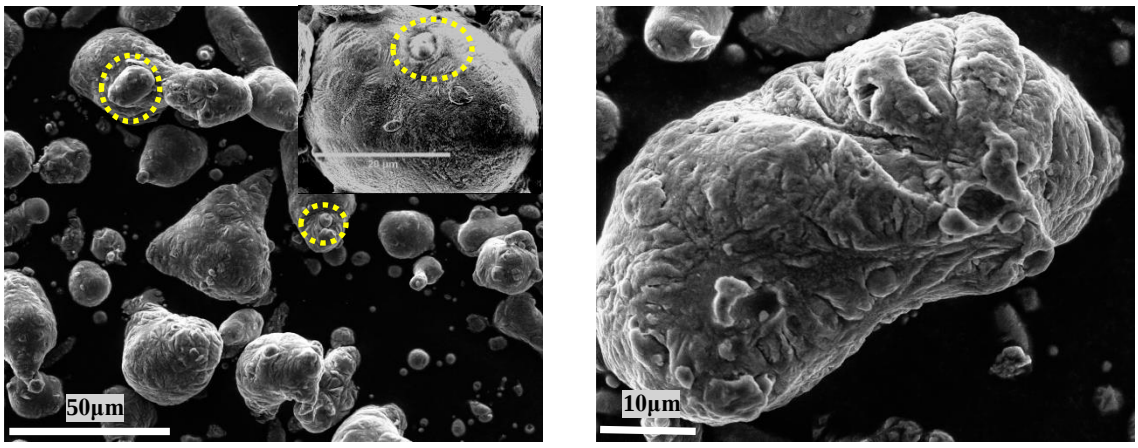

(a) **(b)**

Figure 4.3 Secondary electron (SE) images for 'as sieved' alloy powder: (a) an overview of powder particles, and few particles containing smaller 'fused' particles, (b) a single powder particle showing a rough surface.

SE images of the polished alloy powder particles are shown in Figure 4.4. In Figure 4.4 (a), the overall view can be observed. In Figure 4.4 (b), a high magnification image of the inside of the alloy powder particle shows a dark grey aluminium matrix containing the light grey spherical intermetallic particles. The spherical intermetallic particles were the most abundant species in the alloy, which later turn out to be I-phase particles.

The example of varying microstructure of within the large and small size powder particles can be observed in Figure 4.4 (c, d). Figure 4.4 (c), shows a ~50μm powder particle (P1) which had partially engulfed a 15μm particle (P2). The higher magnifications image in Figure 4.4 (d) revealed that the P2 contained a completely engulfed 3μm particle (P3) inside. The microstructure of the particles becomes finer as the size becomes smaller, as observed in Figure 4.4 (d). Cooling rate of the smaller particles is higher as compared to the coarser particles, which results in a finer microstructure of small size particles (Grant, 1983). Sometimes powder particles containing dendritic structures were observed as highlighted by the dotted circles in Figure 4.4 (a). Visually these dendritic intermetallic features were different from the spherical intermetallics (quasicrystalline) particles and these were likely to be other intermetallic phases. As shown in Figure 4.5, the energy dispersive X-ray spectroscopic (EDX) analyses were carried out on various powder particles. The EDX spectra and the average measured composition are shown in the inset table in Figure 4.5.

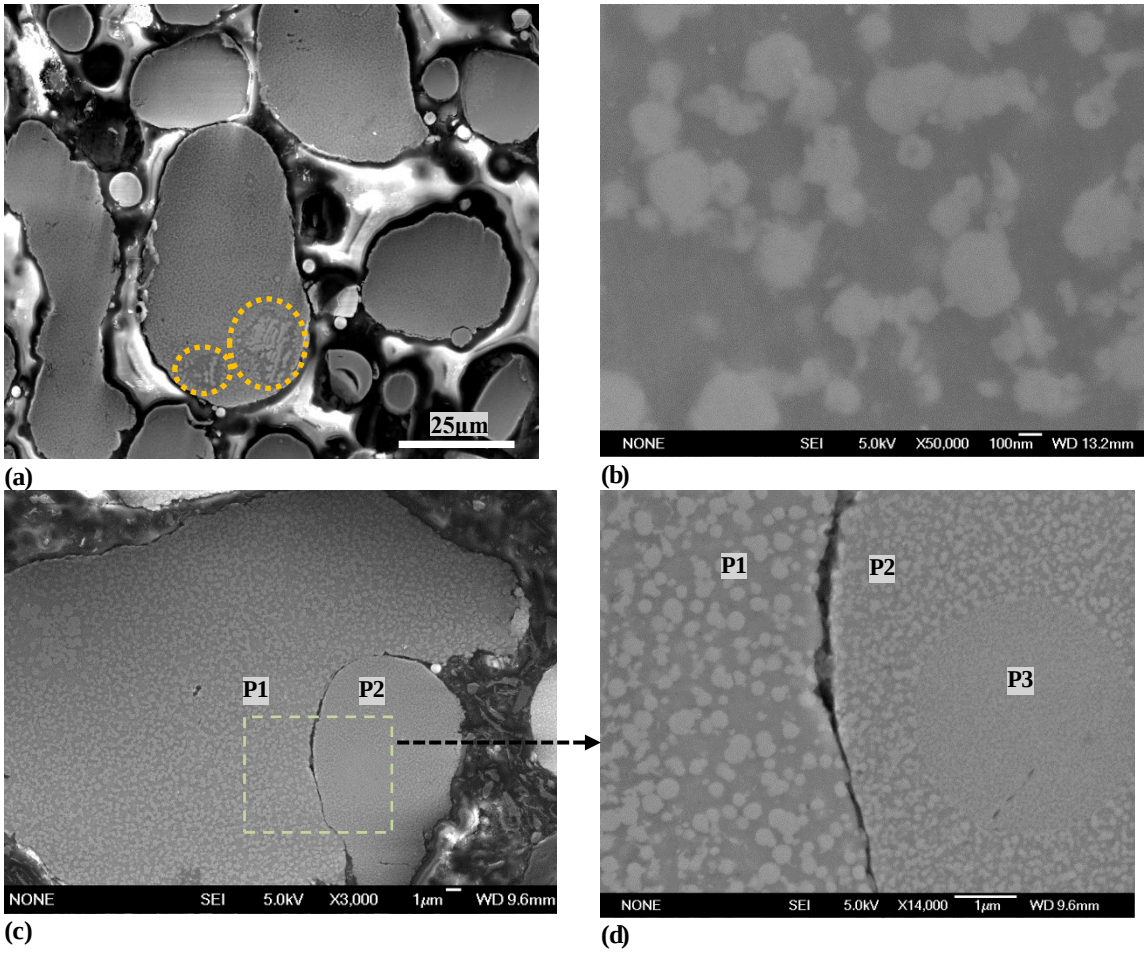

Figure 4.4 SE image for polished (alloy) powder particles: (a) overview of the polished particles, orange circles indicate possible intermetalics (b) high magnification view of a polished alloy powder particle. Within each powder particle, spherical I-phase can be seen embedded in a dark aluminium matrix, (c) a larger powder particle (P1) partially engulfs another particle P2 which completely engulf a small particle P3, (d) high magnification of image(c) showing three types of particles. The microstructure of the I-phase become finer as the powder particle size is reduced.

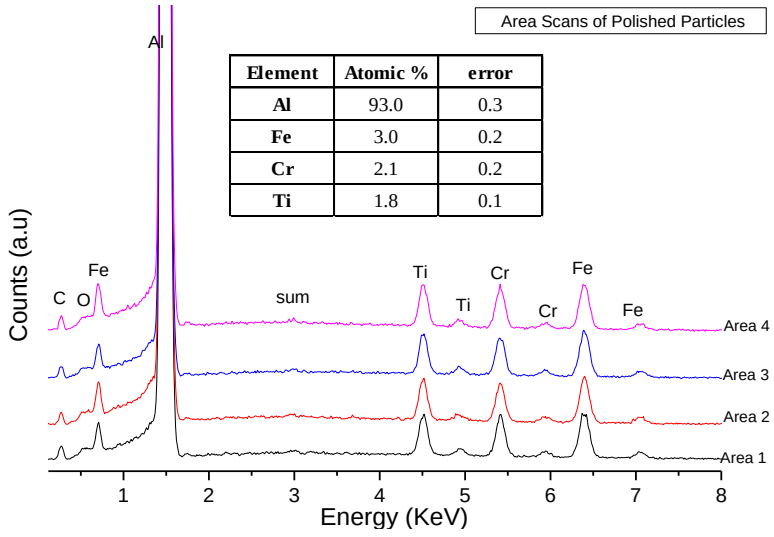

Figure 4.5 EDX analyses of the NQX-P alloy in SEM.

4.1.5 Transmission electron microscopy (TEM)

Bright field (BF) TEM micrographs in Figure 4.6 show a light α-aluminium matrix containing darker I-phase particles. The size of most of the particles ranged from 20nm to 200nm, and the average particle size for the I-phase was 151±11nm (section 4.3.6.2). Occasionally, some large size (>400nm) I-phase particles were observed. The particles were sometimes found forming clusters as seen in Figure 4.6 (b). The I-phase is characterised by its typical 5-fold symmetric convergent beam diffraction pattern, which is shown from a dark I-phase particle in Figure 4.6 (c).

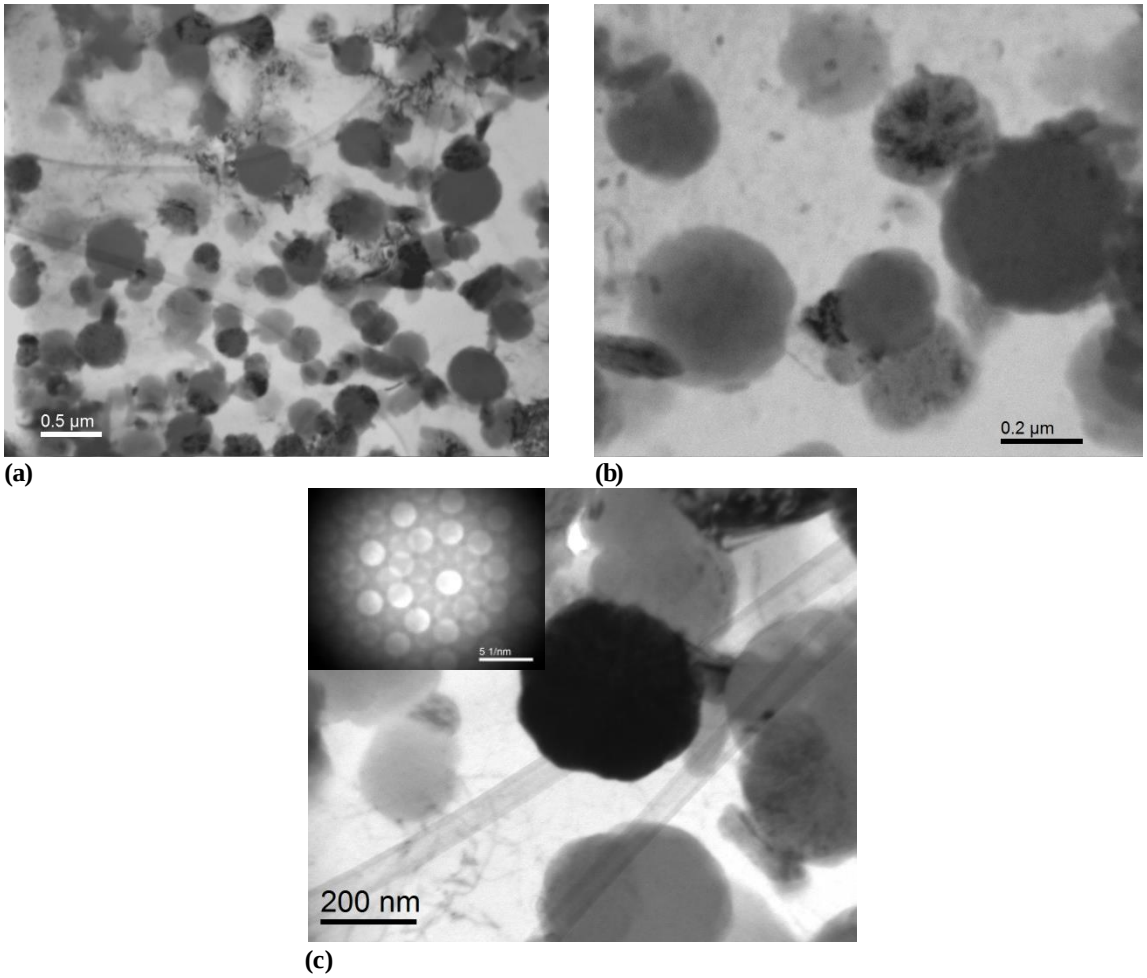

(a) **(b)**

(c)

Figure 4.6 Bright field BF TEM images showing: (a) overall view, (b) various size I-phase particles (c) a fivefold diffraction pattern from an I-phase particle in the centre

4.2 Powder Consolidation

The NQX alloy powders were consolidated in bars using extrusion. The theoretical calculations were performed to estimate the specific work (or the pressure) required for the extrusion of the alloy powder.

4.2.1 Calculation of the total specific work (or pressure) for extrusion

Appendix 1 provides the details (literature and the calculations) for the estimation of the extrusion pressures[B], summarised in this section. The total specific work for extrusion is the sum of all the individual components of the work required for extrusion (Hosford and Caddell, 2011). The mathematical expressions for the individual components are provided in Table 4.2. The efficiency of the extrusion process is the ratio of the ideal work to the total work.

Table 4.2 Components of specific work required for extrusion and their mathematical relations with various parameters.

Ideal Work	Redundant Work	Work against friction (in die shoulder)	Work against friction (in container wall)	Total Work	Efficiency
w_{ideal}	w_{red}	$w_{F,sh}$	$w_{F,w}$	W_{total}	η
$K\frac{\varepsilon^{n_{sh}+1}}{n_{sh}+1}$	$\frac{2}{3}\tan\alpha K\frac{\varepsilon^{n_{sh}}}{n_{sh}+1}$	$\frac{2w_{ideal}\mu}{\mathrm{Sin}2\alpha}$	$\frac{4\mu L_0\sigma_{yeild}}{D_0}$	Σw	$w_{ideal}/\Sigma w$

In Table 4.2, K is the strength coefficient, whilst n_{sh} is the strain hardening coefficient. Initially, the K and n_{sh} values were taken from the literature for similar alloys, and the calculations were refined after finding the actual values of the NQX alloy in chapter 6 and 7, provided in Table 4.3. μ is the coefficient of friction for the lubricant Hexagonal Boron Nitride, used as ~0.1-0.16 from literature (Martin et al., 1992). ε is the true strain, $\alpha°$ is the die angle (21.6^o), D_o is the initial diameter of the Aluminum can (outer diameter of

[B] 'Specific work required for extrusion' has units of MPa and has been interchangeably used for the 'extrusion pressure'.

the can is ~50mm and it has a wall thickness of 2.5mm), and D_f is the diameter of the extruded bar (14mm). L_o is the initial length of the solid billet at breakthrough during extrusion (~65mm). $\dot{\varepsilon}_{avg}$ is the true average strain rate during extrusion (calculated as ~$0.1s^{-1}$) and σ_{yeild} is the yield strength of the material.

Table 4.3 Calculated specific work (or pressure) for extrusion at different temperatures.

$\dot{\varepsilon}$	T	L_o	μ	σ_{Yield}	K	n_{sh}	W_{ideal}	W_{red}	$W_{F,sh}$	$W_{F,wall}$	Total Work	Efficiency
s^{-1}	°C	mm		MPa	MPa		MPa					
0.1	23	65	0.15	551	800	0.05	1856	212	861	458	3388	0.55
0.1	350	65	0.15	304	390	0.03	907	104	421	253	1684	0.54
0.1	400	65	0.16	213	280	0.05	650	74	301	177	1202	0.54
0.1	400	65	0.1	197	280	0.05	650	74	188	102	1015	0.64

The extrusion work calculations are dependent on several parameters (T, μ, $\dot{\varepsilon}$, K, n_{sh}, L_o, D_o and σ_{yield}). Using values of these parameters in the respective equations in Table 4.2 each component of the specific work required for extrusion and the total work were calculated, which are provided in Table 4.3. The total work or pressure required for extrusion at 400°C is calculated to be 1015 and 1200MPa using μ values of 0.1 and 0.16 respectively. The knowledge of pressure is valuable information for safely performing the extrusion.

4.2.2 Calculation of adiabatic temperature rise

If the extrusion speed is very high such that the heat does not have sufficient time to escape, the process is considered to be adiabatic. The adiabatic temperature rise due to mechanical work can be calculated by Eqn.4.1 (Hosford and Caddell, 2011).

$$\Delta T = \frac{W_{ideal}}{\rho C_p} = \frac{\int_{\varepsilon_1}^{\varepsilon_2} \sigma . d\varepsilon}{\rho C_p} \qquad \textbf{Eqn.4.1}$$

Where ΔT is the temperature change (in K or ^{o}C), and w is the specific work done. ρ is the density and C_p is the specific heat capacity. Initially, ρ and C_p values for aluminium were used from literature. Later the calculations were refined using ρ and C_p values measured for the NQX alloy by Dr Roger Morrell at NPL[C] (Morrell et al., 2015) as mentioned in appendix 5. w_{ideal} is the ideal work for extrusion which was calculated to be ~650 MJ/m^3 in section 4.2.1.

Maximum adiabatic ΔT rise was calculated to be ~220^{o}C, thus a high speed extrusion can raise the temperature of an extrudate at 400°C to a possible 620°C.The powder DSC study suggests that the onset of metastable I-phase transformation is ~525^{o}C and the transformation completes around ~580°C (at 40°C/min heating rate). Therefore; owing to a high extrusion speed the temperature of the extrudate can possibly rise as high as ~620^{o}C during the NQX alloy extrusion, resulting in the transformation of the I-phase.

4.2.3 Extrusion of powders into solid bars

Fourteen bars were produced through extrusion over the research period. Except bar 1 (B1), all bars were extruded at similar conditions. Complete details of the extrusion parameters, temperature conditions, and dimensions of the extrudate are provided in Table 4.4. The surface of the extruded bars was mostly smooth except for a ~150mm portion at the end of the bars. The backside of the bars comprised an Al6082-O alloy from the can. The bars were extruded at a target speed of 1mm/s, and actual average extrusion speed was observed to be 0.9±0.1mm/s. Bar 1 was extruded at a speed of ~8mm/s and it was used to investigate the effect of extrusion speed on the NQX alloy microstructure.

The maximum or breakthrough pressure for the extrusion of the bars (excluding B1) was found between 1015-1220MPa and the average value was 1105±65MPa. The variation in

[C]. NPL,UK was subcontracted to measure several thermal properties (coefficient of thermal expansion, density, specific heat, and thermal diffusivity) of the NQX alloy. The NPL official report is referred to as Morrell et al (2015), and details are in appendix 5. For NQX alloy $C_{p\text{-}400^{o}C}$= 1022 J/Kg.K, $\rho_{400^{o}C}$= 2880 Kg/m^3.

the pressures within bars was considered to be present primarily due to the lubrication, as it was observed that during the extrusion experiments, the lack of thorough lubrication resulted in higher peak pressures. This was the reason for assigning values to the μ from 0.1 to 0.16 in theoretical extrusion pressure calculations (section 4.2.1). The smaller values indicated well cleaned and well-lubricated surfaces resulting in lower peak pressure values. The higher extrusion speed for B1 resulted in a higher peak pressure of 1310MPa (despite a well-lubricated surface), whereas the low extrusion speeds caused lower extrusion pressures (1105±65MPa) in the remaining bars. The 'speed sensitive' behaviour at this stage was attributed to a possible strain rate sensitivity of the NQX alloy (discussed in section 7.4.3).

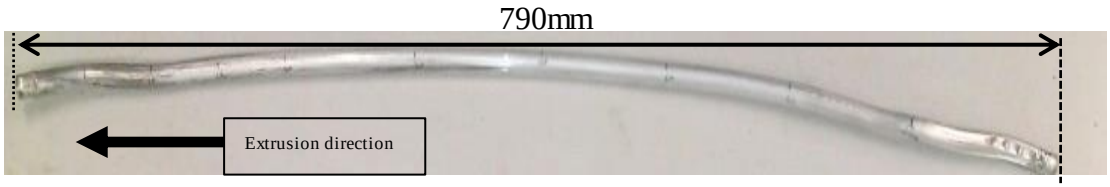

Figure 4.7 Example of an extruded bar of the NQX alloy, the extrusion direction is also indicated.

Extrusion ratio (A_o/A_f) can also affect the total extrusion pressure; a smaller extrusion ratio results in a lower extrusion pressure (Todd et al., 2004). In the present study, an average maximum extrusion pressure of 1105±65MPa was observed at a temperature of 400^{o}C and an extrusion ratio of 12.76:1. Taking into consideration the differences in composition, microstructure and extrusion ratio and other extrusion parameters, overall the average extrusion pressure is comparable to values found in the literature for similar alloys. Todd et al. (2004) extruded the atomised powders of similar composition and powder fraction size at 400^{o}C. Maximum pressures were observed to be 1155, 1313 and 1473MPa for extrusion ratios of 7:1, 10:1 and 14:1 respectively. Rounthwaite (2012)

extruded a similar alloy and powder fraction at an extrusion ratio of 10:1 at 375^{o}C, and observed a maximum pressure of 1094MPa.

Table 4.4 Extrusion parameters for the extruded bars.

Bar No	Peak Extrusion Pressure	Average Extrusion Speed	Remaining Length of the Can (when breakthrough was achieved during extrusion)	Pre-heating Conditions of the Can	Extrusion Container Temperature	Can Dimensions		Powder Weight	Approximate Extruded Bar Dimensions	
	MPa	mm/s	mm		°C	Length (mm)	Outer Diameter (mm)	g	Length (mm)	Diameter (mm)
Bar 1	1306	8.35	700	15min at 400°C then 15min at 415°C	400±3	103	50.9	278	910	14.1
Bar 2	1049	0.82	660			102	50.1	261	810	14.1
Bar 3	1050	0.82	650			102	50.1	251	830	14.1
Bar 4	1078	0.93	650			102	48.9	258	810	14
Bar 5	1166	1.01	650			102	50.5	253	790	14
Bar 6	1175	0.88	640			102	50.3	266	790	14.1
Bar 7	1057	0.9	640			102	50.2	263	600	14.1
Bar 8	1130	0.8	590			102	50.1	275	805	13.9
Bar 9	1200	0.82	620			102	50.1	270	790	14
Bar 10	1040	0.95	610			102	49.6	258	780	14
Bar 11	1220	0.8	590			102	49.5	263	530	14.1
Bar 12	1073	0.93	660			102	49.9	270	810	13.9
Bar 13	1090	0.84	650			102	50.1	269	790	13.9
Bar 14	1015	0.85	650			102	49.8	266	800	13.9

4.3 Characterisation of the Extruded Bars

The extruded bars were characterised using XRD and DSC, and results were compared to find any deviation in the microstructure. All the bars except for the B1 were found to be similar. From here onwards the term 'the bars' will refer to B2 to B14. The microstructure was thoroughly observed with SEM and TEM and found to be similar. Microhardness (chapter 6) results of all the bars were also similar. EBSD was also performed to study the grain sizes.

4.3.1 XRD

The bars were characterised using XRD, which was carried out for both the front and rear end of the useful portion of each bar to ensure microstructural homogeneity. Furthermore, the XRD results illustrated the microstructure repeatability in all bars. Figure 4.8 (a) shows the XRD for the longitudinal section, cross section and filings of one of the bars. XRD results are similar to the atomised alloy powder. α-aluminium peaks were observed at 38.5°, 44.7°, 65.1°, 78.2°, 82.4° and 99.1° corresponding to the (111), (200), (220), (311), (222) and (400) planes (ICSD, 2016). I-phase peaks were observed at 22.8°, 41.1°, 43.2°, 61.1°, 73.2°, similar to the powder alloy samples. Small θ_D-$Al_{13}(Fe, Cr)_{2\text{-}4}$ phase peaks were also present at 2θ positions ~26.3°, 34.6°, 36.8° and 75.5°, which was more prominent in the cross section direction. Figure 4.8 (b) shows the enlarged central section of the XRD, highlighting two main I-phase peaks at 41.1°, 43.2° and θ_D peaks at 34.6° and 36.8° 2θ positions. Figure 4.9 shows the XRD for (longitudinal section) for all extruded bars. The α-aluminium peaks were observed at 2θ positions ~38.5°, 44.7°, 65.1°, 78.2°, 82.4° and 99.1° corresponding to (111), (200), (220), (311),

(222) and (400) planes.The I-phase peaks were observed at ~22.7°, 41.1°, 43.2°, 61.1°, 73.2°. Small Al_3Ti peaks at 39.3° (100% intensity) corresponding to (103) plane and θ_D-$Al_{13}(Fe, Cr)_{2-4}$ peaks at 26.3°, 36.8° were sometimes observed.

Bar1 had a totally different microstructure as no I-phase peak could be identified in the XRD. Instead, it contained peaks from the stable intermetallics. Prominent Al_3Ti peaks were observed at 25.4°, 39.3° (100% intensity), 47.4°, 63.3°, 69.2°, and 75.1°. $Al_{13}Cr_2$ (θ_{Cr}) peaks were found at 36.5°, 40.1°, 41.1°, 41.8° and 43.9°(100% intensity) and $Al_{13}Fe_4$ (θ_{Fe}) peaks were observed at 41.8°, 43.0° (100% intensity) and 43.9° (ICSD, 2016). The phase transformation of the alloy is explained in section 5.2.

The mechanical deformation processes can introduce texture in the materials which can be identified by comparing the peak intensities in the XRD. The (111) has a maximum intensity in the standard XRD pattern for standard aluminium powder sample (ICSD, 2016).The X-ray intensity of the aluminium peaks at 38.5°, 44.7°, 65.1°, 78.2°, 82.4° and 99.1° corresponding to (111), (200), (220), (311), (222) and (400) were normalised using the respective (111) peak intensity for the longitudinal section, the cross section and the filing samples for the NQX alloy. The results are shown in Figure 4.10 along with the standard aluminium powder pattern as a reference. The filing texture followed the standard powder texture. The cross section showed a reduced intensities along (200), (220), (311), which relatively meant a strong texture in the (111) (Figure 4.10). The longitudinal section had the (220) exhibiting the highest intensity, displaying values from 110% to 160% relative to the (111) peak intensity. These observations are consistent with the results of Rounthwaite (2012) and Pedrazzini (2014), for similar extruded alloys in our research group.

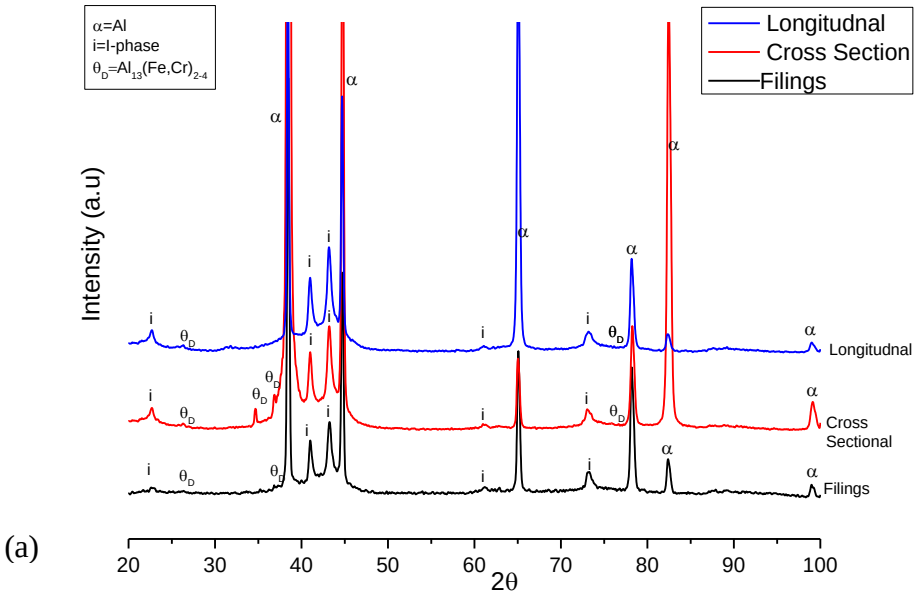

(a)

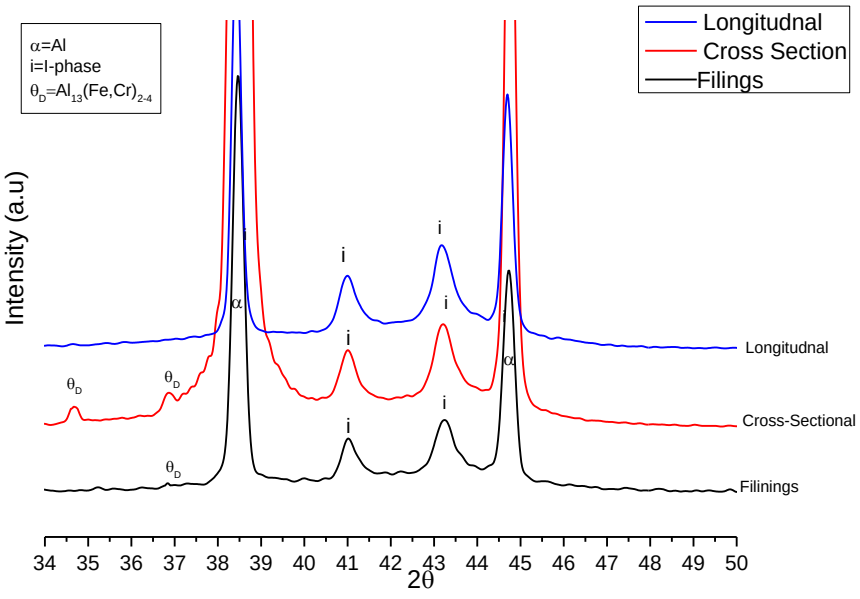

(b)

Figure 4.8 XRD of a bar for the longitudinal section, cross section and filings: (a) overall view (20-100°), (b) magnified view (34-50°).

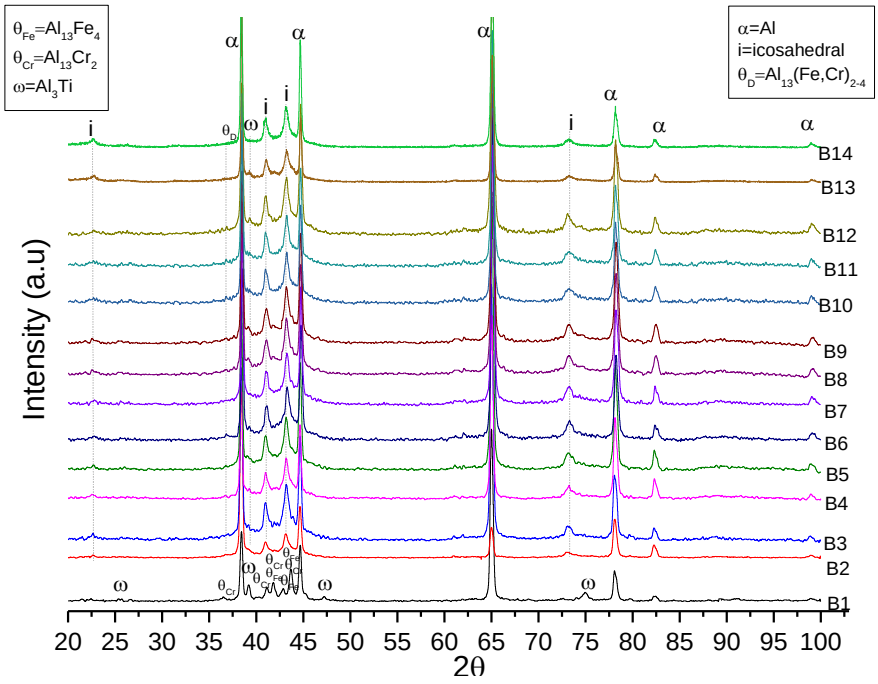

Figure 4.9 XRD of all extruded bars in the longitudinal direction. All bars are similar except bar 1 which contains other intermetallics peaks instead of the I-phase peaks.

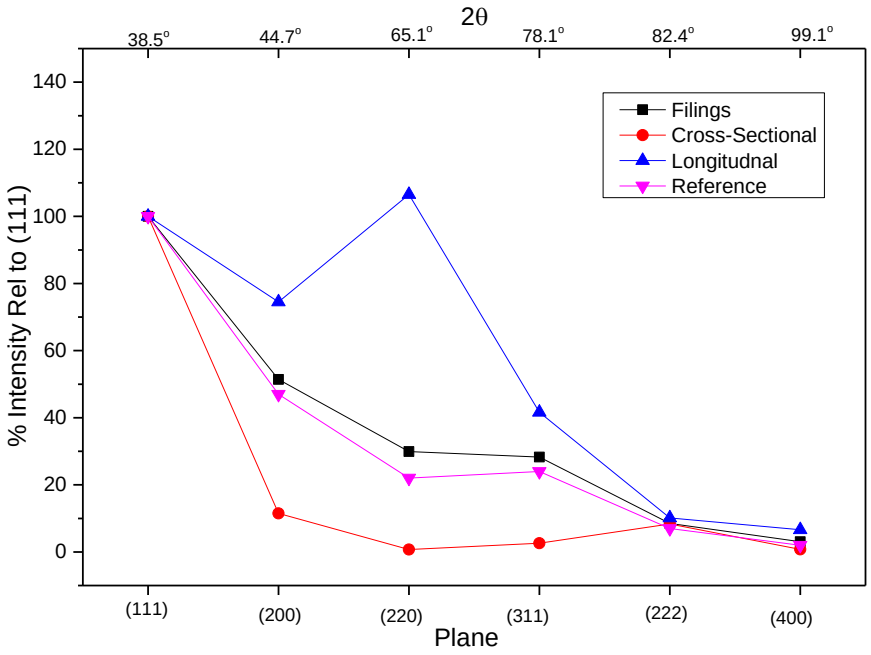

Figure 4.10 An example of the texture in an extruded bar.

4.3.2 DSC

DSC scans for the bars were obtained and are shown in Figure 4.11. The exothermic peak(s) corresponding to the transformation of the metastable I-phase was found to be ~522±4^{o}C, and the onset of the transformation was found in the range ~500±5^{o}C. In all the bars (B2 to B14) the corresponding presence of the I-phase peaks was already confirmed by the XRD analysis (section 4.3.1)

It was also observed that the exothermic I-phase transformation peaks in the extruded NQX alloy samples were ~30-35^{o}C lower than those observed for the NQX alloy powder samples (refer to section 4.1.3 and Figure 4.2) which is consistent with the observations made by Rounthwaite (2012). The mechanical work during the extrusion increases the free energy (or the driving force) for decomposition, and as a result, the metastable peak in the extruded alloy samples shifts to a lower temperature.

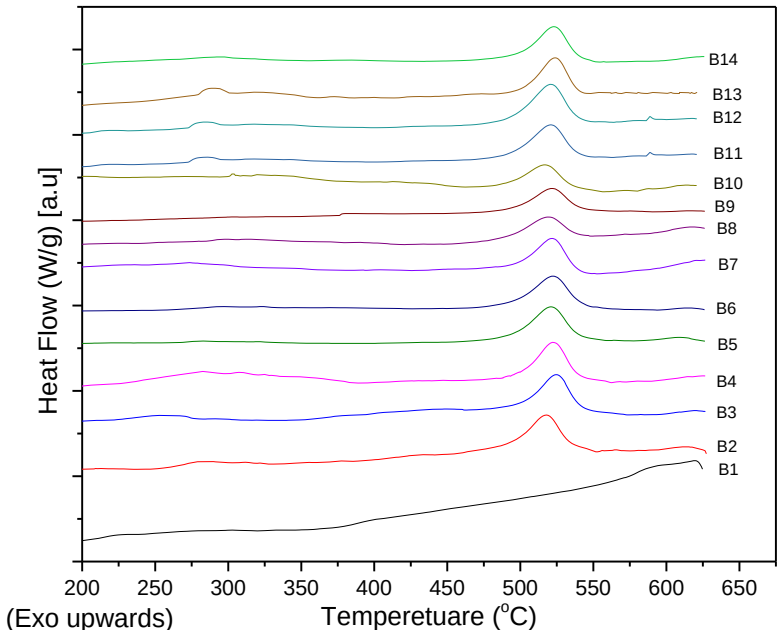

Figure 4.11 DSC of all the extruded bars. The bars contained metastable I-phase peaks (~522^{o}C), except Bar 1 in which no such peak was observed.

Bar 1 showed no metastable phase peak in the DSC, and also exhibited no corresponding I-phase peaks in the XRD analysis. Recalling the calculations of the adiabatic temperature rise due to mechanical work (section 4.2.2) and the DSC analysis (section 4.1.3) which showed the NQX alloy powder completely transformed at temperatures ~580^{o}C, it can be deduced that Bar 1 overheated during the extrusion. The extrusion speed for bar 1 was ~8.3mm/s. The high extrusion speed caused an adiabatic temperature rise and subsequently the I-phase transformations in the alloy. Bar 1 was; therefore, considered a different material for all practical purposes and was not used for mechanical testing.

4.3.3 SEM

SEM was carried out on the extruded bar samples which were cut in longitudinal (Figure 4.12) and cross section directions (Figure 4.13). SEM particle size analysis showed that only a small percentage of the I-phase particles had sizes larger than 400nm and the majority of the microstructure was comprised of fine size I-phase particles.

Highly deformed NQX alloy powder particles appeared well bonded in the extruded samples, as a result, no porosity was identified in the SEM analysis. The extruded bar samples showed the signs that the alloy powder particles had undergone a significant plastic deformation, consequently, those were found to align in the extrusion direction (E.D). Since the microstructure of the constituent alloy powder particles comprised various size I-phase particles, the alignment of the powder particles in the extrusion direction gave rise to a 'band like' appearance. These bands have been marked by blue arrows in Figure 4.12 (a, b).

The microstructure in the cross section samples is shown in Figure 4.13, the extrusion direction (E.D) is in the plane of the paper marked by a ⊙ sign. As a result, the 'band

like' features observed in the longitudinal direction did not appear in the cross section samples.

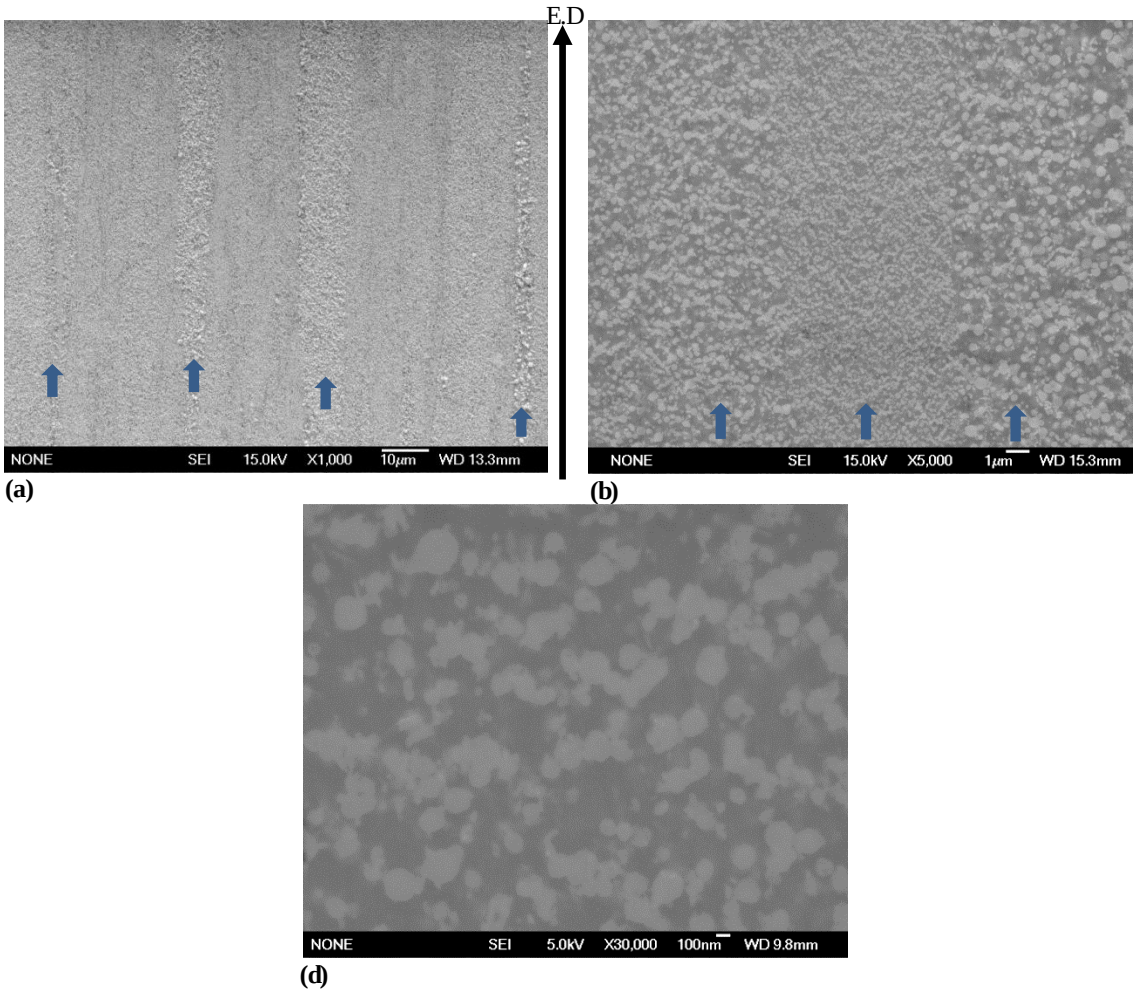

Figure 4.12 SE images for the longitudinal samples. The black arrow indicates the extrusion direction (E.D). The bands are marked with thick blue arrows (a) overall view, (b) intermediate magnification view inside a band. (c) I-phase particles seen at a higher magnification.

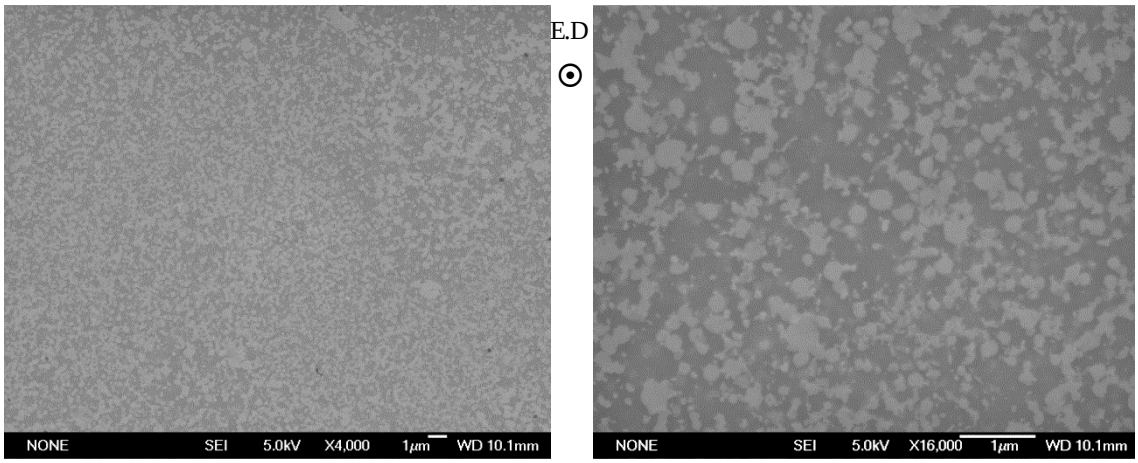

(a) **(b)**

Figure 4.13 SE images for the cross section. The extrusion direction (E.D) is in the plane of the paper. Bands do not appear in this view (a) a low magnification image (b) a high magnification image.

4.3.4 TEM

Figure 4.14 shows the bright field TEM images of the NQX alloy extruded bar. The dark/grey I-phase particles were observed to be spread homogeneously in the light Al matrix. The I-phase particles were observed to have a range of sizes and the majority of these particles were measured from ~20nm to 400nm. The fivefold diffraction pattern associated with the I-phase particles is shown from a particle marked as 'I' in Figure 4.14 (b).

Mostly the aluminium grains were observed to have grain sizes from 200nm to 700nm. Examples of Al grains is shown in Figure 4.14 (c) which contains two aluminium grains marked as M1 and M2 having diameters ~200nm-300nm. Figure 4.14 (d) shows the diffraction pattern from the Al grain (M1) in [001] zone axis. However, only a small number of Al grains could be identified using TEM.

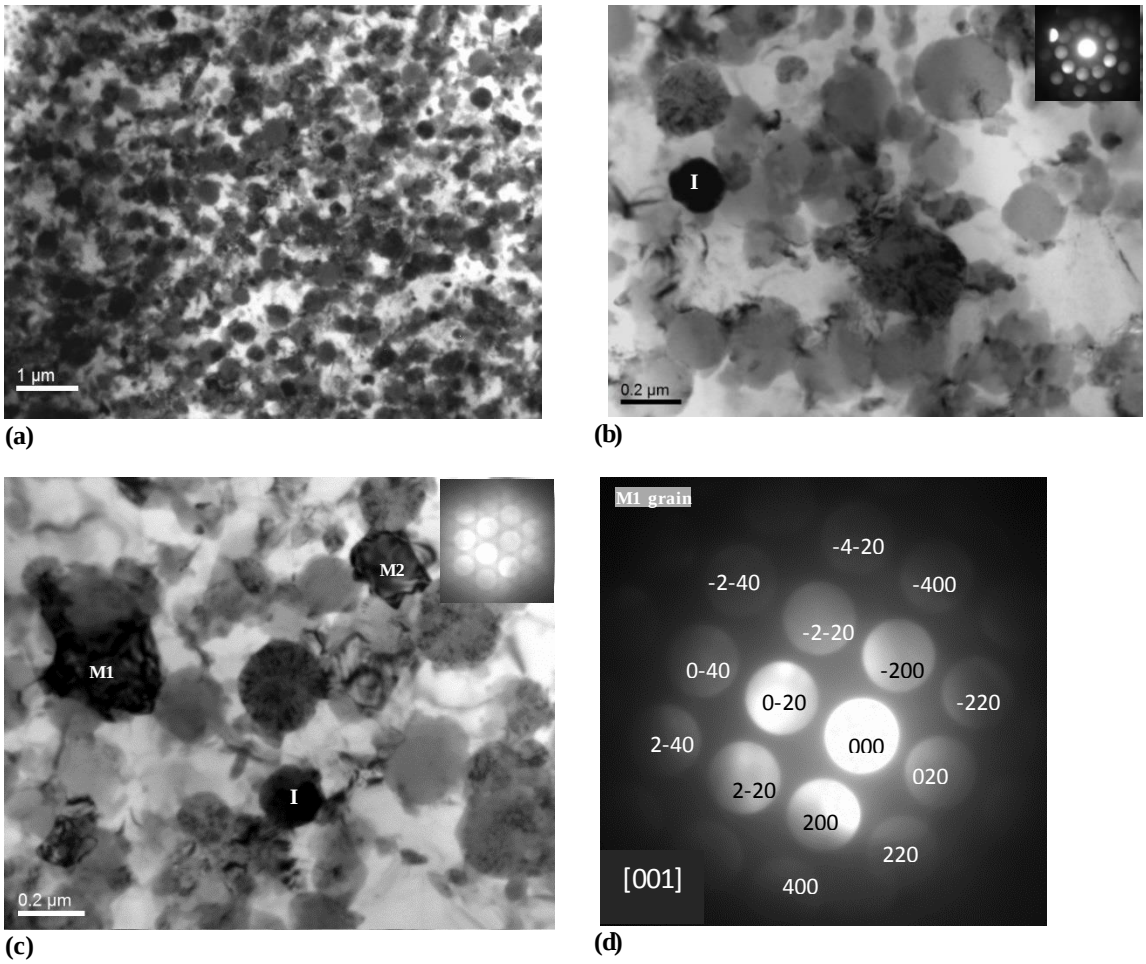

Figure 4.14 TEM images of various bars: (a) overall view, (b) various size I-phase particles, and a fivefold diffraction pattern from one such I-phase particles marked as 'I', (c) two Al grains are marked by 'M1' and 'M2' and I-phase particles. A three-fold pattern for I-phase particle marked by 'I' is also shown (d) a diffraction pattern from an aluminium grain 'M1' in [001] zone axis.

EDX analysis of the matrix and the quasicrystalline particles was carried out as shown in Figure 4.15. The atomic percent chemical compositions are provided in the inset table, which shows that only a small amount of foreign elements is present in the aluminium solid solution that is Fe (0.35%), Cr (0.4%) and Ti (1.05%).

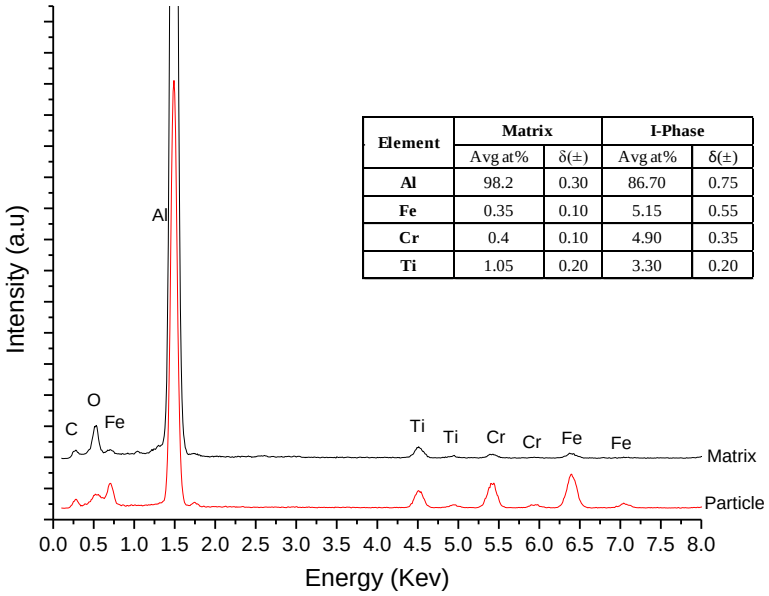

Element	Matrix		I-Phase	
	Avg at%	δ(±)	Avg at%	δ(±)
Al	98.2	0.30	86.70	0.75
Fe	0.35	0.10	5.15	0.55
Cr	0.4	0.10	4.90	0.35
Ti	1.05	0.20	3.30	0.20

Figure 4.15 EDX analysis from TEM, inset table provides the at% composition of the matrix and the particles

4.3.5 EBSD

TEM studies were only possible for smaller areas, and fewer grains could be identified in each sample. EBSD was used to measure the grain size and orientation for larger areas ($10x10\pm2x2\mu m^2$) in the samples obtained from both the cross section and longitudinal directions of the extruded bar. Figure 4.16 (a) provides the inverse pole figure (IPF) colour map code and the grain boundary colour code. Figure 4.16 (b) and Figure 4.16 (d) show EBSD IPF image and the grain size distribution (from Appendix 3) respectively for the longitudinal sample. Figure 4.16 (c) and Figure 4.16 (e) show EBSD IPF image and the grain size distribution (from Appendix 3) respectively for the cross section sample. Extrusion direction (E.D) is marked by a direction arrow for the longitudinal section and by a ⊙ sign in the cross section sample. IPF is the volume fraction of crystals containing one of the lattice directions parallel to the sample axis (Gambin, 2013). The grains in the longitudinal section were aligned and elongated along the

direction of extrusion, whereas the grains in the cross section were more equiaxed. Both the longitudinal and cross section EBSD scans contained ~10-35% of the total boundary fraction as the low angle grain boundaries, as seen in (Figure 4.16 (b, c)). As mentioned earlier, the distributions of the grain diameter against the respective area fraction is shown in (Figure 4.16 (d) and (e)) for longitudinal and cross section sample which are obtained from the 'unique grain colour maps' provided in Appendix 3. The grain sizes were observed to range from submicron to a few microns; however, the majority area fraction of the alloy was comprised of the submicron size grains. The average grain size was larger (~473nm) in the longitudinal grains as compared to the cross section grains (432nm).

The pole figures for the cross section sample were symmetric around the extrusion axis as shown in Figure 4.17 (a), and the lattice orientation distribution was independent of rotation about this axis. <111> was the most abundant texture component parallel to the extrusion direction in Figure 4.17 (b). This is consistent with the XRD study of texture in the cross section sample (Figure 4.10). The texture in EBSD was fairly local (corresponding to the ~100μm^2 scanned area), whereas the one from XRD contained the information from the complete sample (~100mm^2 area). The extruded bars became heavily textured in the extrusion direction, so the local (from EBSD) and the general (from XRD) textures exactly matched for the cross section samples, whereas variations did exist in the longitudinal texture, probably due to the localised effects.

Extrusion is a 'constrained tension' process which is a combination of tension and hydrostatic pressure (Gambin, 2013). As a result of deformation, one (or more) crystallographic direction(s) become parallel to the (extruded) bar axis and the pole figures

become axially symmetric as seen in Figure 4.17 (a). This type of texture is referred to as a 'fibre texture'. In f.c.c metals, the fiber texture has <111> and/or <100> components, whereas in aluminium extrusions, a high concentration of <111> is developed (Gambin, 2013). The texture in the cross section samples was important as it contains the symmetry axis for the extruded bars, and all mechanical tests were conducted such that the tensile and the extrusion axis were aligned.

To initiate slip in a single crystal during a tensile test, the applied tensile stress (σ) must produce a resolved minimum shear stress (τ) in the slip plane (Dieter and Bacon, 1986). The tensile and the shear stresses can be equated as the following.

$$\sigma = M\tau \qquad \textbf{Eqn. 4.2}$$

Where M is called the Taylor factor which has an average value of ~3.07 for a polycrystalline untextured fcc material (Abbaschian and Reed-Hill, 2008). The values of M are 3.67, 3.67 and 2.44 for the <111>, <110> and <100> texture components respectively. From the IPF maps it was estimated that ~70% contains the <111> texture component, whilst the rest is <100>, which is consistent with the literature (Rollett, 2008). The average Taylor factor for these extruded samples was calculated as ~3.3 which was used to calculate the contributions of various strengthening mechanisms in section 8.2.3.

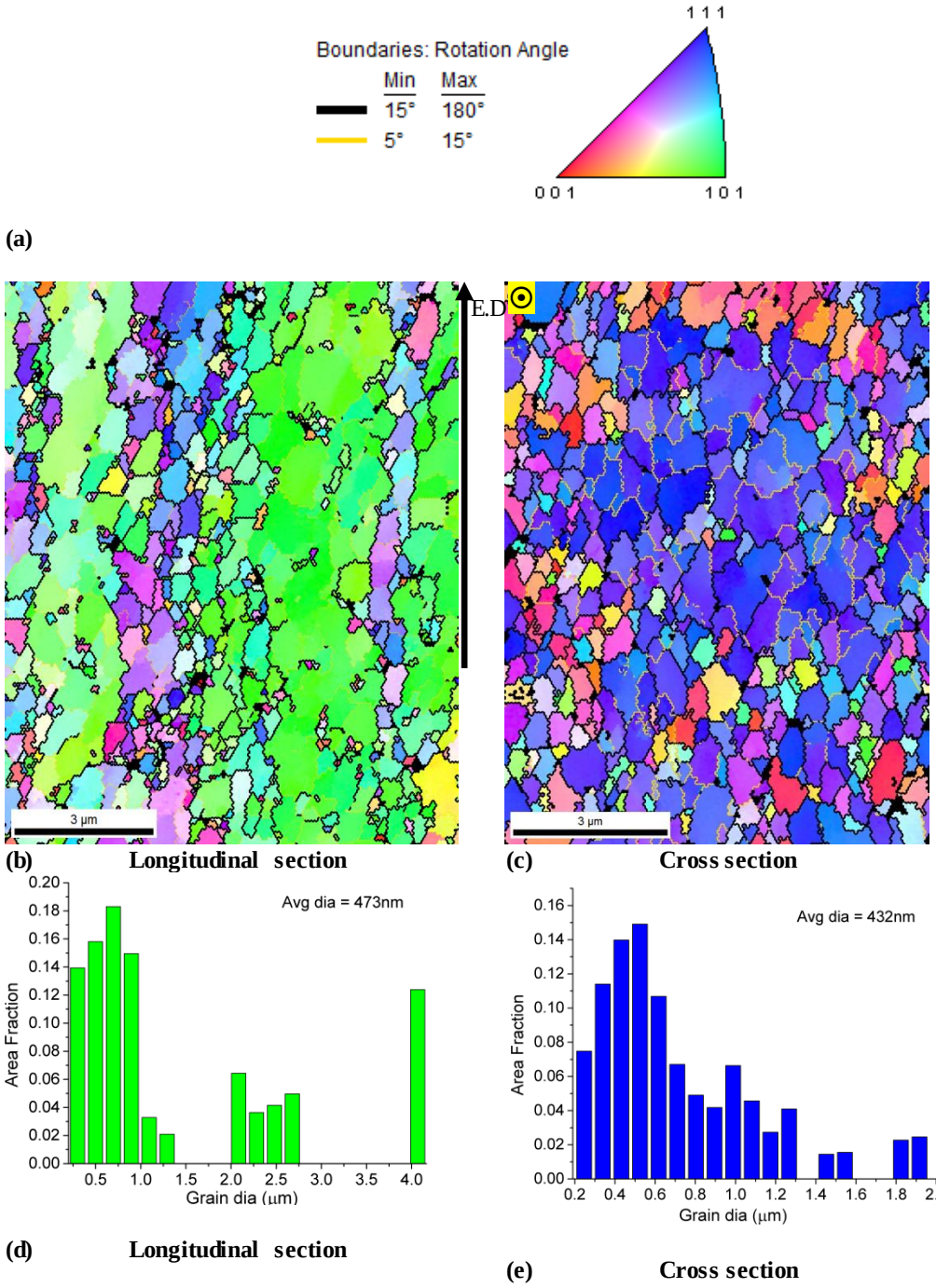

Figure 4.16 (a) Colour coding for small and large angle grain boundaries and inverse pole figures. (b) EBSD (IPF) image for the longitudinal sample, the grains are alligned in the extrusion direction, (c) EBSD (IPF) image for the cross section sample, (e) grain size distribution for the longitudinal section, (d) grain size distribution for the cross section.

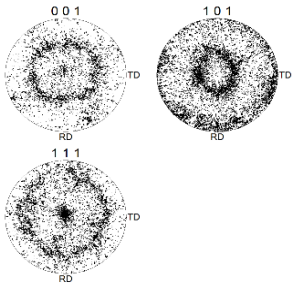

(a) Cross section

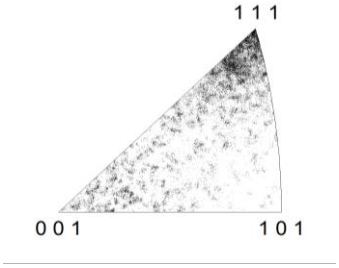

(b) Cross section

Figure 4.17 (a) Pole figures for the cross section, (b) inverse pole figures for cross section.

4.3.6 Particle size distribution, volume fraction and interparticle spacing

The sizes of distribution of the I-phase particles, their volume fraction and interparticle spacing was calculated using TEM and SEM work for the extruded alloy samples and applying stereology methods.

4.3.6.1 Volume fraction

SEM images of intermediate magnifications (16K and above) from the cross section and the longitudinal section of the extruded bar were used for the I-phase volume fraction analysis. A total area of ~380 μm^2 was scanned with image processing software. Exploiting the contrast between (dark) aluminium matrix and (bright) I-phase particles, the relative area fractions were calculated. Since the area fraction of a 2D surface and corresponding volume fraction in a 3D volume are proportional (Friel, 2000); therefore, the I-phase particle area fraction or the volume fraction, f_v was found to be 44±3%. Similar I-phase volume fractions have been reported in the literature. For example, Inoue and Kimura (2001) found a 45% volume fraction for the I-phase in atomised and extruded $Al_{93}Fe_3Cr_2Ti_2$ alloy. Also, assuming all particles being the I-phase, Audebert et

al. (2002) reported a volume fraction of 42% in melt-spun ribbons of $Al_{93}Fe_3Cr_2Ti_2$ alloy.

4.3.6.2 Particle size and distribution

Both TEM and SEM images were used to measure the particle sizes. However, smaller (<~40 nm) particles were difficult to image in SEM due to problems of poor contrast and 'charging up' at high (~>40KX) magnifications. Therefore, particle size data measured from TEM was further used to perform statistical analyses. Measurements were performed on a total of ~400 particles. Figure 4.18 shows the particle size distribution, percent relative frequency of the particle count, and percent cumulative frequency of the particle count against the particles size (diameters), binned at 40nm intervals. Various statistical distributions were fitted and 'log normal distribution' was found to be appropriate for the variability of the dataset. The mean particle size is found to be 151±11nm from the distribution.

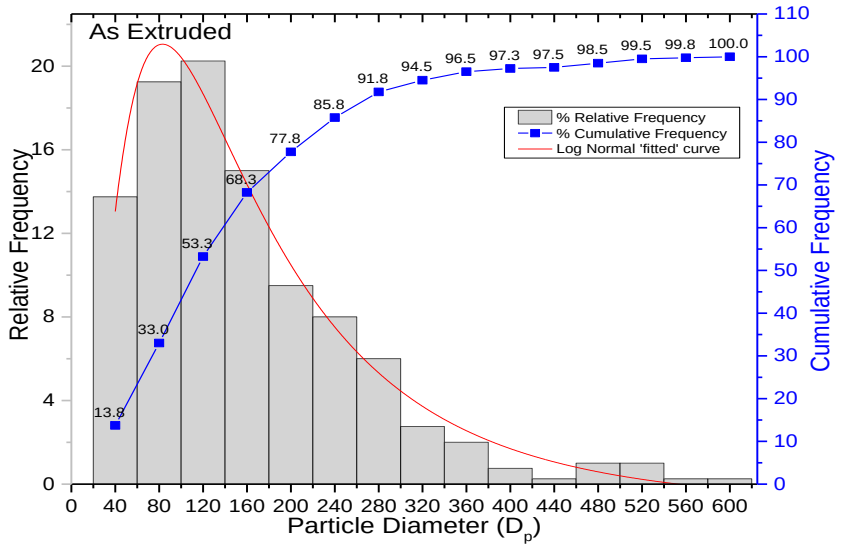

Figure 4.18 Statistical analysis showing percent relative frequency and percent cumulative frequency for quasicrystalline particle size data, binned in 40nm brackets. A log normal distribution curve was fitted.

4.3.6.3 Interparticle distance

The particles are assumed to be spheres of a diameter (D_p) which are randomly distributed and have a volume fraction (f_v). With particle mean planar diameter ($D_{p,s}$) known[D], the mean random edge to edge interparticle planar distance (λ_s) can be calculated theoretically using Eqn. 4.3 (Dieter and Bacon, 1986).

$$\lambda_s = \frac{2D_{p,s}}{3f_v}(1-f_v) \qquad \textbf{Eqn. 4.3}$$

Mean edge to edge interparticle distance was calculated to be 105nm using Eqn. 4.3. Table 4.5 provides a summary of the measured average particle diameter, particle volume fractions, and inter-particle distance.

Table 4.5 Particle diameter, volume fraction and interparticle edge to edge distances

Particle diameter (D_p in nm)			Average Planar Diameter ($D_{p,s}$ in nm)	Volume Fraction (f)	Mean Random Interparticle Planar Spacing (λ_s in nm)
Min	Max	Mean			
10	598	151±11	123±9	0.44±0.03	105±8

It was assumed that all the particles are spherical having a random distribution (but no clustering), and randomly oriented. Despite some limitations, the analysis provides the basis for the theoretical estimations of the strengthening contribution provided by the I-phase particles in section 8.2.3.

[D] $D_{p,s} = D_p \sqrt{(2/3)}$ (section 2.3.3)

4.4 Summary

The 25-50μm size NQX powder alloy characterisation showed that the metastable nano size I-phase particles were the major intermetallic present in the α-Al matrix. A small quantity of other intermetallic θ_D-$Al_{13}(Fe, Cr)_{2-4}$ and Al_3Ti was also present in the atomised powder alloy. The total specific work (or pressure) required for extrusion was calculated (1015 to 1220MPa) and found to be similar to the extrusion pressures observed during the extrusion (1105±65MPa). The differences in extrusion pressures observed within the bars were most likely due to the differences in lubrication. The microstructure of all the extruded bars was similar with the exception of bar 1. The high extrusion speed and the resultant increase in the adiabatic temperature transformed the I-phase in bar 1.The powder particles were plastically deformed during extrusion and they appear well bonded and do not contain porosity. The difference in the microstructure of the extruded atomised powder particles gives rise to banding in the longitudinal direction. The energy input during extrusion process lowers the DSC peak position of the extruded alloy by ~30-35°C in comparison to the powder alloy.

The extruded NQX alloy also contained the I-phase as the only major intermetallic present in the aluminium matrix. The volume fraction of the I-phase particles was measured to be 44%. A log normal distribution was found appropriate to describe the particle size distribution, and a mean particle diameter of 151±11nm was obtained.

Most of the grains in the alloy are found to have ultrafine size (<1μm) and the average equivalent grain diameter is ~473nm in longitudinal direction and ~432nm in cross section. The extruded bars have a strong <111> texture and Taylor's factor was calculated to be ~3.3.

References

Abbaschian, R. and Reed-Hill, R. (2008) *Physical metallurgy principles*. Cengage Learning.

Audebert, F., Prima, F., Galano, M., Tomut, M., Warren, P. J., Stone, I. C. and Cantor, B. (2002) 'Structural characterisation and mechanical properties of nanocomposite Al-based alloys', *Materials transactions*, 43(8), pp. 2017-2025.

Cahn, J. W., Shechtman, D. and Gratias, D. (1986) 'Indexing of icosahedral quasiperiodic crystals', *Journal of Materials Research*, 1(01), pp. 13-26.

Dieter, G. E. and Bacon, D. (1986) *Mechanical metallurgy*. McGraw-Hill New York.

Friel, J. J. (2000) *Practical guide to image analysis*. ASM international.

Galano, M., Audebert, F., Cantor, B. and Stone, I. (2004) 'Structural characterisation and stability of new nanoquasicrystalline Al-based alloys', *Materials Science and Engineering: A*, 375, pp. 1206-1211.

Galano, M., Audebert, F., Stone, I. and Cantor, B. (2009) 'Nanoquasicrystalline Al–Fe–Cr-based alloys. Part I: Phase transformations', *Acta Materialia*, 57(17), pp. 5107-5119.

Galano, M., Marsh, A., Audebert, F., Xu, W. and Ramundo, M. (2014) 'Nanoquasicrystalline Al-based matrix/γ-Al 2 O 3 nanocomposites', *Journal of Alloys and Compounds*.

Gambin, W. (2013) *Plasticity and textures*. Springer Science & Business Media.

Grant, N. J. (1983) 'Rapid solidification of metallic particulates', *JOM*, 35(1), pp. 20-27.

Hosford, W. F. and Caddell, R. M. (2011) *Metal forming: mechanics and metallurgy*. Cambridge University Press.

ICSD (2016) *http://icsd.cds.rsc.org/*.

Inoue, A. and Kimura, H. (2001) 'Fabrications and mechanical properties of bulk amorphous, nanocrystalline, nanoquasicrystalline alloys in aluminum-based system', *Journal of light metals*, 1(1), pp. 31-41.

Kim, K., Xu, W., Tomut, M., Stoica, M., Calin, M., Yi, S., Lee, W. and Eckert, J. (2007) 'Formation of icosahedral phase in an Al 93 Fe 3 Cr 2 Ti 2 bulk alloy', *Journal of alloys and compounds*, 436(1), pp. L1-L4.

Manaila, R., Florescu, V., Jianu, A. and Radulescu, O. (1989) 'On the transition-metal quasisublattice in icosahedral Al-Cr-Fe phases', *Philosophical Magazine B*, 60(5), pp. 589-599.

Martin, J., Le Mogne, T., Chassagnette, C. and Gardos, M. N. (1992) 'Friction of hexagonal boron nitride in various environments', *Tribology transactions*, 35(3), pp. 462-472.

Mondolfo, L. F. (1976) *Aluminum alloys: structure and properties'; 1976. London-Boston: Butter Worths & Co Ltd*.

Morrell, R., Mildeova, P., Chapman, L., P N Quested and Gisby, J. (2015) *Thermal Expansion, Specific Heat, Thermal Diffusivity and Thermal Conductivity Estimation of an Aluminium Alloy*, Teddington, UK: National Physical Laboratory2015090077/1).

Otooni, M. A. (2013) *Elements of rapid solidification: fundamentals and applications*. Springer Science & Business Media.

Pedrazzini, S. (2014) *Characterisation and Mechanical Properties of Bulk Nanostructured Al-based Composites for High Temperature Applications.* DPhil Thesis, University of Oxford.

Rollett, A. D. (2008) *Applications of Texture Analysis: Ceramic Transactions.* John Wiley & Sons.

Rounthwaite, N. J. (2012) *Development of Bulk Nanoquasicrystalline Alloys for High Strength Elevated Temperature Applications.* DPhil Thesis, University of Oxford.

Sahoo, K. and Stone, I. (2005) 'Effect of Si on the formation and stability of the icosahedral quasicrystalline phase in Al–Fe–Cr–Ti alloys', *Philosophical magazine letters,* 85(5), pp. 231-245.

Todd, I., Chlup, Z., O'Dwyer, J., Lieblich, M. and García-Escorial, A. (2004) 'The influence of processing variables on the structure and mechanical properties of nano-quasicrystalline reinforced aluminium alloys', *Materials Science and Engineering: A,* 375, pp. 1235-1238.

5. Thermal Stability of the Extruded NQX Alloy Bars

This chapter deals with the study of phase transformation of the bulk extruded NQX alloy. The activation energy of the alloy was calculated through non-isothermal transformation kinetics using the Kissinger method by performing varying heating rate DSC experiments. The alloy samples were also isothermally annealed for 100hrs at five elevated temperatures. The changes in the microstructure were studied using XRD, DSC, SEM, TEM, STEM, and EBSD.

5.1 Activation Energy of the NQX Alloy Decomposition

The temperature dependent decomposition/reaction in a material can be assumed to follow an Arrhenius type relation provided in Eqn. 5.1 (Kissinger, 1957).

$$\frac{dx}{dt} = A_k(1-x)^n e^{-\frac{E_a}{RT}} \qquad \textbf{Eqn. 5.1}$$

Where x is the fraction decomposed or reacted, dx/dt is the rate of reaction, A_k is a pre-factor, n is the order of reaction, E_a is the activation energy, T is the absolute temperature, and R is the gas constant.

The rate of reaction is at a maximum when its first derivative is zero, and at that instant, the equation can be written as the following (Kissinger, 1956, Kissinger, 1957).

$$\ln\left(\frac{\beta}{T_p^2}\right) = \ln\left[A_k\left(\frac{R}{E_a}\right)\right] - \left[\left(\frac{E_a}{R}\right)\frac{1}{T_p}\right] \qquad \textbf{Eqn. 5.2}$$

Where β is the heating rate or dT/dt, T from Eqn. 5.1 becomes T_{max} or $T_{p,}$ which is the temperature corresponding to the maximum rate of reaction or the peak temperature.

The activation energy is an important kinetic parameter in the alloy phase transformations. Kissinger's method (Eqn. 5.2) provides a single value of the activation energy for the complete reaction and it has been extensively used in literature. During the non-isothermal reactions, the change of heating rate results in a change in the peak position in the DSC curves. Each peak position and the corresponding heating rate is noted, the semi log-log plot between β/T_p^2 vs $1/T_p$ yields a straight line having a slope of $-E_a/R$, which provides the value of activation energy for the transformation[A].The 'as extruded' NQX alloy samples were heated at four different rates (80, 40, 20 and 10^{o}C/min) and corresponding peak positions were identified. The peak positions were observed to shift towards lower temperatures as the heating rate decreases, as seen in Figure 5.1. The graph between β/T_p^2 vs $1/T_p$ is shown in Figure 5.2 and an activation energy value of the transformation of the I-phase was found to be 250±4kJ/mol. In comparison, the activation energy for diffusion of Fe in Al has been reported in the range of 183-259kJ/mol, for Cr diffusion in Al it is ~243-282kJ/mol, and for Ti in Al, it is ~260kJ/mol (Du et al., 2003). Thus, the diffusion of any one element, a combination of any two or all three elements (Fe, Cr, Ti) in Al can be involved in the phase transformation of the I-phase, requiring a further study of the phase transformations of the alloy.

Another method of finding the activation energy was postulated by Ozawa (1970) which assumes that the extent of reaction is independent of the heating rate. The method was also used (not shown here) to validate the result by Kissinger's methods and it also provided the same value of the activation energy as 250±4kJ/mol.

[A] Equation 5.2 is for the 1st order reactions, similar relations also hold for higher order reactions.

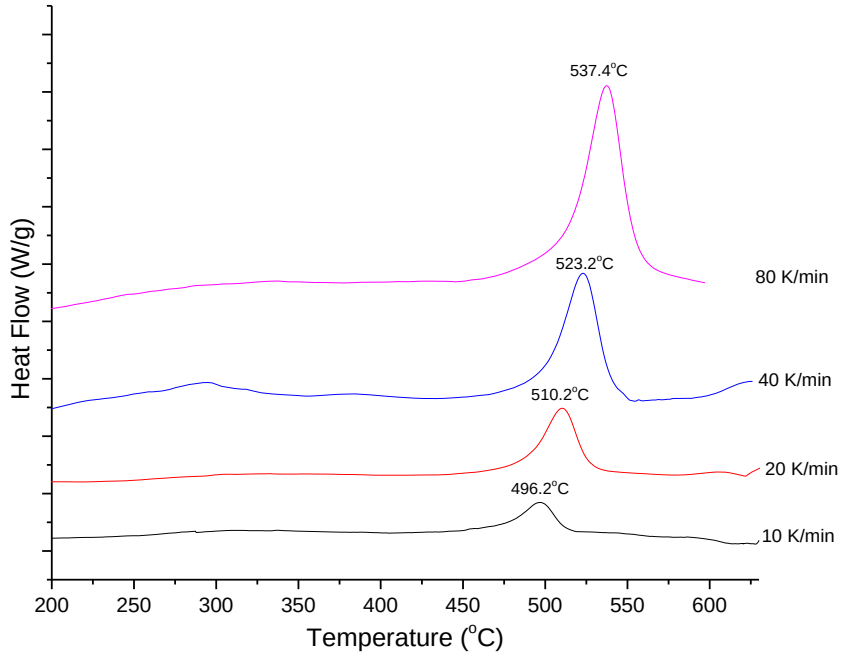

Figure 5.1 DSC runs of 'as extruded' NQX alloy carried out at four heating rates.

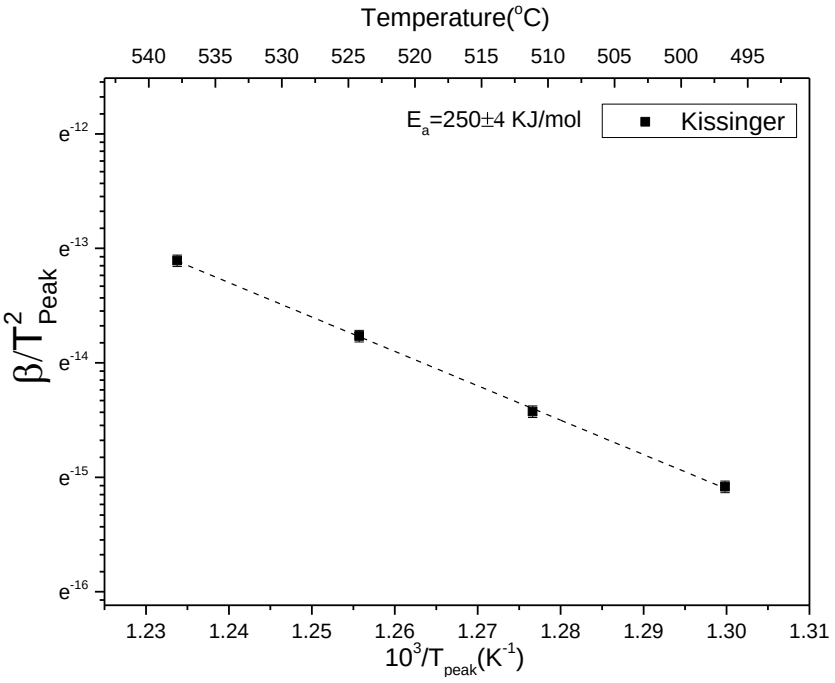

Figure 5.2 Kissinger plot for the NQX alloy. The slope of the fitted dashed lines times the gas constant provides the activation energy of the transformation.

5.2 Characterisation of the Extruded NQX Alloy after Annealing

This section covers the study of microstructural changes as a result of the annealing heat treatments. The mechanical properties of the annealed NQX alloy are provided in chapter 6 and a general discussion encompassing both the microstructure and properties is in chapter 8.

Five extruded bar NQX alloy samples were annealed for 100h at 250, 300, 350, 400 and 450°C each[B]. In addition, one sample was annealed at 650°C for one hour to allow a complete transformation of the metastable I-phase for comparison. ~650°C is the precipitation temperature for the stable Al_3Fe phase in the Al-Fe phase diagram (Mondolfo, 1976). The non-equilibrium solidification produces metastable phases, and at high enough annealing temperatures e.g.~>400-500°C, the metastable intermetallics in Al-Fe system transform into a stable Al_3Fe phase (Belov et al., 2002).

5.2.1 SEM

The SEM images of the annealed samples are shown in Figure 5.3 to Figure 5.5. Figure 5.3 (a, b) shows sample 250°C/100h, Figure 5.3 (c, d) contains sample 300°C/100h, and Figure 5.3 (e, f) has the SEM images of sample 350°C/100h. The microstructure in samples 250°C/100h and 300°C/100h was similar to the 'as extruded' samples studied in section 4.3.

Figure 5.3 (e, f) shows the SEM images of the sample 350°C/100h. Most of the particles had size ranges as of above mentioned samples. In addition, large (~>500nm) irregular trapezium shaped particles also appeared at a few places marked by the thick arrows in Figure 5.3 (e, f). Sample 400°C/100h is shown in Figure 5.4 (a, b). It contained particles of similar shapes as observed in the 350°C/100h sample, including a slightly higher

[B] The nomenclature of the samples is mentioned in Table 3.1 which shows both the temperature and the annealing time such as 250°C/100h, 300°C/100h, and 350°C/100h, 400°C/100h, 450°C/100h, and 650°C/1h.

quantity of trapezium shaped particles. However, the sizes of the particles increased and a few particles as large as ~800nm were sometimes observed.

The sample 450^{o}C/100h is shown in Figure 5.5, which contains up to a few microns long, rod-shaped particles marked by orange arrows. The EDX mapping revealed that these elongated particles were mainly an Al/Fe intermetallic. A range of sizes (40nm to 800nm) of round particles was also observed in the sample, whilst trapezium shaped particles were not seen anymore.

It was noted from the contrast that the trapezium shaped particles and the elongated Al/Fe intermetallics in corresponding samples were generally not a 'single' particle but comprised different types of particles sitting on top of each other. It was later confirmed by the STEM analysis (section 5.2.4).

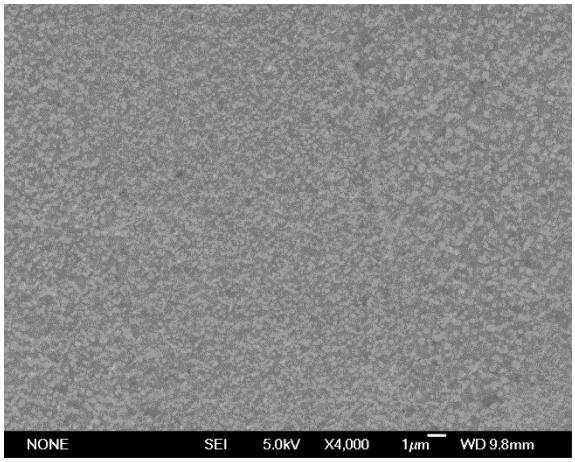

(a) 250°C/100h

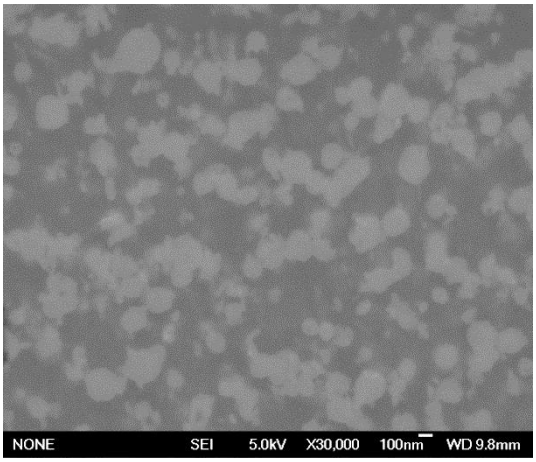

(b) 250°C/100h

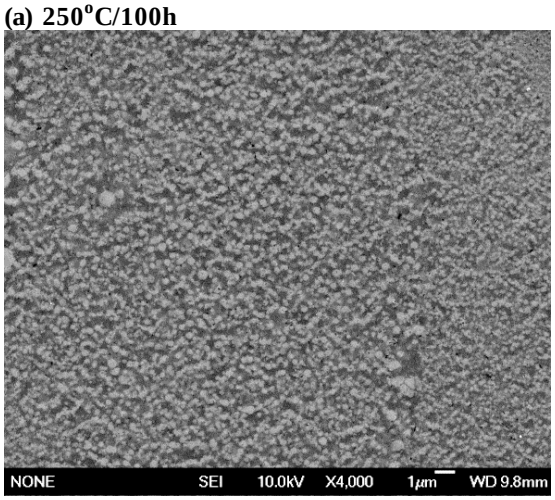

(c) 300°C/100h

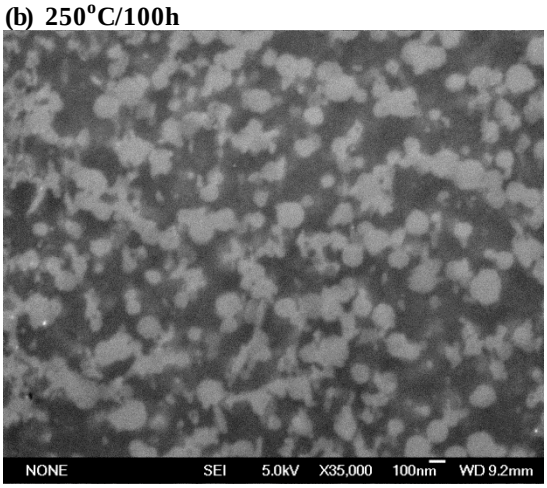

(d) 300°C/100h

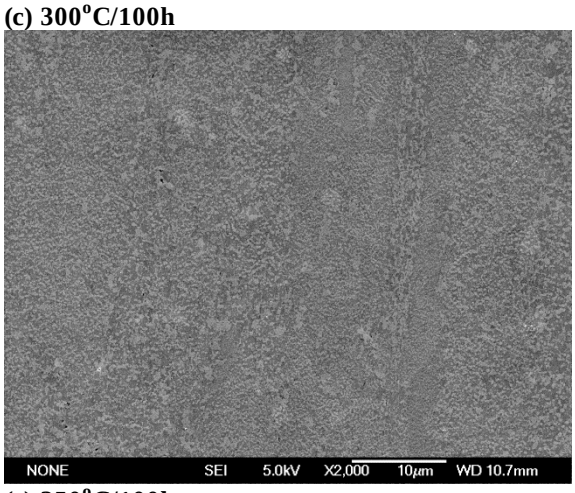

(e) 350°C/100h

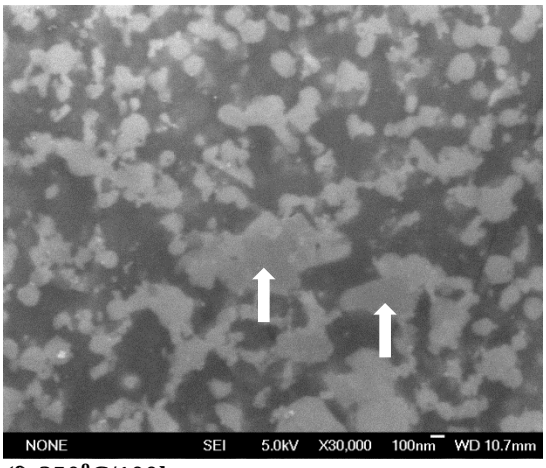

(f) 350°C/100h

Figure 5.3 SEI images for 100h annealed samples: (a) 250°C/100h longitudinal sample, (b) 250°C/100h cross sectional sample, (c, d) 300°C/100h longitudinal samples, (e, f) 350°C/100h longitudinal sample.

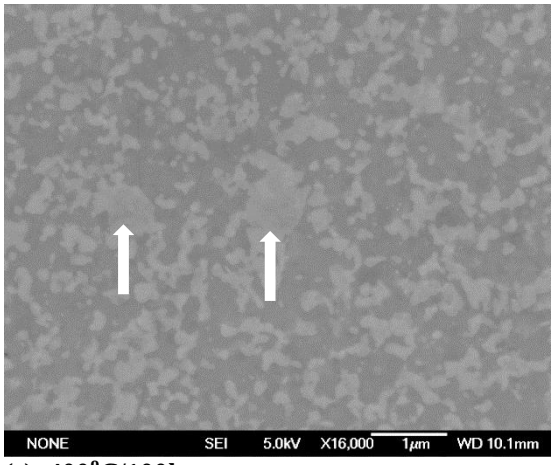

(a) 400°C/100h

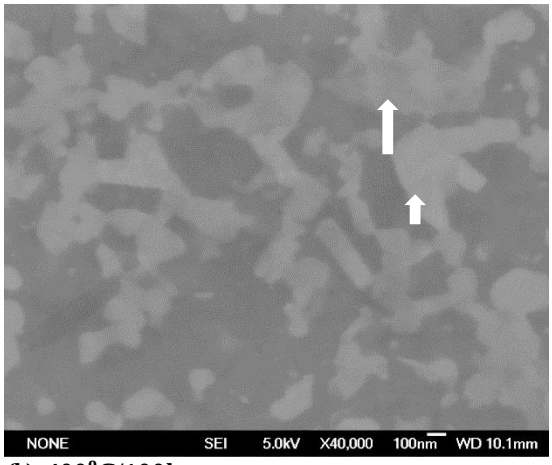

(b) 400°C/100h

Figure 5.4 SEI images for 400°C/100h samples, trapezium shaped particles are marked by white arrows: (a) lower magnification (cross sectional) image, (b) higher magnification image.

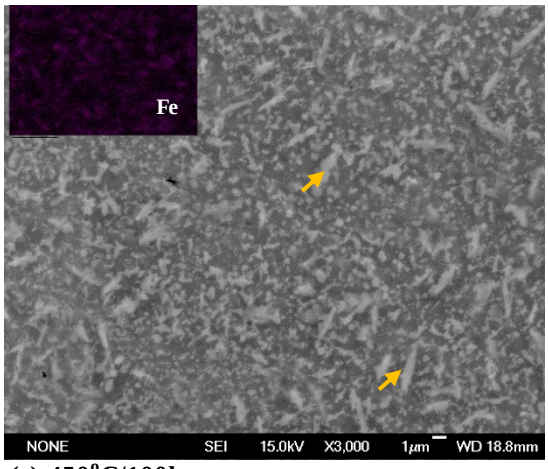

(a) 450°C/100h

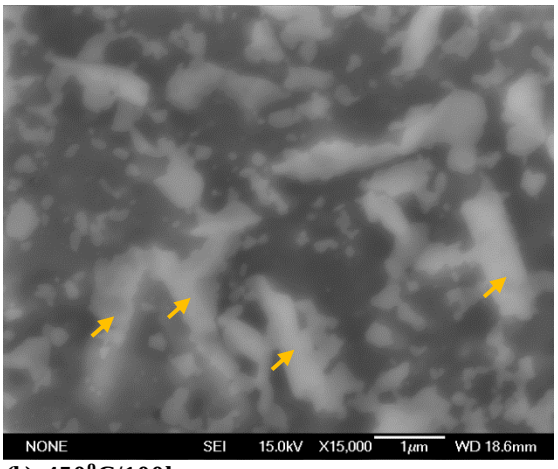

(b) 450°C/100h

Figure 5.5 SEI images for 450°C/100h sample: (a) low magnification image shows rod shaped elongated Al/Fe particles, a few are marked by orange arrows, (b) higher magnification image, the elongated particles show varying contrast due to a particle sitting on top of other.

5.2.2 DSC

DSC of all the annealed samples was carried out and compared with the 'as extruded' samples. It was established in section 4.3.2 that the exothermic peak at ~ 522±4°C in the 'as extruded' sample was due to the transformation of the metastable quasicrystalline phase. The same exothermic peaks were also observed at ~520°C in the samples 250°C/100h and 300°C/100h. In sample 350°C/100h, only a small peak was observed at ~519°C indicating that some of the metastable I-phase had transformed. Samples annealed

at higher temperatures 400°C/100h and 450°C/100h showed no exothermic peaks, which confirmed that the metastable I-phase had already transformed.

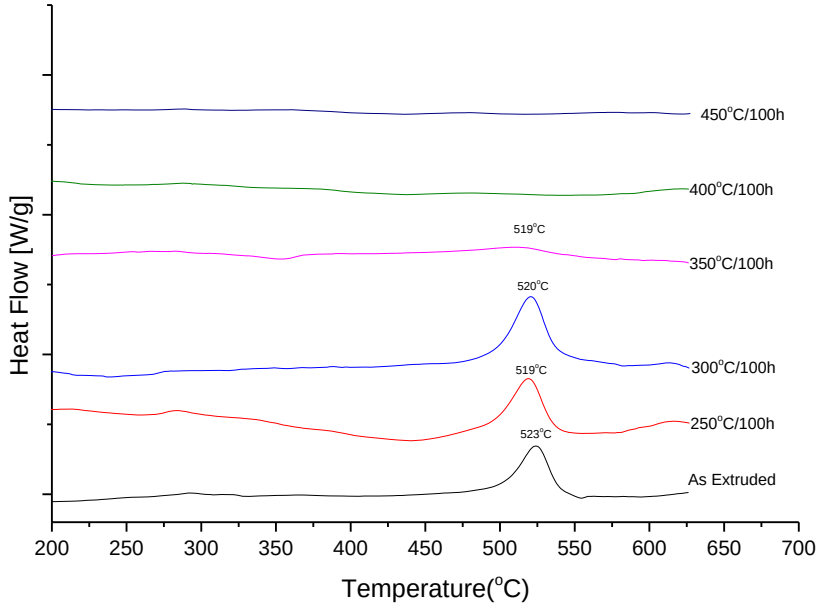

Figure 5.6 DSC comparison for 'as extruded' and 100h annealed samples. The metastable peak in sample 350°C/100h is very small and becomes non-existent in samples 400°C /100h and 450°C/100h.

5.2.3 XRD

XRD was carried out on all the annealed samples, and the patterns are shown in Figure 5.7. For all XRD patterns, aluminium peaks were observed at 38.5°(111), 44.7°(200), 65.1°(220), 78.2°(311), 82.4°(222) and 99.1°(400) 2θ positions; the corresponding planes are mentioned next to the angle. I-phase peaks were observed in samples 250°C/100h, 300°C/100h and 350°C/100h at 2θ positions of 22.7°, 41°, 43.2°, 61.1°, 73.2° which are similar to those indexed by Galano and coworkers (Galano et al., 2004, Galano et al., 2009, Galano et al., 2014) on the melt-spun alloy of a similar composition.

The intermetallic phases and their 2θ peak positions for the 'as extruded' and all the annealed samples are mentioned in Table 5.1. Also, the 2θ position corresponding to 100% intensity is highlighted as bold. Table 5.1 and the Figure 5.7 may be referred to

locate the peaks and their 2θ position for this section. The XRD patterns for samples 250°C/100h and 300°C/100h were similar to the 'as extruded' sample. In these samples, the only prominent intermetallic phase was the I-phase, and very small peaks of stable ω-Al_3Ti and metastable θ_D-$Al_{13}(Fe, Cr)_{2-4}$ were observed.

In sample 350°C/100h, the I-phase was still present but had a smaller volume fraction. Small metastable θ_D-$Al_{13}(Fe, Cr)_{2-4}$ peaks were also observed next to the I-phase peaks. ω-Al_3Ti increases in volume fraction as its 100% intensity peak became noticeable and also few other weak peaks started to appear in this sample. The intermetallic phases peaks including θ_{Cr}-$Al_{13}Cr_2$ and metastable δ-Al_6Fe also started to emerge for the first time in sample 350°C/100h.

In sample 400°C/100h, the I-phase did not exist any longer. ω-Al_3Ti, δ-Al_6Fe and θ_{Cr}-$Al_{13}Cr_2$ phases increase in their volume fraction as their 100% intensity peaks become more prominent. In addition, several new peaks emerged for all of these intermetallics. θ_{Fe}-$Al_{13}Fe_4$ phase appeared for the first time in this sample and its 100% intensity peak position was observed having an offset of -0.2°.

In sample 450°C/100h, the δ-Al_6Fe phase peaks disappeared and instead several new θ_{Fe}-$Al_{13}Fe_4$ phase peaks started to appear; moreover, the 100% intensity peak was observed at its actual 2θ position without any offset. The volume fractions of ω-Al_3Ti and θ_{Cr}-$Al_{13}Cr_2$ phases increased as their peaks which became even more noticeable.

XRD of the sample 650°/1h, which was heated to 650°C in order to ensure the completion of the phase transformation, was found exactly similar to the sample 450°C/100h. This means that the sample 450°C/100h can be considered the one in which the I-phase fully transformed into stable intermetallics. Whereas the sample 400°C/100h is the one in which although the I-phase transformed yet the metastable Al_6Fe was present. Sample 350°C/100h is the one in which a noticeable microstructural transformation started

whereas the samples 300°C/100h and 250°C/100h were similar to the ‘as extruded’ sample.

The texture of the cross section and longitudinal samples in the ‘as extruded’ and the annealed state is shown in Figure 5.8. All the cross section samples were heavily textured in (111), similar to the ‘as extruded’ samples. In all the longitudinal samples, peaks corresponding to (220) planes were found to have high relative intensities in comparison to the reference (textureless) sample. Overall, the texture of the NQX alloy in annealed condition is consistent with the ‘as extruded’ condition; the latter was studied in section 4.3.1 and reproduced in Figure 5.8.

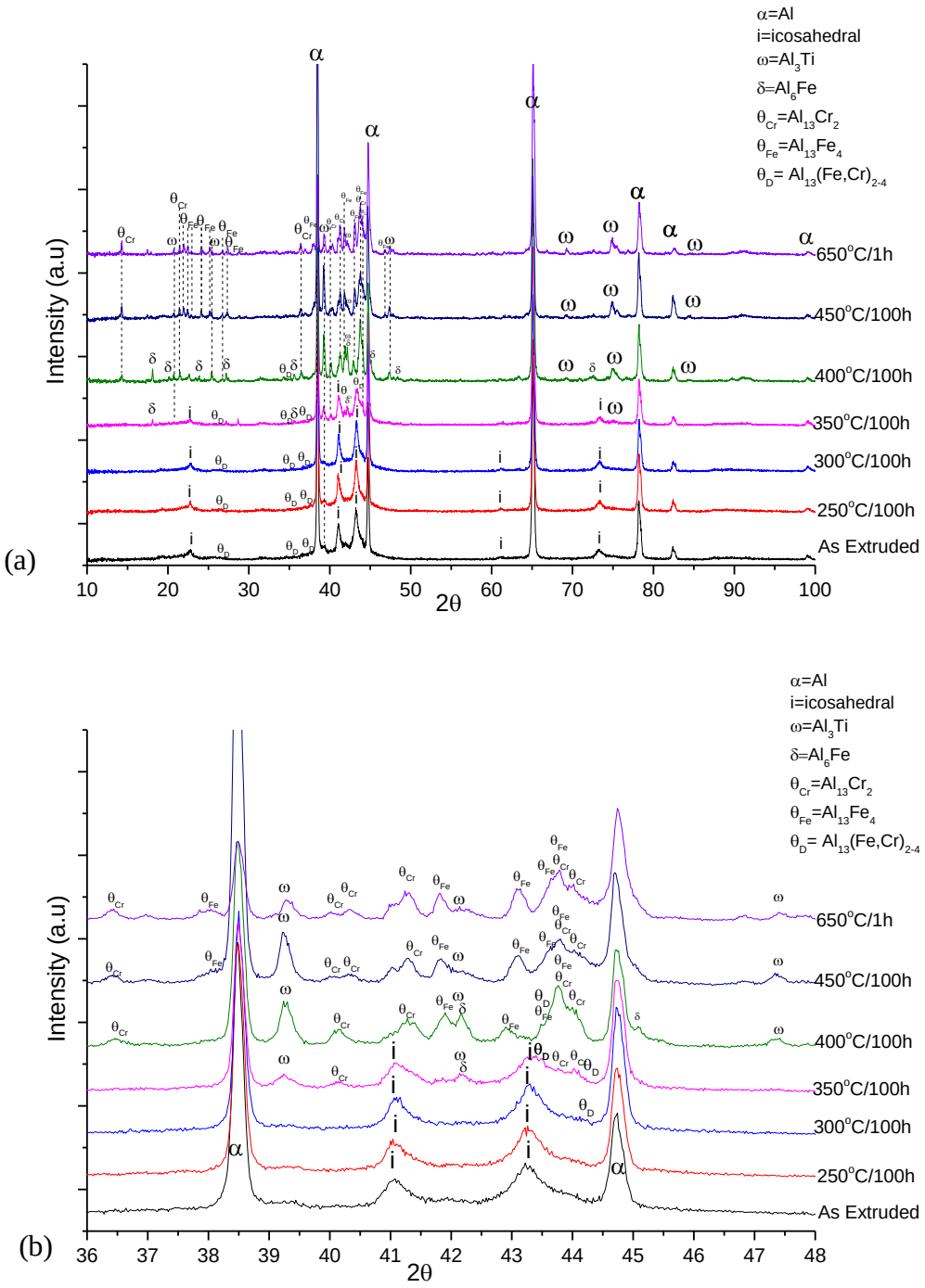

Figure 5.7 XRD comparison for the 'as extruded' and annealed samples. Phase transformation starts in 350°C/100h sample and completes in the 450°C/100h sample[C] (a) overall view (10-100°) (b) magnified view (36-48°).

[C] 650°/100h sample is exact similar to 450°/100h sample.

Table 5.1 Peak positions of various intermetallics in annealed samples.

Sample	2θ position of the present phase						
	I-Phase	**θ_D-$Al_{13}(Fe, Cr)_{2-4}$**	**ω-Al_3Ti**	**θ_{Cr}-$Al_{13}Cr_2$**	**θ_{Fe}-$Al_{13}Fe_4$**	**δ-Al_6Fe**	
As Extruded	22.7°, 41.0°, **43.2°**, 61.1°, 73.2°.	26.3°,34.6°, 36.8°,75.5° (weak)	**39.3°**	Nil	Nil	Nil	
250°C/100h	22.7°, 41.0°, **43.2°**, 61.1°, 73.2°.	26.3°,34.6°, 36.8°,75.5° (weak)	**39.3°**	Nil	Nil	Nil	
300°C/100h	22.7°, 41.0°, **43.2°**, 61.1°, 73.2°.	26.3°,34.6°, 36.8°,75.5° (weak)	**39.3°**	Nil	Nil	Nil	
350°C/100h	22.7°, **41.1°,** 43.2°, 61.1°, 73.2°.	36.8°, 43.4°, 44.2°	**39.3°**, 42.1°, 47.4°,69.2°	40.1°, **43.8°**,	Nil	18.1°, 35.6°, **42.2°** (weak)	← Trans. Start
400°C/100h	Nil	26.3°,34.6°, 43.5°, 44.2°	20.7°,25.4° ,**39.3°**,42.1 °,47.4°,69. 2°,75.0°,84 .4°	14.3°, 21.4°, 36.4°, 40.1°, 41.3°, **43.8°**,	41.8°,**42.9°** ,43.5°,43.8 °,46.9°	18.1°,20.1°, 23.9°,27.2°, 35.6°,**42.2°**, 45.1°,48.5°, 72.0°	
450°C/100h	Nil	-	20.7°,25.4° ,**39.3°**,42.1 °,47.4°,69. 2°,75.0°,84 .4°	14.3°, 21.4°, 36.4°, 40.1°, 41.3°, **43.8°**,	22.0°,22.4° ,22.9°,24.2 °,25.1°,26. 7°,27.438. 0°,41.8°, **43.1°**, 46.9°	Nil	← Trans. Complete
650°C/1h	Nil	-	20.7°,25.4° ,**39.3°**,42.1 °,47.4°,69. 2°,75.0°,84 .4°	14.3°, 21.4°, 36.4°, 40.1°, 41.3°, **43.8°**,	22.0°,22.5° ,22.9°,24.2 °,25.1°,26. 7°,27.438. 0°,41.8°, **43.1°**, 46.9°	Nil	

2θ peak positions corresponding to 100% intensity are in bold, Trans. = transformation

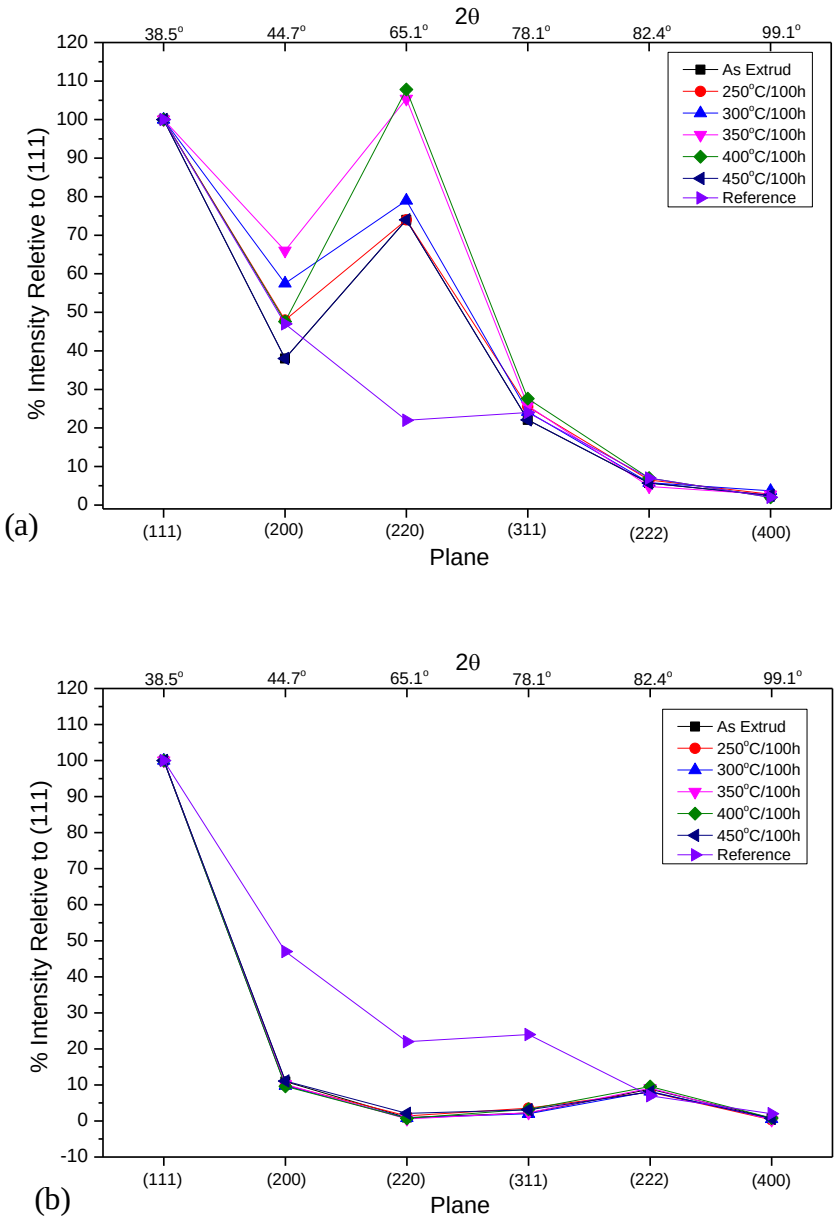

Figure 5.8 Texture of the 'as extruded' and annealed samples: (a) longitudinal samples, (b) cross section samples.

5.2.4 TEM and STEM

The annealed samples were analysed using BF TEM images, EDX analysis, diffraction pattern indexing and STEM/EDX mapping. Samples 250°C/100h, 300°C/100h were similar to the 'as extruded' NQX alloy samples. A noticeable phase transformation started in sample 350°C/100h; however, particle sizes were not much different than the previously mentioned samples. Microstructure significantly changed for samples 400°C/100h, 450°C/100h, 650°C/1h whereas samples 450°C/100h and 650°C/1h are similar. The I-phase transformation is completed in samples 450°C/100h and 650°C/1h and these contained Al_3Ti, $Al_{13}Cr_2$ and $Al_{13}Fe_4$ intermetallics. Detail of the each of the annealed samples is provided in the following sections.

5.2.4.1 100 hours annealing at 250°C

Figure 5.9 shows BF TEM images of sample 250°C/100h. Figure 5.9 (a) shows a general overview, and the microstructure was observed to be similar to the 'as extruded' samples studied in section 4.3. Near-spherical I-phase particles were seen embedded in Al matrix and a fivefold diffraction pattern from an I-phase particle is shown Figure 5.9 (c). Figure 5.9 (b, c) show two Al grains 'M1' (650nm) and 'M2' (720nm). Figure 5.9 (c) shows the diffraction pattern from Al grain 'M2' in $[\bar{1}21]$ zone axis. Very small (~20-30nm) size particles were also sometimes observed inside the grains.

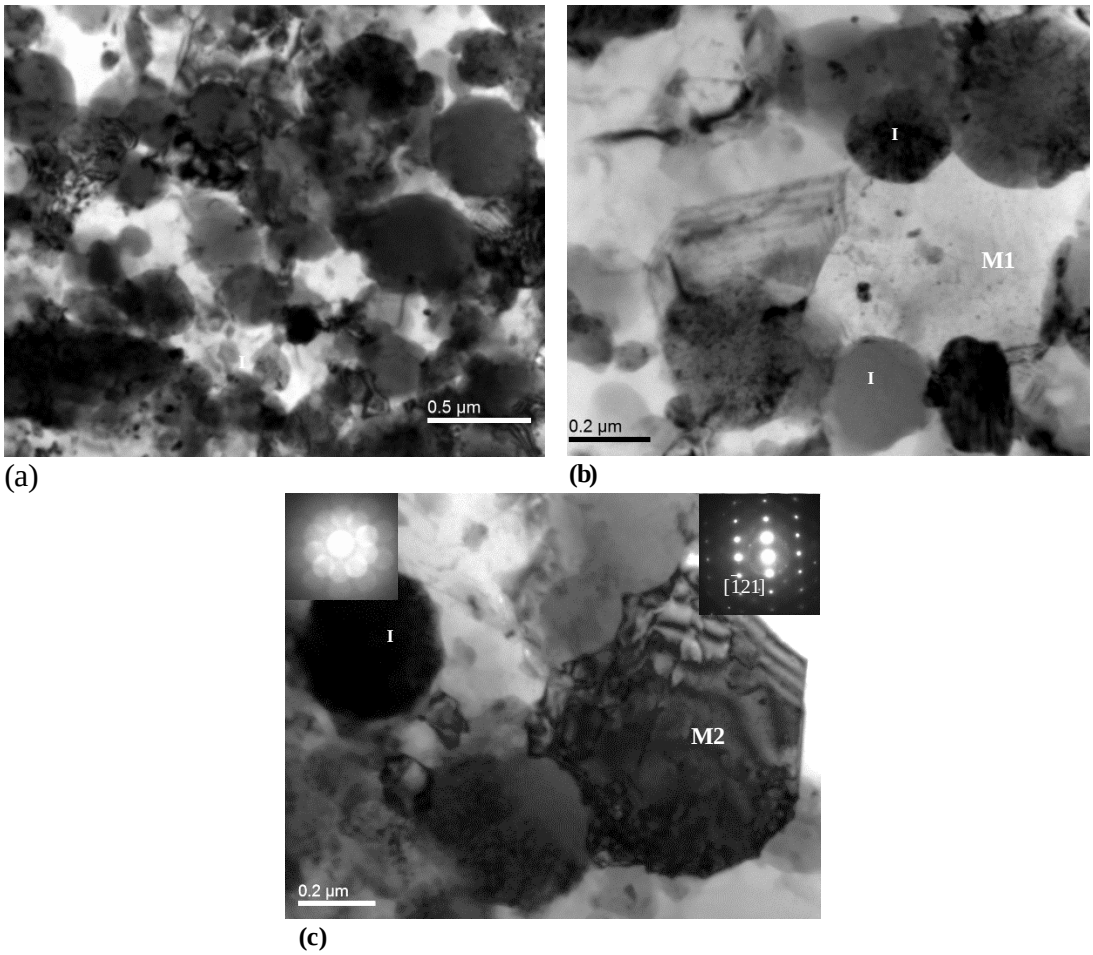

Figure 5.9 BF TEM images of sample 250°C/100h. (a) overall view, (c, b) few I-phase particles are marked as 'I' and Al grains are marked as M1 and M2. A fivefold diffraction pattern from an I-phase particle is shown in figure (c). The diffraction pattern of Al grain M1 in $[\bar{1}21]$ is also shown.

5.2.4.2 100 hours annealing at 300°C

BF TEM images of sample 300°C/100h is shown in Figure 5.10, whereas STEM images are shown in Figure 5.11. Figure 5.10 (a) shows the overall view. In general, the microstructure was similar to the 'as extruded' and 250°C/100h samples. Spherical I-phase particles were observed and the average composition of the I-phase is shown in the inset table provided in Figure 5.10 (c). No noticeable change in the I-phase particles shape, size range and the chemical composition , or in the Al grain size was observed in comparison with the 'as extruded' samples (discussed in section 4.3). However, at a few places very small dark regions of possible newly forming particles were observed sitting next to I-phase particles, as seen in Figure 5.10 (b). BF TEM image in Figure 5.10 (b) was analysed using STEM and EDX mapping and shown in Figure 5.11. The small regions next to the I-phase show a higher concentration of Al/Fe or Al/Ti in the STEM EDX/mapping. Once such region of higher Al/Fe concentration 'A' and another Al/Ti higher concentration region 'B' have been marked in Figure 5.10 and Figure 5.11 and their chemical compositions have also been provided. These regions were likely very small Al_6Fe and Al_3Ti particles as (later) confirmed in the characterisation of the samples annealed at higher temperatures. However, the volume fraction of such particles was very low and the majority of the microstructure included the I-phase particles.

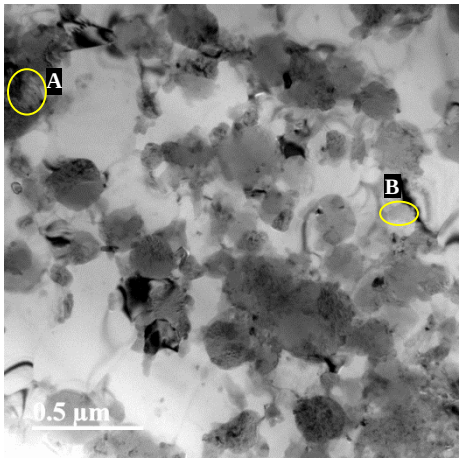

(a)

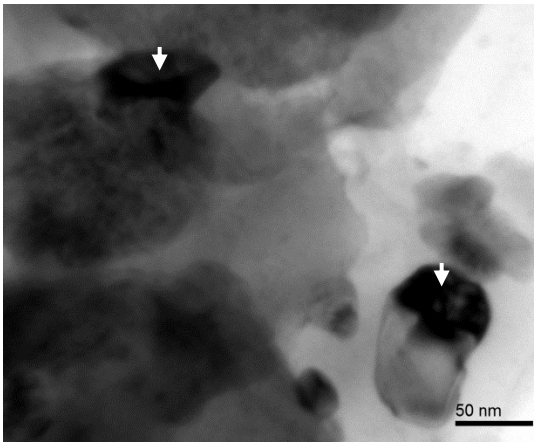

(b)

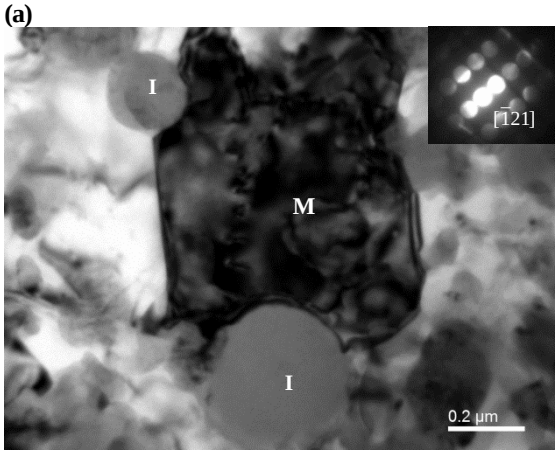

(c)

	I-phase (at%)
Al	85.9±0.3
Fe	5.3±0.4
Cr	5.3.0±0.2
Ti	3.4.0±0.1

(d)

Figure 5.10 BF TEM images for sample 300°C/100h: (a) overall view showing the distributed I-phase particles in Al matrix. The EDX/mapping was carried out on the same image and provided in Figure 5.11, (b) small dark regions of newly forming particles next to the I-phase particles, highlighted by arrows, (c) a 740nm size Al grain 'M' and I-phase particles is surrounded by I-phase particles, (d) composition of I-phase particles.

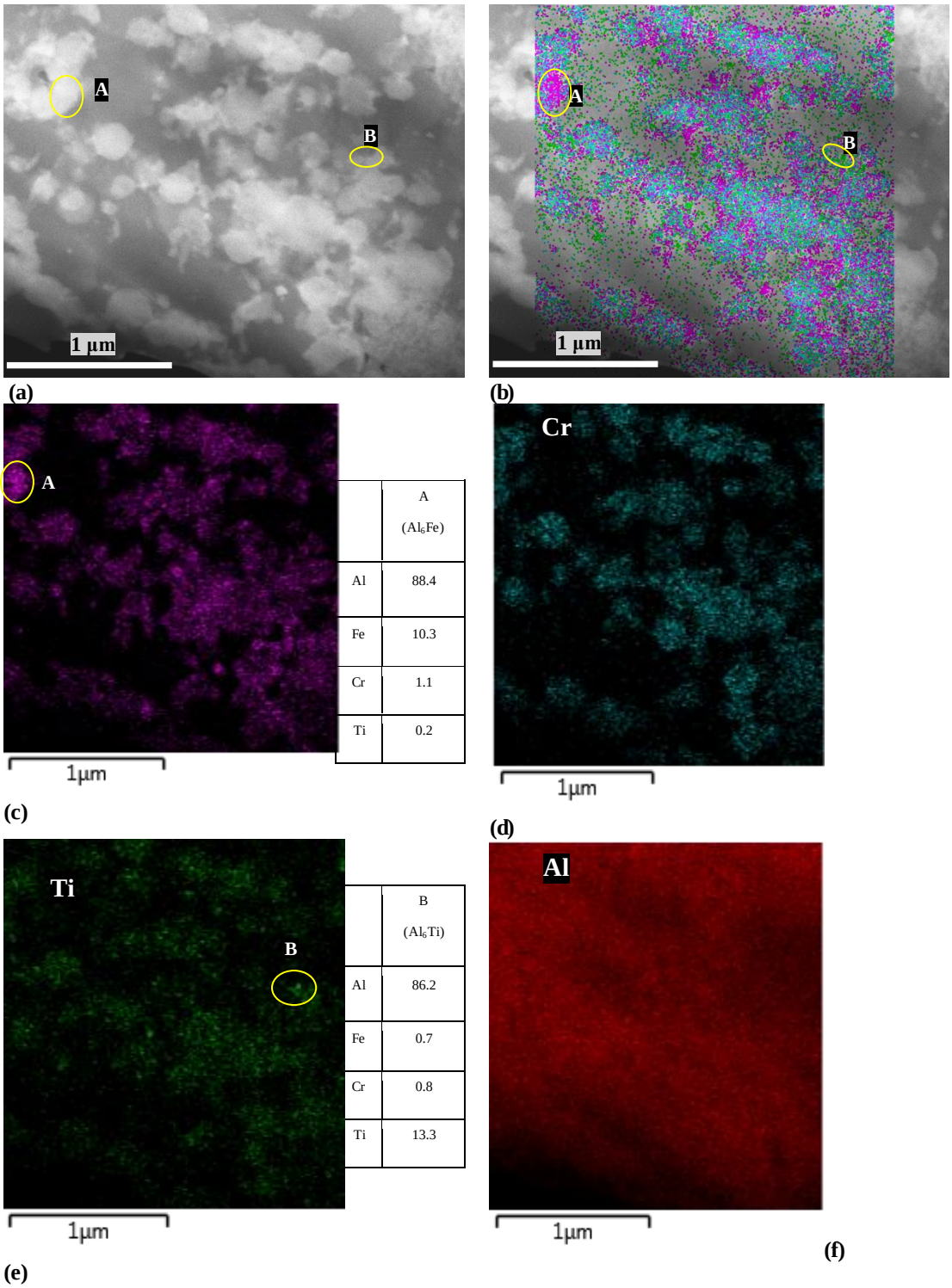

Figure 5.11 STEM images and EDX mapping for Al, Fe, Cr and Ti elements in sample 300°C/100h from the same image in Figure 5.10 (a). Small Al/Fe particle 'A' was likely Al_6Fe, another small Al/Ti 'B' particle was likely Al_3Ti particle.

5.2.4.3 100 hours annealing at 350°C

BF TEM images of sample 350°C/100h sample is shown in Figure 5.12, whereas STEM images are shown in Figure 5.13. Figure 5.12 (a) shows an overall view of the microstructure as seen in the BF TEM images. A noticeable phase transformation has started in the sample. Fewer I-phase particles found in this sample, and one such ~350nm diameter I-phase particle 'I' and the corresponding five-fold diffraction pattern is shown in Figure 5.12 (a). The particle shapes and chemical compositions were observed to be different from those observed in samples 300°C/100h, 250°C/100h or the 'as extruded' samples. However, the particle and the grain sizes were similar. A large trapezium-shaped particle 'A' and its indexed diffraction pattern is shown in Figure 5.12 (a, b), whereas its STEM EDX mapping can be seen in Figure 5.13. The particle was identified to be likely Al_6Fe using the diffraction pattern indexing, EDX and XRD results. EDX mapping also revealed that most of the intermediate sized, round aluminium intermetallic particles contained both Cr and Fe, whereas likely Al_3Ti particles sat next to these particles. Figure 5.12(d) shows a~760nm size Al grain in a [001] zone axis.

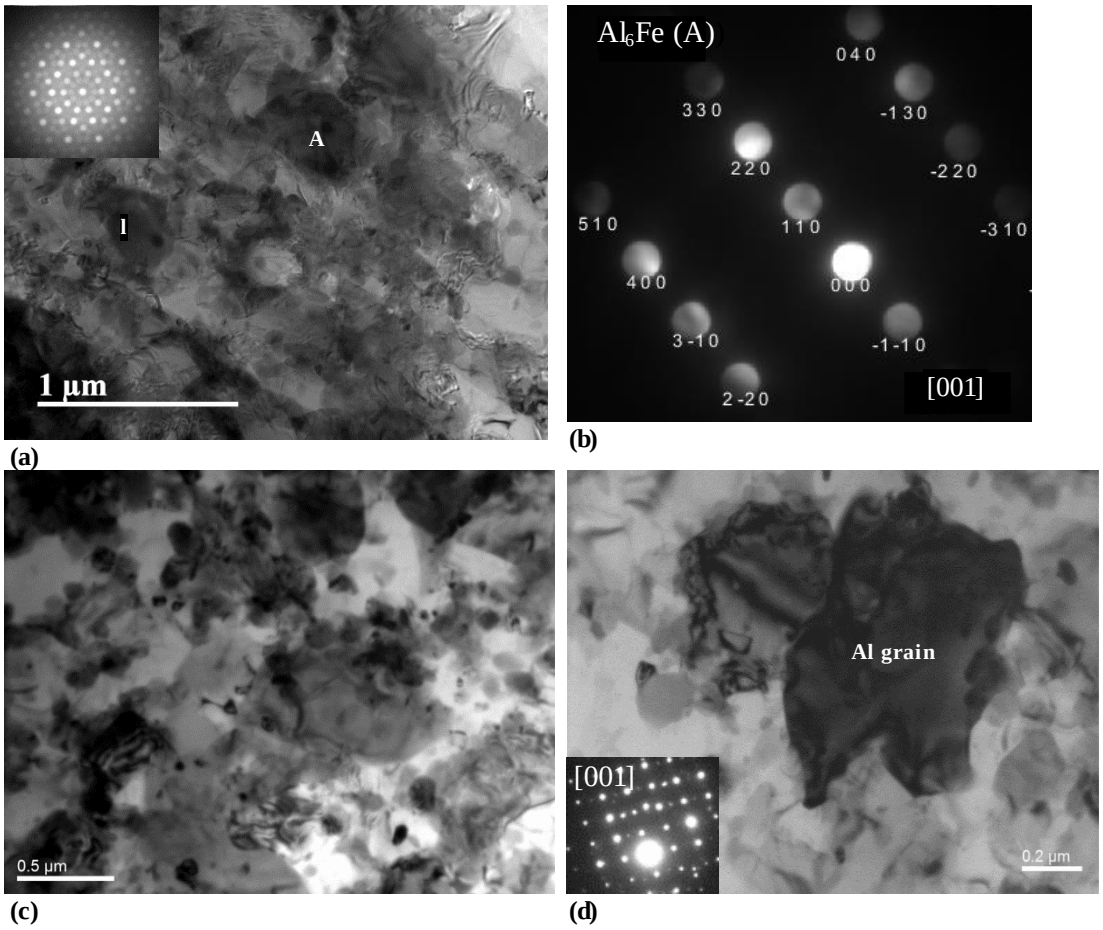

Figure 5.12 BF TEM images for sample 350°C/100h: (a) a trapezium shaped likely Al_6Fe particles marked with arrow, an I-phase particle (marked as 'I') and its five-fold DP, (b) indexed DP for Al_6Fe particle 'A', (c) an overview of microstructure showing low contrast trapezium particles and range of round particles, (d) a ~760nm Al grain in [001] zone axis.

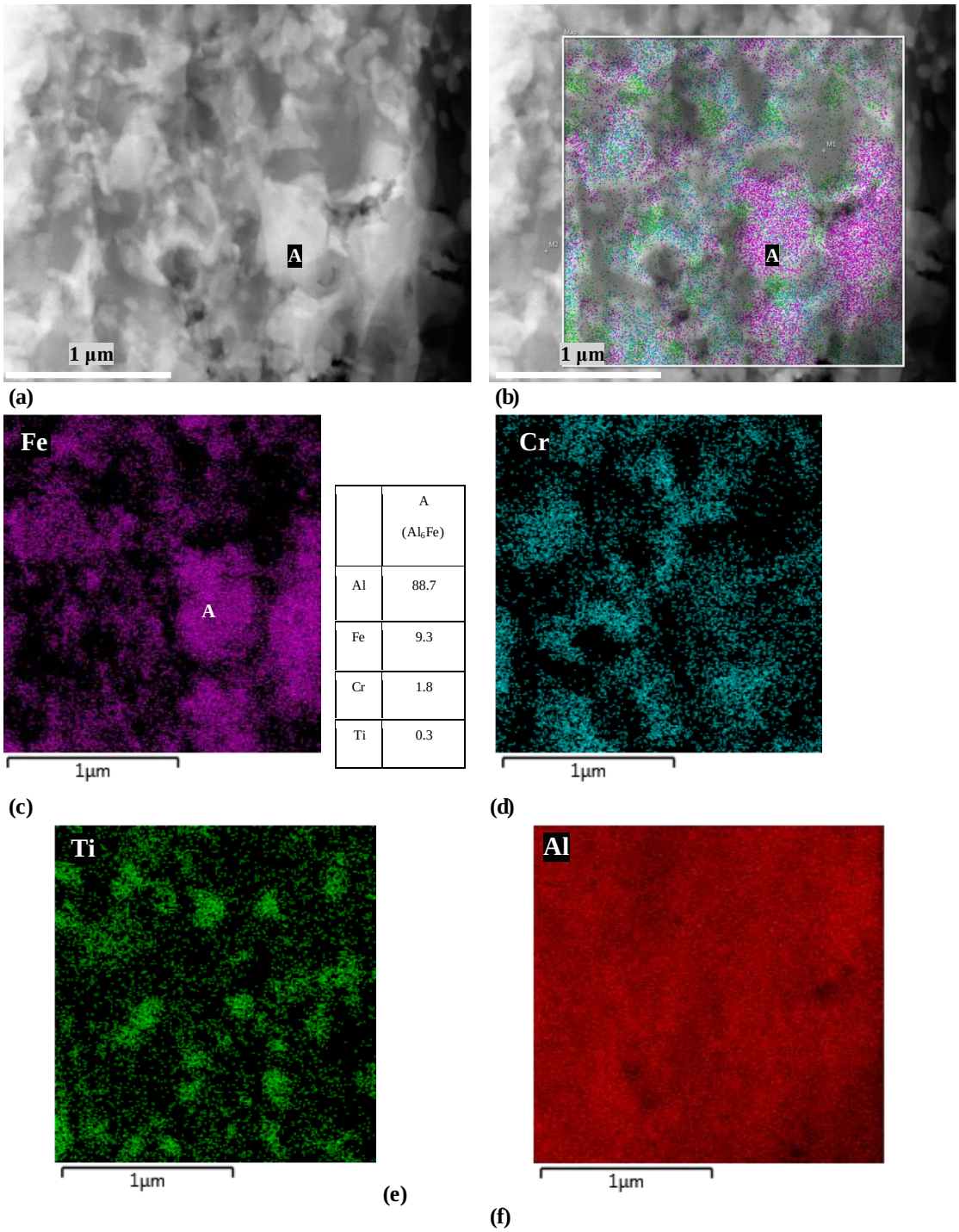

	A (Al_6Fe)
Al	88.7
Fe	9.3
Cr	1.8
Ti	0.3

Figure 5.13 STEM images and EDX mapping for Al, Fe, Cr and Ti elements in sample 350°C/100h, from same image in Figure 5.12 (a) large trapezium shaped particle was identified to be most likely Al_6Fe. All Al/Cr particles contain some Fe. Likely Al_3Ti particles are relatively small and spherical and sit next to the Al (Cr, Fe) particles.

5.2.4.4 100 hours annealing at 400°C

BF TEM results for the sample 400°C/100h are shown in Figure 5.14 whereas the STEM results are shown in Figure 5.15. A general overview is shown in Figure 5.14 (a) and Figure 5.15 (a). In Figure 5.14 (a, b) and Figure 5.15 (a-c, e) a large trapezium shaped particle 'A' was identified as likely Al_6Fe whereas a small <200nm, round particle 'B' was identified as likely Al_3Ti, using diffractions pattern indexing, EDX and XRD results. Three round Al/Fe intermetallic particles 'C', 'D', and 'E' containing Cr are shown in Figure 5.14 (d), and the compositions are shown in Figure 5.14 (e).

The particles found in the sample were possibly :(i) round, <~400nm which are Al intermetallics containing both Fe and Cr, (ii) round, <~250nm likely Al_3Ti particles and (iii) a few ~>500nm trapezium shaped likely Al_6Fe particles.

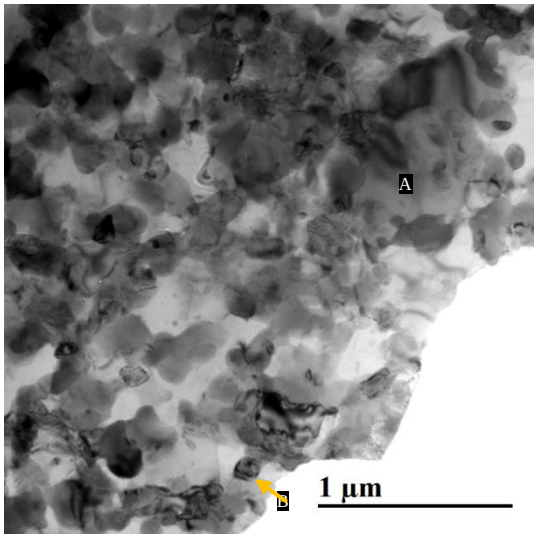

(a)

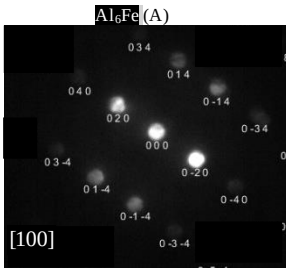

	A(Al_6Fe)
Al	88.2±0.1
Fe	10.9±0.4
Cr	1.0±0.3
Ti	-

(b)

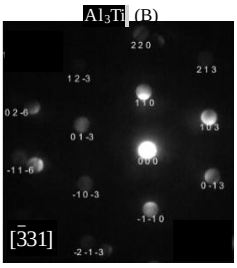

	B(Al_3Ti)
Al	82.5±0.2
Fe	0.3±0.1
Cr	0.9±0.2
Ti	16.3±0.3

(c)

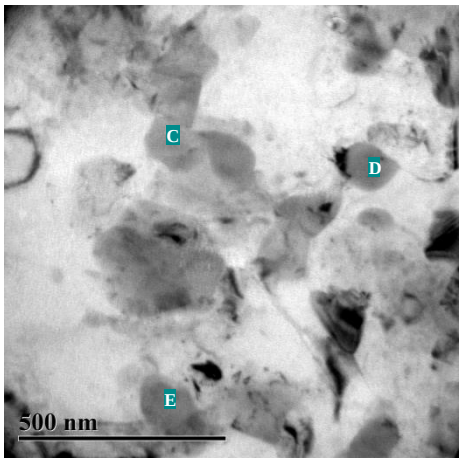

(d)

	C	D	E
Al	88.0	86.6	86.3
Fe	7.2	7.7	8.4
Cr	3.8	4.7	4.1
Ti	1.0	1.1	1.2

(e)

Figure 5.14 BF TEM images for the sample 400°C/100h: (a) overall view shows a trapezium shaped likely Al_6Fe particle 'A' and a round likely Al_3Ti particle 'B', (b, c) chemical compositions and the indexed DP of particles 'A' and 'B', (d, e) intermediate size round particles 'C', 'D', and 'E'; the table contains their chemical compositions.

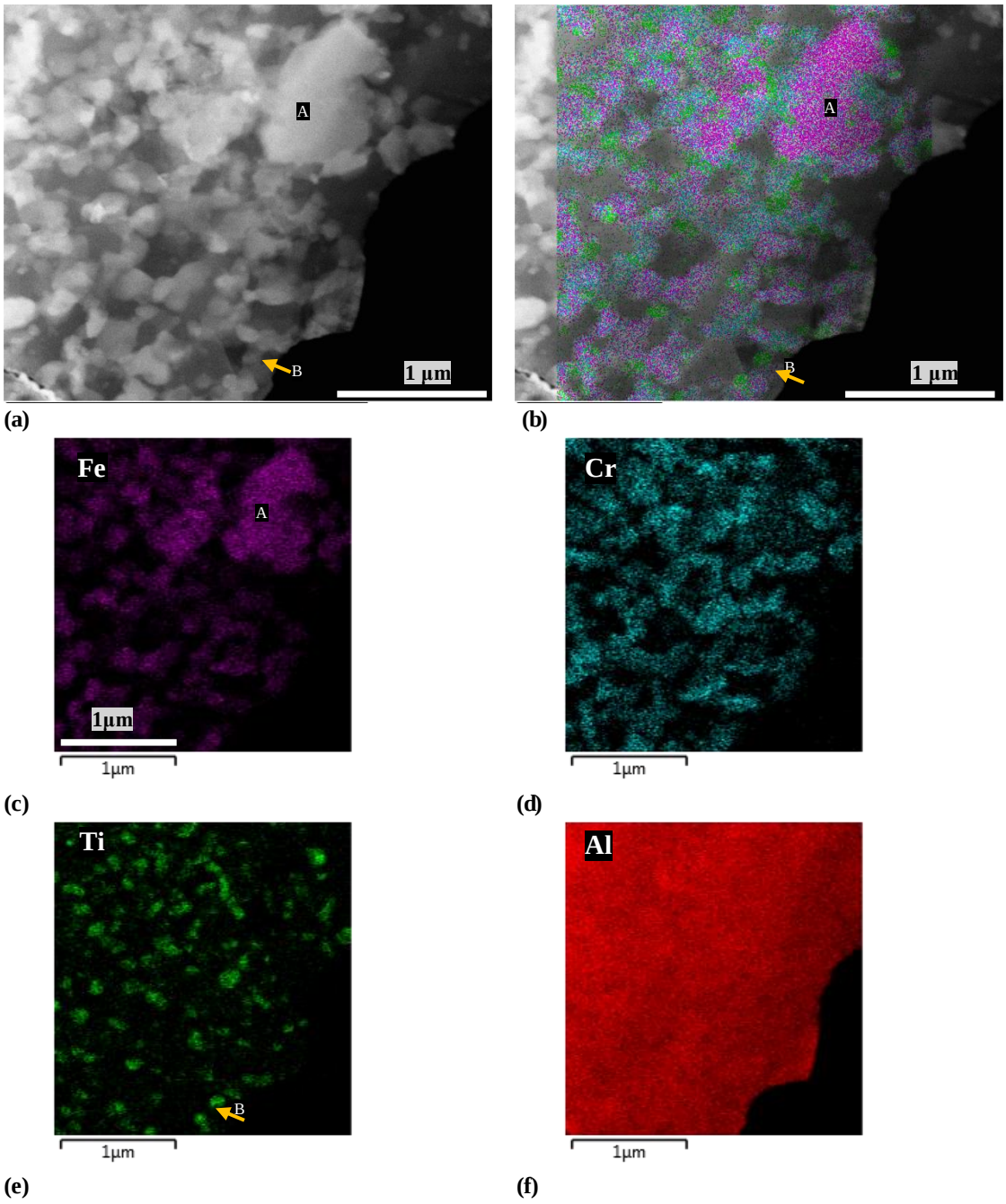

Figure 5.15 STEM images and EDX mapping for Al, Fe, Cr and Ti elements in sample 400°C/100h. The STEM image is taken from the same region as shown in the TEM bright field image in Figure 5.14(a). Trapezium shaped particle A(A_6Fe) and round particle B(Al_3Ti) are shown.

5.2.4.5 100 hours annealing at 450°C and 1hour annealing at 650°C

BF TEM results for the sample 450°C/100h are shown in Figure 5.16 whereas the STEM results are shown in Figure 5.17. Low magnification BF TEM images in Figure 5.16 (a, c) show (up to) a few micron long Al/Fe phase. The observations matched with the SEM analysis (section 5.2.1, Figure 5.5) of a similarly annealed sample. Figure 5.16 (c, d) shows an elongated particle 'C', its indexed DP and the chemical composition. Figure 5.17 (b) and (c) show the STEM image and the EDX map of another elongated particle 'A'. The elongated Al/Fe particles were identified to be $Al_{13}Fe_4$ phase containing very small Cr.

The particles found in the sample were mainly (i) 200nm-800nm size, round, Al/Cr intermetallics (containing some Fe), (ii) round, <~300nm Al_3Ti particles, and (iii) ~>1μm longer rod shaped $Al_{13}Fe_4$ particles.

STEM and EDX mapping for sample 650°C/1h is shown in Figure 5.18. The chemical composition and shapes of the particles in sample 650°C/1h were similar to as observed in sample 450°C/100h. However, the size of the particles is larger. An elongated likely $Al_{13}Fe_4$ particle 'A' is shown in Figure 5.18 (a, c). Also, another particle 'B' in Figure 5.18 (a, d) was supposedly the $Al_{13}Cr_2$ phase (containing some Fe) identified using its DP indexing from Figure 5.18 (d), EDX and the XRD results.

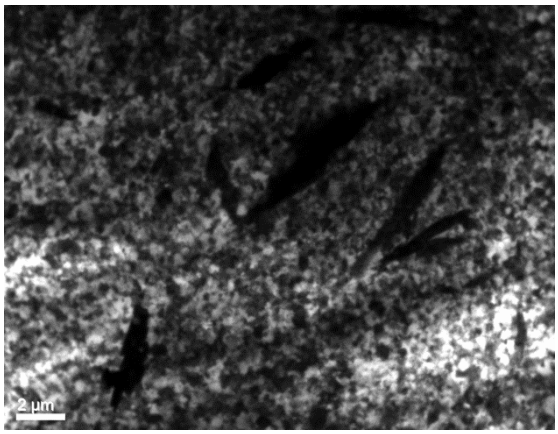

(a)

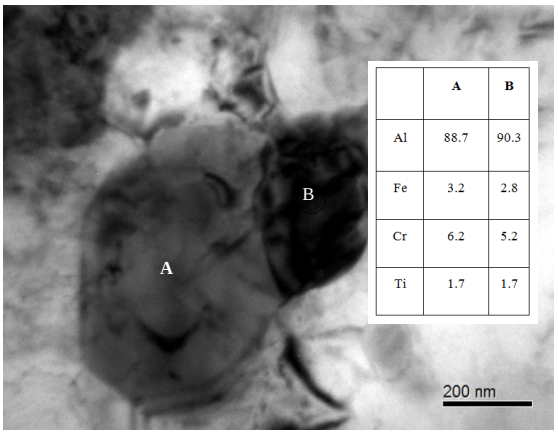

	A	B
Al	88.7	90.3
Fe	3.2	2.8
Cr	6.2	5.2
Ti	1.7	1.7

(b)

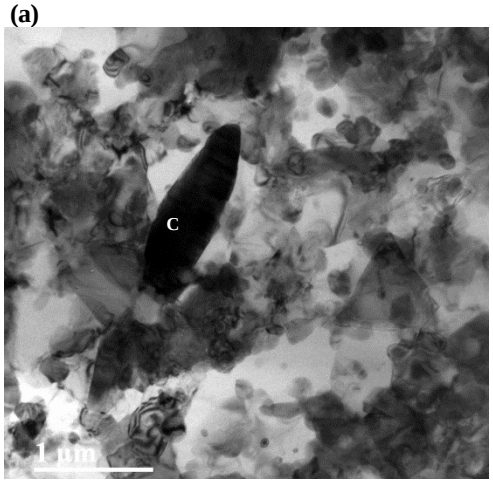

(c)

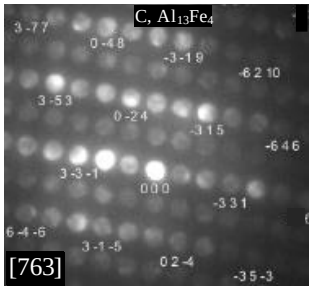

	C($Al_{13}Fe_4$)
Al	80.8±0.3
Fe	18.9±0.4
Cr	0.5±0.3
Ti	-

(d)

Figure 5.16 BF TEM images for the 450°C/100h sample: (a) overall view showing elongated $Al_{13}Fe_4$ particles, (b) higher magnification images of likely $Al_{13}Cr_2$ particles containing Fe, (c, d) an elongated possible $Al_{13}Fe_4$ particle 'C', it's indexed DP and chemical composition.

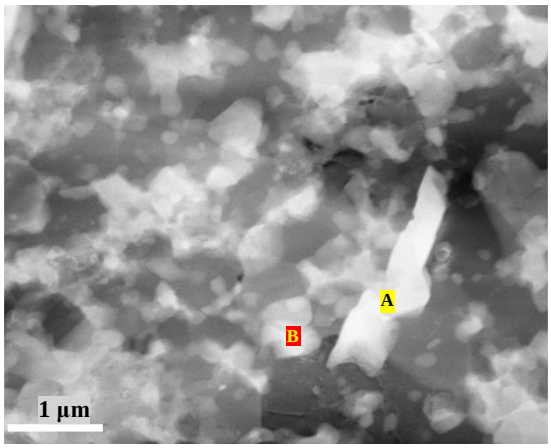

(a)

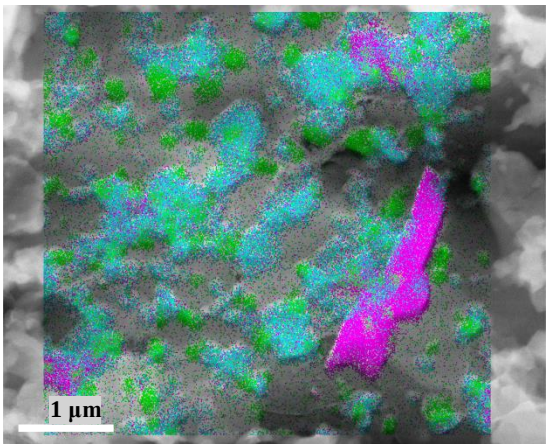

(b)

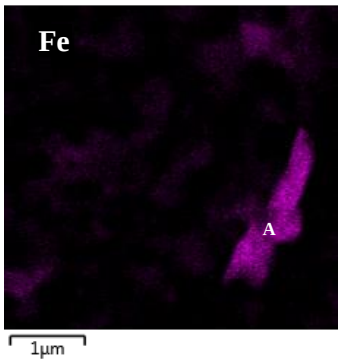

	A($Al_{13}Fe_4$)
Al	80.8±0.3
Fe	18.9±0.4
Cr	0.5±0.3
Ti	-

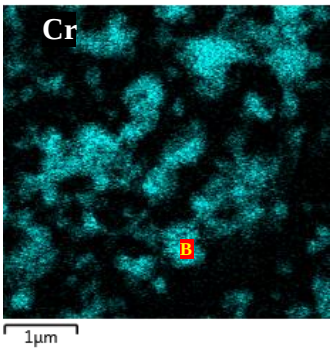

	B($Al_{13}Cr_2$)
Al	88.8±0.3
Fe	3.0±0.2
Cr	6.5±0.5
Ti	1.7±0.1

(d)

(c)

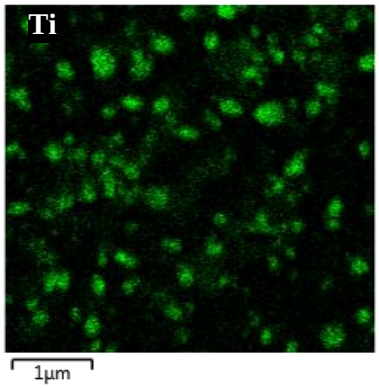

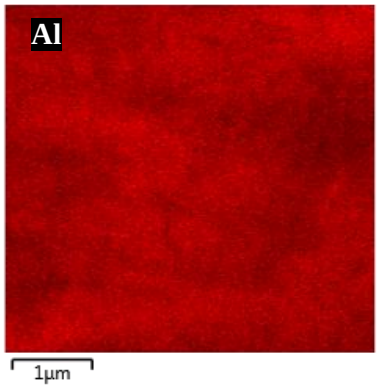

(e) (f)

Figure 5.17 STEM images and EDX mapping for Al, Fe, Cr and Ti elements in sample 450°C/100h. Elongated particle A($A_{l3}Fe_{4)}$ and round particle B($Al_{13}Cr_2$) are shown.

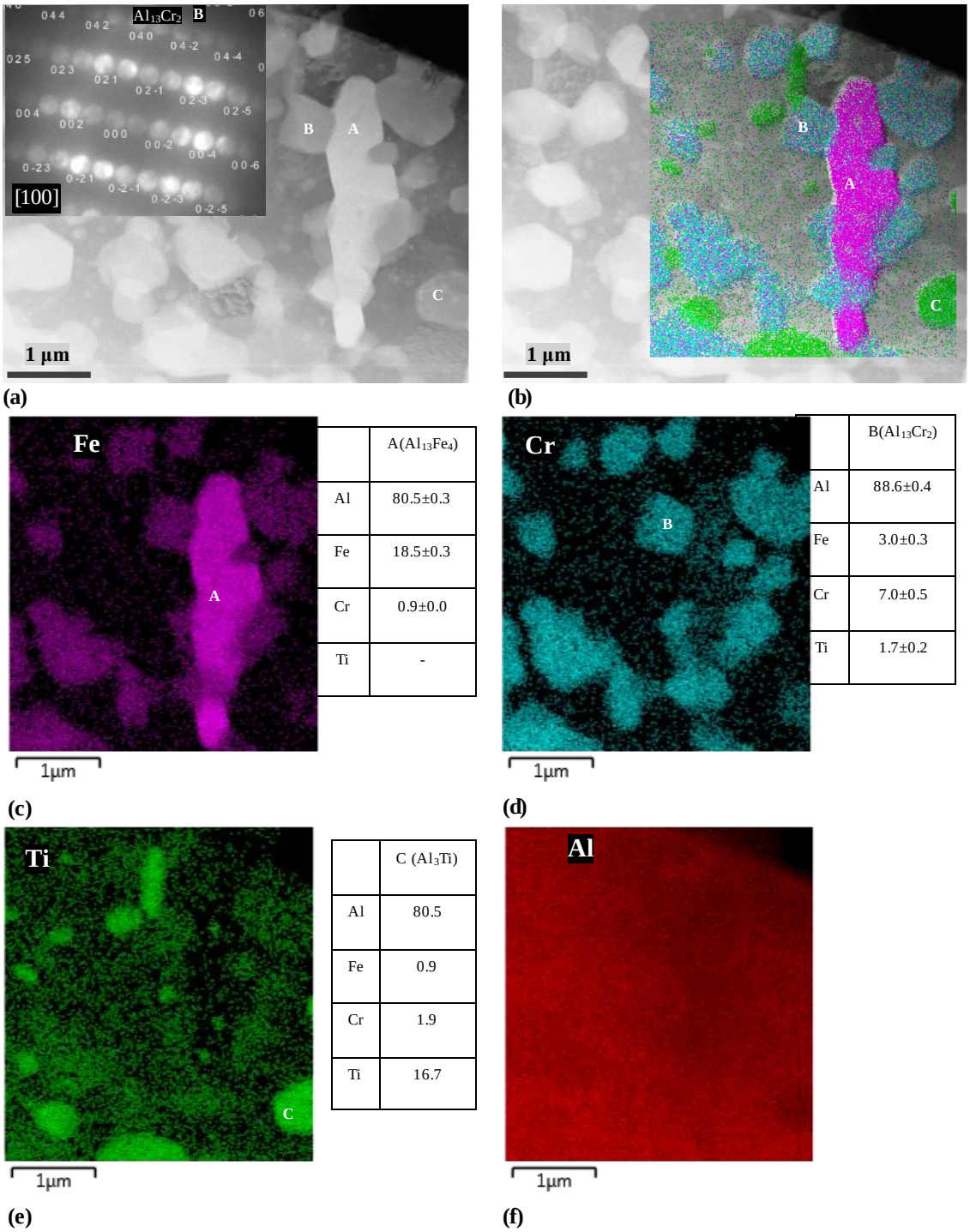

	A($Al_{13}Fe_4$)
Al	80.5±0.3
Fe	18.5±0.3
Cr	0.9±0.0
Ti	-

	B($Al_{13}Cr_2$)
Al	88.6±0.4
Fe	3.0±0.3
Cr	7.0±0.5
Ti	1.7±0.2

	C (Al_3Ti)
Al	80.5
Fe	0.9
Cr	1.9
Ti	16.7

Figure 5.18 STEM images EDX mapping for Al, Fe, Cr and Ti elements for sample 650°C/1h. Elongated particle 'A' ($A_{l3}Fe_4$), round particle 'B' ($Al_{13}Cr_2$) and round particle 'C' (Al_3Ti) can be seen; an indexed DP for particle 'B'($Al_{13}Cr_2$) in [100] zone axis is also shown.

The grain size measurement for the annealed samples is mostly found in the range of 250nm to 800nm. In high temperature annealed sample 450°C/100h, the grains were measured in a slightly larger range between 380nm to ~1000nm, as seen in Figure 5.19 (a) to (h). It was noted that several grains were oriented at small angles with respect to each other. This was observed in Figure 5.19 (a) to (h), which contains a series of BF TEM micrographs for the sample 450°C/100h acquired by rotating the sample by a few degrees.

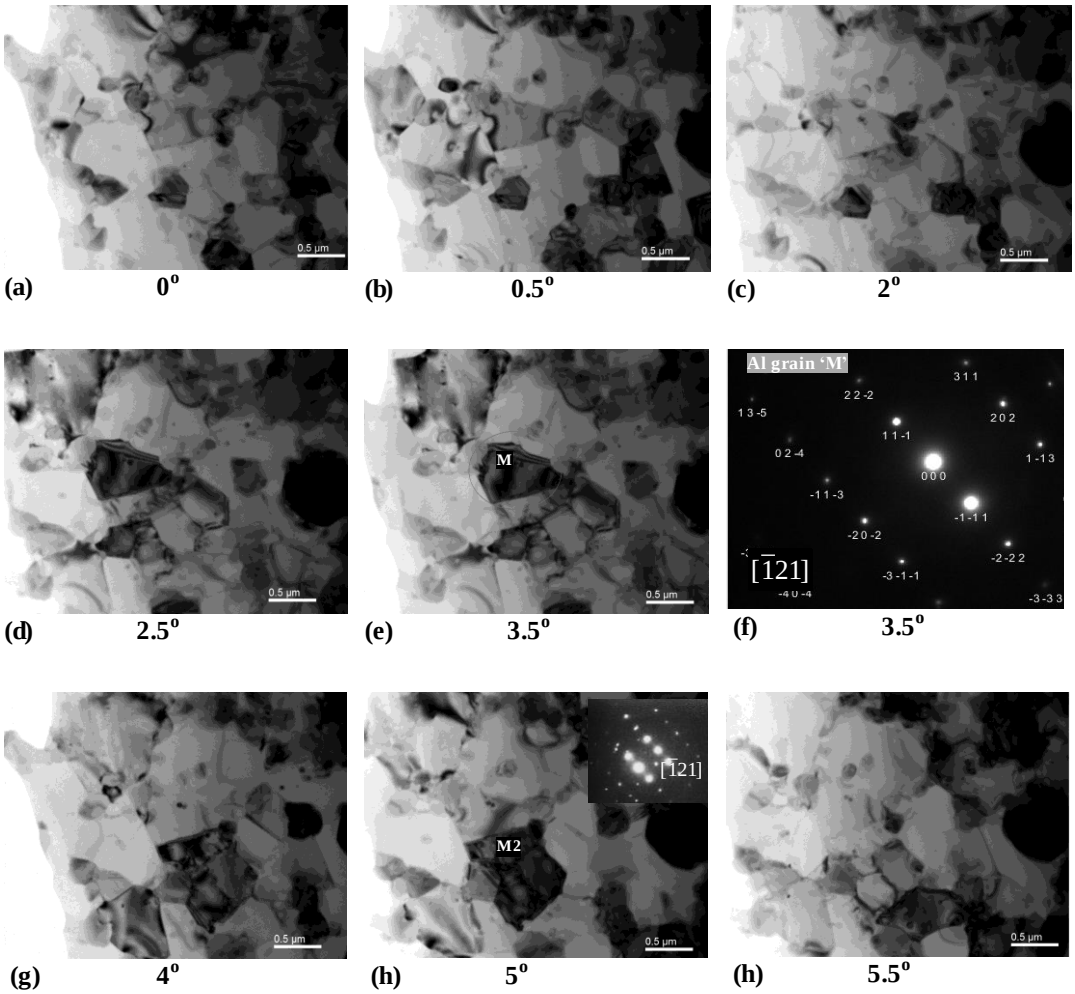

Figure 5.19 BF TEM images for the 450°C/100h sample, showing Al grains.

Measuring a statistically significant number of grains using only TEM was deemed impractical; therefore, EBSD was used to measure the grain size and the texture, as described in next section.

5.2.5 EBSD

Figure 5.20 shows the inverse pole figure colour code and the grain boundary colour codes used in all the EBSD IPF maps. Figure 5.21, Figure 5.22, Figure 5.23, Figure 5.24 and Figure 5.25, correspond to the annealed samples 250^{o}C/100h, 300^{o}C/100h, 350^{o}C/100h, 400^{o}C/100h and 450^{o}C/100h respectively. Within these aforementioned samples, Figure (a) and Figure (b) contain the representative EBSD IPF images (containing the information of the inverse pole figures) for the longitudinal and cross section samples respectively. The relevant extrusion directions are also marked. Diameters and average area fractions of the grains are shown in figure (c) and (d) of all the above mentioned samples. The grain size distributions are best represented by the 'unique grain colour maps' which have been provided in Appendix 3. The grains in longitudinal direction were aligned in the extrusion direction. In these annealed samples the average grain size in the longitudinal direction was ~470nm to 530nm, whereas the average size in the cross section direction was between 410nm to 510nm. In comparison to the others, the samples 400^{o}C/100h and 450^{o}C/100h register a small increase in the average grain size (~30nm to 100nm) in both the longitudinal and cross section directions. The grain sizes range from submicron to a few microns, with the majority being submicron (<1μm).

Figure (e) contains the inverse pole figure for all the cross sectional samples. In all of the annealed cross section samples, the fibre texture <111> was observed. This is similar to as observed in the 'as extruded' samples, and explained in section 4.3.5. The <111> texture is exactly similar to as observed in the XRD study (Figure 5.8) of the annealed samples. Dark portion in the some samples is an artefact of polishing, and consequently, the TSL software could not identify the grains in those regions, as seen in Figure 5.22 (b) Figure 5.23 (b).

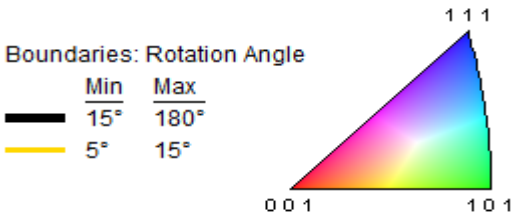

Figure 5.20 Colour code for inverse pole figure (IPF) map and grain boundaries.

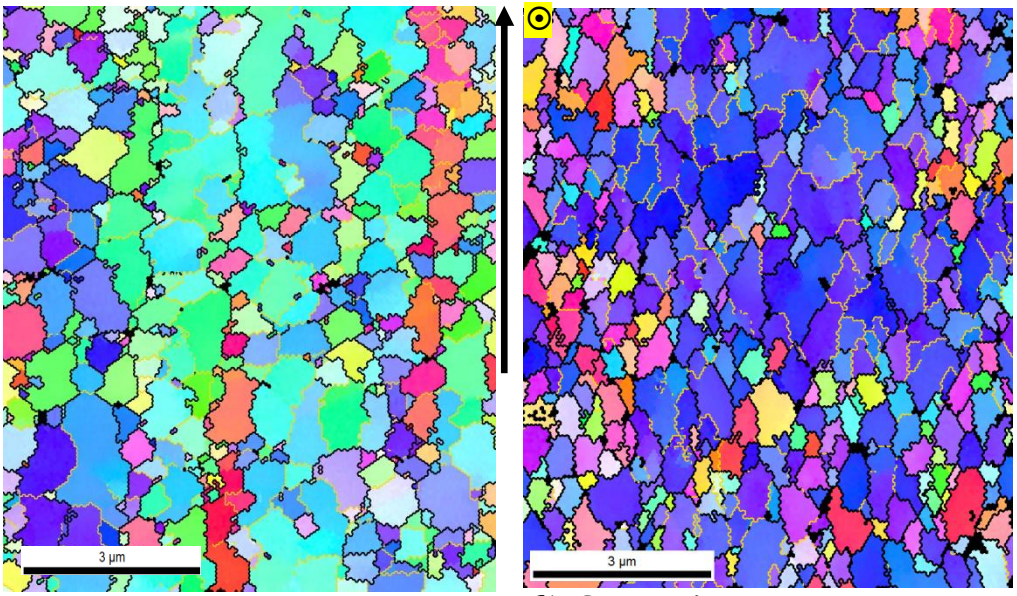

(a) Longitudinal section (b) Cross section

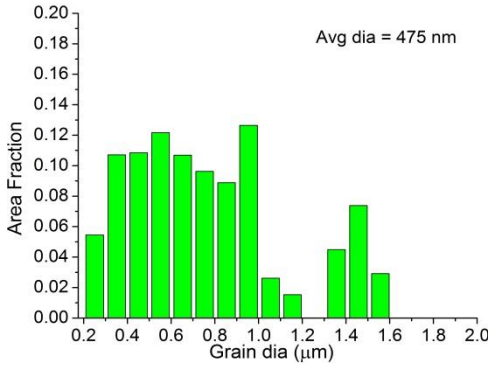

(c) Longitudinal section

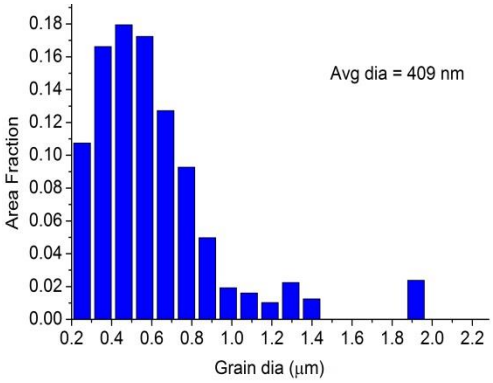

(d) Cross section

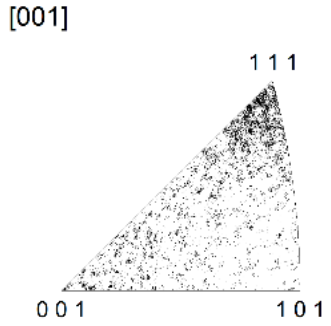

(e) Cross section

Figure 5.21 EBSD analysis for the 250°C/100 sample: (a, c) IPF, and grain diameter size distribution in longitudinal sample, (b, d) IPF, and grain diameter size distribution in cross sectional sample, (e) inverse pole figure map.

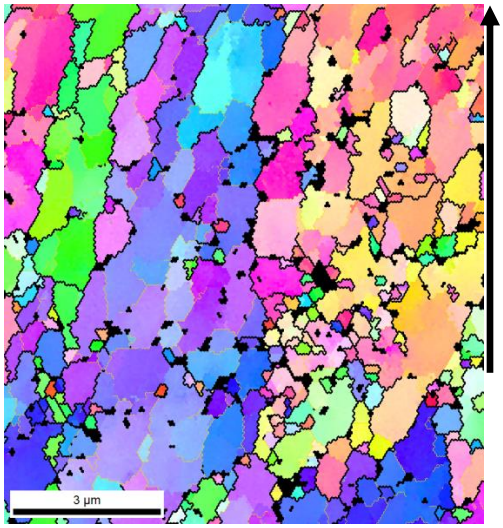

(a) Longitudinal section

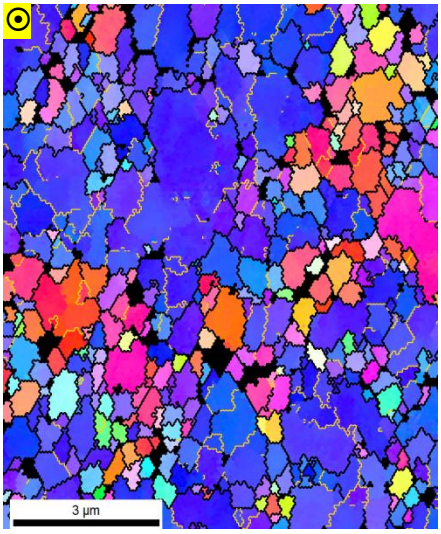

(b) Cross section

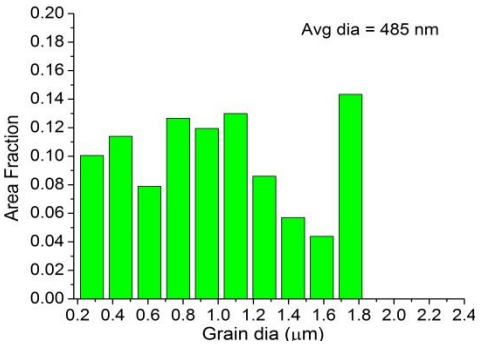

(c)

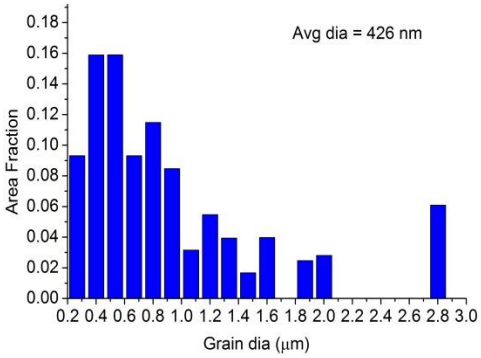

(d) Cross section

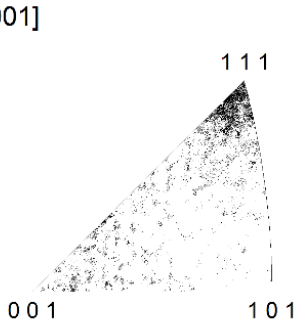

(e) Cross section

Figure 5.22 EBSD analysis for the 300°C/100 sample: (a, c) IPF, and grain diameter size distribution in longitudinal sample, (b, d) IPF, and grain diameter size distribution in cross sectional sample, (e) inverse pole figure map.

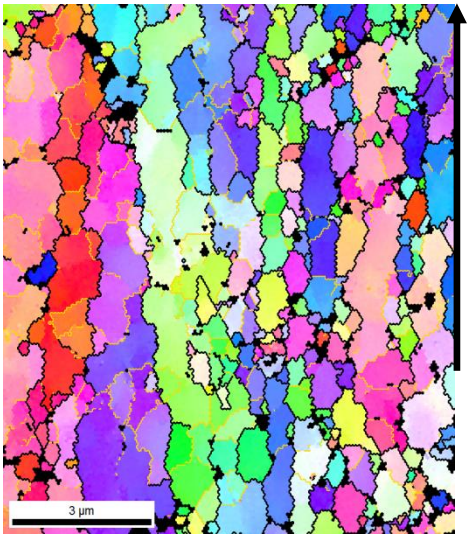

(a) Longitudinal section

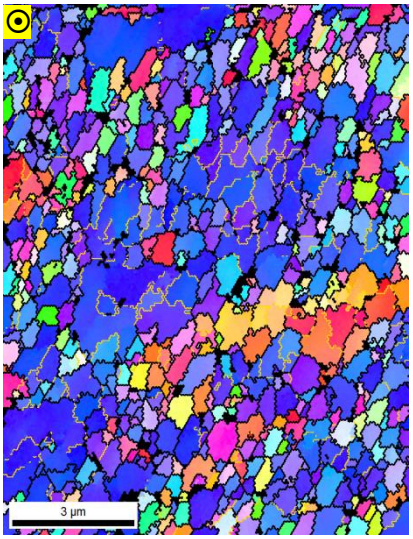

(b) Cross section

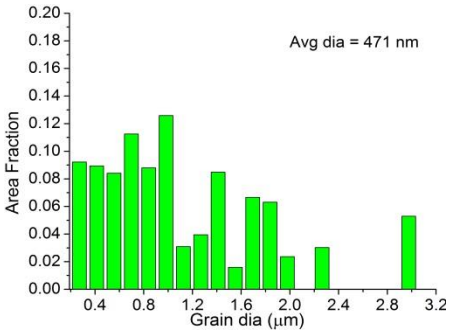

(c)

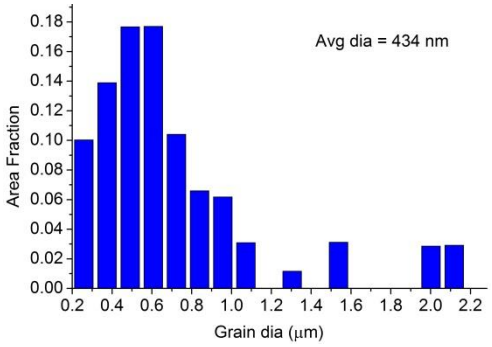

(d) Cross section

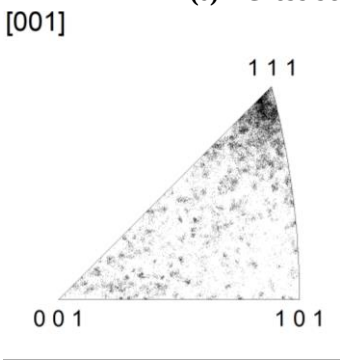

(e) Cross section

Figure 5.23 EBSD analysis for the 350°C/100 sample: (a, c) IPF, and grain diameter size distribution in longitudinal sample, (b, d) IPF, and grain diameter size distribution in cross sectional sample, (e) inverse pole figure map.

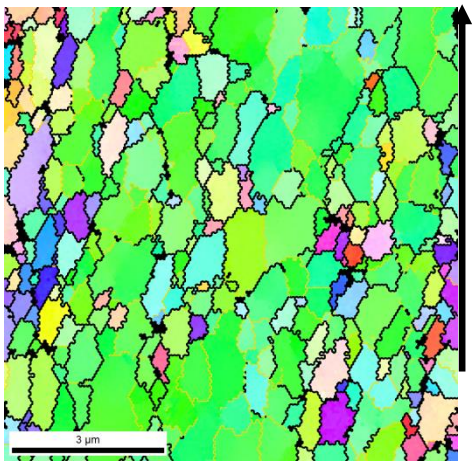

(a) Longitudinal section

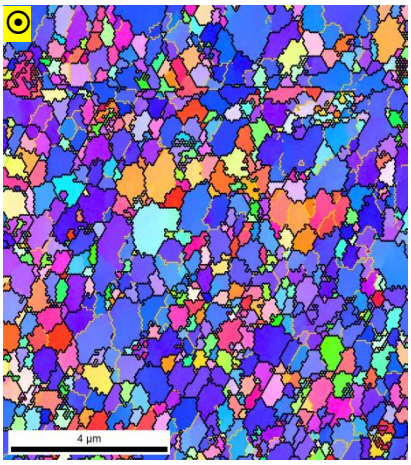

(b) Cross section

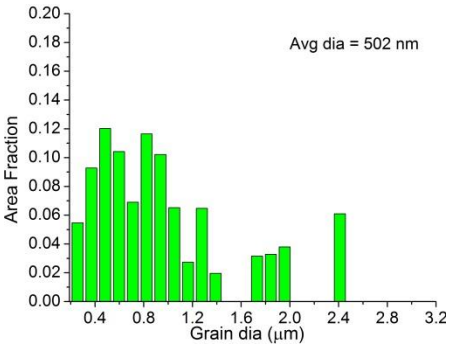

(c) Longitudinal section

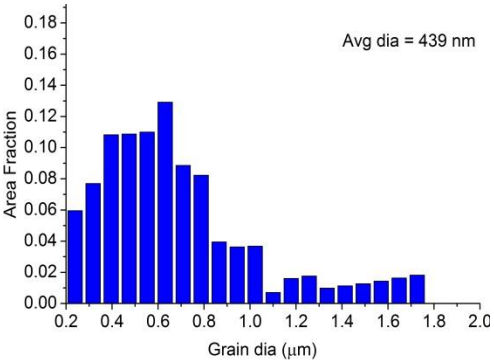

(d) Cross section

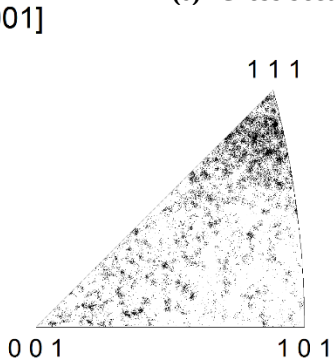

(e) Cross section

Figure 5.24 EBSD analysis for the 400°C/100 sample: (a, c) IPF, and grain diameter size distribution in longitudinal sample, (b, d) IPF, and grain diameter size distribution in cross sectional sample, (e) inverse pole figure map.

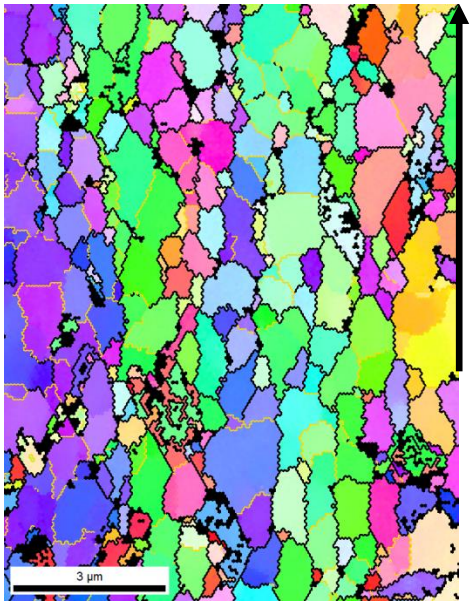

(a) Longitudinal section

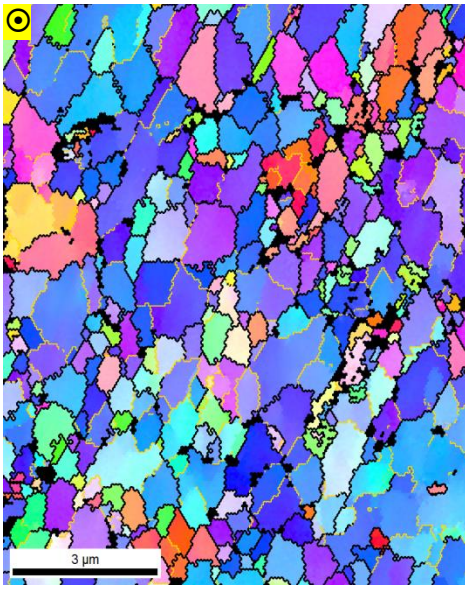

(b) Cross section

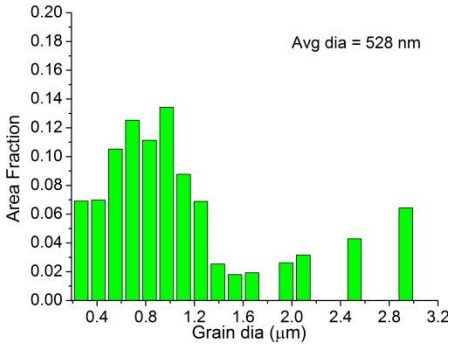

(c) Longitudinal section

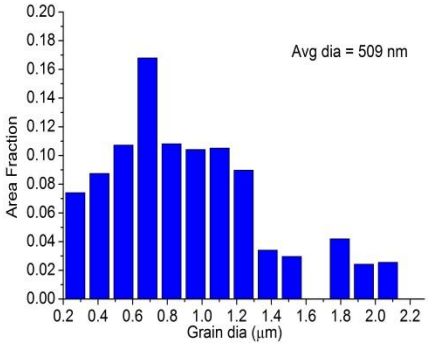

(d) Cross section

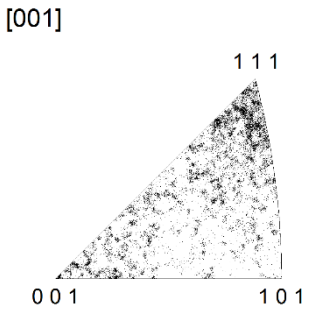

(e) Cross section

Figure 5.25 EBSD analysis for the 450°C/100 sample: (a, c) IPF, and grain diameter size distribution in longitudinal sample, (b, d) IPF, and grain diameter size distribution in cross sectional sample, (e) inverse pole figure map.

5.3 Discussion

5.3.1 Phases in the annealed samples

As a result of the microstructural study of all the annealed samples, Table 5.2 shows the summary of probable phases, their sizes, shapes, and the range of chemical compositions. The phase analysis was carried out using XRD, which was supported by EDX analysis and diffraction pattern indexing from STEM and TEM respectively.

Table 5.2 A summary of particles observed in the I-phase transformed samples.

Major constituent elements	Al, Fe	Al, Fe	Al, Fe	Al, Ti	Al, Cr
Shape/Size	Trapezium (large)	Round (small to medium)	Elongated (very large)	Round (small to medium)	Round (small to large)
Observed in sample	350°C/100h and 400°C/100h	350°C/100h and 400°C/100h	450°C/100h and 650°C/1h	350°C/100h, 400°C/100h, 450°C/100h, 650°C/1h,	350°C/100h, 400°C/100h, 450°C/100h, 650°C/1h,
Al (at%)	87.0-89.0	85.3-89.3	80.0-83.0	80.5-83.0	86.4-89.2
Fe(at%)	9.3-11.1	5.7-8.2	16.5-19.3	0.5-1.2	2.4-3.5
Cr(at%)	0.8-1.8	2.7-4.3	0.3-0.6	0.4-2.0	5.3-7.9
Ti(at%)	0.0-1.0	0.8-1.8	0.0-0.1	15.3-16.7	1.5-2.0
Probable intermetallic	Al_6Fe	$Al_{13}(Fe, Cr)_{2-4}$	$Al_{13}Fe_4$	Al_3Ti	$Al_{13}Cr_2$ having dissolved Fe

Very large~>1μm, large 0.5-1.0μm, medium ~0.2-0.5 μm, small <0.2 μm

Due to very small size and/or thickness of the particles, the EDX analysis contained slightly higher Al than the expected stoichiometric composition of the most likely phase. One example in the present work is $Al_{13}Fe_4$, which contained 76.5 at% Al, but ~80-83 at% Al was measured. In an $Al_{91}Fe_4Cr_3Ti_2$ I-phase containing alloy formed by laser remelting, Gargarella et al. (2009) also measured similar higher Al compositions in Al_3Ti and $Al_{13}Fe_4$ intermetallics. Metastable intermetallics such as Al_mFe, Al_xFe, and Al_9Fe_2

(containing 80-90% Al) are sometimes present in the Al-Fe systems. However, no such intermetallics were found in during the characterisation of any of the annealed samples.

There was no noticeable I-phase transformation in the 'as extruded' and 250°C/100h, samples. In samples 300°C/100h the formation of a few very small likely Al_3Ti and Al_6Fe particles was observed in TEM. However, the volume fraction of these phases was so low that these remained undetected in XRD and the overall microstructure was similar to the 'as extruded' alloy.

A discernable phase transformation started in the 350°C/100h sample in which ~500nm large trapezium-shaped Al_6Fe, 200nm<~Al_3Ti round and Al(Fe, Cr) particles, started to appear. Table 5.2 also shows that the Al/Fe particles contain some Cr, and the Al/Cr particles have Fe. Al-Cr phases (e.g. $Al_{13}Cr_2$) can dissolve a significant quantity of Fe, whereas Al-Fe alloys (e.g. Al_3Fe) can dissolve up to 4% Cr (Mondolfo, 1976, Belov et al., 2002).

In sample 400°C/100h, 100% intensity XRD peak (very low volume fraction) for $Al_{13}Fe_4$ was found at 42.9° as opposed to the 43.1° 2θ position. Similarly, the 100% intensity peak of Al_6Fe (containing 2% Cr) appears at ~42.2° rather than 42.4°. The presence of foreign elements in the lattice causes intermetallic compositions to differ from their stoichiometry, giving rise to lattice distortions and shifting XRD peaks. Similar observations were made by Yearim and Shechtman (1982), and separately by Ziani et al. (1995) in the study of RS Al-Fe-Cr alloys.

At higher temperatures (in 450°C/100h sample), $Al_{13}Fe_4$ (distorted) particles rejected the excess Cr, and the 2θ peak position shifted to the expected 43.1°, and elongated $Al_{13}Fe_4$ was observed. The presence of Al_3Ti, $Al_{13}Cr_2$, and $Al_{13}Fe_4$ in the samples annealed at elevated temperatures is consistent with the observations made by Audebert et al. (2002), Galano et al. (2004) and García-Escorial et al. (2015), in alloys of a similar composition.

A summary of the phases present in the annealed alloy samples as a result of the micro-structural study is provided in Table 5.3.

Table 5.3 Summary of phases present in the annealed samples.

Sample	**I-Phase**	**$Al_{13}(Fe, Cr)_{2-4}$**	**Al_3Ti**	**$Al_{13}Cr_2$**	**Al_6Fe**	**$Al_{13}Fe_4$**
As Extruded	✓	✓(small)	✓(small)	-	-	-
250°C/100h	✓	✓(small)	✓(small)	-	-	-
300°C/100h	✓	✓(small)	✓(small)	-	-	-
350°C/100h	✓	✓	✓	✓	✓(small)	-
400°C/100h	-	✓	✓	✓	✓	✓(small)
450°C/100h	-	-	✓	✓	-	✓

Small indicates a small volume fraction

5.3.2 Particle sizes, volume fractions and grain sizes

As mentioned already that microstructure of the samples 250°C/100h and 300°C/100h were similar to the 'As extruded' sample. Moreover, in sample 350°C/100h although the phase transformations were underway but the majority of the particle sizes were not observed to be changing. Moreover, as will be found in chapter 6 all of these samples had similar mechanical properties as the 'As extruded' sample. Therefore, the particle size distribution of samples 250°C/100h, 300°C/100h and 350°C/100h samples was assumed to be similar to the 'as extruded' sample. The particle size distribution of the 'As extruded' is reproduced from section 4.3.6 as Figure 5.26.

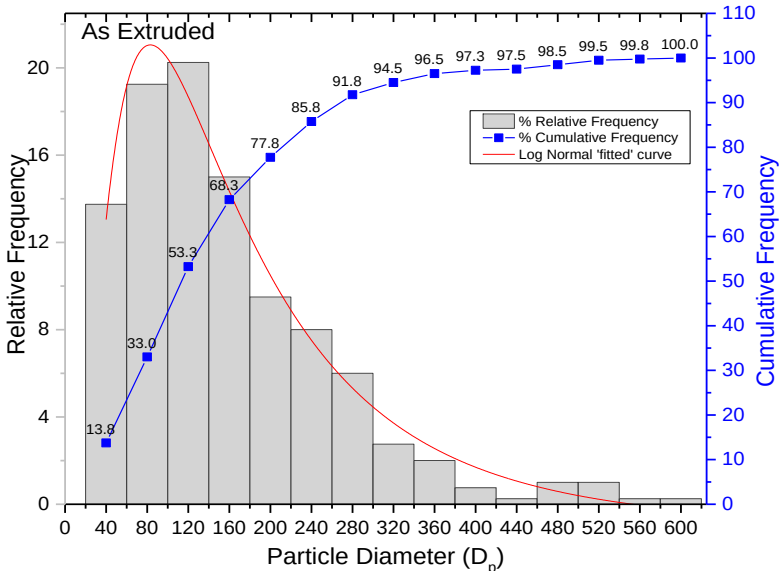

Figure 5.26 Particle size distribution showing percent relative frequency and percent cumulative frequency for I-phase particles in 'as extruded' sample. A log normal distribution curve was fitted having a mean diameter of 151±11nm.The samples 250°C/100h, 300°C/100h and 350°C/100h were assumed to have the similar particle size distribution.

The microstructures of the samples 400°C/100h and 450°C/100h were completely different from the 'As extruded' or other annealed samples. The particle size distribution of the samples 400°C/100h and 450°C/100h is shown Figure 5.27 and Figure 5.28 respectively, in comparison to the 'as extruded' sample, the quantity and spread of larger particles (>500nm) increased in these samples. The particle sizes and volume fractions of these samples were measured using the methods explained in section 4.3.6 by analysing ~200 particles for each of these samples. Log-normal distribution curves were fitted and the mean particle diameter was found to be 193±7nm and 239±9nm for 400°C/100h and 450°C/100h samples respectively which are larger than that found in the 'as extruded' sample (151±11nm) using the same distribution.

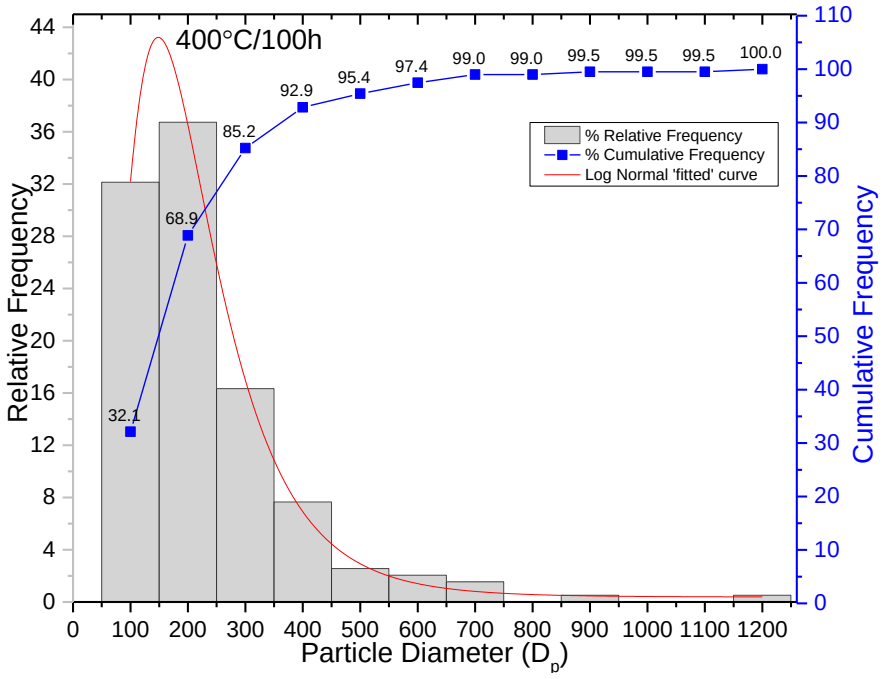

Figure 5.27 Particle size distribution showing percent relative frequency and percent cumulative frequency for intermetallic particles in sample 400°C/100h. A log normal distribution curve was fitted having a mean diameter of 193±7nm.

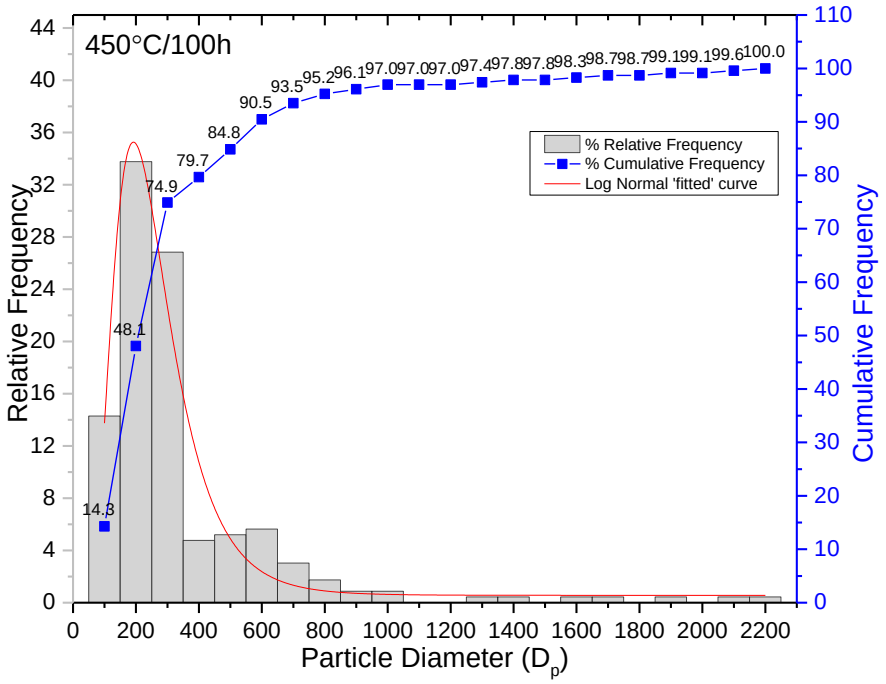

Figure 5.28 Particle size distribution showing percent relative frequency and percent cumulative frequency for intermetallic particles in sample 400°C/100h. A log normal distribution curve was fitted having a mean diameter of 239±9nm.

A summary of the volume fractions, particle sizes, mean planar random interparticle distance and measured longitudinal and cross section grain sizes (from EBSD) are provided in Table 5.4.

Table 5.4 Summary of the particle sizes, volume fraction and grain sizes in various samples[D].

Sample	Volume Fraction	Mean Particle Diameter	Mean Planar Particle Diameter	Mean Random Interparticle Planar Distance	Mean Planar Grain Diameters	
					D_{Long}	D_{Xsec}
	f_v	D_P (nm)	$D_{P,s}$ (nm)	λs (nm)	nm	nm
As Extruded	0.44	151±11	123±9	105±8	470	430
250°C/100h					475	409
300°C/100h					485	426
350°C/100h					471	434
400°C/100h	0.42	193±7	158±6	145±6	502	439
450°C/100h	0.42	239±9	195±7	180±7	528	509

5.4 Summary

The activation energy for the transformation of the I-phase was 250kJ/mol. A noticeable I-phase transformation started after 100h annealing at 350°C which completed after 100h annealing at 450°C. The average particle size increases from 151nm in the 'as extruded' samples to 193nm and 239nm in 400°C/100h and 450°C/100h respectively, due to the I-phase transformation and subsequent particle growth. Grain sizes remained unaffected as long as the I-phase existed in the sample, and after the I-phase transformation, the average grain size increased by ~50-100nm. The summary of the characterisation is provided in Table 5.5.

[D] D_p is mean particle diameter (from log normal distribution), mean random planar interparticle distance was calculated using planar diameter $D_{p,s}$ which is $\sqrt{(2/3)}$ times the particle diameter D_p. D_{Long} and D_{Xsec} are the mean planar grain sizes in longitudinal and cross section directions. Error in fv=±0.03, standard deviation in grain diameter measurement is of the order of ~170nm .

Table 5.5 A summary of characterisation of as extruded and 100hrs annealed bulk extruded samples.

Sample	SEM and EBSD	TEM and/or STEM	DSC	XRD
As Extruded	The I-phase volume fraction is 44%. <111> fiber texture is present. Cross section grains have a mean grain size of ~432nm. Average longitudinal grain size is ~40nm larger.	I-phase (confirmed by fivefold diffraction patterns) and α-Al phases are present. Average I-phase particle size is ~151nm. Grain size is from ~250-800.	Metastable (icosahedral) phase is present, indicated by a visible peak at ~522^{o}C ,	α- Al peaks and I phase, very small Al_3Ti and $Al_{13}(Fe,Cr)_{2-4}$
250°C/100h	As above	As above	As above	As above
300°C/100h	As above	The overall microstructure is similar to the 'as extruded alloy. Occasionally very small Al_6Fe and Al_3Ti particles start to appear next to the I-phase particles.	As above	As above
350°C/100h	Few large size (~500nm) irregular trapezium shape particles are seen in addition to a large number of small spherical shape particles. Al grains sizes are similar to the previous samples	Fewer particles are identified as I-phase. Mostly Al_3Ti and Al(Fe,Cr) particles are observed. A few likely Al_6Fe trapezium shape particles can also be seen. Grain sizes are similar to the 'as extruded' sample.	Metastable (I-phase) phase is present in small quantity , indicated by a small, diffused peak at ~520^{o}C	α- Al peaks are visible, I-phase peaks are broadened and mostly shifted towards right as θ_D-$Al_{13}(Fe,Cr)_{2-4}$. Al_3Ti peaks become prominent, small $Al_{13}Cr_2$ and Al_6Fe peaks appear.
400°C/100h	Irregular trapezium shape particles in addition to small spherical particles are seen. Average grain size increased slightly.	I-phase no longer exists. Larger size likely Al_3Ti and Al(Fe,Cr) particles are observed as well as a few trapezium shape likelyAl_6Fe are also found.	No metastable I-phase peak at ~520^{o}C.	No I-phase peaks are found. Al_3Ti, Al_6Fe and $Al_{13}Cr_2$ peaks become prominent. Small $Al_{13}Fe_4$ peaks appear and have a small offset due to dissolved Cr.
450°C/100h	Up to few microns long, iron containing elongated particles becomes visible in addition to small spherical particles. Average grain size increased by ~50-100nm.	Submicron to few micron long likely $Al_{13}Fe_4$ is found. Most of possible $Al_{13}Cr_2$ (containing Fe) particles exist in 200-800nm range. Most of the small (<300nm) particles are likely Al_3Ti. Grains are mostly 380-1000nm in size.	As above	α- Al peaks Al_3Ti, stable $Al_{13}Fe_4$ and $Al_{13}Cr_2$ phase peaks are visible. Metastable Al_6Fe peaks disappear.

References

Audebert, F., Prima, F., Galano, M., Tomut, M., Warren, P. J., Stone, I. C. and Cantor, B. (2002) 'Structural characterisation and mechanical properties of nanocomposite Al-based alloys', *Materials transactions*, 43(8), pp. 2017-2025.

Belov, N. A., Aksenov, A. A. and Eskin, D. G. (2002) *Iron in aluminium alloys: impurity and alloying element*. CRC Press.

Du, Y., Chang, Y., Huang, B., Gong, W., Jin, Z., Xu, H., Yuan, Z., Liu, Y., He, Y. and Xie, F.-Y. (2003) 'Diffusion coefficients of some solutes in fcc and liquid Al: critical evaluation and correlation', *Materials Science and Engineering: A*, 363(1), pp. 140-151.

Galano, M., Audebert, F., Cantor, B. and Stone, I. (2004) 'Structural characterisation and stability of new nanoquasicrystalline Al-based alloys', *Materials Science and Engineering: A*, 375, pp. 1206-1211.

Galano, M., Audebert, F., Stone, I. and Cantor, B. (2009) 'Nanoquasicrystalline Al–Fe–Cr-based alloys. Part I: Phase transformations', *Acta Materialia*, 57(17), pp. 5107-5119.

Galano, M., Marsh, A., Audebert, F., Xu, W. and Ramundo, M. (2014) 'Nanoquasicrystalline Al-based matrix/γ-Al 2 O 3 nanocomposites', *Journal of Alloys and Compounds*.

García-Escorial, A., Natale, E., Cremaschi, V. J., Todd, I. and Lieblich, M. (2015) 'Quasicrystalline Al93Fe3Cr2Ti2 alloys', *Revista de Metalurgia*, 51(4), pp. 10.3989/revmetalm. 054.

Gargarella, P., Almeida, A., Vilar, R., Afonso, C., Rios, C., Bolfarini, C., Botta, W. and Kiminami, C. (2009) 'Microstructural characterization of a laser remelted coating of Al 91 Fe 4 Cr 3 Ti 2 quasicrystalline alloy', *Scripta Materialia*, 61(7), pp. 709-712.

Kissinger, H. E. (1956) 'Variation of peak temperature with heating rate in differential thermal analysis', *Journal of research of the National Bureau of Standards*, 57(4), pp. 217-221.

Kissinger, H. E. (1957) 'Reaction kinetics in differential thermal analysis', *Analytical chemistry*, 29(11), pp. 1702-1706.

Mondolfo, L. F. (1976) *Aluminum alloys: structure and properties'; 1976. London-Boston: Butter Worths & Co Ltd*.

Ozawa, T. (1970) 'Kinetic analysis of derivative curves in thermal analysis', *Journal of Thermal Analysis and Calorimetry*, 2(3), pp. 301-324.

Yearim, R. and Shechtman, D. (1982) 'The structure of rapidly solidified Al-Fe-Cr alloys', *Metallurgical Transactions A*, 13(11), pp. 1891-1898.

Ziani, A., Michot, G., Pianelli, A., Redjaimia, A., Zahra, C. and Zahra, A. (1995) 'Transformation of the quasicrystalline phase Al-Cr-Fe induced by rapid solidification', *Journal of materials science*, 30(11), pp. 2921-2929.

6. Physical and Mechanical Properties of the Extruded NQX Alloy at Room Temperature

This chapter shows the results for the room temperature mechanical properties (such as microhardness, elastic constants, yield strength, ultimate tensile strength and fatigue behaviour) measured/calculated in the 'as extruded' and annealed conditions. In addition, density was also measured for the extruded bars.

6.1 Density

The densities of all the bars were measured and the values were found between 2.94 to 2.95g/cm^3 (or 10^3.kg/m^3), as shown in Figure 6.1. The mean density value and standard deviation of all the bars is 2.949±0.003g/cm^3, depicted by a dashed line. In order to verify the validity of the measurement procedure, the density of a conventional alloy (Al6061-T6) was measured and found to be 2.70±0.002g/cm^3, which is similar to the values reported in the literature (Hatch, 1984).

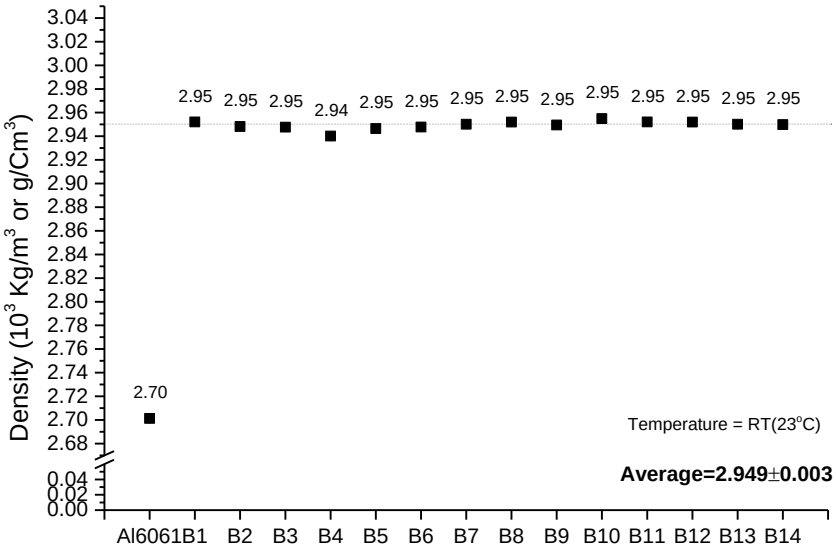

Figure 6.1 Measured density of all extruded NQX alloy bars compared to a conventional Al alloy (average value is depicted by the dashed line).

The NQX alloy density is found to be 9% higher (2.95g/cm^3) than pure Al (2.70g/cm^3) due to the presence of higher density elements such as: Fe (7.9g/cm^3), Cr (7.2g/cm^3) and Ti (4.4g/cm^3). Luo et al. (2005) worked on a mechanically alloyed and extruded $Al_{93}Fe_3Cr_2Ti_2$ (with no I-phase), and reported a density value of 2.92g/cm^3. Densities of commercial high strength Al alloys vary as a function of alloying element. For example density of Al7075 (Al-Zn alloy) is 2.81g/cm^3 whereas Al8090 (Al-Li) alloy have a density of 2.55 g/cm^3. For most of the 1xxx, 5xxx, and 6xxx series alloys have a density close to 2.7g/cm^3(Gale and Totemeier, 2003).

6.2 Dynamic elastic constants

6.2.1 'As extruded' condition

The room temperature Young's modulus (E), shear modulus (G), and Poisson's ratio (υ) for the alloy were measured/calculated using a dynamic[A] method on five samples. FEA modelling was also carried out using 'Abaqus 6.13' and the resulting average values of the elastic constants are provided along with the average experimental values in Table 6.1. The E was measured to be 92.3±0.4GPa, G as 34.5±0.2GPa, and υ was calculated to be ~0.337±0.005. The modelled values were found within the error range of the experimental values. A comparison of E found in the present study and literature is provided in Table 6.1. G and υ values for the present study are also reported.

[A] Impulse excitation of vibration method using ASTM E-1876 is explained in section 3.4.3.

Table 6.1 Values of dynamic elastic constants in comparison with Al alloys from literature.

Composition (at%) or Alloy	Test Method	Young's modulus (GPa) E	Shear modulus (GPa) G	Poisson's ratio ν	Reference
$Al_{93}Fe_3Cr_2Ti_2$	Dynamic (experimental results)	92.3±0.4	34.5±0.2	0.337±0.004	This work (NQX alloy)
	Dynamic (modelled results)	92±0.4	34.4±0.2	0.335±0.004	
$Al_{93}Fe_3Cr_2Ti_2$	Quasi-static (tensile)	81	-	-	(Chlupová et al., 2011)
$Al_{93}Fe_3Cr_2Ti_2$	As above	82	-	-	(Rounthwaite, 2012)
$Al_{93}Fe_3Cr_2Ti_2$		92	-	-	(Chlupova et al., 2016)
2024	Not known	73.4	28	0.33	ASM, 1990)
2618		74.4	28	0.33	
6061		69	-	-	
7075		71	-	-	
8090		79	-	-	(Totten and MacKenzie, 2003)
Pure Al		70	26	~0.33	(Martienssen and Warlimont, 2006)

As can be observed in Table 6.1, the values of E and G of NQX alloy are found ~32% and ~26% higher than those observed for pure Al respectively. Also, E and G values for the NQX alloy are 16-35% and 23-33% higher respectively, than those observed for conventional Al alloys. υ for the NQX alloy was found between 0.33 and 0.34 which are the typical values for conventional Al alloys (Hatch, 1984, ASM, 1990).

Rounthwaite (2012), and separately Chlupová et al. (2011) used quasi-static tensile tests and reported the E values as ~82MPa for the I-phase containing $Al_{93}Fe_3Cr_2Ti_2$ (25-50μm powder fraction size) extruded alloy. In a later work Chlupova et al. (2016) mentioned the E values for the same $Al_{93}Fe_3Cr_2Ti_2$ alloy to be ~92GPa also from quasi-static tensile tests. The NQX can, therefore, be regarded as an alloy having considerably higher values of elastic constants (E and G) in comparison with the conventional Al alloys.

6.2.2 'Annealed' condition

Each of the five[B] samples used in the measurement of the elastic constants of the NQX alloy at room temperature in the 'as extruded' condition were annealed for 100hrs at 250°C, 300°C, 350°C, 400°C or 450°C. The elastic constants were then re-measured to investigate the effects of the annealing temperature. E, G and υ values[C] for each of the five samples, before and after 100hrs annealing are shown in Figure 6.2, Figure 6.3 and Figure 6.4 respectively. The light colour shade in each of these figures represents the NQX alloy samples in the 'as extruded' condition, and the dark colour patterned shade represents the samples after 100hrs of annealing. Elastic constants were also obtained by modelling using FEA. Both modelled and experimental results were found within 0.5% of each other. The sample dimensions, excitation modes, values of excitation frequencies, and resulting E, G and υ values of both experimental and modelled results of the NQX alloy are provided in Table 6.2 for the five samples in the 'as extruded' and annealed conditions. The values of elastic constants are unaffected in the 250°C/100h or 300°C/100h samples. The value of E increased by ~1.5% in the 350°C/100h sample. A significant effect on E can be observed in the 400°C/100h and 450°C/100h samples, an increase in the annealing temperature also increases the E from 92.3GPa (as extruded) to 99.3GPa (450°C/100h sample). Similar relative increasing trends were observed in G and υ values.

[B] Five samples in the 'as extruded' condition were named as 1_El, 2_El, 3_El, 4_El, and 5_El. After 100h annealing at different temperature the samples were named as 'annealing temperature/annealing time' e.g. 250°C/100h etc. as explained in Table 3.1.

[C] The random error in a set of measurement of E or G values in a single sample is <0.04GPa, calculated error in ν is ~ 0.0004. The overall error in E, G and ν is 0.4GPa, 0.2GPa and 0.005 respectively which has been shown in the figures.

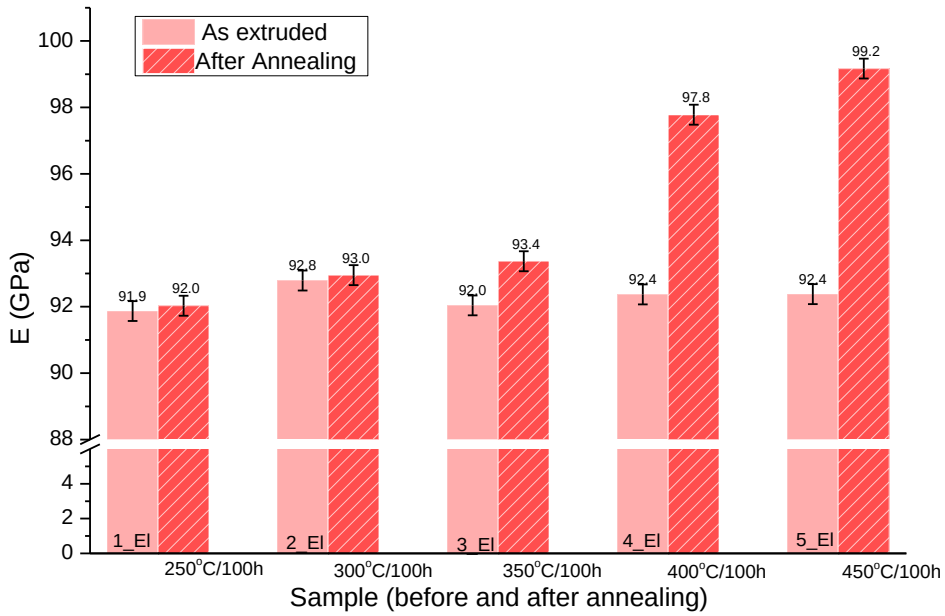

Figure 6.2 The Young's modulus of the NQX alloy in the 'as extruded' condition and after 100h annealing at different temperatures.

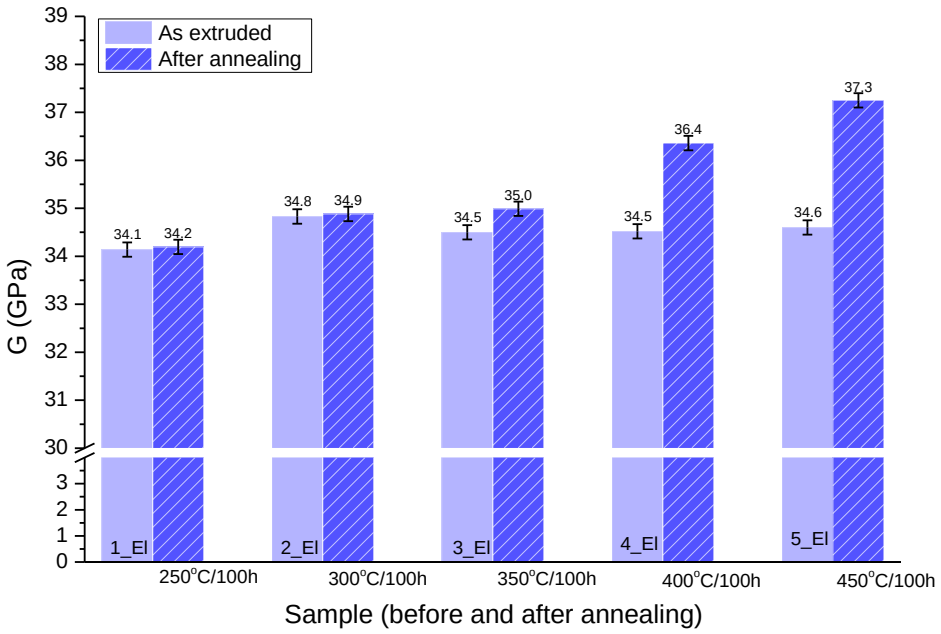

Figure 6.3 The shear modulus of the NQX alloy in the 'as extruded' condition and after 100h annealing at different temperatures.

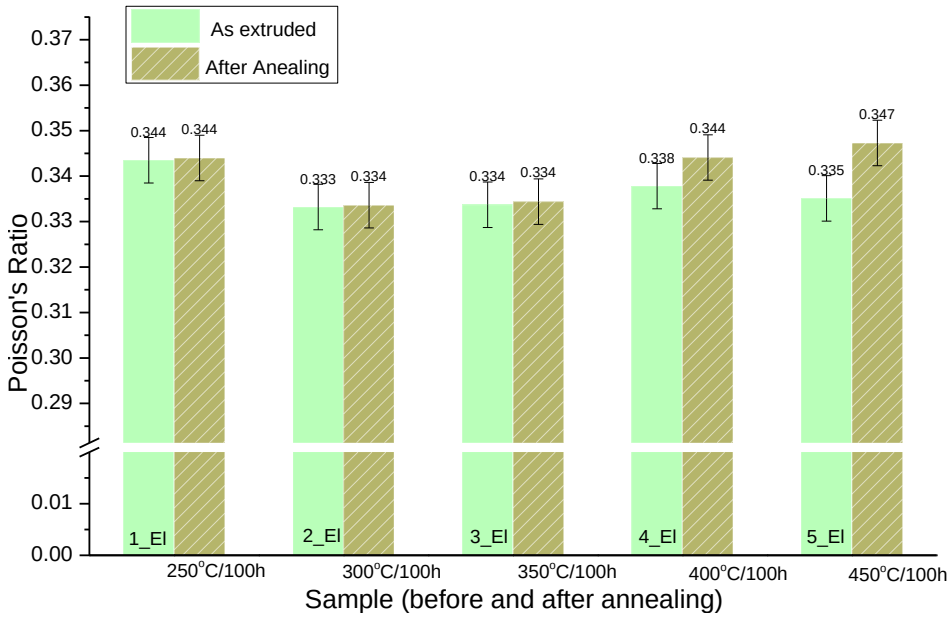

Figure 6.4 The Poisson's ratio of the NQX alloy calculated in the 'as extruded' condition and after 100h annealing at different temperatures.

Table 6.2 Summary of the experimental and modelled values of the elastic constants, before and after the 100hrs annealing at elevated temperatures.

Sample	Dimen-sion		Frequency (Hz)			Elastic Constants (*GPa)			Sample	Frequency (Hz)			Elastic Constants (*GPa)		
	mm		Exct. mode	Exp. value	Modelled value		Exp. value	Modelled	Annealed for 100hrs at a certain Tempera-ture		Exp. value	Modelled		Exp. value	Modelled
1_El	L	34.14	Flex I	34672	34674	E	91.9	91.5	250^{o}C/ 100h	Flex I	34713	34712	E	92.0	91.7
	W	8.363	Flex O	34646	34656	G	34.2	34.3		Flex O	34693	34694	G	34.2	34.3
	T	8.357	Tors	45850	45850	ν	0.344	0.335		Tors	45893	45895	ν	0.344	0.336
2_El	L	34.02	Flex I	31504	31507	E	92.8	92.6	300^{o}C/ 100h	Flex I	31532	31532	E	93.0	92.7
	W	7.766	Flex O	33244	33249	G	34.8	34.7		Flex O	33274	33276	G	34.9	34.8
	T	7.237	Tors	46216	46215	ν	0.333	0.334		Tors	46255	46251	ν	0.334	0.334
3_El	L	27.03	Flex I	42175	42169	E	92.0	91.7	350^{o}C/ 100h	Flex I	42494	42475	E	93.4	93
	W	6.277	Flex O	35215	35215	G	34.5	34.3		Flex O	35474	35479	G	35.0	34.8
	T	4.986	Tors	56512	56514	ν	0.334	0.336		Tors	56913	56913	ν	0.334	0.336
4_El	L	31.13	Flex I	38243	38250	E	92.4	92.0	400^{o}C/ 100h	Flex I	39331	39336	E	97.8	97.3
	W	7.655	Flex O	36698	36699	G	34.5	34.4		Flex O	37736	37741	G	36.4	36.3
	T	7.235	Tors	50326	50326	ν	0.338	0.336		Tors	51650	51646	ν	0.344	0.342
5_El	L	30.87	Flex I	38880	38880	E	92.4	92.0	450^{o}C/ 100h	Flex I	40247	40252	E	99.2	98.8
	W	7.672	Flex O	35766	35758	G	34.6	34.5		Flex O	370024	37022	G	36.9	36.6
	T	6.853	Tors	50525	50528	ν	0.335	0.336		Tors	52109	52101	ν	0.347	0.348

Exct. = Excitation, **Exp.** = experimental, **L** = length, **W** = width, **T** = thickness, **Flex I** = in-plane flexural, **Flex O** = out of plane flexural, **Tors** = torsional.
*** ν is a dimensionless parameter**, Error in experimental value of frequency is <±10Hz, statistical error in a single set of measurement of E or G values in one sample is <0.05GPa, calculated error in ν is ~ 4E-4. The overall error including the systematic errors in E, G and ν is 0.4GPa, 0.2GPa and 0.004 respectively.

6.3 Microhardness

Results for the room temperature microhardness for all the extruded bars are shown in Figure 6.5. The microhardness values for bars B2 to B14 are found to be between 191 to 199μHV_{500}, and the average value of 195±3 μHV_{500} is represented by a dotted line in Figure 6.5. In chapter 4 it was established that Bar 1 has a different microstructure due to the I-phase transformation, and it can be observed in Figure 6.5 that its microhardness value is significantly lower (177±2 μHV_{500}) than the average of all the other bars containing untransformed I-phase. Microhardness of high strength conventional Al alloys such as Al7075-T6 and Al2014-T6 is ~150HVN and 135HVN respectively (ASM, 1990).

The microstructure of the samples annealed at 250^{o}C, 300^{o}C, 350^{o}C, 400^{o}C, and 450^{o}C for 100hrs was analysed in chapter 5. The microhardness of the annealed samples measured at room temperature is shown in Figure 6.6. The microhardness values for the 250^{o}C/100h, 300/100h^{o}C, and 350^{o}C/100h annealed samples were found to be ~193±3 μHV_{500} which is similar to the 'as extruded' value of 195±3 μHV_{500}. The microhardness value dropped to 175±2 μHV_{500} for the 400^{o}C/100h sample, and further to 150±2 μHV_{500} for the 450^{o}C/100h sample.

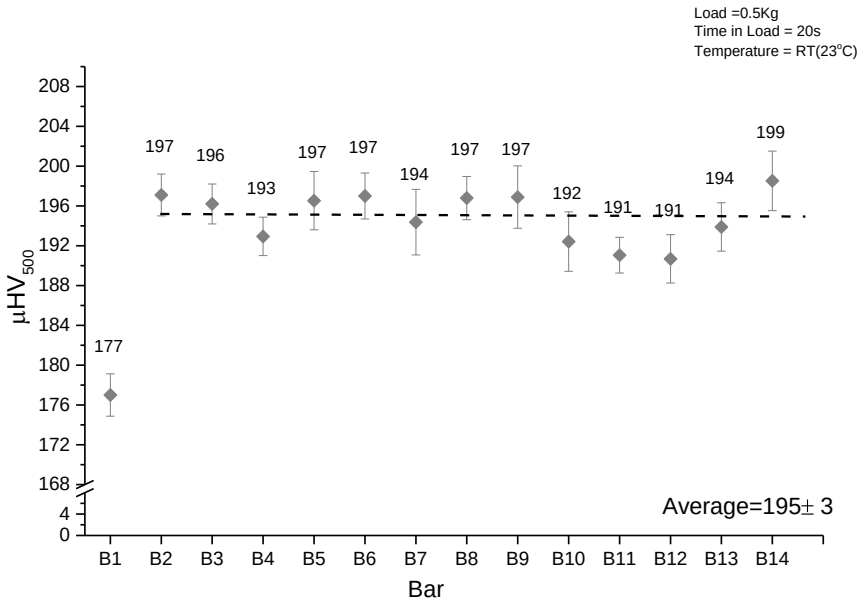

Figure 6.5 Microhardness for all extruded bars (the dotted line is the average value sans B1).

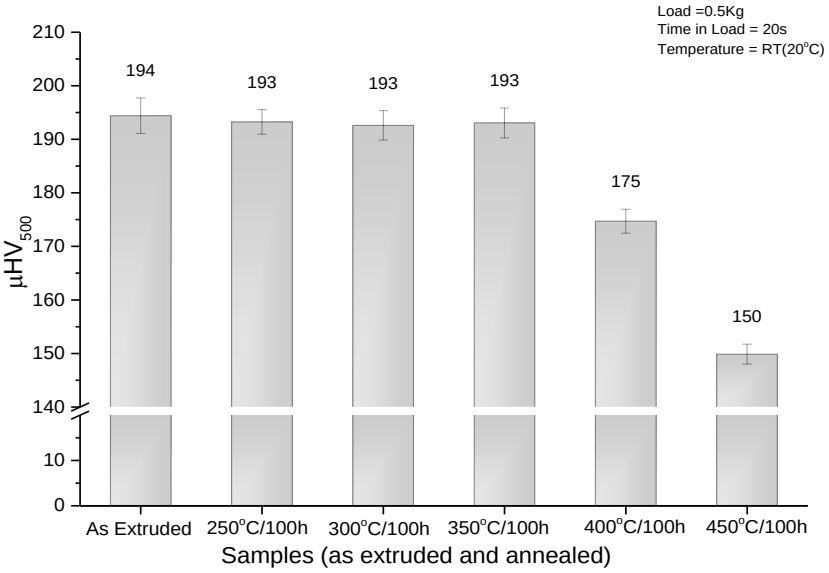

Figure 6.6 Room temperature microhardness values for the 'as extruded' and 100h annealed samples.

6.4 Tensile tests

Room temperature tensile tests were carried out at four different crosshead speeds corresponding to nominal strain rates of 10^{-2}, 10^{-3}, 10^{-4}, and $10^{-5}s^{-1}$. The resulting true stress-true strain graphs are shown in Figure 6.7. Based on the engineering stress-strain curves[D], the values for the ultimate tensile strength (UTS), yield strength, and elongation to failure for room temperature tensile tests (at all strain rates) are provided in Table 6.3. The UTS of the NQX alloy varies from 640MPa to 598MPa for the highest to the lowest strain rate. The UTS is of the order the high strength conventional Al alloys such as 7075-T6 (570MPa) or 7178-T6 (607MPa) (ASM, 1990). The elongations to failure vary from 4.7% to ~7 %, without any particular trend with respect to the strain rate. The flow stress generally decreases with a decrease in the strain rate; however, the yield strength for the 'as extruded' alloy at $10^{-5}s^{-1}$ and $10^{-4}s^{-1}$ are equal (taking errors into account), and this is referred to as the 'yield strength anomaly' (discussed in section 7.4.5). The plastic portion(s) of the graphs appear to have small values of slopes, indicative of low strain hardening (discussed in section 7.4.2). Changing the strain rate by one order of magnitude does not have a significant effect on the flow stress of the NQX alloy. No study in the open scientific literature could be found on the effect of the strain rate on the NQX alloy at room temperatures.

Figure 6.8 shows the room temperature true stress-true strain graphs for the 'as extruded' samples in comparison with 250^{o}C/100h, 300^{o}C/100h, 350^{o}C/100h, 400^{o}C/100h and

[D] In order to make comparisons between the values of commercial Al alloys given in the handbooks, the engineering values for the NQX alloy tensile properties are provided in Table 6.3. The conversions for true stress and true strain to engineering stress and strain curves are provided in Appendix '3'. The true stress-true strain curves are important as the flow stress values obtained from those will be used for various calculations in chapter 7 e.g: strain hardening exponent, strength coefficient, hardening rate, strain rate sensitivity exponent, stress exponent and activation energy.

450°C/100h samples at a strain rate of $10^{-4}s^{-1}$. The engineering values of the UTS, yield strength and elongation to failure are provided in Table 6.3. The graphs and the tensile strength values are similar for the 'as extruded' alloy for the 250°C/100h and 300°C/100h samples, whereas the 400°C/100h and 450°C/100h samples, show a loss in the tensile properties.

Table 6.3 Room temperature tensile strength, yield strength, and elongation, based on engineering stress-strain curves for the 'as extruded' NQX alloys (four strain rates), and after 100hrs annealing at elevated temperatures (at $10^{-4}s^{-1}$)[E].

Sample	Strain rate	Elongation to failure	Yield Strength	Tensile Strength
	s^{-1}	ε_f (%)	σ_y (MPa)	σ_{UTS} (MPa)
As Extruded	10^{-2}	5.7	545	640
As Extruded	10^{-3}	6.4	534	620
As Extruded	10^{-4}	6.4	526	612
As Extruded	10^{-5}	4.8	528	598
100 hrs annealed samples				
250°C/100h	10^{-4}	6.1	522	609
300°C/100h	10^{-4}	6.6	523	610
350°C/100h	10^{-4}	4.0	521	613
400°C/100h	10^{-4}	1.8	435	545
450°C/100h	10^{-4}	1.7	410	512

[E] Only one sample for each condition was tested; therefore, random statistical errors pertaining to repetition of measurements cannot be assigned. However, it was ensured that the sample broke within the gauge length otherwise the result was discarded and the test was repeated.
Other sources of errors can be associated in the strength measurements of these tests which include errors in load cell measurement, errors in measurement of the minimum gauge diameter, errors in load cell zeroing etc). These have been identified to be <5MPa or <0.8%.

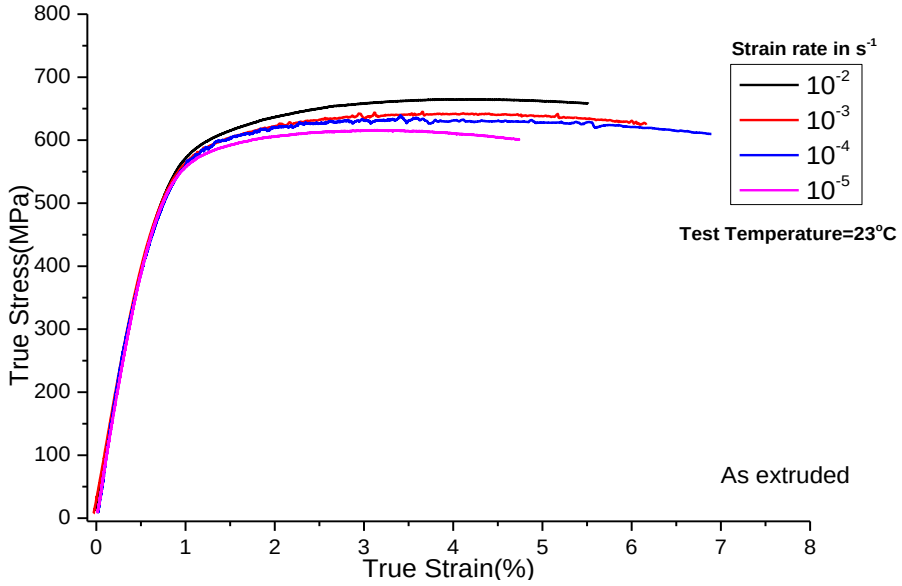

Figure 6.7 Room temperature tensile tests at four strain rates for the 'as extruded' NQX alloy.

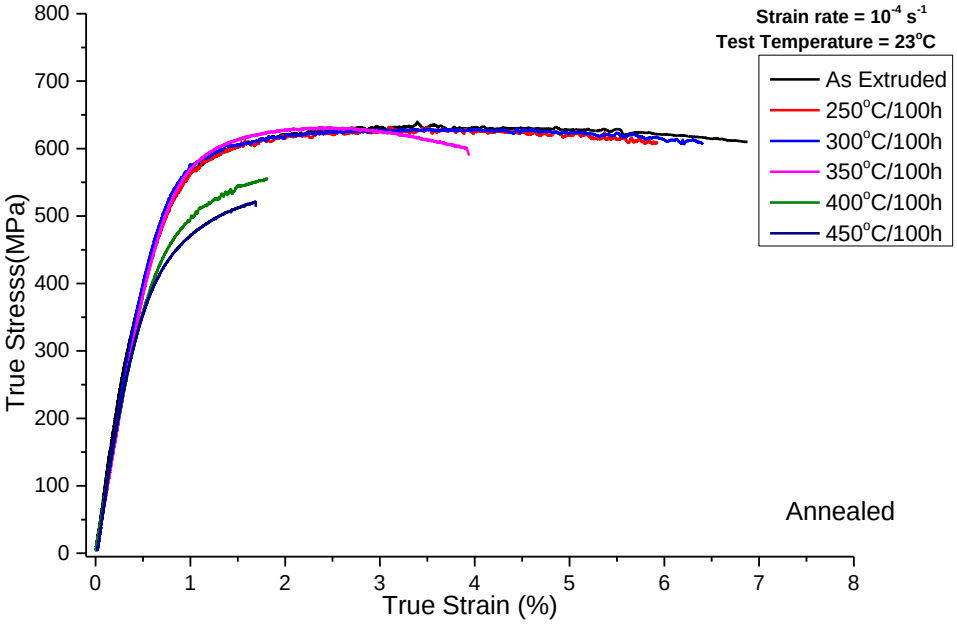

Figure 6.8 Room temperature tensile tests at $10^{-4}s^{-1}$ for the 'as extruded' NQX alloy, and after 100h annealing at various temperatures.

6.5 Fractography

Analysis of the fractured surfaces obtained from tensile tests was carried out. Two types of fracture initiations were observed, (i) from the surface, and (ii) from internal inhomogeneities or inclusions (marked by dotted circles in relevant figures). The elongation to failure ($\varepsilon_{failure}$) of both types of fractures is similar. Representative examples of various types of samples and fractured surfaces are shown in Figure 6.9 and Figure 6.10.

Figure 6.9 shows fractured surfaces for the 'as extruded' alloy in room temperature tensile tests. Figure 6.9 (a) to (d) shows fracture surfaces for the test conducted at a strain rate of $10^{-2}s^{-1}$. As indicated by the arrows in Figure 6.9 (a), the fracture originated from the surface. The shear dimples of diameter ~200-500nm appear next to the fracture origin as seen in Figure 6.9 (b) and (c). The dimples contain a single or few I-phase particles inside as seen in Figure 6.9 (d). Figure 6.9 (e) and (f) shows fractures from room temperature test at $10^{-4}s^{-1}$. Figure 6.9 (e) is an example of a fracture originating from a subsurface Fe-containing Al intermetallic inclusion ($dia_{inclusion}$ ~53μm). The shear dimples are observed in the immediate vicinity of the fracture origin.

Figure 6.10 shows the fractured surfaces for 100hrs annealed samples tested at $23^{o}C$ and $10^{-4}s^{-1}$. Figure 6.10 (a) shows the $250^{o}C$/100hrs sample surface with a fracture initiating from a ~47μm Mg-containing Al inclusion. Figure 6.10 (b) shows the $300^{o}C$/100hrs sample and a fracture initiating from a ~23μm Ti-containing Al intermetallic inclusion. In Figure 6.10 (c) and (d), the $450^{o}C$/100hrs sample fracture is an example of surface initiation. Figure 6.10 (d) shows two 1-3μm long $Al_{13}Fe_4$, elongated particles inside similarly shaped dimples, which are marked by the arrows.

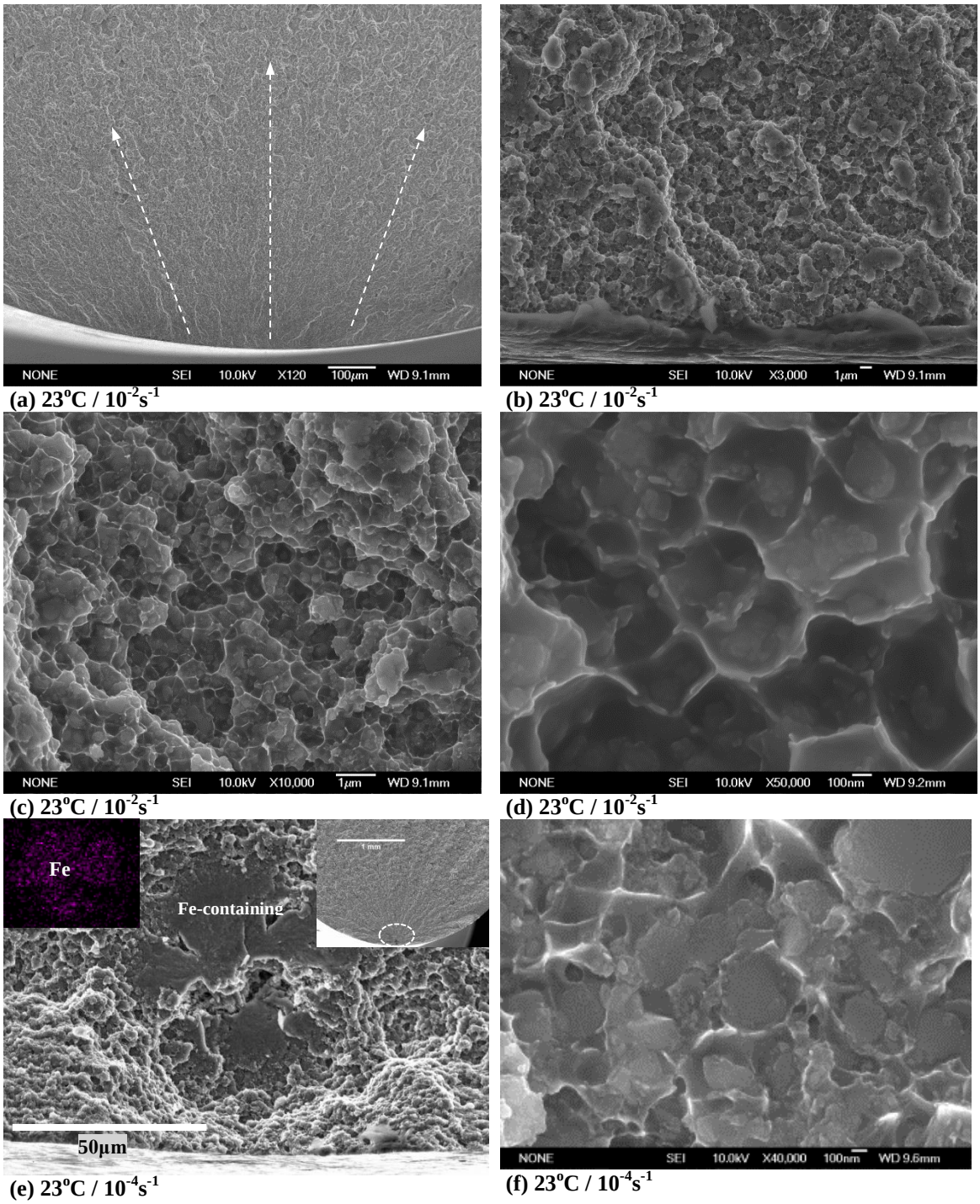

Figure 6.9 Fractured surfaces of samples tested at T= 23°C: (a) $\dot{\varepsilon}=10^{-2}s^{-1}$, overall view for fracture initiation from the surface, (b) $\dot{\varepsilon}=10^{-2}s^{-1}$, a magnified view of the fractured surface near initiation, (c) $\dot{\varepsilon}=10^{-2}s^{-1}$, submicron and micron size shear dimples are present all over the fractured surface, (d) $\dot{\varepsilon}=10^{-2}s^{-1}$, shear dimples at high magnification with I-phase particles inside, (e) $\dot{\varepsilon}=10^{-4}s^{-1}$, a subsurface Fe-containing Al intermetallic, (f) <1μm size shear dimples at intermediate and high magnifications showing I-phase particles inside.

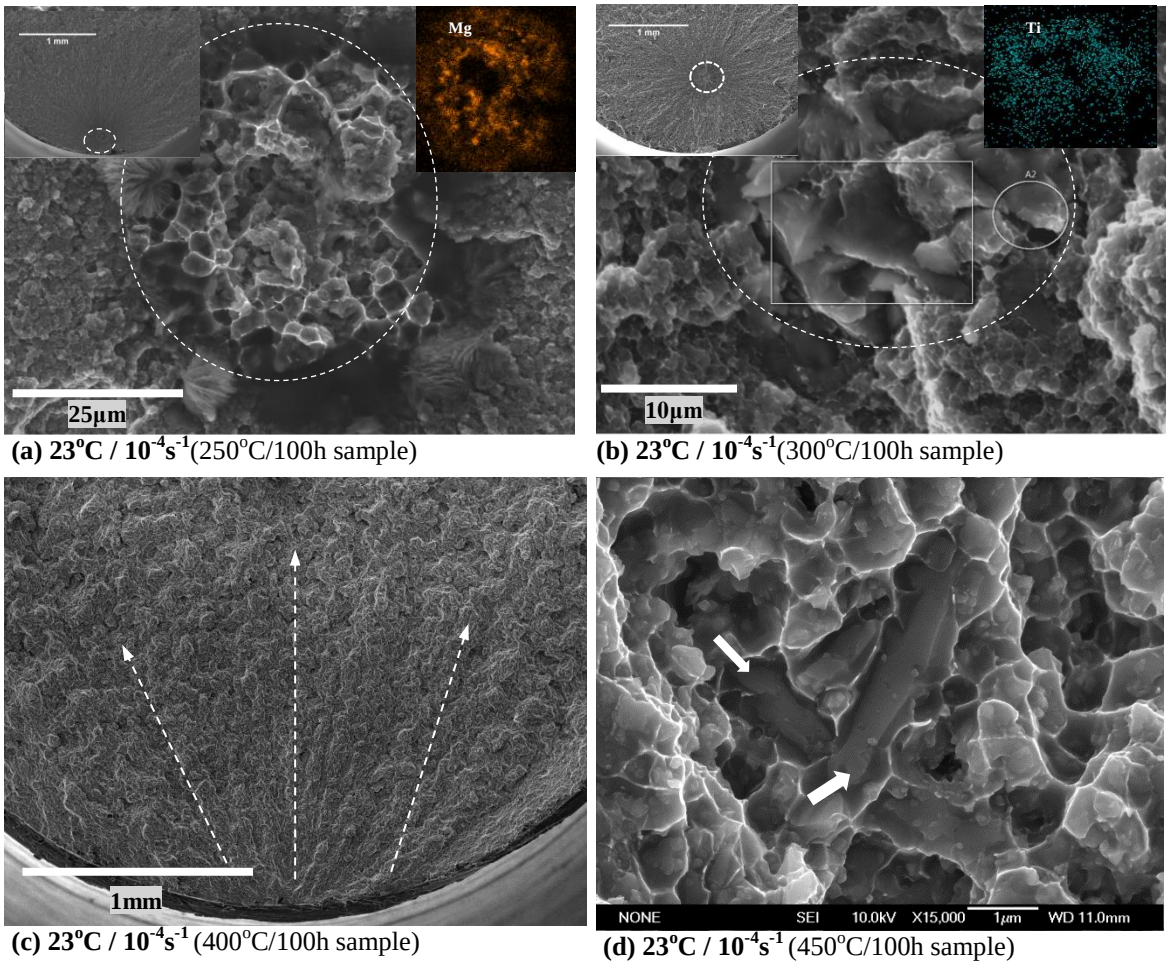

(a) 23°C / $10^{-4}s^{-1}$(250°C/100h sample)

(b) 23°C / $10^{-4}s^{-1}$(300°C/100h sample)

(c) 23°C / $10^{-4}s^{-1}$ (400°C/100h sample)

(d) 23°C / $10^{-4}s^{-1}$ (450°C/100h sample)

Figure 6.10 Fractured surfaces for samples annealed at temperature for 100hrs, tested at T= 23°C and $\dot{\varepsilon}=10^{-4}s^{-1}$: (a) 250°C/100h sample, the fracture origin from a Mg-containing Al intermetallic inclusion is marked by a dotted circle, (b) 300°C/100h sample: fracture from a Ti-containing Al intermetallic inclusion marked by a dotted circle, (c) 450°C/100h sample: the fracture started from the surface, (d) shape and size of shear dimple is inclusion dependent.

6.6 Fatigue in the NQX Alloy

Room temperature fatigue testing of the NQX alloys was conducted in high cycle fatigue (HCF) and very high cyle fatigue (VHCF) regime using frequencies of 60Hz and 20kHz respectively, at a load ratio (R) of 0.1. Additional HCF testing of a conventional Al alloy was also carried out for comparison.

6.6.1 SN curves

Figure 6.11 shows SN curves for the NQX alloy marked as squares (RT, f=60Hz), and circles (RT, f=20kHz). HCF fatigue tests were also carried out on an Al6061-T6 alloy for comparison, as shown by blue triangles in Figure 6.11. All the points in the SN curves had lower σ_{max} values than the respective yield strengths of the materials; therefore, the cycling could be assumed to be elastic during all fatigue tests[F]. Higher mean stress and high values of stress amplitude resulted in early fatigue failure. Also, higher σ_{max} caused the surface fracture initiations, whereas lower σ_{max} resulted in the internal fracture initiation[G]. The fracture initiation regions are marked on the SN curves in Figure 6.11 which are separated by an approximate vertical dotted line around ~10^5 cycles.

The fatigue strength of the NQX alloy appears much higher than the Al-6061-T6 as the NQX alloy has inherent high yield strength. All the fractures in Al6061-T6 samples initiated from the surface.

[F] Yield strength of the NQX alloy (at $10^{-2}s^{-1}$) is 545MPa at 23°C, whereas Al6061-T6 has yield strength of 275MPa.

[G] Symbols 'i' or 'S' indicate the fracture initiation point, 'i' stands for internal defect or inclusion and 'S' is for surface failure initiation, 'i+S' stands for inclusion near the surface.

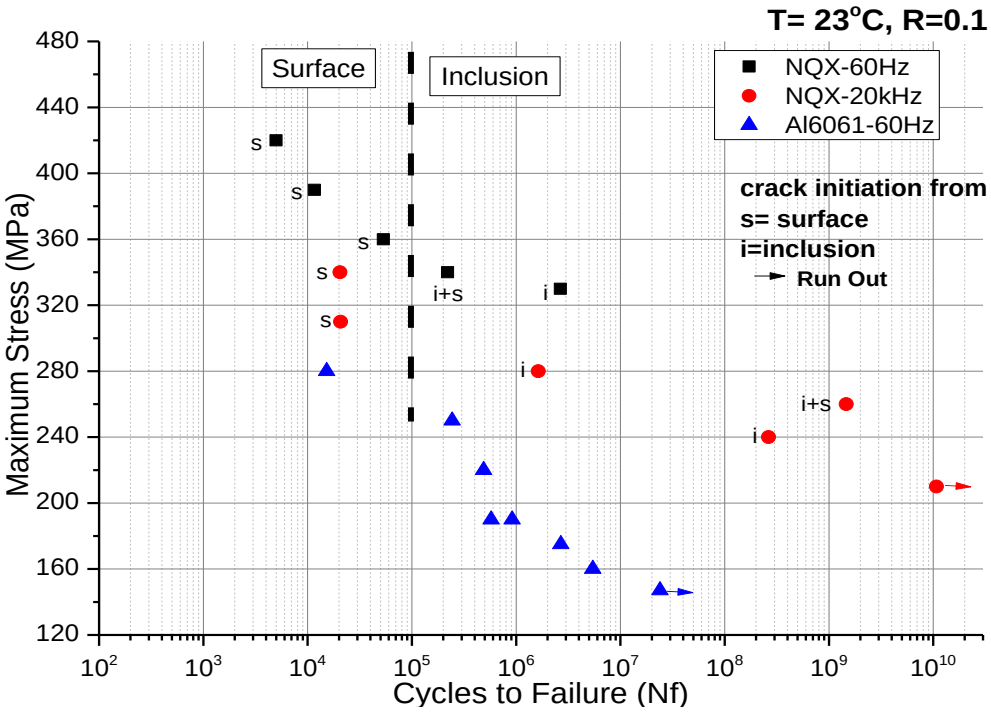

Figure 6.11 SN curves for the NQX alloy using conventional (60Hz) and ultrasonic (20kHz) frequencies. Symbols 'i' or 'S' indicate the fracture initiation point, 'i' stands for internal defect or inclusion and 'S' is for surface failure initiation, 'i+S' stands for inclusion near the surface. SN curve of a conventional alloy Al6061-T6 using conventional frequency (60Hz) is also provided for comparison.

6.6.2 Fractography

On the fatigue fractured surfaces of the NQX alloy, ridges, vein patterns and/or radial fan type features were evident, pointing towards the origin of the fracture, and a few examples are shown in Figure 6.12 (a, and c-inset). Similar to the tensile fractographs, there were predominantly two types of fracture origins **(i)** from the surface, shown in Figure 6.12 (a, b), and **(ii)** caused by the inclusions, as shown in Figure 6.12 (c, d). The inclusions were both metallic and non-metallic in nature, and their chemical composition was probed by EDX analysis. A summary of all the inclusions found in the fatigue tests is provided in Table 6.5.

Unlike the tensile fractographs, the fractured surface could be divided into three zones namely (a) overload failure zone (b) fatigue failure zone and (c) transition zone. The zones, their microscopic features and the figure references representing these zones are provided in Table 6.4.

Table 6.4 Types of zones and microscopic features observed in fatigue samples.

Zone	Microscopic feature	Reference Figure No.
Overload failure zone	Area is away from fracture origin, plastic deformation is visible, tiny dimples contain I-phase particles	Figure 6.12 (a, c) and (f-left)
*Fatigue failure zone	Starts from the fracture origin. Does not show plastic deformation, it has a relatively smooth area without dimples. The zone appears in the form of a 'fisheye' if there is inclusion at the centre.	Figure 6.12 (d) and (f-right)
Mixed or transition zone	A region of up to several tens of microns wide present in between fatigue failure and overload failure zones and contains features from both zones.	Figure 6.12 (e)

* The fatigue failure zone appears in the form of a 'fisheye' when there is an inclusion at it's centre, in that case, it has also been referred as 'fisheye' region.

The fatigue crack initiated from either surface or inclusion propagates to form a 'fatigue failure zone' which has a flat surface with no visible plastic deformation or shear dimples. When fatigue failure zone contained inclusion at the origin, an optically dark 'fisheye' appearance could be observed. Outside this 'fisheye' or the fatigue failure zone, an overload failure zone was observed which had shear dimples similar to the tensile fractographic surfaces. In between these two regions, a transition region existed of up to few tens of microns which contained features from both zones. In tensile

fractures, the shear dimples started to appear next to the fracture origin, and no fatigue failure or transition zone exist.

A summary of all the fatigue tests for the NQX alloy, including test conditions, failure cycles, the origin of the crack initiation, and the chemical nature of the inclusions are provided in Table 6.5.

Table 6.5 A summary of room temperature fatigue failures.

Test Condition	Max Load (MPa)	Cycles to Failure	Crack Initiation at	Nature of Inclusion
HCF (60Hz, 23°C)	420	4986	Surface	
	390	11622	Surface	
	360	53320	Surface	
	340	220199	Subsurface (inclusion)	Ca/O/Si
	330	2.65E06	Inclusion	Fe/O
VHCF (20kHz, 23°C)	340	20432	Surface	-
	310	20738	Surface	-
	280	1.63E06	Inclusion	Si/O
	260	1.47E09	Subsurface (Inclusion)	Ca/O/Si
	240	2.63E08	Inclusion	Al/Ti/O
	210	1.07E10	Run out	-

Fractured Al6061alloy samples show a different behaviour than NQX alloy. The fracture initiated from the surface in all the samples. The fatigue crack started from the surface and progressively grew to reach a critical size which ultimately started the overload rupture at that load. The area of fatigue crack growth region was dependent on the maximum stress of the cycle, smaller the σ_{max} larger the area as seen in Figure 6.13 (a) and (b). Macroscopically the fatigue region was relatively flat and planar; microscopically it had ~3μm wide prominent fatigue striations in samples failing at a higher number of cycles as seen in Figure 6.13 (c). The overload failure region had typical shear dimples but much larger size than the NQX alloy as seen in Figure 6.13 (d).

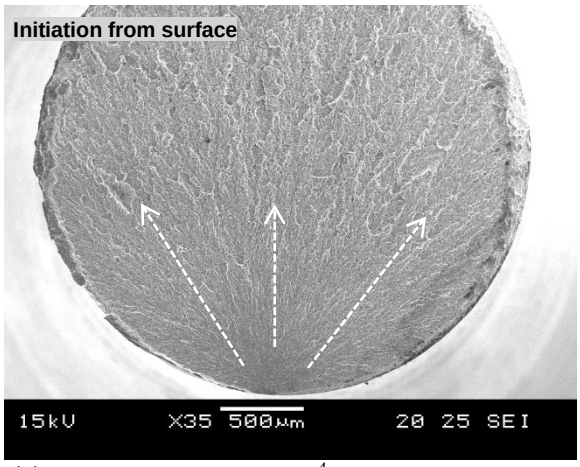

(a) σ_{max}=310MPa, N_f=2.07 x10^4

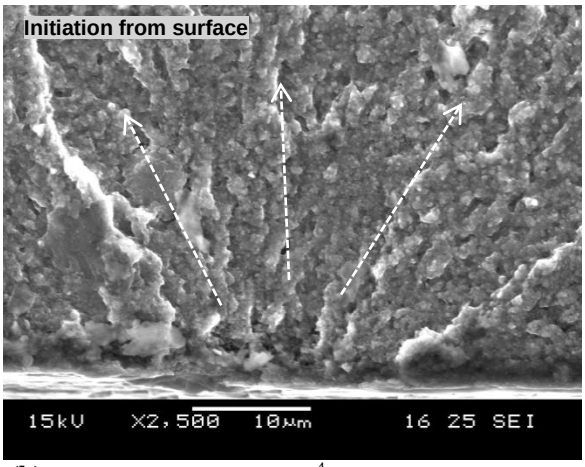

(b) σ_{max}=310MPa, N_f=2.07 x10^4

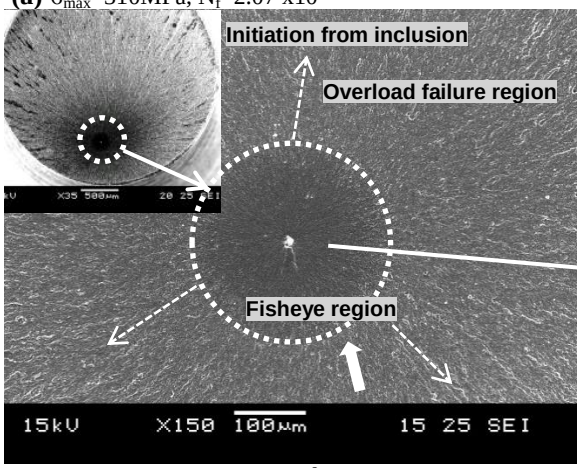

(c) σ_{max}=240MPa, N_f=2.63x10^8

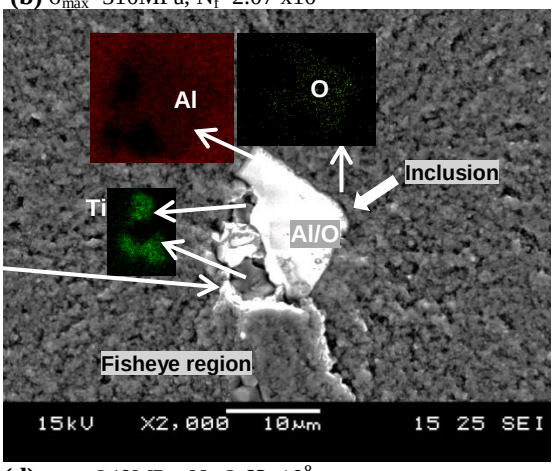

(d) σ_{max}=240MPa, N_f=2.63x10^8

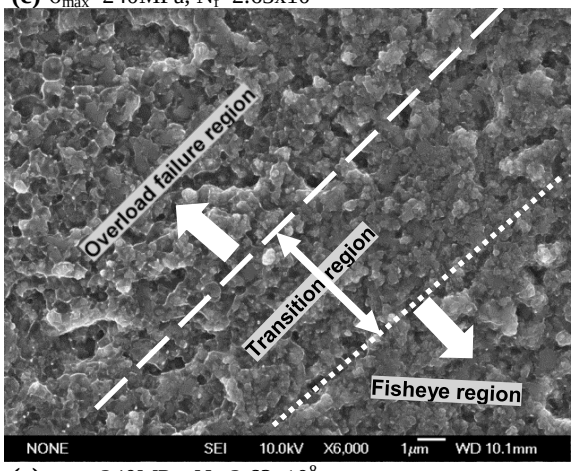

(e) σ_{max}=240MPa, N_f=2.63x10^8

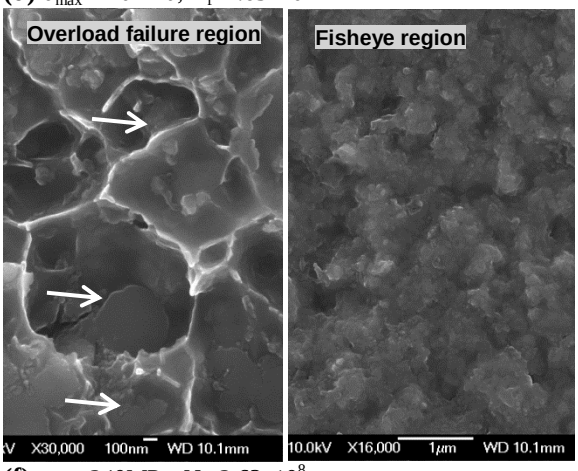

(f) σ_{max}=240MPa, N_f=2.63x10^8

Figure 6.12 SEM images for the NQX fatigue failures in the VHCF tests, f= 20 kHz, T= 23°C: (a) surface initiation, (b) surface initiation at a higher magnification, (c) the fisheye formation due to an inclusion, (d) an Al/Ti inclusion and its EDX mapping, (e) a few micron wide transition region has mixed fracture features, this zone is between fisheye and overload regions, (f) shear dimples and probable I-phase particles inside, a few are marked with arrows.

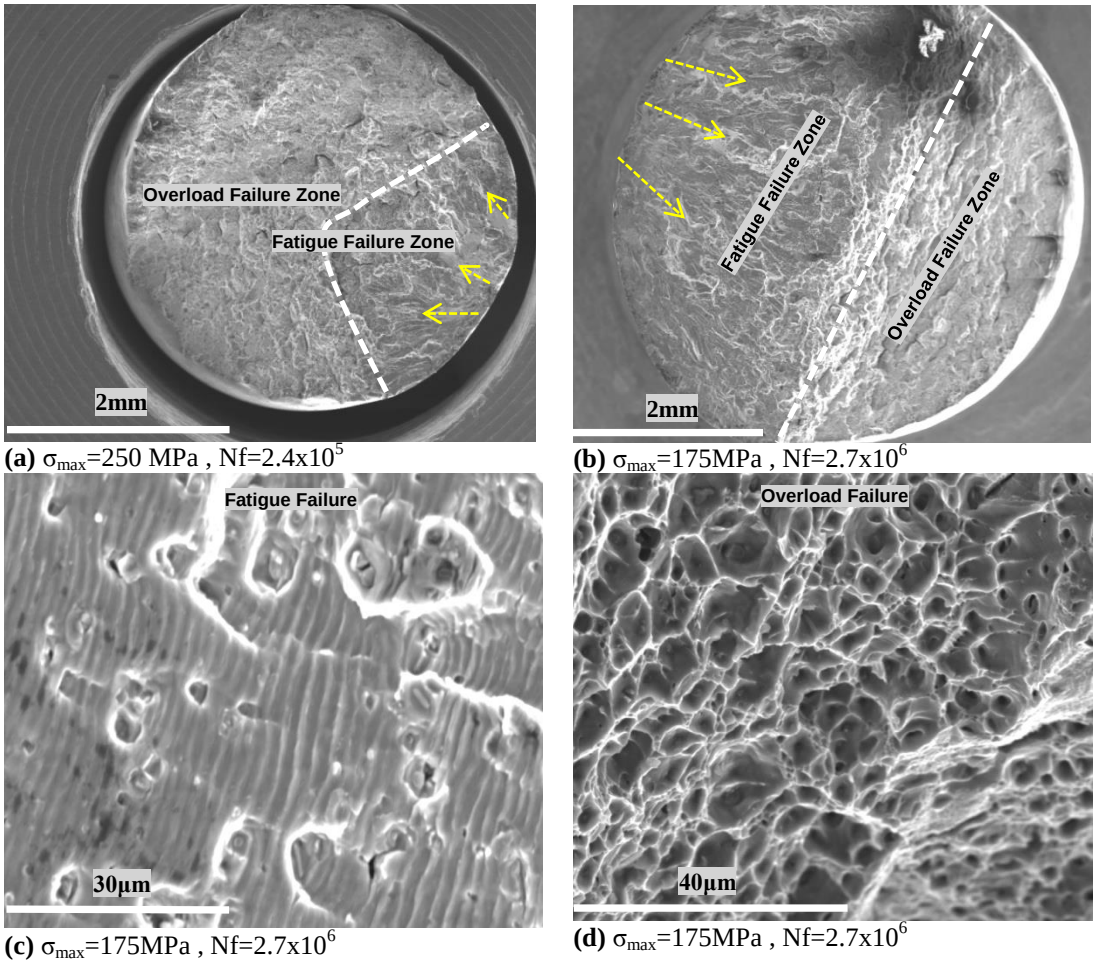

(a) σ_{max}=250 MPa , Nf=2.4x10^5

(b) σ_{max}=175MPa , Nf=2.7x10^6

(c) σ_{max}=175MPa , Nf=2.7x10^6

(d) σ_{max}=175MPa , Nf=2.7x10^6

Figure 6.13 SEM images for fatigue failure in a conventional 6061-T6 at f= 60Hz, T= 23^{o}C. The fractured surfaces show fatigue and overload failure regions: (a) overall view showing two failure zones, (b) overall view, which shows that load reduction increased the fatigue failure zone, (c) striations in fatigue failure zone, (d) typical shear dimples in overload failure zone.

6.7 Summary

Room temperature mechanical properties and density the NQX alloy in the 'as extruded' and annealed conditions were measured. A detailed discussion of the room temperature properties in connection with the microstructure and strengthening mechanisms is carried out in sections 8.1 and 8.2.

NQX alloy has a 9% higher density than Al and most of its conventional alloys. E and G of the NQX alloy are ~32% higher than pure Al. Moreover, E and G values for the NQX alloy are ~16-35% and ~23-33% higher respectively, than those observed for conventional Al alloys. Annealing temperatures above 350°C result in an increase in the E and G values of the NQX alloy. The maximum increase in E and G (~7GPa and ~2.4GPa respectively) were noted for the highest annealing temperature of 450^{o}C.

Microhardness of the NQX alloy is ~20% higher than the high strength conventional Al-alloys (Al7076-T6) whereas the UTS is comparable to the high strength conventional Al alloys. Annealing temperatures above 350°C result in a decrease in the microhardness, UTS, yield strength and the strain to failure of the NQX alloy tested at room temperature. The maximum decrease in the microhardness and UTS values was noted to be 45% and ~16% respectively corresponding to the highest annealing temperatures of 450°C.

Fracture of the NQX alloy has a ductile nature. Sometimes inclusions were found to initiate the fracture; however, those do not appear to adversely affect the elongation to failure.

Fatigue fracture is surface dominated at high stresses or low failure cycles and interior dominated at low stresses or high failure cycles. The alloy has a high fatigue strength.

References

ASM (1990) *Nonferrous Alloys and Special-Purpose Materials, vol. 2. ASM International, Materials Handbook*: ASM International.

Chlupova, A., Chlup, Z. and Kruml, T. (2016) 'Fatigue properties and microstructure of quasicrystalline AlFeCrTi alloy', *International Journal of Fatigue*, 91 (1), pp. 251–256.

Chlupová, A., Chlup, Z., Kruml, T., Kuběna, I. and Roupcová, P. 'Microstructure, tensile properties and fatigue behaviour of bulk nano-quasicrystalline al alloy $AL_{93}FE_3CR_2TI_2$', *Nano Con*, Brno, Czech Republic, 21-23 September.

Gale, W. F. and Totemeier, T. C. (2003) *Smithells metals reference book*: Butterworth-Heinemann.

Hatch, J. E. (1984) *Aluminum: properties and physical metallurgy.* ASM International.

Luo, H., Shaw, L., Zhang, L. and Miracle, D. (2005) 'On tension/compression asymmetry of an extruded nanocrystalline Al–Fe–Cr–Ti alloy', *Materials Science and Engineering: A*, 409(1), pp. 249-256.

Martienssen, W. and Warlimont, H. (eds.) (2006) *Springer handbook of condensed matter and materials data*: Springer Science & Business Media.

Rounthwaite, N. J. (2012) *Development of Bulk Nanoquasicrystalline Alloys for High Strength Elevated Temperature Applications.* DPhil Thesis, University of Oxford.

Totten, G. E. and MacKenzie, D. S. (2003) *Handbook of Aluminum: Vol. 1: Physical Metallurgy and Processes.* CRC Press.

7. Mechanical Properties of the Extruded NQX Alloy at Elevated Temperatures

Elastic constants and tensile properties were measured at temperatures up to 500°C in this chapter. Additionally, fatigue behaviour at 300°C was also investigated.

Measured mechanical properties paved the way for calculating the parameters for the analysis of high temperature deformation mechanisms in the NQX alloy, which are discussed later in this chapter, and further elaborated in chapter 8.

7.1 Elastic constants at elevated temperatures

Elevated temperature graphs for E, G, and υ of the NQX alloy, which include the measurements for both the 'I-phase containing' (which is the 'as extruded' condition), and 'I-phase transformed' conditions, are shown in Figure 7.1, Figure 7.2, and Figure 7.3 respectively. E, G and υ[A] were measured from 50^{o}C to 350°C for the I-phase containing alloy ('as extruded' condition), and these are shown using 'solid symbols' in aforementioned figures. Afterwards, the same sample was heated separately at 2^{o}C/min up to 500^{o}C and held for 30mins to transform the I-phase. Subsequently the E, G and υ were measured from 50^{o}C to 500°C, for the 'I-Phase transformed' condition and shown using 'open symbols', as seen in Figure 7.1, Figure 7.2, and Figure 7.3 respectively. The values of the elastic constant measured at 20°C are also included for comparison. The transformation of the I-phase was confirmed by the XRD analysis which was performed in section 7.2.1 and shown in Figure 7.9. Further, the dynamic E, G and υ of pure Al were acquired from literature (McLellan and Ishikawa, 1987) and included alongside NQX alloy results in Figure 7.1, Figure 7.2, and Figure 7.3 for comparison.

[A] υ was calculated (not measured) from E and G using an assumption of a homogenous and isotropic solid.

It was observed that for both 'I-phase containing' and 'I-phase transformed' conditions, an increase in temperature results in a steady decrease in both the E and G values, and a steady increase in ν of the NQX alloy, as shown in Figure 7.1, Figure 7.2 and Figure 7.3 respectively. As observed in Figure 7.3, ν for the NQX alloy and pure Al[B] have similar behaviour, whereby both show a similar slightly increasing trend up to 250°C. However, beyond 250°C, pure Al shows a strong increase in ν whereas the NQX alloy does not show this behaviour.

It was also noted that E, G and υ values are increased permanently as a result of the I-phase transformation at all temperatures. For example, the elastic constant values for the 'I-phase containing' alloy at 50°C were measured to be E~90.1±0.3GPa, G~34.2±0.2GPa, and υ~0.318±0.005. The values in the 'I-phase transformed' condition increased to E~96.3±0.5GPa, G~36.1±0.2GPa and υ~0.334±0.004.

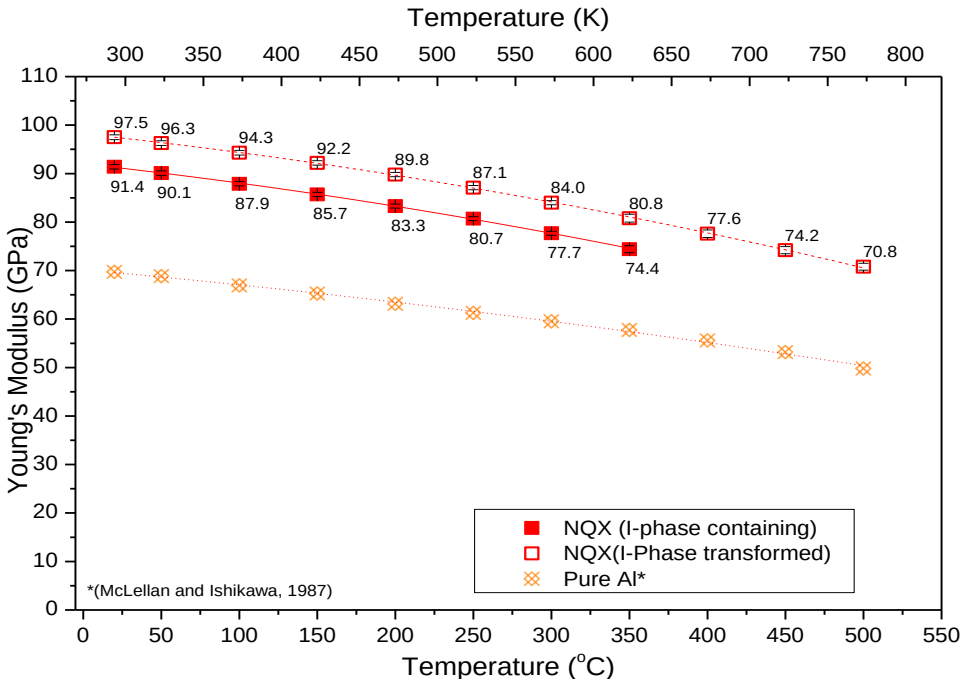

Figure 7.1 Average Young's modulus values of the NQX alloy at various temperatures, before and after the I-phase transformations, in comparison with pure Al (McLellan and Ishikawa, 1987).

[B] The work of McLellan and Ishikawa (1987) only showed E and G values. υ values of pure aluminium shown in Figure 7.3 are calculated using the relation of isotropic homogenous solid E=2G(1+ υ). An approximation of homogenous and isotropic material has also been used for finding the υ of the NQX alloy.

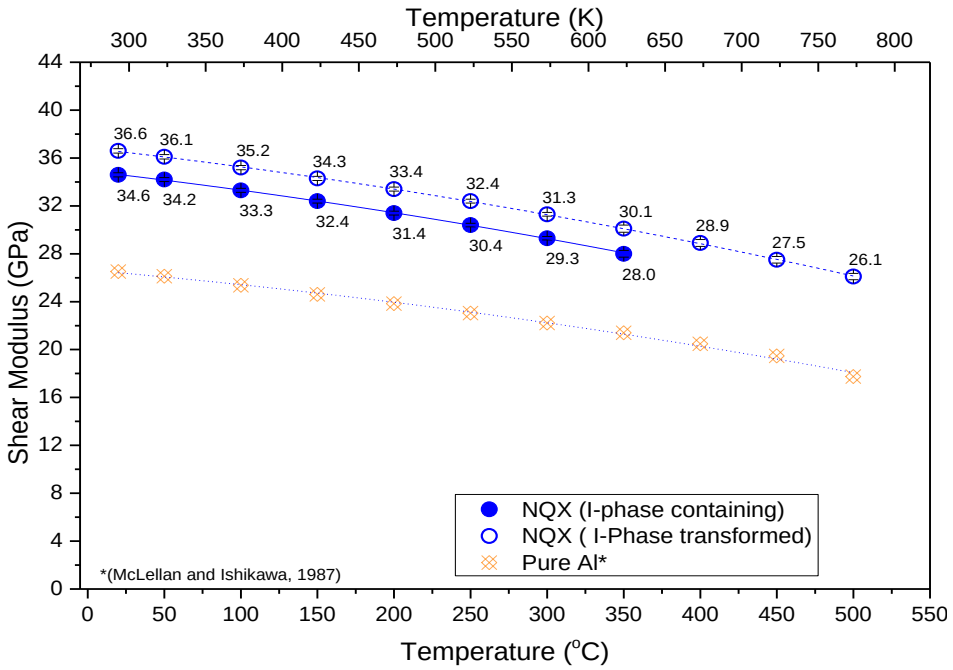

Figure 7.2 Average shear modulus values of the NQX alloy at various temperatures, before and after the I-phase transformations, in comparison with pure Al (McLellan and Ishikawa, 1987).

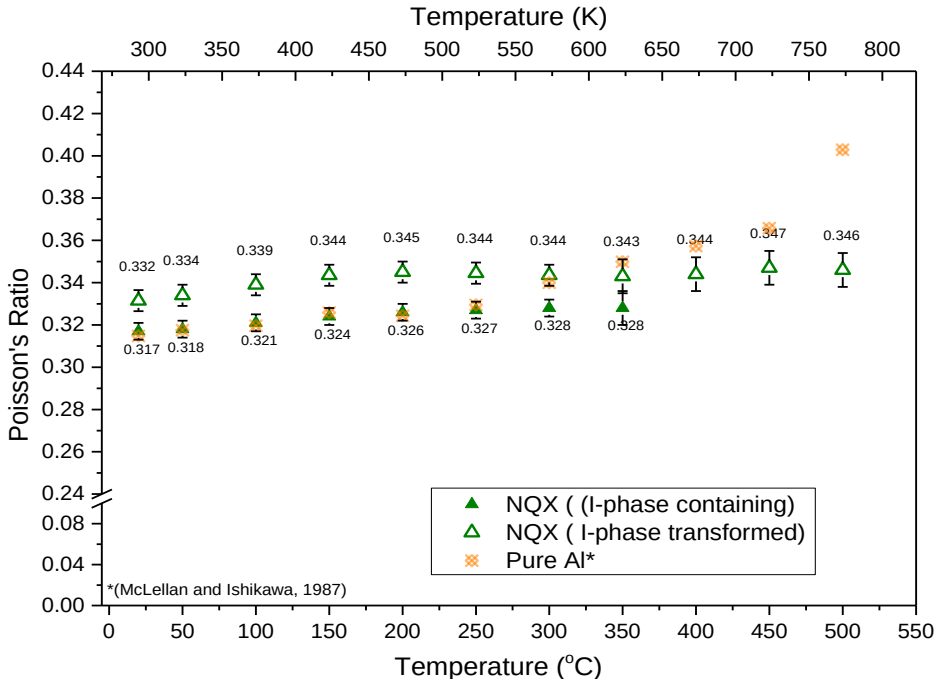

Figure 7.3 Average Poisson's ratio values of the NQX alloy at various temperatures, before and after the I-phase transformations in comparison with pure Al (McLellan and Ishikawa, 1987).

7.2 Tensile Tests

True stress-true strain curves were plotted from the tensile tests carried out at elevated temperatures (150°C, 200°C, 250°C, 300°C, 350°C and 400°C), and four strain rates ($\dot{\varepsilon}$) $10^{-2}s^{-1}$ (Figure 7.4), $10^{-3}s^{-1}$ (Figure 7.5), $10^{-4}s^{-1}$ (Figure 7.6), and $10^{-5}s^{-1}$ (Figure 7.7). Corresponding room temperature tests are also included for comparison. In addition, strain rate jump tests explained in chapter 3, were also carried out at 425°C, 450°C, 475°C, and 500^{o}C (see Figure 7.8). The general shape of the plastic flow is similar for most of the tensile curves at elevated temperatures, and the majority portion of most of the flow curves is found to be parallel to the x-axis; therefore, a steady state stress value can be assumed for those. In a true steady state the strain hardening is balanced by the recovery and an equilibrium dislocation structure can be assumed (Chateau, 2011). The relative flatness of the curves also indicates an overall low strain hardening exponent value for the alloy (measured in section 7.3). Table 7.1 provides the values of the engineering UTS, the yield strength, and plastic strain to failure.

Elevated temperature tensile strength of the NQX alloy is unmatched in comparison with conventional alloys. For example, UTS of the NQX alloy corresponding to various strain rates at 300°C is found from 290MPa to 374MPa. In comparison, the UTS of high strength Al7075-T6 and Al2618-T6 is found less than 65MPa (ASM, 1990), which is at least 4.4 to 5.7 times lower than the NQX alloy.

It was observed that in the NQX alloy, generally, decreasing strain rate or increasing temperature reduces the flow stress (Table 7.1). However, an opposite behaviour was noted at a strain rate of $10^{-5}s^{-1}$ and temperatures of 23°C and 150°C, in that the yield strength was observed to be independent of the strain rate.

10^{-2} s^{-1} tests (Table 7.1, Figure 7.4) show an increasing strain to failure as the temperature increases. However, an opposite behaviour was observed for lower strain rates, $\dot{\varepsilon}= 10^{-3}$,

10^{-4}, and $10^{-5}s^{-1}$ tests (Figure 7.5, Figure 7.6 and Figure 7.7 respectively). For these strain rates, the plastic strain to failure initially decreased with increase in temperature and then increased again for further increase in the temperature[C].

.

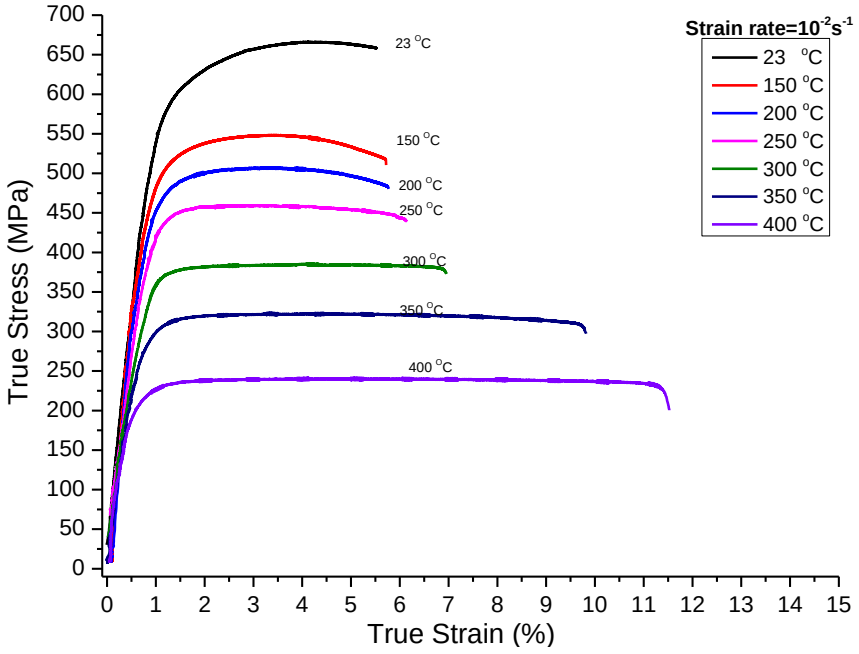

Figure 7.4 True stress-true strain graphs at various temperatures at the strain rate of $10^{-2}s^{-1}$. Room temperature tests are included for comparison.

C

Each tensile test was performed once, if the failure occurred in the gauge section. However, tensile tests corresponding to $10^{-4}s^{-1}$at 250°C, and $10^{-5}s^{-1}$at 150°C and 200°C were repeated two to three times. These tests showed abnormal jumps in stress followed by severe ductility loss, and the fractures occurred before a steady state was achieved.The results shown here are the 'best' curves for these tests which could show some plasticity. This ductility loss helped to establish the window of the 'anomalous behaviour' .

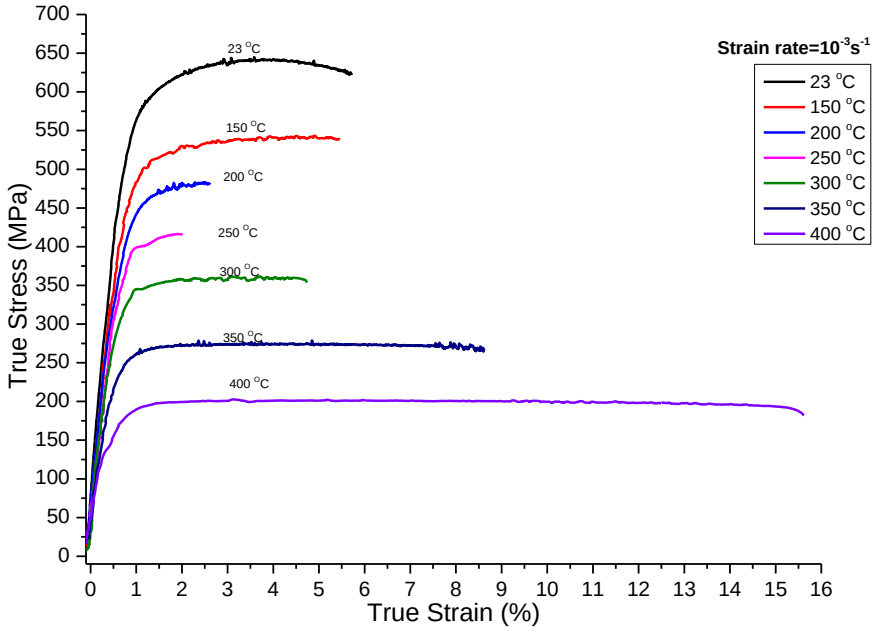

Figure 7.5 True stress-true strain graphs at various temperatures at the strain rate of $10^{-3}s^{-1}$. Room temperature tests are included for comparison.

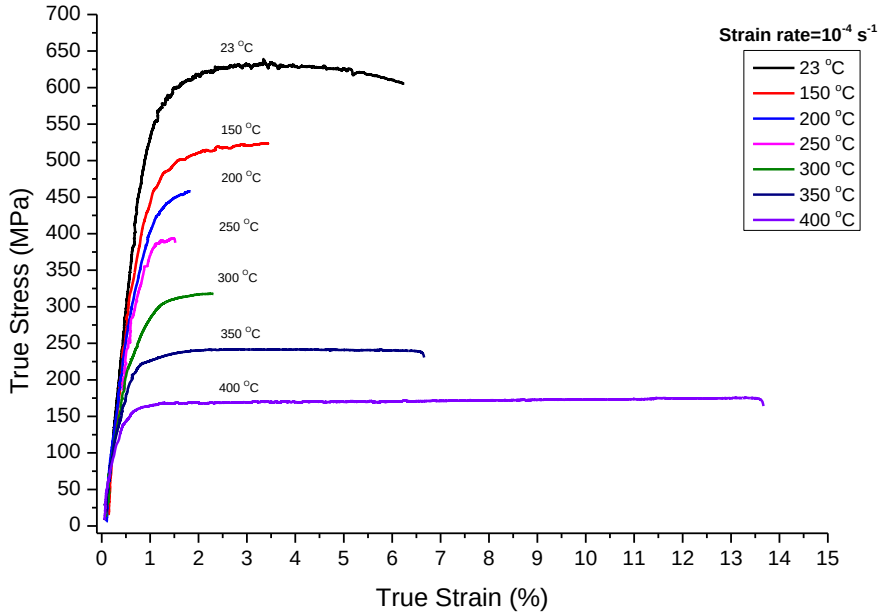

Figure 7.6 True stress-true strain graphs at various temperatures at the strain rate of $10^{-4}s^{-1}$. Room temperature tests are included for comparison.

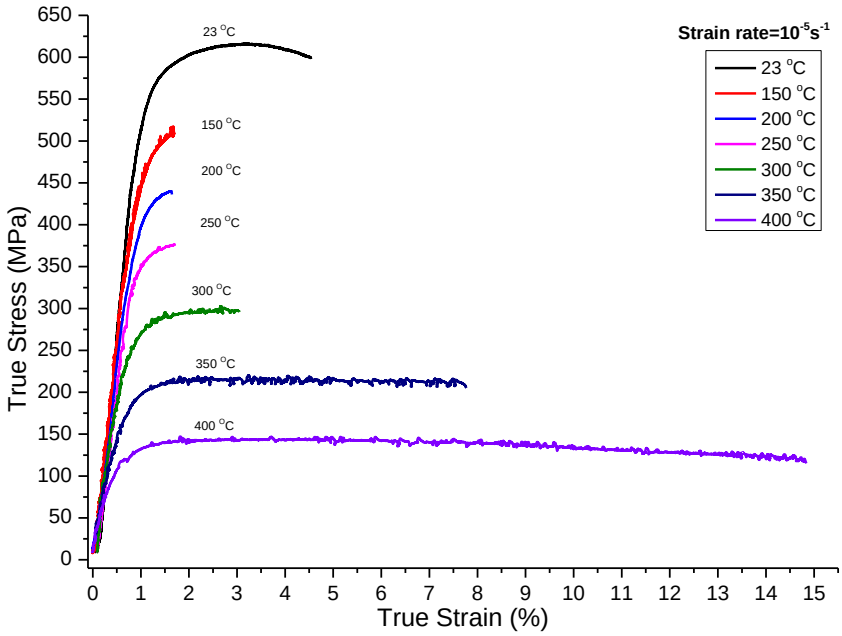

Figure 7.7 True stress-true strain graphs at various temperatures at the strain rate of $10^{-5}s^{-1}$. Room temperature tests are included for comparison.

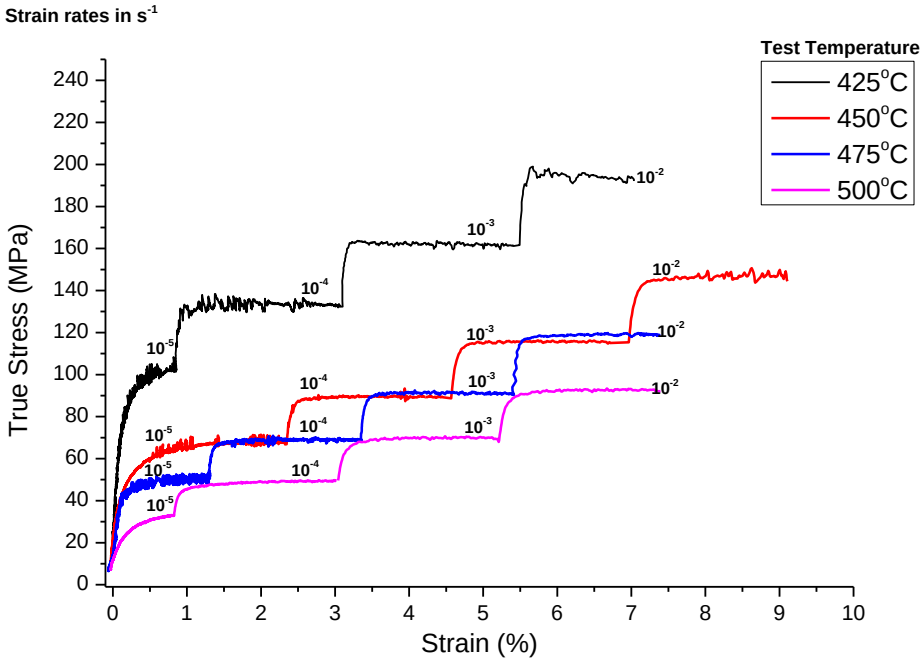

Figure 7.8 True stress-true strain graphs for the strain rate jump tests at 425°C, 450°C, 475°C and 500°C. Nominal strain rate value in s^{-1} is mentioned next to each portion of the curve.

Table 7.1 Values for the elongation to failure, yield strength, and ultimate tensile strength measured from engineering stress-engineering strain curves.

Temperature (°C) ↓	Plastic Failure Strain	Plastic Failure Strain	Plastic Failure Strain	Plastic Failure Strain	Yield Strength	Yield Strength	Yield Strength	Yield Strength	UTS	UTS	UTS	UTS
	%	%	%	%	MPa	MPa	MPa	MPa	MPa	MPa	MPa	MPa
Strain Rate (s^{-1}) →	10^{-2}	10^{-3}	10^{-4}	10^{-5}	10^{-2}	10^{-3}	10^{-4}	10^{-5}	10^{-2}	10^{-3}	10^{-4}	10^{-5}
23	4.6	5.0	6.2	3.6	545	534	528	528	640	620	612	598
150	4.8	4.6	2.4	0.9	485	471	452	454	532	519	507	500
200	4.9	1.8	0.8	0.5	450	426	415	405	493	470	450	441
250	5.3	1.2	0.5	0.7	419	388	362	348	449	406	388	370
300	6.2	4.1	1.3	2.1	352	320	280	265	374	351	318	290
350	9.4	8.2	6.0	7.2	286	247	212	187	314	267	235	210
400	11.4	16.2	13.8	15.2	197	167	150	119	233	195	165	140
	Jump Tests								**Flow stress MPa**			
425	Not applicable								186	156	133	101
450									137	111	86	67
475									112	88	68	51
500									91	65	46	31

UTS= ultimate tensile strength , The errors in strength are considered to be <0.8% (section 6.4).

7.2.1 Characterisation of the NQX alloy tested at elevated temperature between 350-500°C

It was observed in chapter 5 that the transformation of the I-phase started after 100hrs annealing at 350°C. However, this may not apply to the samples involved in tensile testing at the same temperature, as their exposure time to the elevated temperatures was only ~1.5-3 hours. Further, it was deemed important to perform XRD analysis after the elevated temperature mechanical tests in order to detect possible microstructural changes due to phase transformations. Tensile test samples from $\dot{\varepsilon}=10^{-5}s^{-1}$ [D] and T=350°C and 400°C, all strain rate jump tensile test samples (T= 425°C, 450°C, 475°C, and 500°C) and the sample used for measuring the elastic constants from 23°C to 500°C were characterised using XRD, as shown in Figure 7.9[E]. The sample nomenclature was explained in Table 3.1.

Short duration temperature exposure during tensile tests does not cause transformation in the 350°C/Tensile sample. However, in the 400°C/Tensile sample, some XRD peaks (Al_3Ti, θ_D-$Al_{13}(Fe,Cr)_{2-4}$, $Al_{13}Cr_2$) are visible, whereas several small peaks (corresponding to $Al_{13}Fe_4$, Al_6Fe, and a few $Al_{13}Cr_2$ peaks) are still forming, meaning that the I-phase transformation has started in the sample. In 425°C/Tensile, 450°C/Tensile, 475°C/Tensile, 500°C/Tensile, and 500°C/Elastic samples, the XRD patterns match with the 400°C/100hrs annealed sample (reproduced from chapter 5) in which I-phase transforms into metastable (Al_6Fe) and stable ($Al_{13}Cr_2$, $Al_{13}Fe_4$, Al_3Ti) intermetallics.

Microhardness of all samples involved in tensile testing above 350°C was measured at room temperature as shown in Figure 7.10. Microhardness of 350°C/Tensile sample is 195μHV_{500} which is equal to the 'as extruded' alloy. The microhardness values for the

[D] Tests at $10^{-5}s^{-1}$ are the slowest. Total exposure time is the soaking time + testing time. Generally, the test standard ASTM-E21 recommends a minimum 20min of soaking time, but in an effort to better stabilise the microstructure a soaking time of ~1.25 hour was used in all of the samples.

[E] Nomenclature of these samples is 350°C/Tensile, 500°C/Elastic etc, which is explained in Table 3.1.

425^{o}C/Tensile, 450^{o}C/Tensile, 475^{o}C/Tensile, and 500^{o}C/Tensile samples are found close to those observed for the long duration annealed 400^{o}C/100h sample (174μHV$_{500}$). An elevated temperature exposure of up to 350^{o}C during mechanical tests does not cause any change in either the microstructure or the properties of the NQX alloy.

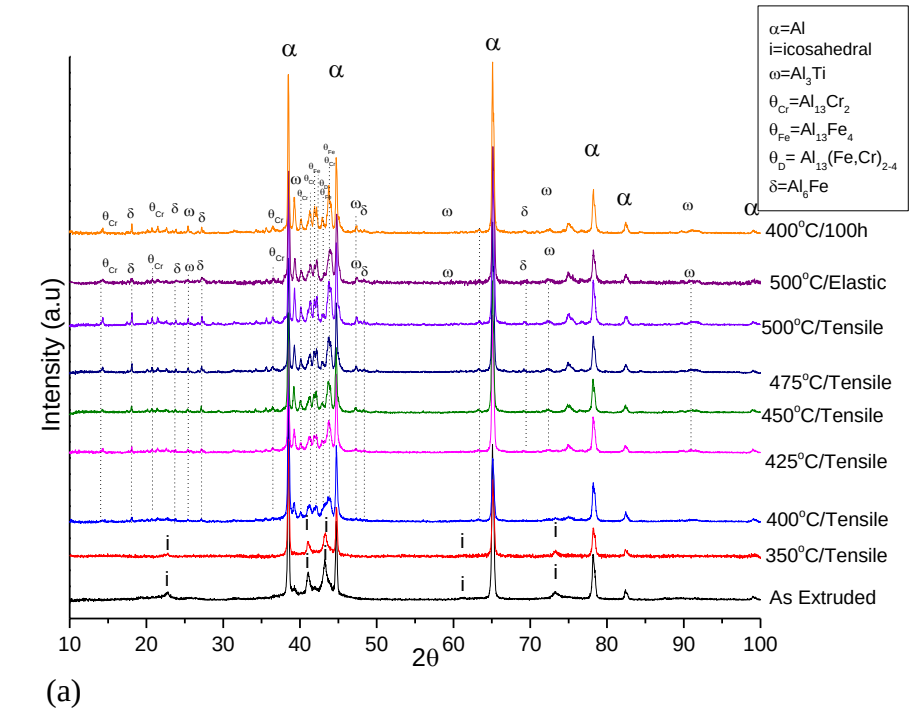

(a)

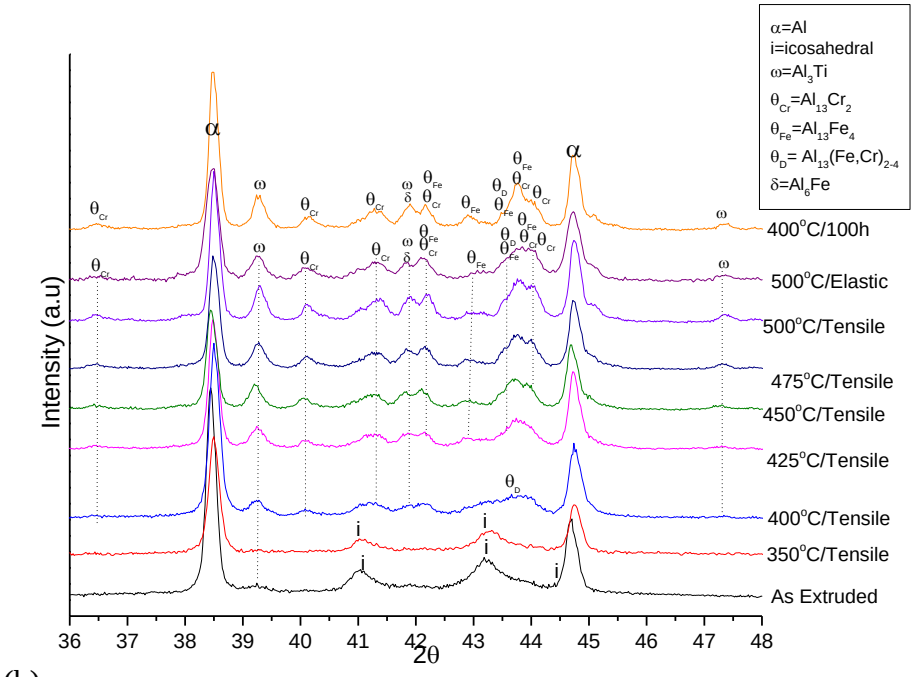

(b)

Figure 7.9 XRD patterns of the 'as extruded' bar, and samples tensile tested at temperatures between 350°C to 500°C; additionally, XRD of the 400°C/100h sample has been provided for comparison: (a) overall view (10-100°), (b) magnified view (36-48°).

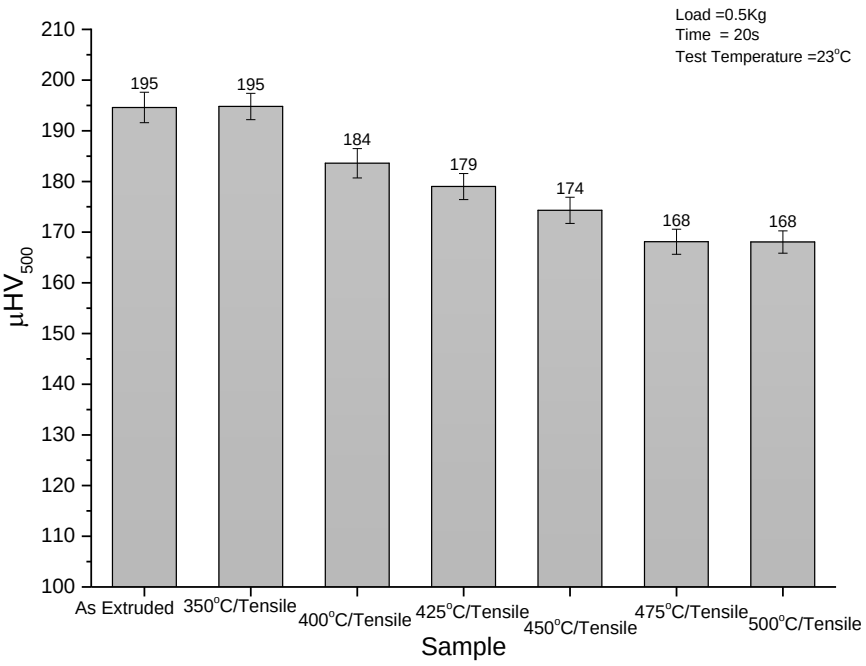

Figure 7.10 Comparison between the room temperature microhardness of the 'as extruded' bar with samples tensile tested at temperatures between 350-500°C.

7.2.2 Fractography of tensile tests conducted at elevated temperatures

Figure 7.11 shows a few examples of the fractured surfaces from the elevated temperature tensile test samples. The fracture initiations found in the fractographic analysis of the elevated temperature tensile samples were similar to the room temperature samples (section 6.5). However, 'Sn' was observed to be the major inhomogeneity in the elevated temperature samples which could not be found in the fractographs of the room temperature samples. Figure 7.11 (a, b) shows the fracture surface for T=150^{o}C and $\dot{\varepsilon}=10^{-5}s^{-1}$ in which the fracture initiation pointed towards an apparent 'pore' of ~2μm diameter. EDX analysis inside the pore and the surrounding area indicated the presence of 'Sn' (Figure 7.12); however, no large Sn particle was observed. In Figure 7.11 (a, right inset), a relatively flat area of ~100μm diameter (marked with a red dotted circle) was observed around the fracture origin. The area (termed as 'Sn affected area') was found without any shear dimples, which was unlike the observations made in case of all other inclusions.

Outside this 'Sn affected area', the fractured surface has typical shear dimples. Probably, the 'pore' was originally a small 'Sn' particle which softened and melted at elevated temperatures ($T_{melting, Sn}$ =232^{o}C), and caused the fracture initiation.

Figure 7.11(c) shows a fracture surface for T=250^{o}C and $\dot{\varepsilon}$=10^{-4}s^{-1}. EDX mapping showed a ~20μm size Sn/Pb/Zn alloy particle as the fracture initiation point, indicated by a dotted circle. Shear dimples were observed on the complete fracture surface and their sizes were dependent on the size of particles present inside. Figure 7.11 (c, inset) is an example of a small size ~70nm dimple (marked by an orange dotted circle) containing a tiny particle.

Figure 7.11 (d) shows a fracture surface for the T=350^{o}C and $\dot{\varepsilon}$=10^{-3}s^{-1} tensile sample, where it can be seen that the fracture initiated from a ~15μm Ti-containing aluminium intermetallic inclusion. Strain rate jump tests have the highest testing temperatures in this work, from 425^{o}C to 500^{o}C. The 425^{o}C jump test fractured sample can be observed in Figure 7.11 (e, f). In these samples, the fracture(s) initiated from the surface and dimples were observed to be up to a few microns large, containing several particles, as seen in Figure 7.11 (f). Cracks and cavitation were observed on the fracture surfaces, marked by arrows in Figure 7.11 (d-inset, e and f). The cavitation was found to be more frequent in the samples tested above ~350^{o}C.

Figure 7.12 shows the EDX spectra for a few Al/Fe, Al/Ti and Sn-containing inclusions.

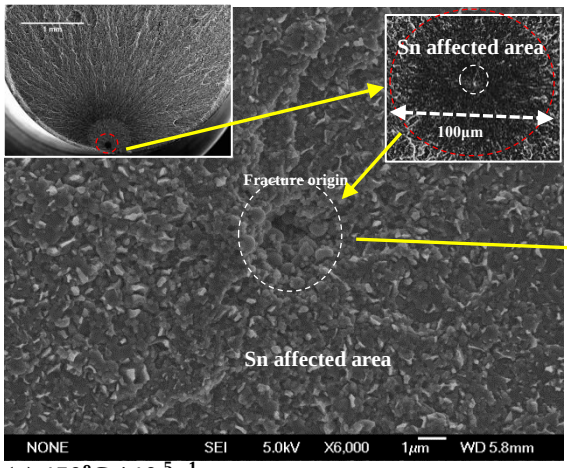

(a) 150°C / $10^{-5}s^{-1}$

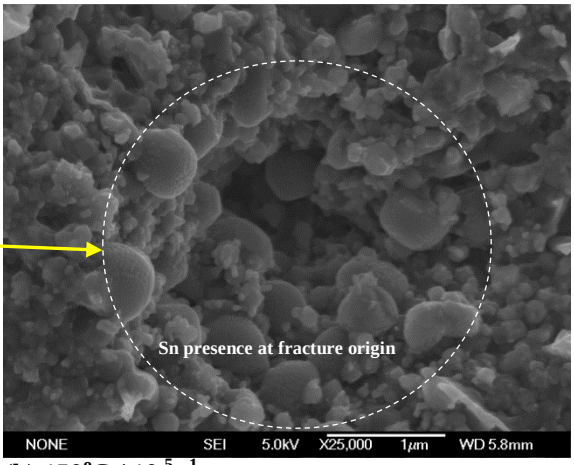

(b) 150°C / $10^{-5}s^{-1}$

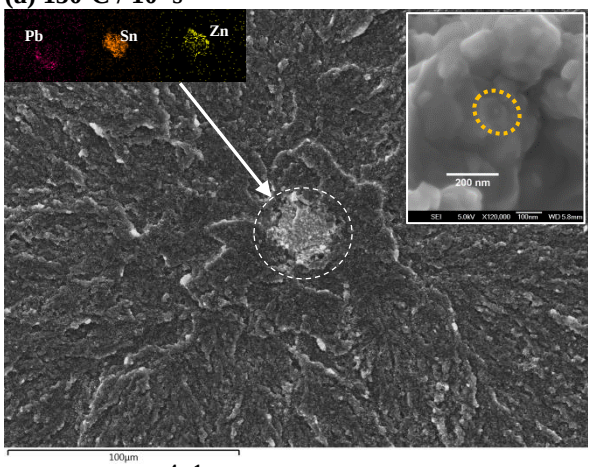

(c) 250°C / $10^{-4}s^{-1}$

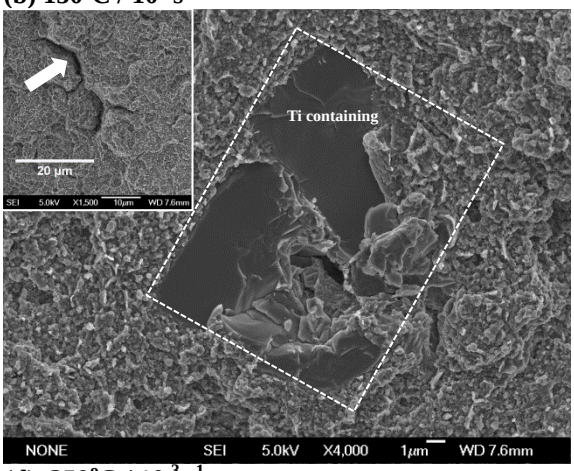

(d) 350°C / $10^{-3}s^{-1}$

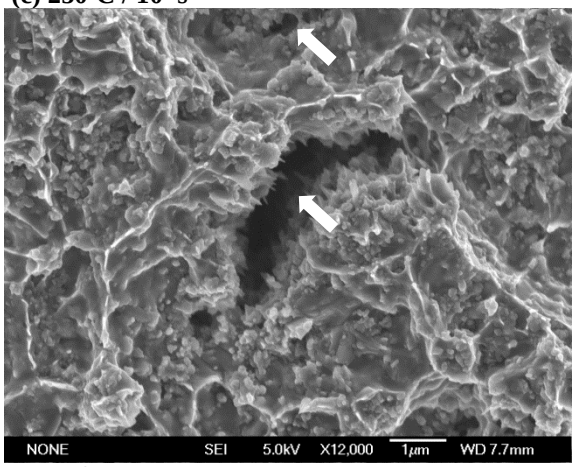

(e) 425°C / jump tests

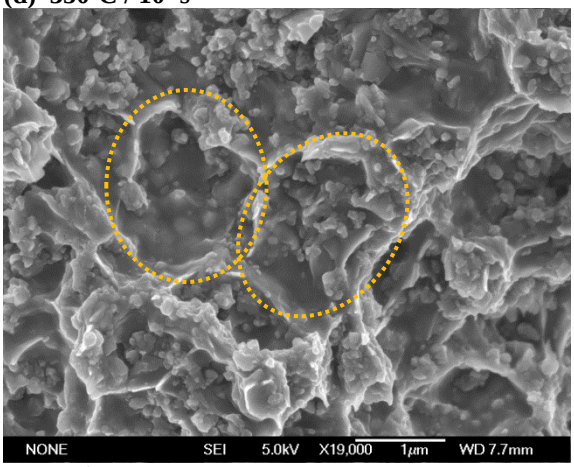

(f) 425°C / jump tests

Figure 7.11 Fractured surface of the sample tested at various temperatures and strain rates: (a, b) T= 150°C and $\dot{\varepsilon}=10^{-5}s^{-1}$, fracture initiation from an apparent pore in the center which previously contained 'Sn', (c) T= 250°C and $\dot{\varepsilon}=10^{-4}s^{-1}$, a likely fracture initiation from a Sn/Zn/Pb particle, inset figure shows <70nm diameter shear dimple, (d) T= 350°C and $\dot{\varepsilon}=10^{-3}s^{-1}$, fracture initiation from a Al/Ti intermetallic, (d, inset) possible cracking or cavitation, marked by an arrow, (e, f) fractured surface of sample tested with strain rate jump tests at high temperatures strain rate jump test T=425°C, (e) cavitation and cracking (f) dimple coalescence contains several particles.

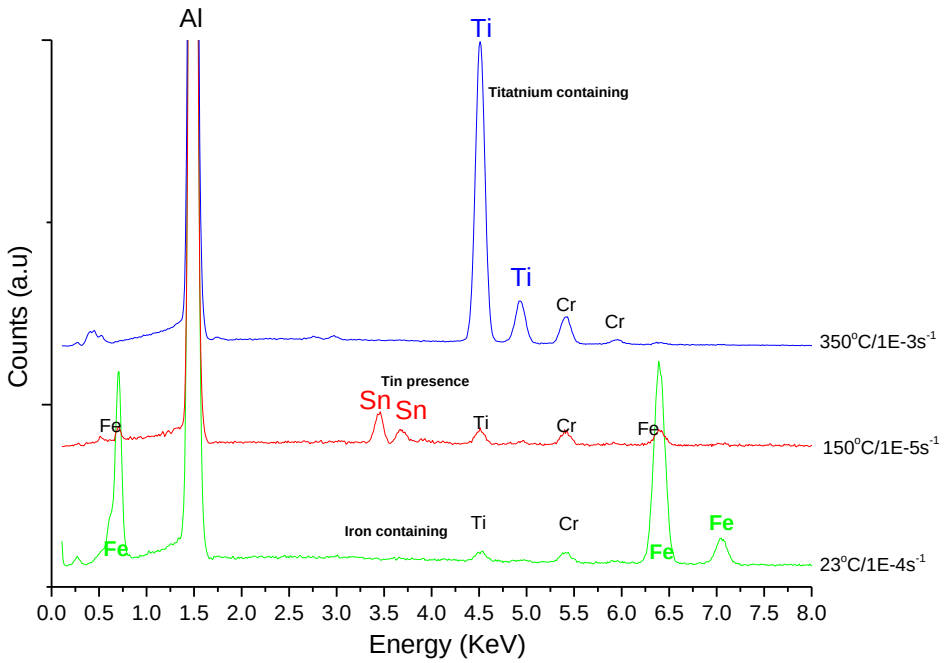

Figure 7.12 Examples of some EDX spectra from inclusions present inside the fractured surfaces causing the fracture initiations.

7.3 Fatigue in the NQX Alloy

HCF testing of the NQX alloys was also carried out at 300°C at a load ratio (R) of 0.1 and at a conventional frequency (40Hz). 300°C was chosen as the testing temperature because the NQX alloy is thermally stable until 300°C even after long exposures (section 5.3). Moreover, it is a temperature at the extreme upper end of any aluminium alloy based thermo-mechanical application, as discussed in section 2.2.

7.3.1 SN curves

Figure 7.13 shows SN curves for the NQX alloy which are marked as diamonds (300°C, f=40Hz). An SN curve of an elevated temperature conventional Al alloy (2618-T651) at 260°C by Kaufman (2008) is also shown for comparison. The yield strength of the NQX alloy at T=300°C and $\dot{\varepsilon} = 10^{-2}s^{-1}$ is 352MPa which is higher than all σ_{max} values of the SN

curve and so the cycling can be considered to be elastic. Higher mean stress and high values of stress amplitude resulted in early fatigue failure.

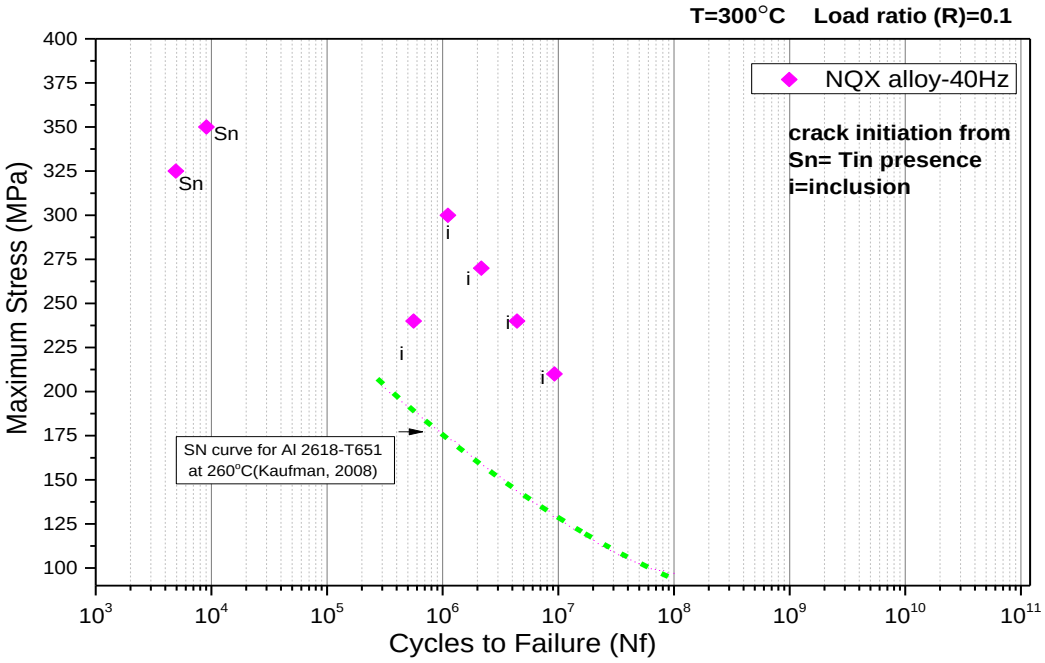

Figure 7.13 Comparison of the SN curves for the NQX alloy at 300°C. SN curve of an elevated temperature conventional Al alloy 2618-T651 tested at 260°C, R=0.1, extracted from Kaufman (2008) is also provided.

7.3.2 Fractography

The fracture origin in high temperature fatigue was only caused by internal inhomogeneities regardless of the applied load. This was unlike the room temperature fatigue which contained failures from both the surface and the inclusions.

Similar to the room temperature tests, the 'overload failure zone' Figure 7.14 (a-inset, b-inset), 'fatigue failure zone' (Figure 7.14 (b-inset, c, e)) and 'transition zone' (Figure 7.14 (b)) were observed in the fractured samples. 'Fisheye' appearance was observed around all the inclusions, and outside the 'fisheye' the overload failure zone containing the shear dimples was observed. Overall, the fractured surfaces were observed to be less flat in the 300°C HCF samples than those found in the room temperature fatigue tests. In the 300°C

HCF tests, the average dimple size was slightly larger and contained a number of I-phase particles inside, as shown in Figure 7.14(b inset).

The inclusions were found to be: (i) molten Sn, other metals or intermetallics (Al/Ti/O), and (ii) non-metallic (Si/Ca/O), as revealed by the EDX analysis. The molten Sn was involved in two of the failures corresponding to the samples at the highest stresses/or the lowest N_f. The Sn was observed to be spread around the point of origin as seen in Figure 7.14(a). This was similar to the observations in the most of the high temperature tensile test samples (section 7.2.2). No other fatigue sample failed due to Sn. A summary of all the inclusions found in the fatigues tests is provided in Table 7.2.

Table 7.2 Summary of fatigue failures in the present study.

Test Condition	Max Load (MPa)	Cycles to Failure	Crack Initiation at	Nature of Inclusion
HCF (40Hz, 300^{o}C)	350	9074	Internal	Sn (molten)
	325	4972	Internal	Sn (molten)
	300	1.11E6	Inclusion	Si/O
	270	2.154E6	Inclusion	Ti/O
	240	4.398E6	Inclusion	Si/O/Ca
	240	561324	Inclusion	Al/Ti/O
	210	9.264E6	Inclusion	Al/Ti

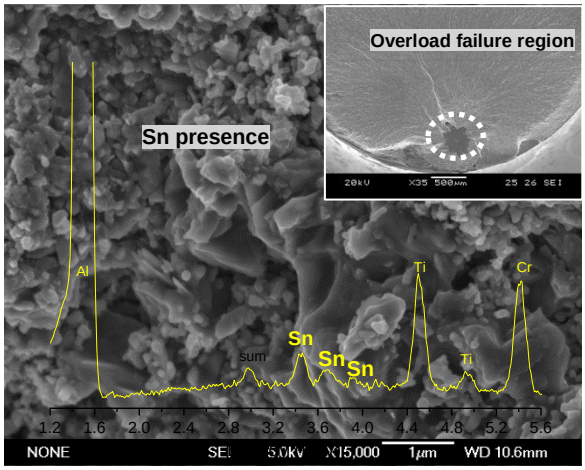

(a) σ_{max}=350MPa , N_f=9070

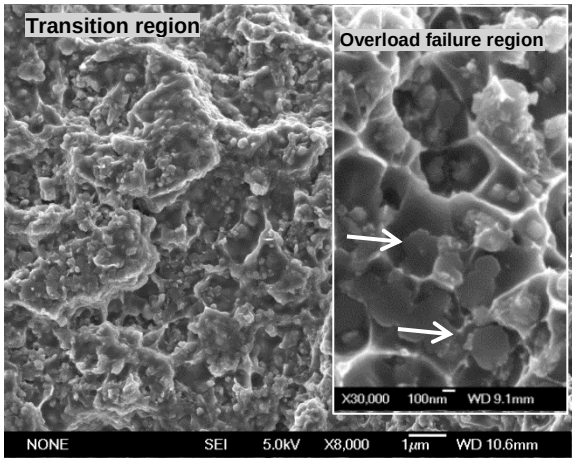

(b) σ_{max}=350MPa , N_f=9070

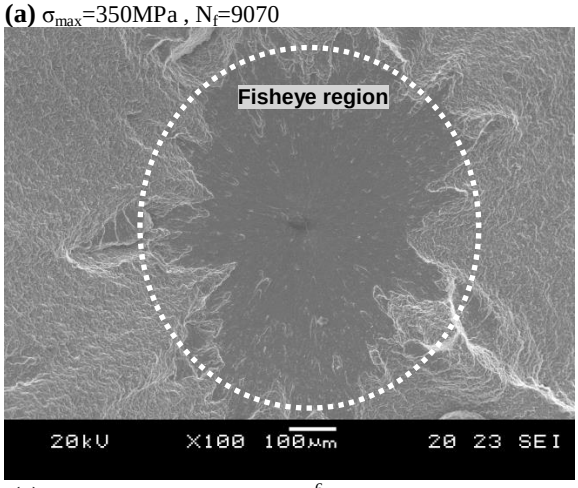

(c) σ_{max}=300MPa , N_f=1.16x10^6

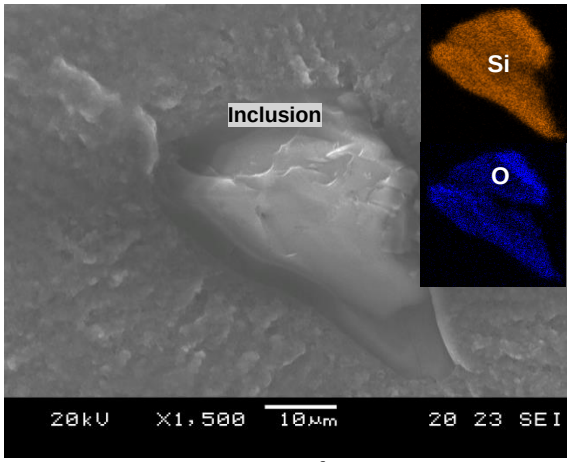

(d) σ_{max}=300MPa , N_f=1.16x10^6

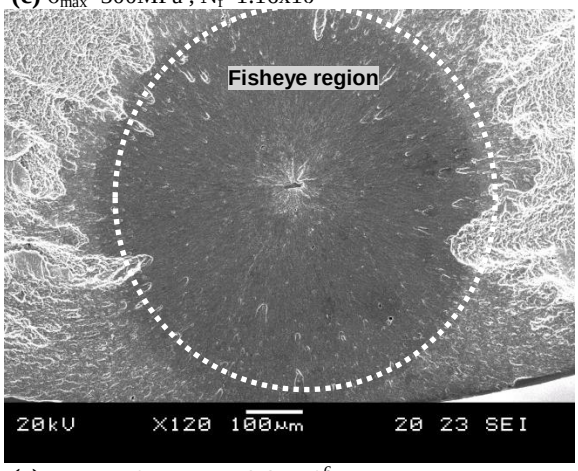

(e) σ_{max}=210MPa , N_f=9.64x10^6

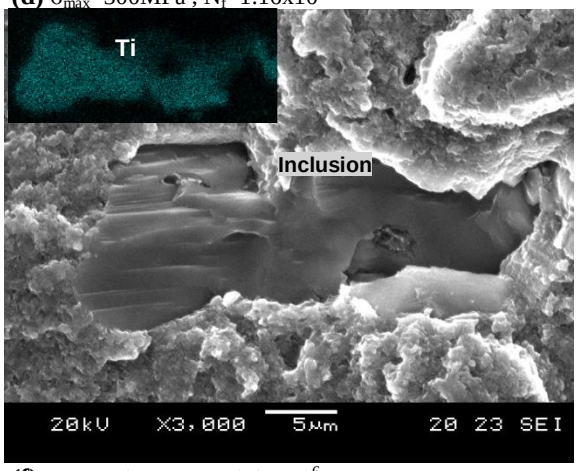

(f) σ_{max}=210MPa , N_f=9.64x10^6

Figure 7.14 SEM images for the NQX fatigue failures in the HCF tests, f= 40Hz, T= 300°C: (a) Sn traces found at the origin of the fracture as shown by the overlayed EDX spectra, the inset figure shows the overall fracture surface having a fisheye marked with dotted circle, whereas the rest was the overload failure zone, (b) a larger transition region with the mixed fracture features, the inset figure shows the overload failure region containing probable I-phase particles marked with arrows , (c) the fisheye due to the inclusion, (d) a Si/O inclusion and its EDX mapping, (e) a fisheye due to an inclusion, (f) Ti-containing Al intermetallic inclusion and its EDX mapping.

7.4 Discussion

7.4.1 Elastic constants

In both the 'I-phase containing' ('as extruded') and the 'I-phase transformed' condition the NQX alloy shows at least 30% higher values of E and G than pure Al between 23-350°C. The transformation of the I-phase results in ~>6.5% and >5.7% permanent increase in the E and G values respectively, at all temperatures in comparison to the 'I-phase containing' ('as extruded') condition.

With increasing temperature, both the NQX alloy and pure aluminium show a similar decreasing trend in their E and G values. The temperature behaviour of elastic constants of the NQX alloy, both in the 'I-phase containing' and the 'I-phase transformed condition', was approximated by fitting straight lines[F] in Figure 7.1and Figure 7.2 and using equations of the form (Frost and Ashby, 1982) given below.

$$E(T) = E_0 + \frac{dE}{dT}(T - 293) \qquad \textbf{Eqn. 7.1}$$

$$G(T) = G_0 + \frac{dG}{dT}(T - 293) \qquad \textbf{Eqn. 7.2}$$

Where T is the temperature in K, E(T) is the Young's modulus at temperature T, E_o is the Young's modulus at 293K, dE/dT is the slope of E vs T graph. Also, G(T) is the shear modulus at temperature T, G_o is the shear modulus at 293K, dG/dT is the slope of G vs T graph. The equations and the values of the slopes were calculated and provided in Table 7.3.

[F] Behaviour can also be approximated by fitting a 2nd order polynomial (not shown here).

Table 7.3 Parameters used for simple linear fitting for the temperature behaviour of E and G of the NQX alloy.

	Linear model, E(T) in GPa	**Moduli at 293K (GPa)**	**Reference**
Elastic Modulus	$E(T)=E_0+dE/dT(T-293)$		
Constants	dE/dT	E_0	
'I-phase containing' sample	-4.85E-02	92.0	This work
'I-phase transformed sample'	-4.78E-02	97.5	
Pure Al*	-3.70E-02	69.7	(McLellan and Ishikawa, 1987)
Shear Modulus	$G(T)=G_0+dG/dT(T-293)$		
Constants	dG/dT	G_0	
'I-phase containing' sample	-1.88E-02	34.6	This work
'I-phase transformed sample'	-1.91E-02	36.6	
Pure Al*	-1.54E-02	26.0	(McLellan and Ishikawa, 1987)

7.4.2 Strain hardening

Plastic true stress-true strain behaviour can be modelled using Hollomon, Ludwick, Swift, or Voce relations (Chateau, 2011). The Hollomon equation (Eqn. 7.3) is the most widely used and the simplest relation providing information about the stretch formability of metals and alloys (Dieter and Bacon, 1986)

$$\sigma = K\varepsilon_p^{n_{sh}}\Big|_{T,\dot{\varepsilon},} \quad \text{or} \quad n_{sh} = \frac{\log\sigma}{\log\varepsilon_{plastic}}\Big|_{T,\dot{\varepsilon}} \qquad \textbf{Eqn. 7.3}$$

Where σ is the true stress, ε_p is the true plastic strain, K is the strength coefficient which is the strength value at ε=1, and n_{sh} is the strain hardening exponent. n_{sh} is an important material parameter whereby in tensile loads, higher n_{sh} values are known to delay necking (Ma, 2006).

Figure 7.15 (a) shows the strain hardening coefficients obtained by plotting the true stress (till UTS) vs true plastic strain on a log-log scale. Figure 7.15 (b) shows the values of strength coefficient (K) at various temperatures.

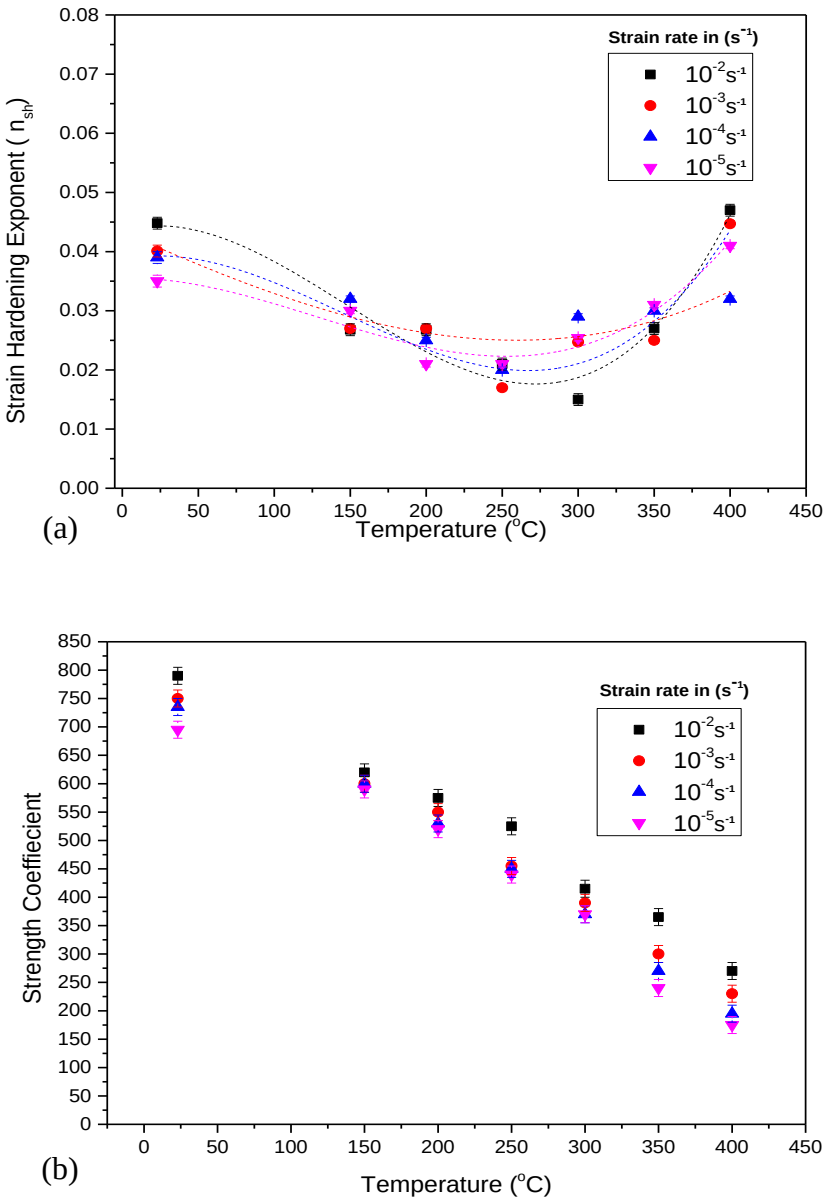

Figure 7.15 Strain hardening parameters for the NQX alloy at various strain rates and temperatures: (a) strain hardening exponent (n_{sh}), (b) strength coefficient (K)

The n_{sh} values have been found to be between ~0.02-0.05 in the test temperature range of 23°C to 400°C, at various strain rates as seen in Figure 7.15 (a). A room temperature

comparison of n_{sh} and K values of the aluminium alloys with the NQX alloy is provided in Table 7.4.

Table 7.4 Room temperature strain hardening parameters for Al alloys.

Alloy	n	K (MPa)	Reference
1100-O	0.2	180	(Kaufman, 2008)
2014-T6	0.06	600	
2024-T851	0.05	590	
5052-O	0.13	210	(Kuhn and Medlin, 2000)
6061-O	0.2	205	
6061-T6	0.05	410	
7075-O	0.17	400	
7075-T6	0.11	860	
NQX	~0.04-0.05	~700-800	This work

Generally aluminium alloys have high stacking fault energy and as a result, cross slip can take place easily. Therefore, Al alloys do not significantly strain-harden (Dieter and Bacon, 1986). Further, ultrafine grained materials show smaller strain hardening than the coarse grained counterparts (Pineau et al., 2016). The presence of the second phase also reduces the strain hardening ability. These could be the contributing factors for having a low n_{sh} value in the NQX alloy under study.

7.4.3 Strain rate hardening

Higher strain rates cause higher flow stress and Eqn. 7.4 explains the relation between the strain rate and the true stress (Dieter and Bacon, 1986).

$$\sigma = C\dot{\varepsilon}^{m}\Big|_{\varepsilon,T} \; or \; m = \frac{\log\sigma}{\log\dot{\varepsilon}}\Big|_{\varepsilon,T} \qquad \textbf{Eqn. 7.4}$$

Where σ is the true stress, $\dot{\varepsilon}$ is true strain rate, C is the strength coefficient of the equation, and m is the strain rate sensitivity (SRS) exponent. Inverse of strain rate sensitivity exponent is called as stress exponent (n_{se}) and given by $n_{se} = \frac{\log\dot{\varepsilon}}{\log\sigma}\Big|_{\varepsilon,T}$.

True stress (σ) values were obtained at a fixed strain[G] and those were plotted against true strain rate on a log-log scale (Figure 7.16), and slope of the lines provided the value of the m, at a constant temperature. In Figure 7.17, the axes for both the variables were interchanged. As a result, the slope provided the n_{se}.

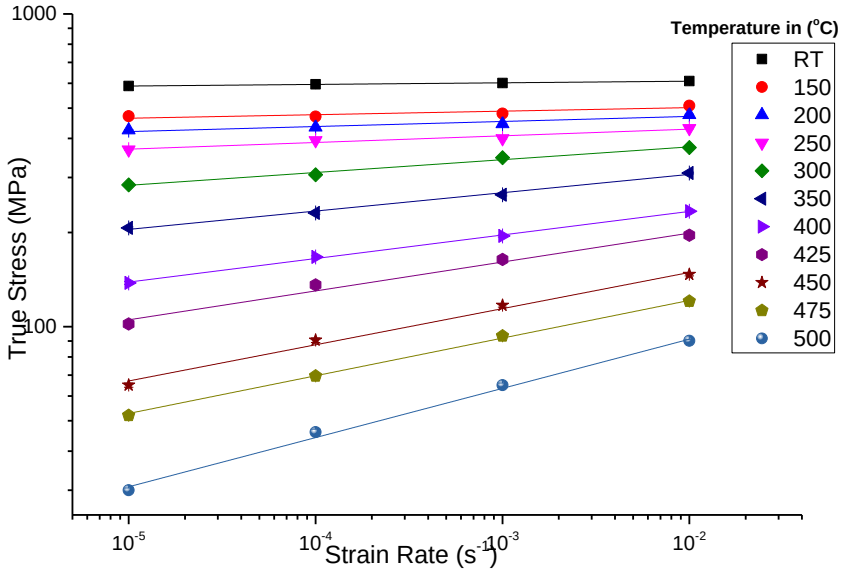

Figure 7.16 True stress vs strain rates in a log-log scale. The slope of each line provides m at a constant temperature.

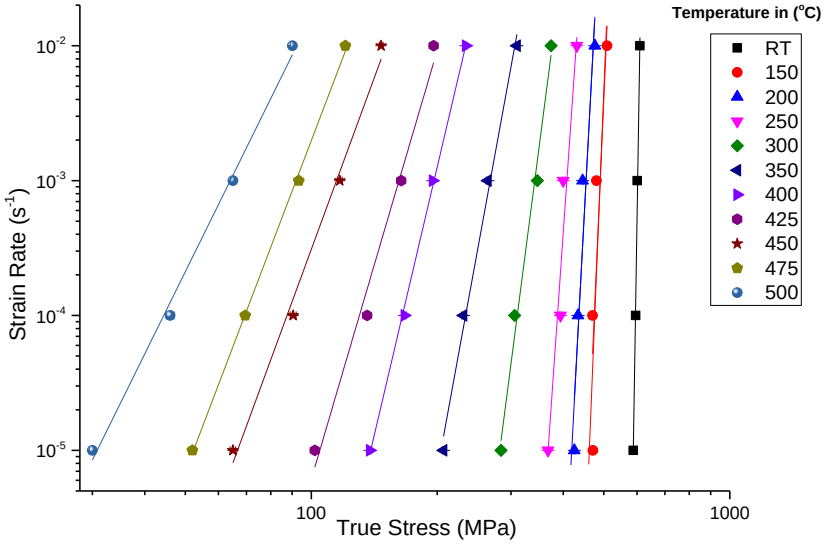

Figure 7.17 Strain rates vs true stress in log-log scale. The slope of each line provides n_{se} at a constant temperature.

[G] Strain value was chosen as ε~1.4. A steady state was achieved for all samples tested at 300°C and above. However, for samples showing reduced ductility (150 to 250°C) a true steady state could not be achieved and flow stress values were used for a fixed strain.

Figure 7.18 shows the graphs of the m and n_{se} vs temperature from 23°C to 500°C, whereas Table 7.5 provides the data.

Table 7.5 The values of m and n_{se}, and their corresponding errors[H].

Temperature	SRS exponent	error	Stress exponent	error
T (°C)	m	δm	n_{se}	δn_{se}
23	0.0052	0.0004	192.2	13.8
150	0.0113	0.0042	70.3	14.1
200	0.0162	0.0034	57.8	12.4
250	0.0213	0.0035	44.7	7.3
300	0.0410	0.0028	23.9	1.8
350	0.0586	0.0033	17.0	1.0
400	0.0754	0.0020	13.2	0.4
425	0.0924	0.0071	10.6	0.9
450	0.1106	0.0038	8.9	0.3
475	0.1205	0.0032	8.2	0.2
500	0.1573	0.0059	6.3	0.3

Generally, in conventional aluminium alloys, the m values lie between 0-0.2 in the temperature range of 23°C to 500°C (Kaufman, 2008). The RS alloys show lower strain rate sensitivity in comparison as seen in literature. For example Skinner et al. (1989) also found m for various rapidly solidified Al alloys (see Table 2.5 for compositions) from ~0 to 0.07 for temperatures up to 327°C. m for a bulk RS Al-Fe-V-Si alloy has been found between 0 to 0.04 in a temperature range of 23 to 400°C by Mitra (1992). These m values match closely to those found in present study.

[H] The errors at 150°C are calculated excluding the negative strain rate sensitivity term corresponding to $10^{-5}s^{-1}$.

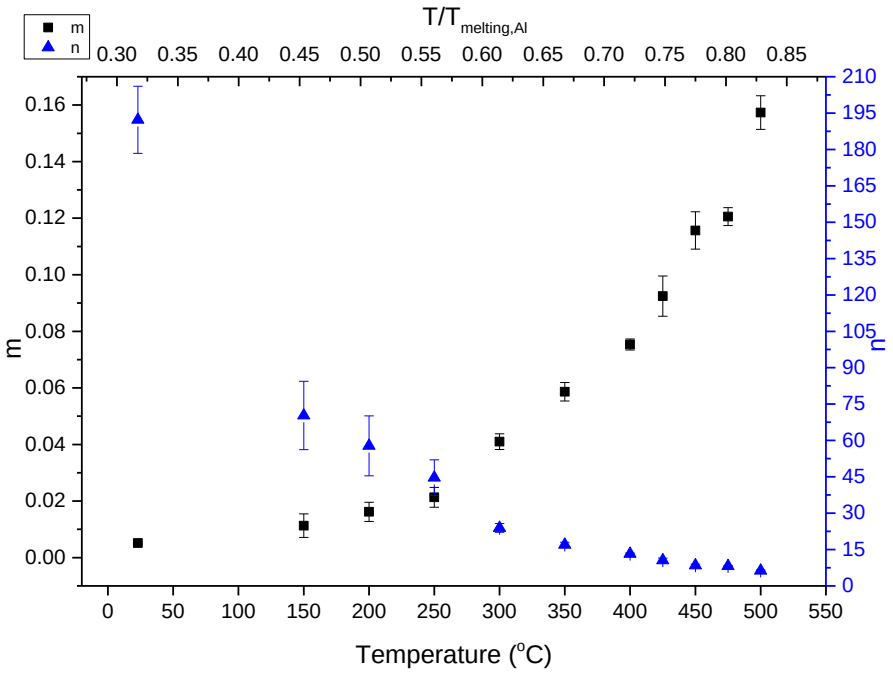

Figure 7.18 The values of m and n_{se} between 23°C and 500°C.

7.4.4 Temperature and the strain rate effect

The temperature and strain rate effect can be combined in a creep equation given as the following as mentioned in section 2.7.

$$\dot{\varepsilon} = C_1 \left(\frac{\sigma}{G} \right)^{n_{se}} e^{\left(-\frac{Q}{RT} \right)} \qquad \textbf{Eqn. 7.5}$$

Normalisation of the stress with either E or G of the matrix is recommended as it helps to explain the power law creep better (Kassner and Pérez-Prado, 2000), by excluding the effect of temperature on the athermal stress (Mukherjee, 2002). Most researchers have used G for compensation (Kassner and Pérez-Prado, 2000), and it has also been used in the present work.

Kassner and Pérez-Prado (2000) consider the creep test (in which the 'application of a constant stress generally results in a steady state strain rate'), and the quasi-static tensile test (in which 'applying a constant strain rate may result in a steady state flow stress') as

equivalent. The activation energies of the plastic flow in the tensile test can be found from the following equation.

$$Q = -R\frac{\delta \ln \sigma}{\delta(1/T)}\bigg|_{\varepsilon} \times \frac{\delta \ln \dot{\varepsilon}}{\delta \ln \sigma}\bigg|_{T} \qquad \textbf{Eqn. 7.6}$$

After modulus compensation, the equation can be written as

$$Q = -R\frac{\delta \ln(\sigma/G)}{\delta(1/T)}\bigg|_{\varepsilon} \times \frac{\delta \ln \dot{\varepsilon}}{\delta \ln(\sigma/G)}\bigg|_{T} \qquad \textbf{Eqn. 7.7}$$

The normalised true steady state stress (σ_{ss}/G) was plotted against the inverse of temperature (10^3 /T) (K^{-1}) at various strain rates, and the graph is shown in Figure 7.19. In order to find the slope, exponential curves were fitted in the ln(σ/G) vs 10^3/T graph and shown as dashed lines in Figure 7.19. These curves were numerically differentiated to find the value of slope at particular temperatures.

Also, $\dot{\varepsilon}$ vs (σ/G) were plotted to obtain a linear fit on a log-log scale. The slopes provided the value of $\frac{\delta \ln \dot{\varepsilon}}{\delta \ln(\sigma/G)}$ at various temperatures; and its behaviour is similar to n_{se} as shown in Figure 7.20. The values of apparent activation energy (Q_{app}) were then calculated using Eqn. 7.7, and shown in Figure 7.21 and it increases with the increase in temperature up to 400°C. Between 400-500°C the Q_{app} tends to reach a high but constant value.

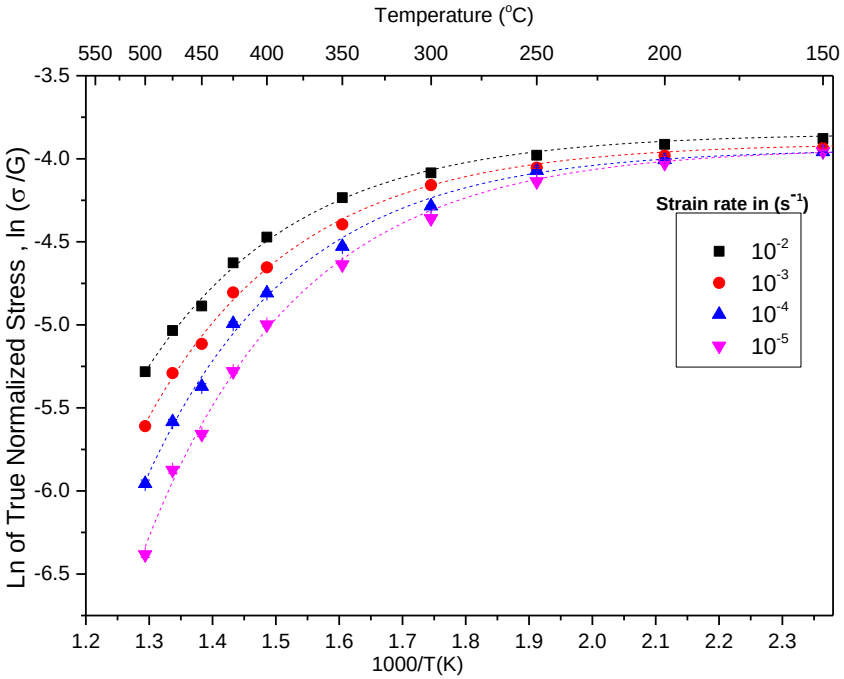

Figure 7.19 Ln(σ_{ss}/G) vs (10^3/T) plot from 150°C to 500°C at four strain rates. Dashed lines are fitted curves.

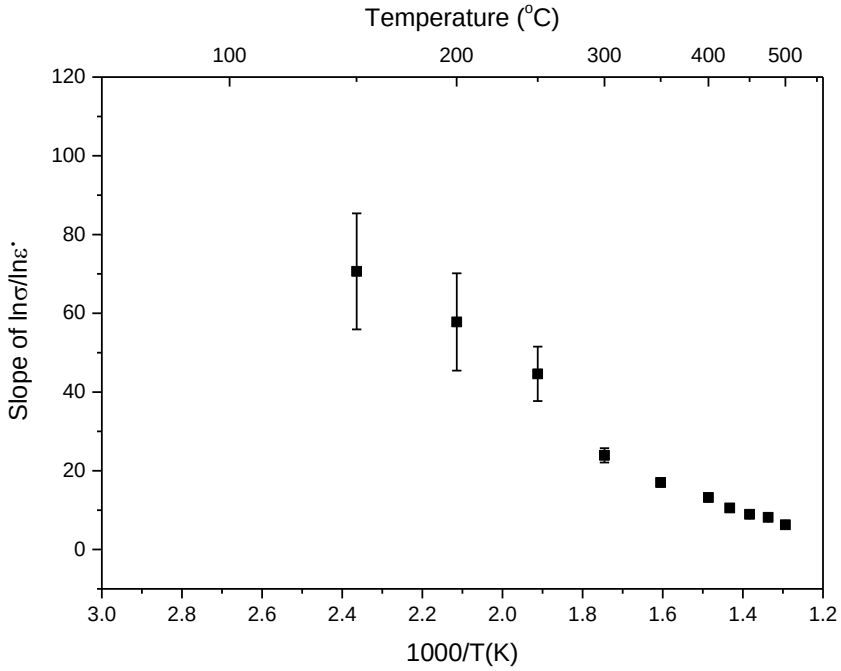

Figure 7.20 Slope of ln ε̇/ ln(σ/G) plotted against temperature (150°C to 500°C).

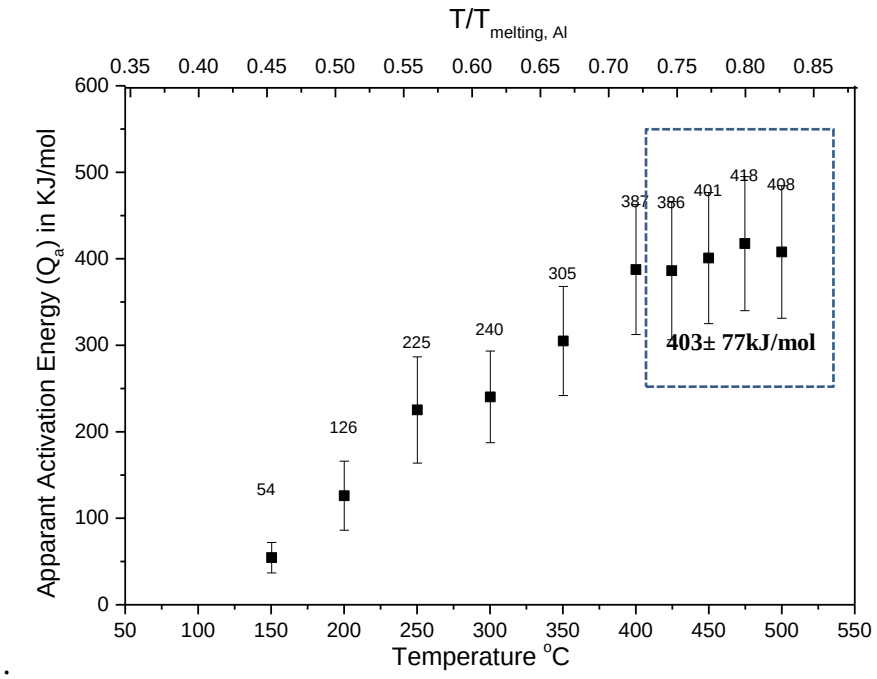

.

Figure 7.21 Apparent activation energies from 150°C to 500°C were found by Eqn. 7.7 .

Pure polycrystalline Al shows a change in Q from Q_{pd} (82kJ/mol)[I] at ~(0.3-0.48T_m) [J] to Q_{sd} (142kJ/mol) at ~>0.6T_m (Luthy et al., 1980), whereas n_{se} is ~5 which is associated to dislocation climb being the rate controlling mechanism (section 2.7.1). Higher values of n_{se} and Q_{app} are commonly observed dispersion strengthened alloy systems such as RS Al alloys (section 2.7.2).

The NQX alloy microstructure mainly consists of the I-phase for all tensile tests carried at 350°C; and 250-350°C (0.56-0.66T_m) can be considered as the highest temperature for the NQX based application. The n_{se} values in this temperature region are found from ~45 to 17 and the Q_{app} values are ~225kJ/mol to 305kJ/mol. In comparison, an RS Al-Fe-V-Si alloy was found to have n_{se} and Q_{app} values as ~32 to 13 and 360kJ/mol respectively in the temperature range 237°C to 479°C (Pharr et al., 1988). Also, another RS Al-Fe-V-Si-

[I] Q_{pd} is the activation energy for pipe diffusion which is significantly less than the activation energy for self-diffusion (Q_{sd}).
[J] T_m is the melting temperature of Al (933K).

Er alloy was observed to have n_{se} and Q_{app} ~14 and 340kJ/mol respectively at 375°C (Griffith et al., 1982).

In the NQX alloy, the I-phase transformation started in 400°C/tensile sample. The micro-structure of all samples tested at 425°C and above can be considered having an 'I-phase transformed' state and similar to 400°C/100h sample (section 7.2.1). In the 425-500°C (0.75-0.83T_m) temperature region, the n_{se} and Q_{app} tend to approach nearly constant values which are ~11-6 and ~400kJ/mol respectively.

The presence of dispersoids cause high values of n_{se} and Q_{app}, which has been associated with a so-called 'threshold stress' below which creep is assumed to be absent. It will be discussed in detail in chapter 8.

7.4.5 Anomalous mechanical behaviour

The anomalous mechanical behaviour was also exhibited by the NQX alloy up to ~250°C, which can be due to dynamic strain ageing (DSA). DSA is a plastic instability which can promote ductility loss at certain temperature/strain rate ranges (Antolovich and Armstrong, 2014). It is desirable to examine the mechanical behaviour of the NQX alloy, confirm the occurrence of any anomalous behaviour to define the best working condition for temperature-strain rate range of the NQX alloy.

As mentioned in section 2.6.2, the anomalous behaviour or DSA can have several manifestations, the most crucial of which is the presence of negative strain rate sensitivity. Additionally, the minima in ductility and strain rate sensitivity exponent (m) with increasing temperature, high hardening rate, yield strength anomaly, and the presence of serrations, are the manifestations of the DSA. All of these were found to be present in the NQX alloy in a certain temperature/strain rate range as mentioned in the following section.

- Figure 7.22 and Figure 7.23 show the true stress-true strain graphs at strain rates of 10^{-2}, 10^{-3}, 10^{-4} and $10^{-5}s^{-1}$, at 150°C and 200°C respectively. Regions represented by dotted orange rectangles in Figure 7.22 and Figure 7.23 have been the magnified in the respective figures which show serrations. There are no serrations at the start of the test, but these gradually become prominent as the serrated flow conditions are met. Further, the serrations start to appear slightly earlier for the lower strain rates, whilst at the highest strain rate ($10^{-2}s^{-1}$) the serrations appear late and also become discontinuous (one such example is marked by a blue rectangle in Figure 7.23). Possibly, two types of serrations were observed during the DSA at 150^{o}C. At the lowest strain rate of $10^{-5}s^{-1}$, the serrations can possibly be categorised as the normally found 'type A'. At the intermediate strain rates ($10^{-3}s^{-1}$ and $10^{-4}s^{-1}$) the serrations either conform to type A or type E[K] (Figure 7.22). Occasionally some discontinuous bands or serrations were observed in the flow curves at high strain rates ($10^{-2}s^{-1}$), as seen in Figure 7.23 (inset), marked with a blue rectangle. These were possibly the artifacts caused by the instability in the servo hydraulic system of the test machine.
- Normally, at a constant temperature, a decrease in the strain rate results in a lower flow stress, and vice versa. The NQX alloy; however, shows an anomalous behaviour. In Figure 7.22, it can be observed that the flow stress in the tensile curve at $\dot{\varepsilon}=10^{-5}s^{-1}$ is higher than the flow stress at $\dot{\varepsilon}=10^{-4}s^{-1}$ for the similar strain values. This can be explained by finding the strain rate sensitivity exponent (m). Figure 7.24 shows the m values at various temperatures. m was calculated using Eqn. 7.8 (Dieter and Bacon, 1986).

[K] Serrations were discussed in section 2.6.2. Type E is a higher strain version of type A serrations.

$$m = \left.\frac{\log\sigma}{\log\dot{\varepsilon}}\right|_{\varepsilon,T} \quad or = \left.\frac{\log\left(\frac{\sigma_1}{\sigma_2}\right)}{\log\left(\frac{\dot{\varepsilon}_1}{\dot{\varepsilon}_2}\right)}\right|_{\varepsilon,T} \qquad \textbf{Eqn. 7.8}$$

Where m is the strain rate sensitivity exponent, σ is the value of the flow stress at a particular strain, $\dot{\varepsilon}$ is the strain rate. The left term (logσ/log$\dot{\varepsilon}$) has been used to find the overall values of m, as seen in Figure 7.16. The right hand term[L] in Eqn. 7.8 was used to find the 'm' values using the strain rates of $10^{-4}s^{-1}$ and $10^{-5}s^{-1}$. 'm' values were calculated for all temperatures, and a negative value was observed at 150°C. 'm' vs temperature plots are shown in Figure 7.24, where a 3rd order polynomial was fitted to represent the behaviour. It can be seen that the minima in the curve(s) are observed in the temperature range of ~125-150°C.

- Normally, elongation to failure increases with temperature; however, anomalous behaviour is observed in the NQX alloy where ductility loss occurs with increasing temperature. Figure 7.25 shows the plot of % plastic strain at four strain rates in the range of 23°C to 400°C. The plastic strain minimum for $\dot{\varepsilon}=10^{-5}s^{-1}$ is at 200°C, whereas for $\dot{\varepsilon}=10^{-4}s^{-1}$ and $\dot{\varepsilon}=10^{-3}s^{-1}$ the minimum is observed at ~250°C. No minimum for the plastic strain was found at the highest strain rate of $10^{-2}s^{-1}$.
- DSA promotes a high hardening rate (Rodriguez, 1984). A strain rate of $10^{-5}s^{-1}$ exhibited negative m, so all corresponding σ-ε curves for $\dot{\varepsilon}=10^{-5}s^{-1}$ were used to compute the hardening rates at various temperatures. Polynomial curves were fitted to obtain smooth plastic σ-ε curves, and the hardening rates (dσ/dε) were calculated by numerically differentiating those σ-ε curves. The hardening rate at all the temperatures was plotted until either: (i) the necking condition was

[L] The right hand term of Eqn. 7.8 is used to find 'm' using two strain rates $\dot{\varepsilon}_1$ and $\dot{\varepsilon}_2$ and their corresponding stresses σ_1 and σ_2.

achieved (i.e. $d\sigma/d\varepsilon = \sigma$), or (ii) an early fracture occurred. Figure 7.26 (a) shows the hardening rate ($d\sigma/d\varepsilon$) vs the flow stress at various temperatures. The average hardening rates were also calculated and provided next to each line graph. The average hardening rates at various temperatures are graphically shown in Figure 7.26 (b). It can be observed that the value of the average hardening rate is maximised at 150^{o}C, which is the temperature that corresponds to negative values of the m.

- Figure 7.27 and Figure 7.28 show the behaviour of the yield strength with temperature and strain rate. The graph in Figure 7.27 shows a continuously decreasing yield strength which has a higher gradient at elevated temperatures (beyond ~250^{o}C). At a constant temperature, the yield strength generally decreases with a reduction in the strain rate. Figure 7.28 shows a constant increase of the yield strength as the strain rate increases at a fixed temperature. The slope of the yield strength with the strain rate increases as the temperature increase (see the slope in (2) with respect to slope in (3) in Figure 7.28). In the same Figure, the anomalous increase in the yield strength at 150˚C can be observed when strain rate is reduced from 10^{-4} to $10^{-5}s^{-1}$, it is shown by an orange trend line (1) in Figure 7.28.

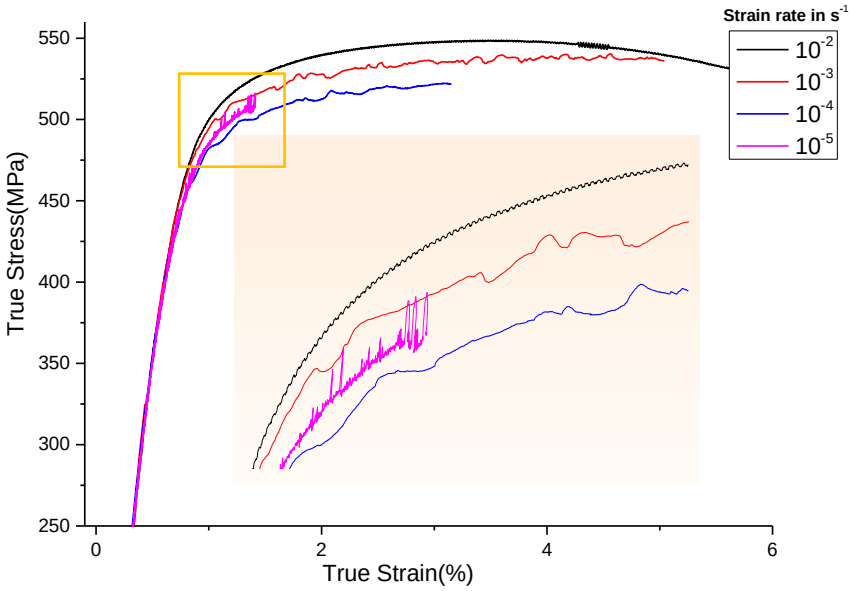

Figure 7.22 σ-ε curves at 150°C at various strain rates.

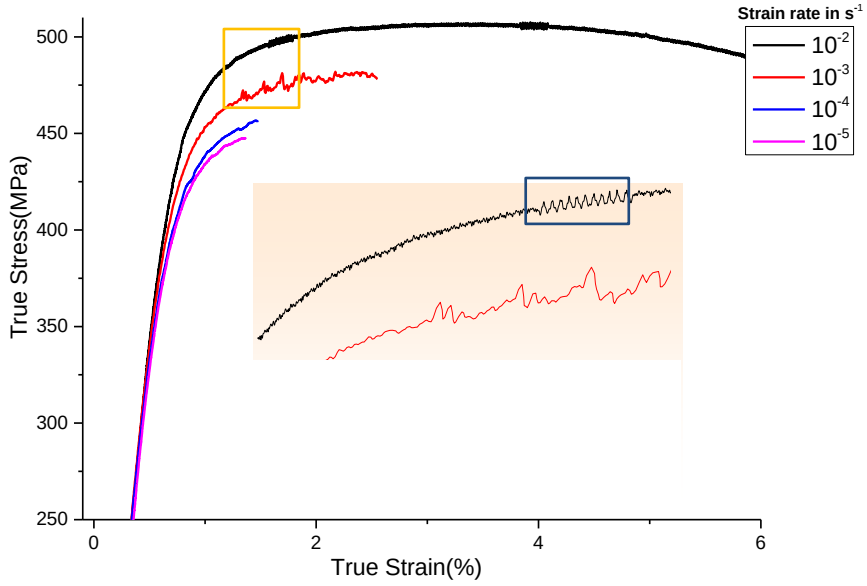

Figure 7.23 σ-ε curves at 200°C at various strain rates.

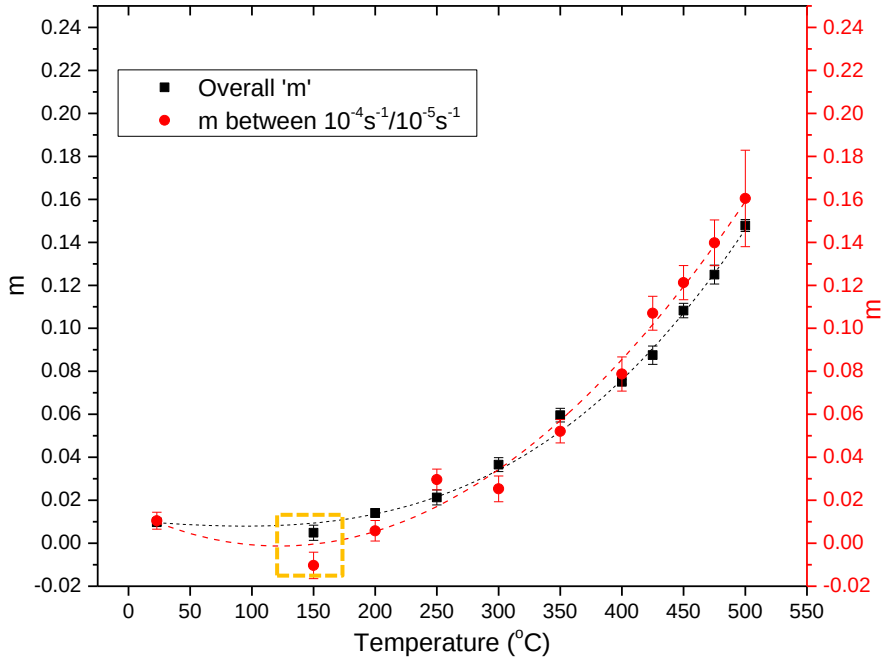

Figure 7.24 Strain rate sensitivity exponent (m) at various temperatures (dashed lines are fitted curves).

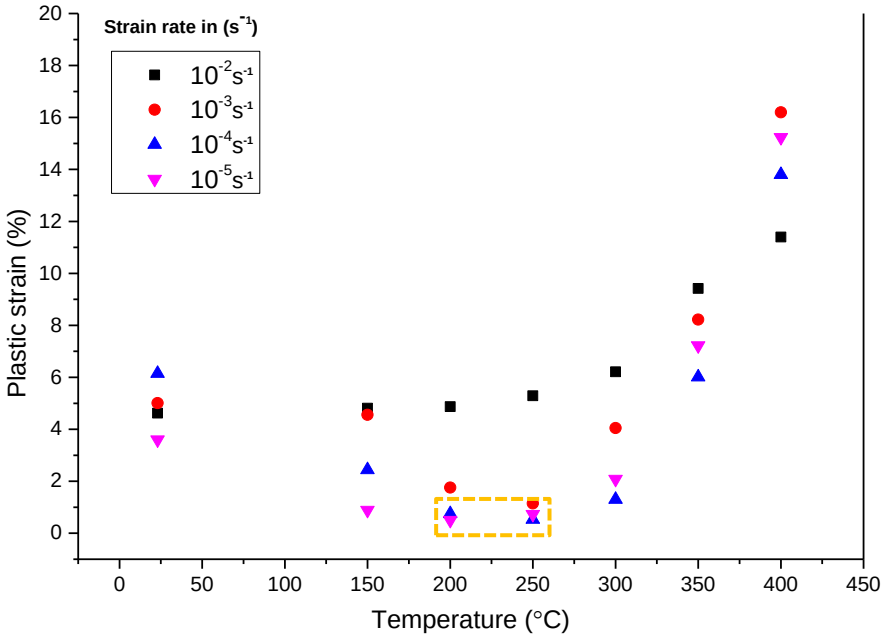

Figure 7.25 Plastic failure strain at various temperatures and strain rates. Orange rectangle marks the temperature range for the occurrence of the minimum.

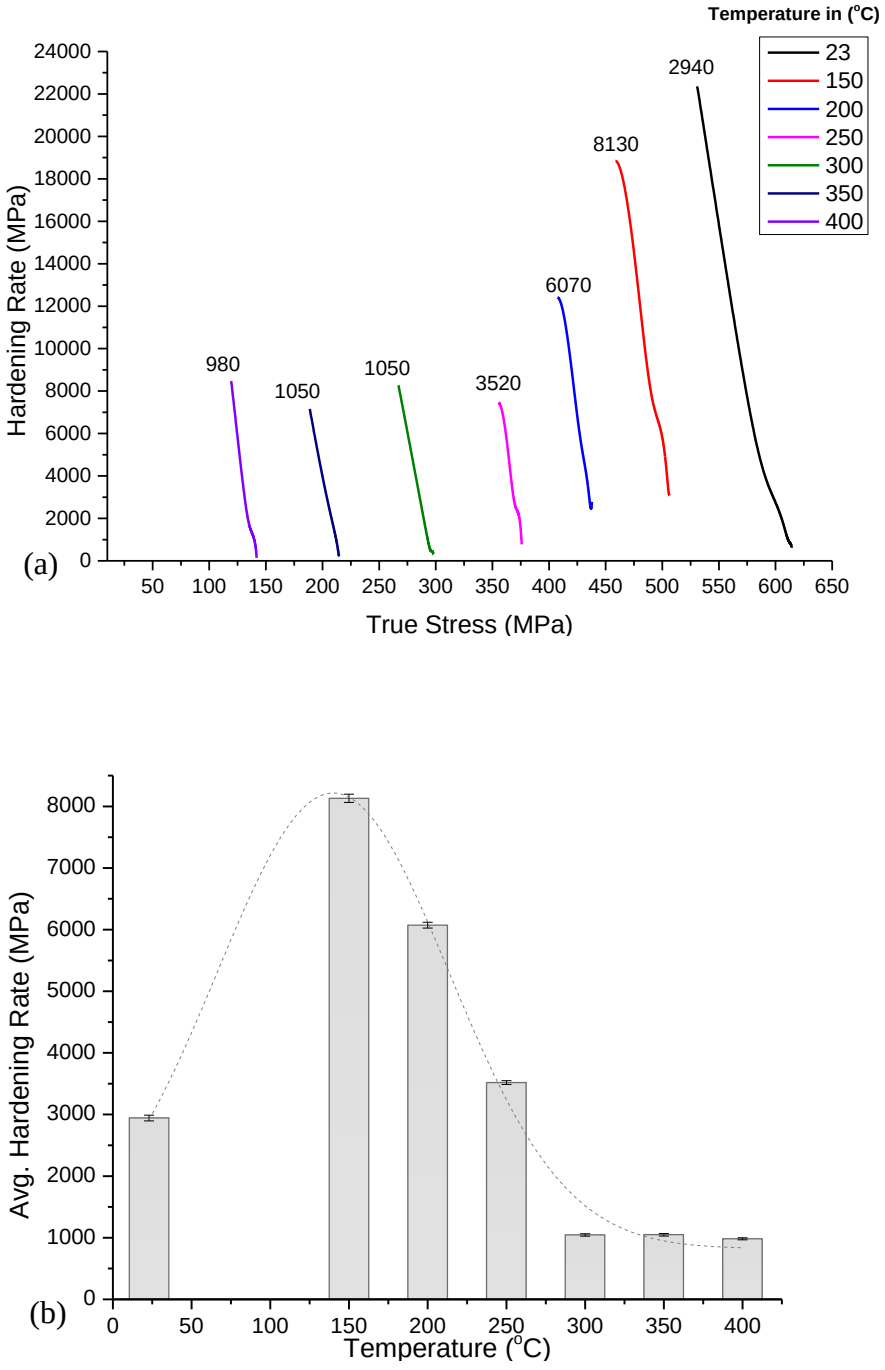

Figure 7.26 Hardening rate at $10^{-5}s^{-1}$: (a) hardening rate vs true stress at $10^{-5}s^{-1}$, at various temperatures, the average hardening rates are provided next to each line, (b) average hardening rate for $10^{-5}s^{-1}$ at various temperatures, the maximum value is found for 150°C which is the temperature associated with negative m value.

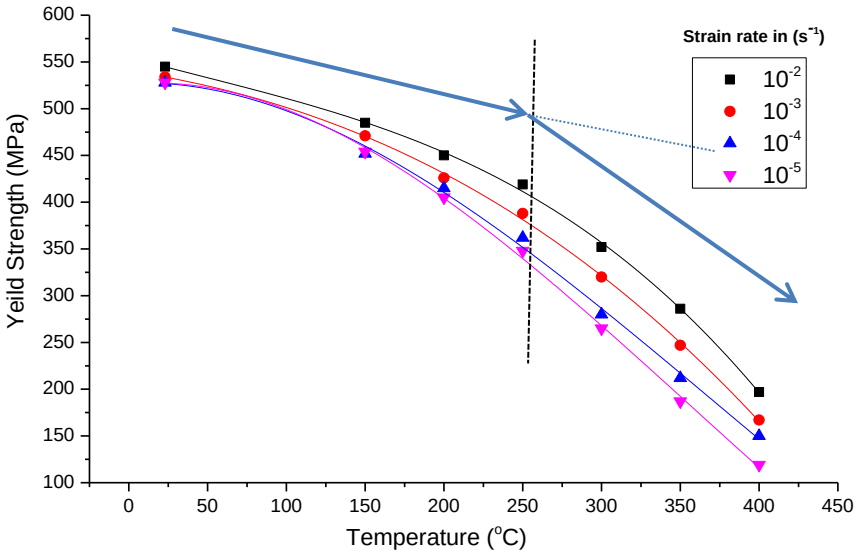

Figure 7.27 Yield strength vs temperature at various strain rates.

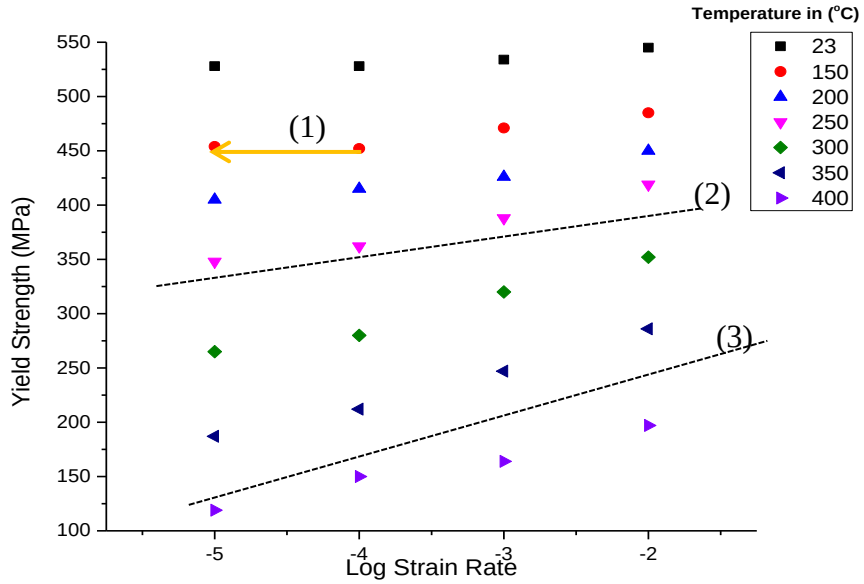

Figure 7.28 Yield strength vs log of strain rate at various temperatures. Line (1) shows the anomalous increase in the yield strength at 150˚C when the strain rate is reduced from 10^{-4} to $10^{-5}s^{-1}$. The change in yield strength with the strain rate increases as the temperature increase (see the slope in Line (2) respect slope in Line (3)).

The diffusion of the solute atoms plays the most important part in DSA. Consequently, the role of temperature and strain rate is instrumental (Hall, 1970, Robinson, 1994), which will be discussed in section 8.3.3.

7.5 Summary

E and G values of the NQX alloy are at least 30% higher than that of pure Al between 23-350°C. Transformation the of I-phase permanently increases the E and G of the NQX alloy by at least 6.5% and 5% respectively between 23-500°C.

The NQX alloy has an unparalleled strength at elevated temperatures, at least 440% higher than the high strength 7075-T6 at 300°C. The NQX alloy shows a low strain hardening ability (n_{sh} ~0.02-0.05) up to 400°C. The NQX alloy shows a moderate strain rate sensitive behaviour at elevated temperature. In 250-350°C region which contains the I-phase the stress exponent values are found very high, from ~45 to 17 and the corresponding Q_{app} values are from 225kJ/mol to 305kJ/mol. Even at very high temperatures and after the transformation of the I-phase at 425-500°C the n_{se} values range from ~10.6 to 6.3. These n_{se} values are high in comparison to pure Al which has a value close to ~4.5. The apparent activation energy at these temperatures (425-500°C) is also found very high ~400kJ/mol in comparison to the Al which has a value of 142kJ/mol for lattice self-diffusion. The microstructure of all the samples tensile tested at 425°C and above had the transformed I-phase and matched with the 400°C/100h sample from annealing studies.

Dynamic strain ageing was found to be present in the alloy in ~150-250°C temperature range which was confirmed by negative strain rate sensitivity at 150°C at $10^{-5}s^{-1}$. Other typical effects of DSA such as: the minima in the ductility and strain rate sensitivity exponent (m) with increasing temperature, high hardening rate, anomalous yield strength behaviour and serrations were also present.

The alloy shows superior fatigue performance at 300°C in comparison with conventional Al alloys. The inclusions can detrimental for NQX alloy fatigue performance.

References

Antolovich, S. D. and Armstrong, R. W. (2014) 'Plastic strain localization in metals: origins and consequences', *Progress in Materials Science,* 59, pp. 1-160.

ASM (1990) *Nonferrous Alloys and Special-Purpose Materials, vol. 2. ASM International, Materials Handbook*: ASM International.

Chateau, J. P. (2011) 'Basics of Mechanical Properties of Metals', in Belin-Ferré, E. (ed.) *Mechanical Properties of Complex Intermetallics Complex Metallic Alloys*: World Scientific.

Dieter, G. E. and Bacon, D. (1986) *Mechanical metallurgy.* McGraw-Hill New York.

Frost, H. J. and Ashby, M. F. (1982) 'Deformation mechanism maps: the plasticity and creep of metals and ceramics'.

Griffith, W., Sanders Jr, R. and Hildeman, G. (1982) 'Elevated Temperature

Aluminium Alloys for Aerospace Applications', in Koczak, M. & Hildeman, G. (eds.) *High Strength Powder Metallurgy Aluminum Alloys*. Warrendale, Pennsylvania: TMS AIME, pp. 209-224.

Hall, E. (1970) *Yield point phenomena in metals and alloys.* Plenum Press.

Kassner, M. and Pérez-Prado, M.-T. (2000) 'Five-power-law creep in single phase metals and alloys', *Progress in Materials Science,* 45(1), pp. 1-102.

Kaufman, J. G. (2008) *Properties of aluminum alloys: fatigue data and the effects of temperature, product form, and processing.* ASM International.

Kuhn, H. and Medlin, D. (2000) 'ASM Handbook. Volume 8: Mechanical Testing and Evaluation', *ASM International, Member/Customer Service Center, Materials Park, OH 44073-0002, USA, 2000. 998*.

Luthy, H., Miller, A. and Sherby, O. (1980) 'The stress and temperature dependence of steady-state flow at intermediate temperatures for pure polycrystalline aluminum', *Acta Metallurgica,* 28(2), pp. 169-178.

Ma, E. (2006) 'Eight routes to improve the tensile ductility of bulk nanostructured metals and alloys', *Jom,* 58(4), pp. 49-53.

McLellan, R. B. and Ishikawa, T. (1987) 'The elastic properties of aluminum at high temperatures', *Journal of Physics and Chemistry of Solids,* 48(7), pp. 603-606.

Mitra, S. (1992) 'Elevated temperature mechanical properties of a rapidly solidified Al-Fe-V-Si alloy', *Scripta metallurgica et materialia,* 27(5), pp. 521-526.

Mukherjee, A. K. (2002) 'An examination of the constitutive equation for elevated temperature plasticity', *Materials Science and Engineering: A,* 322(1), pp. 1-22.

Pharr, G. M., Zedalis, M. S., Skinner, D. J. and Gilman, P. S. (1988) 'High Temperature

Creep Deformation of a Rapidly Solidified Al-Fe-V-Si Alloy', in Yoney, D., Ovecoglu, M. & Nix, W. (eds.) *Dispersion Strengthened Aluminum Alloys, 1988*. Warrendale, Pennsylvania: TMS AIME, pp. 309.

Pineau, A., Benzerga, A. A. and Pardoen, T. (2016) 'Failure of metals III: Fracture and fatigue of nanostructured metallic materials', *Acta Materialia,* 107, pp. 508-544.

Robinson, J. (1994) 'Serrated flow in aluminium base alloys', *International Materials Reviews,* 39(6), pp. 217-227.

Rodriguez, P. (1984) 'Serrated plastic flow', *Bulletin of Materials Science,* 6(4), pp. 653-663.

Skinner, D., Zedalis, M. and Gilman, P. (1989) 'Effect of strain rate on tensile ductility for a series of dispersion-strengthened aluminum-based alloys', *Materials Science and Engineering: A,* 119, pp. 81-86.

8. General Discussion

8.1 Microstructure Characterisation

8.1.1 Phases in the extruded bars

All the NQX alloy powders and bars contained α-aluminium and a quasicrystalline I-phase. A single stoichiometric composition for the I-phase particles in Al-Fe-Cr-Ti alloys is not found in the literature. As seen in Table 8.1, Gargarella et al. (2009), Yamasaki et al. (2007), Kim et al. (2007), and (Inoue and Kimura, 2000) have reported slightly different I-phase particle compositions in the bulk Al-Fe-Cr-Ti alloys. This has been attributed to the ability of various elements substituting each other in the lattice (Dám et al., 2013).

Table 8.1 (TEM) EDX analysis of matrix and particles in various bulk Al-Fe-Cr-Ti alloys containing quasicrystalline phase.

Alloy Composition/ (Processing)		Al		Fe		Cr		Ti		Reference
		at %	±δ	at %	±δ	at %	±δ	at %	±δ	
$Al_{93}Fe_3Cr_2Ti_2$ (Atomized +Extruded)	I-phase	84.2	-	7	-	6.3	-	2.5	-	(Inoue, 1998, Inoue and Kimura, 2000)
$Al_{91}Fe_4Cr_3Ti_2$ (Cast + Remelt)	I-phase	82.9	4	8.3	0.4	7.6	0.4	1.2	0.1	(Kim et al., 2007)
$Al_{92.5}Fe_{2.5}Cr_{2.5}Ti_{2.5}$ (Atomised +Extruded)	I-phase	84.8	-	12.7	2.9	1.3	0.6	1.2	0.6	(Yamasaki et al., 2007)
	Matrix	97	-	0.7	0.6	1.5	0.6	0.8	0.1	
$Al_{91}Fe_4Cr_3Ti_2$ (Spray Formed+ Laser remelted)	I-phase	86.8	0.4	5.4	0.1	5.5	0.1	2.2	0.1	(Gargarella et al., 2009)
	Matrix	98.4	0.5	0.2	0.1	0.8	0.1	0.6	0.1	
$Al_{93}Fe_3Cr_2Ti_2$ (Atomised + Extruded)	I-phase	86.7	0.7	5.1	0.6	4.9	0.3	3.3	0.2	This work
	Matrix	98.2	0.3	0.35	0.1	0.4	0.1	1.05	0.2	

The matrix and the I-phase composition in the present study are found close to those reported by Gargarella et al. (2009) in a laser re-melted spray formed $Al_{91}Fe_4Cr_3Ti_2$ alloy as seen in Table 8.1.

Equilibrium at% solid solubility of the constituent elements in Al is reported to be very small such as Fe (0.024%), Cr (0.4%) and Ti (0.75%) (Belov et al., 2002). Rapid solidification increases the solubility of the alloying elements in the Al matrix, for example, Fe solubility is reported to increase up to 6% in Al-Fe alloys as a result of rapid solidification (Belov et al., 2002). As seen from the matrix composition provided in Table 8.2, in the 'as extruded' condition the Fe solubility is significantly higher, whereas Ti solubility is slightly higher and Cr solubility is similar to their respective equilibrium solid solubilities in Al matrix. The Fe, Cr and Ti solute concentrations in the matrix decrease as a result of prolonged annealing treatments[A] and subsequent intermetallic formation at elevated temperatures, as seen in Table 8.2.

Table 8.2 Matrix (at%) composition comparison for as extruded and 100h annealed samples.

Element	**Stable Equilibrium Solubility at 23°C** after (Belov et al., 2002)	**As Extruded** (at 400°C)	**250°C/ 100h**	**300°C/ 100h**	**350°C/ 100h**	**400°C/ 100h**	**450°C/ 100h**
Al	-	98.2	98.8	99.00	99.15	99.2	99.7
Fe	0.02	0.35	0.15	0.15	0.15	0.15	0.05
Cr	0.4	0.4	0.2	0.15	0.15	0.15	0.1
Ti	0.75	1.05	0.85	0.7	0.55	0.5	0.15

The extruded bars contains α-Al, the I-phase, and very small amounts of θ_D-$Al_{13}(Fe, Cr)_{2-4}$ and Al_3Ti in the 'as extruded' condition, the phases are shown in Table 8.3.

[A] 100hrs at 250, 300, 350, 400, or 450°C followed by air cooling.

Several researchers have observed similar phases in the rapidly solidified Al-Fe-Cr-Ti alloys, prepared by either gas atomisation or melt spinning techniques, a summary of which is provided in Table 8.3. In the NQX alloy, noticeable I-phase transformation does not start even after a prolonged annealing at 300°C. It was observed in the present study as well in a few previous research works (refer to Table 8.3).

After a 100hrs annealing, noticeable microstructure changes start in sample annealed at 350°C and completes at 450°C to result in a high volume fraction of stable intermetallics such as Al_3Ti, $Al_{13}Fe_4$ and $Al_{13}Cr_2$ in α-Al. Similar phases have been reported by several researchers after prolonged annealing at temperatures of 400°C or above, whereas short duration annealing at higher temperatures resulted in the same phases (refer to Table 8.3). However, the effect of the phase transformation on the particle size, size distribution, elastic moduli, and tensile strength has never been studied in the literature which has been undertaken in the present work.

Table 8.3 Summary of phases in Al-Fe-Cr-Ti alloys, with and without annealing heat treatments.

Composition (& Processing)	Heat Treatment (Temperature / Time)	Phases Present	Reference
$Al_{93}Fe_3Cr_2Ti_2$ Atomisation + Extrusion	As Extruded	α-Al, I-phase, $Al_{23}Ti_9$	(Inoue and Kimura, 2001)
	300°C / 200h	α-Al, I-phase, $Al_{23}Ti_9$	
$Al_{93}Fe_3Cr_2Ti_2$ Melt spinning	As spun	α-Al, I-phase, Al_3Ti	(Audebert et al., 2002)
	420°C / 0.75h	α-Al, I-phase, Al_3Ti,θ-Al-(Fe-Cr)	
	550°C / 0.75h	α-Al, I-phase, Al_3Ti,$Al_{13}Fe_4$, $Al_{13}Cr_2$	
$Al_{93}Fe_3Cr_2Ti_2$ Melting, Casting	As cast	α-Al, I-phase, Al_3Ti, θ-Al_{13}(Fe-Cr)$_4$	(Kim et al., 2007)
$Al_{92.5}Fe_{2.5}Cr_{2.5}Ti_{2.5}$ Atomisation + Extrusion	As extruded	α-Al, I-phase	(Yamasaki et al., 2007)
	300°C / 1000h	α-Al, I-phase	
$Al_{93}Fe_3Cr_2Ti_2$ Melt spinning	As produced	α-Al, I-phase, θ_D-Al_{13}(Fe, Cr)$_{4\text{-}2}$	(Galano et al., 2009b)
	300°C / 0.5h	α-Al, I-phase, θ_D-Al_{13}(Fe, Cr)$_{4\text{-}2}$	
	355°C / 0.5h	α-Al, I-phase θ_D-Al_{13}(Fe, Cr)$_{4\text{-}2}$	
	450°C / 0.5h	α-Al, I-phase, Al_3Ti, θ_D-Al_{13}(Fe, Cr)$_{4\text{-}2}$, $Al_{13}Fe_4$, $Al_{13}Cr_2$	
$Al_{95}Fe_{1.1}Cr_3Ti_{0.8}$ Atomisation + processed	Cold compaction+ 550°C/100h	α-Al, Al_3Ti, $Al_{23}Ti_9$, $Al_{13}Fe_4$, $Al_{13}Cr_2$	(Vojtěch et al., 2012)
	Hot extrusion at 480°C	α-Al, Al_3Ti, $Al_{23}Ti_9$,$Al_{13}Fe_4$,$Al_{13}Cr_2$	
$Al_{93}Fe_3Cr_2Ti_2$ Atomisation + Extrusion	As extruded	α-Al, I-phase, $Al_{23}Ti_9$, Al_3Ti	(García-Escorial et al., 2015)
	400°C / 1h	α-Al, I-phase, Al_3Ti, Al_6Fe,	
	400°C / 100h	α-Al, Al_3Ti, $Al_{23}Ti_9$, Al_6Fe, $Al_{13}Fe_4$, $Al_{13}Cr_2$	
	400°C / 1000h	α-Al, Al_3Ti, $Al_{23}Ti_9$, $Al_{13}Fe_4$, $Al_{13}Cr_2$	
$Al_{93}Fe_3Cr_2Ti_2$ Atomisation + Extrusion	As extruded	α-Al, I-phase, small Al_3Ti, and θ_D-Al_{13}(Fe, Cr)$_{4\text{-}2}$	This work
	250°C / 100h	α-Al, I-phase, small Al_3Ti, and θ_D-Al_{13}(Fe, Cr)$_{4\text{-}2}$	
	300°C / 100h	α-Al, I-phase, small Al_3Ti, and θ_D-Al_{13}(Fe, Cr)$_{4\text{-}2}$	
	350°C / 100h	α-Al, I-phase, Al_3Ti, θ_D-Al_{13}(Fe, Cr)$_{4\text{-}2}$, small Al_6Fe and $Al_{13}Cr_2$	
	400°C / 100h	α-Al, Al_3Ti, $Al_{13}Cr_2$, Al_6Fe, $Al_{13}Fe_4$	
	450°C / 100h	α-Al, Al_3Ti, $Al_{13}Cr_2$, $Al_{13}Fe_4$	

8.1.2 Effect of the annealing temperature on particle growth

Table 8.4 has a summary of prominent phases, their volume fraction, mean particle sizes and also the mean planar grain sizes found in the 'as extruded' and annealed NQX alloy samples from chapter 4 and 5.

Table 8.4 A summary of prominent phases, their volume fraction, mean particle diameter, and longitudinal and cross section mean planar grain sizes measured in the 'as extruded' and annealed NQX alloy[B].

Sample	Volume Fraction	Mean Particle Diameter	Mean Planar Grain Size		Particles of Prominent Phase Present
	f_v	D_P	D_{Long}	D_{Xsec}	
	fraction	nm	nm	nm	
As Extruded	0.44	151	470	430	I-phase
250°C/100h			475	409	I-phase
300°C/100h			485	426	I-phase
350°C/100h			471	434	Al_3Ti, θ_D-$Al_{13}(Fe, Cr)_{2-4}$, I-phase
400°C/100h	0.42	193	502	439	Al_3Ti, $Al_{13}Cr_2$, Al_6Fe, $Al_{13}Fe_4$
#450°C/100h	0.42	239	528	509	Al_3Ti, $Al_{13}Cr_2$, $Al_{13}Fe_4$

Transformation complete

The growth of the particles as a result of annealing treatment can be explained by estimating the diffusion lengths, using Einstein's equation below (Campbell, 2008).

$$< R^2 > \approx 2dDt \qquad \textbf{Eqn. 8.1}$$

Where <R> is the three-dimensional vector displacement (in m) of an atom in a certain time, D is the diffusion coefficient (m^2/s), and t is the time (in s), d is the dimensionality of the problem ('3' for a three-dimensional problem). Diffusion is a thermally activated

[B] By 'prominent' phases it refer to the phases which have a considerable volume fraction, as there was a very small volume fraction of some other phase present as seen in Table 8.3. Table 8.4 reproduces the results from chapter 4 and 5. D_{Long}=longitudinal planar gain diameter measured in EBSD, D_{Xsec} =cross section planar gain diameter measured in EBSD, fv=volume fraction, D_p=particle (spherical) diameter measured in TEM (using a log normal distribution).

process. Using the values of bulk diffusion coefficients of Fe, Cr and Ti in Al the diffusion lengths for each element was estimated at various temperatures for a 100hrs annealing time from Eqn. 8.1. The results are provided in Table 8.5.

Table 8.5 Calculated diffusion lengths <R>, for Fe, Cr and Ti atoms in annealed samples.

Sample	Fe		Cr		Ti	
	D	<R>	D	<R>	D	<R>
	m^2/s	m	m^2/s	m	m^2/s	m
450°C/100h	6.70E-17	1.20E-05	5.80E-20	3.54E-07	1.90E-20	2.03E-07
400°C/100h	8.50E-18	4.28E-06	6.30E-21	1.17E-07	1.60E-21	5.88E-08
350°C/100h	7.80E-19	1.30E-06	3.60E-22	2.79E-08	8.20E-23	1.33E-08
300°C/100h	4.60E-20	3.15E-07	1.60E-23	5.88E-09	2.80E-24	2.46E-09
250°C/100h	1.60E-21	5.88E-08	3.90E-25	9.18E-10	4.10E-26	2.98E-10

<R> calculations for a time (t) equals 100 hrs or (3.6E5s), D values used from Mantina et al. (2009).

Diffusion lengths for Ti in samples 250°C/100h and 300°C/100h are estimated to be up to a few nm, whereas for Fe, these are two to three orders of magnitude larger. Fe is the fastest diffusing solute in Al matrix, and as a result, it has the largest values of the expected diffusion lengths in the above mentioned samples (temperature and time being equal). It was noted that the formation of very small Al_6Fe and Al_3Ti started in the sample 300°C/100h (section 5.2.4.2). As the annealing temperature increased further the Al_3Ti particles were found to grow, but the growth was very slow as compared to the Al_6Fe particles. The latter grew to larger than ~500nm trapezium shaped particles in sample 350°C/100h and 400°C/100h (section 5.2.1 and 5.2.4). The low diffusion coefficient of Ti and resultant smaller diffusion lengths prevented the Al_3Ti nuclei from growing into large sizes in comparison with fast diffusing Fe.

Higher temperatures result in larger diffusion lengths and cause larger particle sizes. The diffusion lengths for Cr and Ti in the sample annealed at the highest temperature (450°C/100h) are estimated to be ~355nm and ~205nm respectively, as seen in Table 8.5. These small values of calculated diffusion lengths explain the slow coarsening of

Al_3Ti and $Al_{13}Cr_2$ particles, and also the presence of a high volume fraction of smaller size particles in the samples even after the I-phase transformation as seen in the particle size distribution curve in Figure 5.28. The diffusion length of Fe in the 450°C/100h sample is estimated to be several tens of microns, which explains the presence of several micron long $Al_{13}Fe_4$ particles in the sample as seen in Figure 5.17 and 5.18. The slow particle coarsening and the presence of a large number of small particles in the annealed samples (even after the I-phase decomposition) played a major part in the grain growth inhibition (section 8.1.3) and subsequently, strengthening of the NQX alloy as discussed in section 8.2.3.

8.1.3 Effects of temperature and particles on grain growth

The atoms in a smaller grain, in the neighbourhood of the grain boundaries of a larger grain, are under a compression force, and they tend to migrate across the boundary. This leads to the growth of some grains at the expense of others. By assuming the grain boundary mobility controls the grain growth a general grain growth law can be obtained which is mainly dependent on grain boundary diffusion coefficient (D_{GB}), temperature (T), time (t) and grain boundary interfacial energy (γ_{GB}) given by Eqn. 8.2 (Priester, 2013).

$$d^2 - d_o^2 = 2\alpha_1 \frac{D_{GB}}{kT\delta_{GB}} \gamma_{GB}.t \qquad \textbf{Eqn. 8.2}$$

Where d_o is the initial grain size, d is the final grain size, α_1 is a boundary shape dependent constant, k is the Boltzmann constant, δ_{GB} is the grain boundary thickness.

As compared to coarse-grained materials, the grain growth is faster in ultrafine-grained (diameter<1μm) materials, which adversely affects the strengthening properties. The energy stored at grain boundaries is higher in the case of ultrafine grain materials providing high driving force for the grain growth (Lewandowska et al., 2008). The

majority of the grains in the NQX alloy are found to have sizes in the ultrafine grain range, as seen in EBSD sections 4.3.5 and 5.2.5. It potentially makes the alloy vulnerable to grain growth at elevated temperatures and long annealing times. On the contrary, it was noted that no appreciable grain growth was observed in the samples 250°C/100h, 300°C/100h, and 350°C /100h and only a small growth of ~30-100nm was observed for the samples annealed at very high temperatures (400°C/100h and 450°C /100h). The presence of second phase particles in contact with the boundary lowers the interfacial energy (γ_{GB} term in Eqn. 8.2) and can be a likely cause for grain growth inhibition as explained below.

Zener was the first to postulate that the second phase particles inhibit the grain growth as quoted by Smith (1948). The presence of second phase particles causes a drag and inhibits the boundary migration due to the attractive attachment between the boundary and the particles. A particle in contact with the boundary reduces the effective grain boundary area and lowers the interfacial energy of the system (Kang, 2004). The grain boundary (in contact with a particle) will only detach (or grow) if the net interfacial energy of the system is reduced due to the detachment (Barrales-Mora, 2008). The magnitude of the maximum drag force (F_d) per unit area of the grain boundary and the resulting maximum achievable grain size depends on the volume fraction (f_v), diameter of the second phase particles (d_p), and the grain boundary interfacial energy (γ_{GB}), and the relation is shown in Eqn. 8.3 (Kang, 2004).

$$F_d = -3\gamma_{GB}\frac{f_v}{d_p} \qquad \textbf{Eqn. 8.3}$$

Eqn. 8.3 suggests that a high volume fraction of small size 2nd phase particles produces a larger drag force for the grain growth inhibition. The magnitude of the drag force is reduced with the increase in the particle size or decrease in their volume fraction. The

observations made in the current study of the grain growth in the annealed NQX alloy samples are consistent with this equation. As seen in Table 8.3, no visible particle growth and subsequent grain growth occurred in samples 250°C/100h, 300°C/100h, and 350°C /100h and all these samples contained the I-phase. It was only after the I-phase transformation that the intermetallic particles started to grow larger in samples 400°C/100h and 450°C /100h and some corresponding grain growth was observed. This highlights the impact the I-phase particles have on the grain growth. Even after the I-phase transformation the particle coarsening and subsequent grain growth was small and the alloy was able to retain a high strength despite long annealing at elevated temperatures.

The average increase in grain size (~30-100nm) is even smaller than the standard deviation in the grain size measurement (~170nm). The large value of standard deviation is due to the presence of a wide range of grain sizes in the NQX alloy, from ~200nm up to a few microns (section 5.2.5). The presence of two types of grain sizes that is ultrafine (submicron size) and coarse grain (micron size) is often considered beneficial for the alloys. The larger grains result in a lower strength but improved ductility, whereas materials with smaller grains may suffer a loss of ductility but have an excellent strength (Joshi et al., 2006). The presence of a high volume fraction of hard and thermally stable (up to ~350°C) I-phase particles or the coarsening resistant intermetallics after the I-phase transformation at higher temperatures provide the microstructural stability (e.g. grain growth inhibition) and strengthening to the alloy. Meanwhile, the range of grain sizes provides both strength and ductility to the alloy.

8.2 Room Temperature Mechanical Behaviour

8.2.1 Effect of the I-phase and its transformation on the elastic constants

8.2.1.1 'As extruded' condition

The values of E and G for the NQX alloy were found to be 92GPa and 34.5GPa (section 6.2), whereas for pure aluminium these have been reported as 70GPa and 26GPa in literature (Hatch, 1984). In conventional Al alloys, E is only slightly affected by alloying, cold working, or heat treatments (Dieter and Bacon, 1986). Most conventional Al alloys have E values in 68-78GPa range (ASM, 1990). The effect of each of the element on the Young's modulus of Al in literature was found for Cr (5.5GPa/at%) (Noble et al., 1982), Ti(3.2 GPa/at%) (Noble et al., 1982) and Fe (2GPa/at%) (Belov et al., 2002). The E of Al matrix in the 'as extruded' NQX alloy was therefore calculated as 75GPa.The only prominent intermetallic in the 'as extruded' alloy is the I-phase[C], with a volume fraction of 44±3% (refer Table 8.4). Using the rule of mixtures the average E of the I-phase particle was calculated to be 114±3 GPa. Elastic modulus for some stable quasicrystals has been measured in a few research works as shown in Table 8.6.

Table 8.6 A comparisons of values of measured/calculated E for various icosahedral quasicrystals.

System	E (GPa)	Test Method	Reference
$Al_{70}Pd_{20}Mn_{10}$	200	Tensile test (parallel to 3-fold axis)	(Inoue and Kimura, 2001)
Al-Pd-Mn	180	Ultrasonic	(Dubois and Wei, 2005)
Al-Cu-Fe	170	"	'as above'
Al-Cu-Fe-Ru	140	"	'as above'
Al-Fe-Cr-Ti[D]	114*	Ultrasonic	This work

* Value calculated by using the rule of mixtures and using E of Al matrix as 75GPa.

[C] $Al_{13}(Fe, Cr)_{2-4}$ or Al_3Ti have a very low volume fraction and are therefore neglected.
[D] I-phase composition in present work is $Al_{86.7}Fe_{5.1}Cr_{4.9}Ti_{3.3}$

The Young's modulus depends on the interatomic bonds and type of material. It can be observed that the composition of the I-phase in the present work contains only ~13% of the alloying elements whereas other icosahedral systems have much higher at% of the alloying elements which results in a higher value of E in those systems.

8.2.1.2 'Annealed' condition

Annealing caused microstructural changes (Table 5.6), which affected the elastic constants (section 6.2.2). The E (or G) values of the NQX alloy remained unaffected in samples annealed up to 300°C. A significant increase was only observed in samples annealed at higher temperatures (400°C/100h or 450°C/100h samples) (section 6.2.2) and this exactly matched with the I-phase transformation in the NQX alloy (Table 5.6 and Table 8.3). As the I-phase (E= 114±3GPa) transforms completely into stable intermetallics:Al_3Ti (E=166GPa), $Al_{13}Fe_4$ (E=130GPa) and $Al_{13}Cr_2$ (E~124-140GPa) (Skinner and Zedalis, 1988, L.F, 1976), the corresponding E of the NQX alloy increases from ~92GPa to ~99GPa.

The elastic moduli (E or G) are related to the interatomic bonds whose nature changes due to the transformation of a quasicrystalline I-phase into stable intermetallics of higher elastic moduli. The minimum to the maximum change in E as a result of annealing temperature was therefore assumed a measure of the completion of I-phase transformation. The percentage change of elastic modulus (%ΔE) and the corresponding fraction of the transformed I-phase (y) were calculated for each of the samples annealed for 100 hrs, and the plot is shown in Figure 8.1. The % ΔE follows a sigmoidal curve whose lower bound (%ΔE = y =0) and the upper bound[E] ((%ΔE = 7.4% or y =1) are

[E] Lower bound relates to no change in E or 0% transformation, Upper bound relates to E after completion of 100% transformation.

also marked with dashed lines. An equation of sigmoidal form was fitted in the relation given as the following.

$$y = \frac{1}{1 + e^{-C_4 (T - T_{0.5})}} \qquad \textbf{Eqn. 8.4}$$

Where y is the fraction transformed, T is the temperature in K and $T_{0.5}$ is the temperature for 50% transformation which is 649.5K (375.5°C) in the present case, C_4 is a constant with a value 0.536 for this curve.

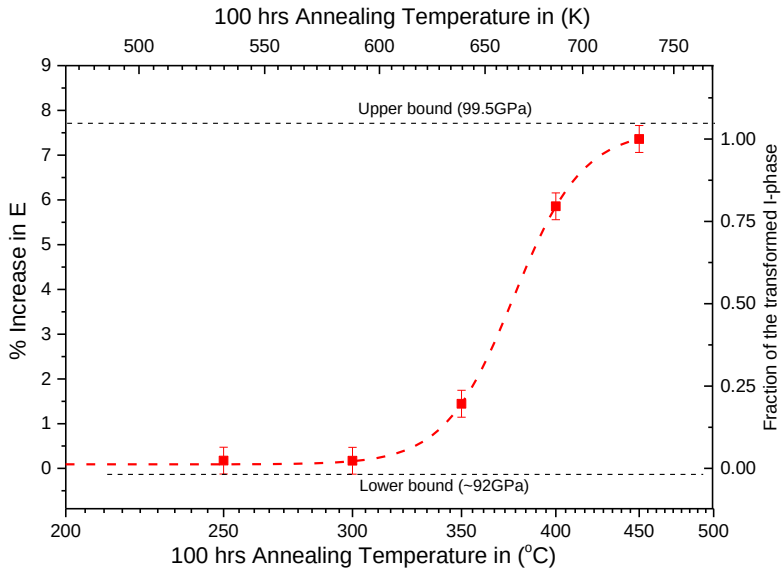

Figure 8.1 Percent change in E vs annealing temperature follows a sigmoidal curve. The curve is likely to shift to higher or lower temperature depending on the annealing time.

Inoue and Kimura (1999) and Yamasaki et al. (2007) observed that no I-phase transformation takes place even after 1000h annealing at 300°C in bulk extruded $Al_{93}Fe_3Cr_2Ti_2$ and $Al_{92.5}Fe_{2.5}Cr_{2.5}Ti_{2.5}$ alloys and it was also confirmed for up to 100hrs at the same temperature in the present work. The annealing at 450˚C for 100h showed that I-phase has been completely transformed as observed in section 5.2. These results are also in agreement with those observed on melt-spun $Al_{93}Fe_3Cr_2Ti_2$ alloys by Audebert et al. (2002) and Galano et al. (2009b).

8.2.2 Effect of the I-phase and its transformation on the microhardness and tensile properties

Figure 8.2 shows the microhardness, UTS and yield strength of the NQX alloy in 'as extruded' and 'annealed' conditions. These results are reproduced from section 6.3 and 6.4, in order to discuss the effect of I-phase and its transformations on the mechanical properties of the NQX alloy.

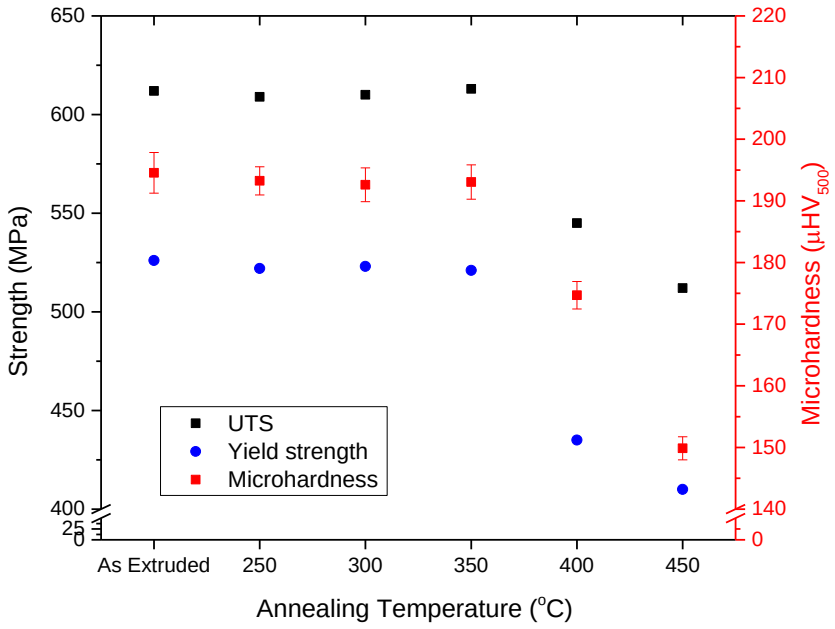

Figure 8.2 UTS, yield strength and microhardness for 'as extruded' and after 100h annealing condition at various temperatures.

8.2.2.1 'As extruded' condition

Room temperature tensile strength of the 'as extruded' alloy was found to be in the range from 598MPa to 640MPa, for the strain rate range from 10^{-5} to$10^{-2}s^{-1}$. In a similar alloy but slightly higher Al content ($Al_{93.3}Fe_{2.9}Cr_{1.8}Ti_{1.9}$) and at a strain rate of $4x10^{-4}$ s^{-1}, Rounthwaite (2012) obtained a tensile strength of 545MPa (11% lower than present work). Chlupová et al. (2011) obtained a strength value of ~595MPa at a crosshead speed of 0.5mm/s in a similar alloy. Comparative room temperature tensile strength values for some of conventional Al alloys are given as: Al2014-T6 (290MPa), Al2024-

T6 (485MPa), Al4032-T6 (260MPa), and Al7075-T6 (~570MPa) (ASM, 1990). The tensile strength of the bulk extruded NQX alloy is 5-10% higher than the high strength 7075-T6 alloy.

Average microhardness value for the 'as extruded' alloy was 195±3 μHV_{500}. In comparison, Rounthwaite (2012) observed a value of 174μHV_{500} (11% lower) on an extruded alloy of alloy but slightly higher Al content ($Al_{93.3}Fe_{2.9}Cr_{1.8}Ti_{1.9}$) extruded at different temperature ($T_{extrusion}$=375^{o}C) having some aluminium contaminations. Todd et al. (2004) found a value of 169μHV_{25} for 25-50μm powder size, extruded $Al_{93}Fe_3Cr_2Ti_2$ alloy using a very low load value. Variation in alloy composition, powder fraction size, presence and quantity of soft contaminants or inclusions in the alloy, extrusion ratio, extrusion temperature, extrusion speed, and most importantly load used for microhardness tests may result in different values of the microhardness and/or tensile strength in the similar bulk extruded alloys. This is why the comparison of absolute values of the strength or microhardness may slightly vary across different studies; however, the values within each single study were consistent.

8.2.2.2 'Annealed' condition

Post annealing room temperature tensile/microhardness behaviour can be correlated to the NQX alloy microstructure (Table 5.6).

The microhardness values for 'as extruded', 250°C/100h, 300°C/100h, and 350°C/100h samples are equal (~193μHV_{500}). These results are in agreement with those observed in the literature. Rounthwaite (2012) heat treated a similar alloy at 250°C for 57hrs, whereas Inoue and Kimura (1999) performed heat treatment on a similar alloy at 300°C for up to 1000hrs, no changes in the values of microhardness were observed in both cases.

The trend of the drop in the microhardness values matches with the microstructural changes related to the I-phase transformation as a result of the annealing temperature. The microhardness value dropped by 11% ($175\mu HV_{500}$) and 23% ($150\mu HV_{500}$) in 400°C/100h and 450°C/100h samples respectively. These samples correspond to the highest annealing temperatures.

In the absence of any microstructural changes the observation that the microhardness values of the 250°C/100h, and 300°C/100h samples were equal to the 'as extruded' alloy points out that there were very little residual stresses present in the 'as extruded' alloy as the alloy was extruded at a very high temperature. The drop in the bulk alloys at very high annealing temperature was primarily due to the growth of intermetallic particles (section 8.2.3).

Similar to the microhardness or the elastic constants trends, the tensile curves for the 250^{o}C/100h, 300^{o}C/100 and 350^{o}C/100h samples were nearly identical to the 'as extruded' tensile curves (section 6.4). In 400^{o}C/100h and 450^{o}C/100h annealed samples the tensile strength drops by 11% (to 545MPa), and 16% (to 512MPa) respectively. The NQX alloy exhibited an unmatched superiority in sustaining elevated temperature annealing treatments as compared to the commercial Al alloys. The NQX alloy shows no change in the mechanical behaviour after a 100h annealing at 300°C. On the other hand, after the same 100h annealing treatment the strength of Al2014-T6, Al2024-T3, Al6061-T6 and Al7075-T6 has been reported to drop by 55%, 46%, 55% and 58% respectively in comparison with their room temperature strength (Rice, 2003).

8.2.3 Strengthening mechanisms at room temperature in the NQX Alloy

This section attempts to estimate the strength contribution by each of the strengthening mechanism using existing models, and compares the calculated yield strength with the experimentally measured yield strength.

8.2.3.1 Major contributors to strengthening

8.2.3.1.1 Grain boundary (GB) strengthening

The grains sizes on a polished planar surface were measured by EBSD, for both the longitudinal and cross section directions. The longitudinal grains were slightly longer than the cross section grains and these could be assumed to form a hypothetical cylinder. The diameter of an equivalent sphere, having the same volume as the cylinder, can be found by $D_{v,equivant} = \sqrt[3]{1.5 D_{long} D_{x-\sec}^2}$. This equivalent sphere diameter was used as the grain size (D) in the Hall-Petch equation (Eqn. 8.5) to estimate the GB strengthening contribution ($\Delta\sigma_{g.b}$) by the grains in the NQX alloy (Hall, 1951, Petch, 1953) (see details in section 2.3.2).

$$\Delta\sigma_{g.b} = \frac{K_{H.P}}{D^x} \qquad \textbf{Eqn. 8.5}$$

where $K_{H.P}$ is the Hall-Petch coefficient, x is the grain size exponent.

There are certain limitations in applying the Hall-Petch equation. The NQX microstructure consists of a range of grain sizes. The larger and/or favourably oriented grains undergo plastic deformation earlier as compared to the smaller and/or unfavourably oriented grains. The yielding occurs over a strain range and the '0.2% yield strength' is rather an approximation of initial deviation from elastic to plastic regime (Miller, 2012). The value of $K_{H.P}$ has been reported to differ in coarse grained and ultrafine grained materials (Pineau et al., 2016). $K_{H.P}$ for aluminium alloys have been reported to exist in

a wide range of values, from 0.07 to 0.28 MPa√m (Thangaraju et al., 2012). $K_{H.P}$ Value for the NQX alloy was; therefore, required to be used from the RS Al-TM bulk alloys containing a comparable microstructure. Brahmi et al. (1997) measured the value of $K_{H.P}$ as 0.171MPa√m in an RS Al-Cr alloy on grain sizes from ~0.69μm to 1.32μm. Ehrström and Pineau (1994) used a value of 0.15MPa√m in an RS Al-Fe alloys; whereas, Frazier and Koczak (1988) measured a value of 0.165MPa√m an Al-Ti alloy. As the grain sizes in NQX alloy were measured to be similar sizes as observed by Brahmi et al. (1997) in an RS Al-5Cr-2Zn (wt%) alloy, in the present study a K_{HP} value of 0.171MPa√m were used.

The value of grain size exponent (x) is 1/2 in the original Hall-Petch equation, and the same value has been used most extensively, although it was noted that other fits were also possible. Baldwin (1958) proposed exponent (x) as 1, and 1/3, whereas Conrad (1963) proposed an exponent value of 1/4 which also resulted in a straight line in the plots of σ_y vs $1/D^x$. Recently, Dunstan and Bushby (2014) used a large body of literature data for several materials (not including aluminium) and fitted grain exponents of 1, 1/2 and 1/4 and obtained straight line plots. However, $K_{H.P}$ was used as a fitting parameter and therefore, was adjustable. Since $K_{H.P}$ values are only known for the exponent value of 1/2 in the RS Al-TM alloys, and the exponent 1/2 is known to be experimentally valid for an extensive experimental data set; therefore, the same exponent has been used in the present study.

The calculations for Hall-Petch contribution are provided in Table 8.7. Hall-Petch contribution is a substantial component (~>46%) of the total alloy strength. It only drops by a small amount (~17MPa) even after 100h annealing at elevated temperatures due to the absence of any appreciable grain growth. GB strengthening has been considered one of the main mechanisms in the RS Al-Fe-X (X=Mo-Zr or V-Si) alloys by

Ehrström and Pineau (1994). Similarly, Vojtěch et al. (2007) estimated 83% of RS Al-Fe-Cr-Ti-Si alloy strength due to the GB strengthening.

Table 8.7 Calculated strength contribution due to grain boundaries.

Sample	Measured Planar Grain Diameter		Equivalent Sphere Diameter	$\Delta\sigma_{g.b}$ (MPa)
	D_{Long}	D_{Xsec}	$D_{v,\ equivalent}$	
As Extruded	471	432	507	240±40
250°C/100h	475	409	492	244±42
300°C/100h	485	426	509	240±40
350°C/100h	471	434	511	239±40
400°C/100h	502	439	526	236±38
450°C/100h	528	509	590	223±32

Error in D_{planar} is of the order of ~170nm.

8.2.3.1.2 Particles dispersion strengthening

The other major strengthening contribution is provided by various intermetallic particles distributed in the aluminium matrix. The microstructure (volume fraction, particle sizes and distribution) has been already discussed in sections 4.3.6 and 5.3.2. The strengthening contribution due to particles can be calculated by modified Orowan's equation given as Eqn. 8.6 (Brown and Ham, 1971) (see section 2.3.3).

$$\Delta\sigma_p = M\frac{0.4Gb}{\pi(1-\upsilon)^{1/2}}\frac{\ln\left(\frac{D_{p,s}}{b}\right)}{\lambda_s} \qquad \textbf{Eqn. 8.6}$$

where υ is Poisson's ratio, $D_{p,s}$ is the mean planar particle diameter which is √(2/3) times the mean particle diameter (D_p) (Brown and Ham, 1971), M is the average Taylor factor (found ~3.3 in section 4.3.5 and 5.2.5), b is the Burgers vector (0.286nm), λ_s is the interparticle spacing which was calculated using $D_{p,s}$ (section 4.3.6.3 and Table 5.5). The volume fraction, mean particle size (obtained from log normal distribution), mean planar particle size, mean planar edge to edge random distance between particles

and the calculated particle strengthening contribution value ($\Delta\sigma_p$) are provided in Table 8.8. The average particle size increases in the samples 400°C/100h, and 450°C/100hr causing a reduction in the particle strengthening contribution as seen in Table 8.8.

Table 8.8 Calculation of strength contribution due to particle dispersion.

Sample	Volume Fraction	Mean Particle Diameter	Mean Planar Particle Diameter	λ_s (using $D_{p,s}$)	$\Delta\sigma_p$
	f_v	D_p (nm)	$D_{p,s}$ (nm)	nm	MPa
As Extruded	0.44	151±11	123	105	223±16
250°C/100h					223±16
300°C/100h					223±16
350°C/100h					223±16
400°C/100h	0.42	193±5	158	145	167±4
450°C/100h	0.42	239±9	195	180	140±5

Particle strengthening contribution is mainly dependent on the particle size and the interparticle distance. In a case of wide ranging particle size distribution the statistical analysis and the calculations may contain inherent errors. However as long as the particles are randomly distributed and statistically significant sample coverage is ensured these errors are not significant (Corti et al., 1974).

In the present study, an ideal microstructure of randomly distributed (but not clustered), randomly oriented and spherical particles have been assumed which may not be valid for some of the particle shapes found in 400°C/100h, and 450°C/100h samples.

8.2.3.2 Minor contributors to strengthening

8.2.3.2.1 Lattice friction and base strength

Lattice friction in the pure fcc metals is found to be very low (Chateau, 2011). Similarly, the yield strength of 99.99% pure aluminium has been reported to be 10MPa to 16 MPa (Ehrström and Pineau, 1994, Kendig and Miracle, 2002). In the present work, the base aluminium strength value (σ_o) has been used as 15MPa.

8.2.3.2.2 Solid solution strengthening

The foreign atoms in the matrix produce misfit strains which interact with the dislocations to cause the solid solution strengthening ($\sigma_{s.s}$).

The contribution of the solid solution strengthening to the yield strength can be estimated using a general equation of the form of Eqn. 8.7 (Ryen et al., 2006, Chateau, 2011).

$$\Delta\sigma_{ss} \approx K_{ss} c^{n_{ss}} \quad \textbf{Eqn. 8.7}$$

Where c is solute concentration, n_{ss} and K_{ss} are the material dependent constants. The value of exponent n_{ss} is in the range 0.5-0.75, which indicates that smaller additions cause a higher relative contribution (Ryen et al., 2006). K_{ss} provides the yield strength increase per at% for each element (Ryen et al., 2006) and its value depends on the matrix and solvent type (ASM, 1990, Campbell, 2008). The K_{ss} values of a few solutes in Al are known in the literature such as Mg (16MPa/at%) (Ryen et al., 2006, Campbell, 2008) Si(10MPa/at%), Zn (3MPa/at%) and Cu (16MPa/at%) (ASM, 1990). Fe, Cr and Ti have low solid solubilities in Al and K_{ss} values are not known at 1.0 at% level. Mahon and Marshall (1996) provided the yield strength increase as a result of 0.02 wt% Fe addition and 0.2% Ti solute addition in Al; however, these results cannot be extrapolated to 1.0 at% values. One important factor affecting the solid solution strength is the atomic size factor $(\delta_{sf})^F$. The δ_{sf} for Fe (-11%), and Cr (-11%) are nearly equal to that of Cu (-11%) and Mg (12%) whereas δ_{sf} of Ti (3%) is very close to that of Zn (5%). The K_{ss} for Fe, Cr and Ti was; therefore, assumed to be 16±3MPa/at%, 16±3MPa/at% and 5±3MPa/at% respectively and also the strength contributions have been assumed to add

[F] $\delta_{sf} = (r_{solute}-r_{Al})/r_{Al}$, where r is the atomic radii and its values are Al (143pm), Fe (128 pm), Cr (128 pm), Ti (147 pm), Mg (160 pm), Cu (128 pm), Zn (137pm) from 'Gale, W. F. and Totemeier, T. C. (eds.) (2003) *Smithells metals reference book*: Butterworth-Heinemann.

linearly. The assumptions were based on the strength behaviour of the elements of similar size factors in Al from literature (Totten and MacKenzie, 2003). The estimated solid solution strengthening values are provided in Table 8.9. As the annealing temperature is increased, the solute content in the matrix gets depleted and the overall solid solution strengthening contribution is reduced even further as seen in Table 8.9.

Table 8.9 Solid solution strengthening contribution in the Al matrix.

Sample	Total $\Delta\sigma_{ss}$ Contribution (MPa)
As Extruded	26±2
250°C/100h	19±2
300°C/100h	17±2
350°C/100h	17±2
400°C/100h	17±2
450°C/100h	10±1

The y-intercept of a Hall-Petch plot provides the information about the frictional stress (σ_o) and the $\Delta\sigma_{ss}$ term combined. This intercept in HP plots has been found to have small values in RS Al-TM alloys. For example, a value of 19MPa was observed by Brahmi et al. (1997) in RS Al-Cr-Zr alloy, resultantly the $\Delta\sigma_{ss}$ is expected to have even smaller value. Vojtěch et al. (2007) also considered a negligible value of $\Delta\sigma_{ss}$ in an RS Al-Fe-Cr-Ti-Si alloy. Similarly a small contribution was calculated in the present study.

8.2.3.2.3 Dislocation strengthening

The strengthening contribution is also supplied by the work hardening which is dependent on the dislocation density. The dislocation density in commercial Al systems after solution treatments or annealing can be around ~10^{10}-$10^{12}$$m^{-2}$ (Lumley, 2010) which increases during the mechanical tests up to ~10^{12}-$10^{13}$$m^{-2}$ after a few percent deformation, and up to 10^{15}-$10^{16}$$m^{-2}$ after heavy (cold) deformation (Smallman and Bishop, 1999). Dislocation density values for the NQX alloy extruded at 400°C could not be found in the open scientific literature. However, it is known that during elevated

temperature deformation, the effect of dislocation multiplication is countered by recovery, an evolution of recovered sub-grain structure has the dislocation density values around ~$10^{10}m^{-2}$ (Lumley, 2010). The values of microhardness, yield strength and UTS in the 'as extruded' and annealed samples (250°C/100h, and 300°C/100h) were equal and all of these had similar microstructures. Therefore, it was deduced that the dislocation densities in all these samples also have similarly low values. The yield point occurs around ~1% of the total strain and has a small corresponding plastic strain. A dislocation density of ~$2x10^{12}$ m^{-2} has been observed by Hansen (1977) at ~1% strain values in the annealed Al samples. The dislocation density value of the similar order of magnitude (~$2x10^{12}$ m^{-2} to 10^{13} m^{-2}) was assumed at the yield point (ε<~1%) in the NQX alloy and the strengthening contribution (σ_{dis}) using Taylor's equation (Eqn. 8.8) was calculated to be ~7 to16 MPa respectively.

$$\Delta\sigma_{w.h} = \alpha_{w.h} MGb\sqrt{\rho}_{dis} \qquad \textbf{Eqn. 8.8}$$

Where $\Delta\sigma_{w.h}$ is the contribution to flow stress due to work hardening, $\alpha_{w.h}$ is a pre-factor ~0.2 (Totten and MacKenzie, 2003), M (3.3) is Taylor's factor, G (26GPa) is the shear modulus, b (0.286 nm) is the Burgers vector.

8.2.3.3 Experimental and calculated strength comparison

The strength contribution by each mechanism in various samples is summarised in Table 8.10. The superposition of the strengthening contribution by various mechanisms can be calculated using linear, Pythagorean or general approaches[G] (Kocks, 1985, De Vaucorbeil et al., 2013). A linear addition assumes that the operative length scales and the obstacle strengths of the involved mechanisms are different, so the contribution of each mechanism is independent of the others. The total strength can be assumed to be

[G] Linear: $\sigma_{Total} = \sigma_1 + \sigma_2$, Pythagorean: $\sigma^2_{Total} = \sigma^2_1 + \sigma^2_2$, General: $\sigma^n_{Total} = \sigma^n_1 + \sigma^n_2$ (n is between 1 to 2)

an arithmetic sum of all the individual contributions (Kocks, 1985). This is the most widely used method in the literature for the calculation of total strength of Al-based alloys with the ultrafine grain size. In Pythagorean addition, the root-mean-square of the individual contributions is used, considering that the obstacle strength and the operative length scales of the mechanisms are the same, and the mechanisms interact with each other (Kocks, 1985). Linear and Pythagorean approaches were used for the addition of strength contribution by mechanism, and results of linear approach provide better results as seen in Table 8.10. Theoretically calculated results are comparable with the experimental yield strength value(s) for all the samples. In the present study, it was assumed that the strengthening mechanisms especially particle strengthening and GB strengthening act independently of each other. The linear addition results provide a better estimate in comparison with the experimental yield strength in the present case as seen in Table 8.10. Figure 8.3 graphically shows the percentage strength contribution by each mechanism in the calculated NQX alloy strength. Combined both the GB and particle strengthening mechanisms account for >89% of the strength of the alloy.

The microstructure in all these calculations has been assumed to be ideal, and several assumptions[H] have been made for the addition of strengthening contribution.

[H] **Assumptions:** 1. All the particles are spherical, randomly oriented, and randomly distributed in the sample. 2. Particle size distribution of as extruded 250°C/100h, 300°C/100h and 350°C/100h samples is similar and can be described with 'log normal' distribution. 3. The operative length scales and obstacle strength of various strengthening mechanisms are different and their strength can be assumed to be linearly added. It is to be noted that the mean planar inter particle 'random' distance used in the present work is a more conservative guess as compared to the mean planar interparticle distance for 'uniformly distributed' particles. The latter predicts smaller distance (λ) and higher $\sigma_{particle}$.

Table 8.10 Calculated strengthening contributions due to various mechanisms and experimentally measured yield strength.

Sample	Strength Contribution (Calculated)					Total Calculated Strength	Experimental
	σ_o	$\Delta\sigma_{ss}$	$\Delta\sigma_{dis}$	$\Delta\sigma_{gb}$	$\Delta\sigma_p$		σ_{yield}
As Extruded	15	26±2	16	240±40	223±16	520±44	526
250°C/100h	15	19±2	16	244±42	223±16	517±46	522
300°C/100h	15	17±2	16	240±40	223±16	511±44	523
350°C/100h	15	17±2	16	239±40	223±16	510±44	521
400°C/100h	15	17±2	16	236±38	167±4	451±39	435
450°C/100h	15	10±1	16	223±32	140±5	404±33	410

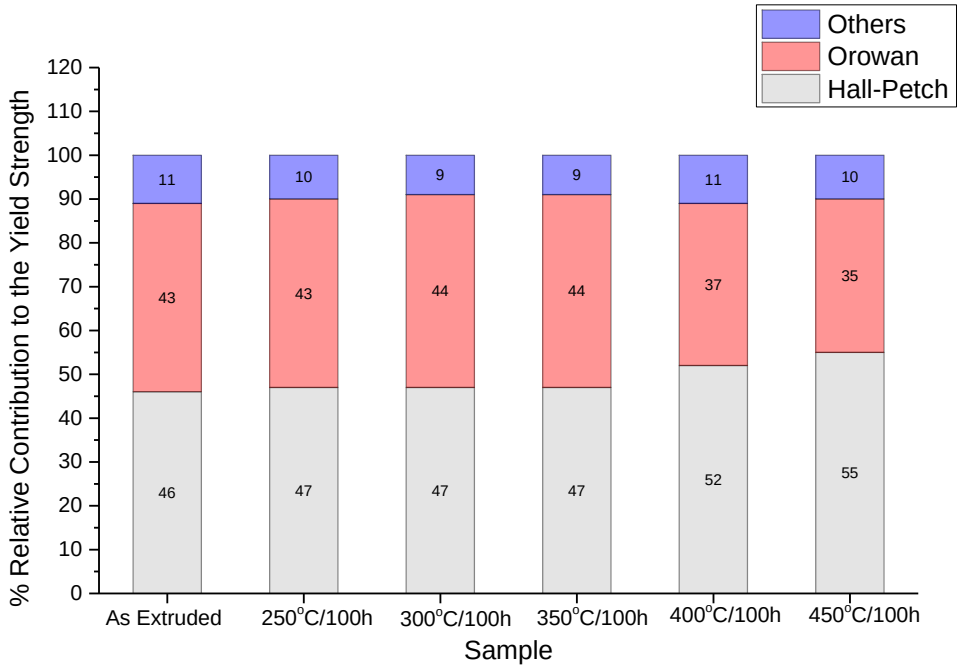

Figure 8.3 Percentage calculated strengthening contribution of various mechanisms in 'as extruded' and 'annealed' samples.

8.3 Elevated Temperature Tensile Behaviour

8.3.1 Strength comparison of the NQX alloy with conventional Alloys

Tensile testing of the extruded NQX alloy on a wide range of temperatures (23^{o}C-500^{o}C) and multiple quasi-static strain rates helped to understand the mechanical behaviour. The alloy has a smooth decrease in the strength with increasing temperature in comparison with conventional Al alloys which suffer a rapid strength drop with increase in temperature beyond 150^{o}C. Figure 8.4 shows the UTS vs temperature graph of the NQX alloy at four strain rates; the UTS decreases smoothly over the test temperature range. The NQX alloy has 3 to 8 times higher strength than conventional Al alloys at elevated temperatures (~300^{o}C) as seen in the Figure 8.4.

Elevated temperature strength along with the thermal stability potentially makes the NQX alloys a strong candidate for elevated temperature applications. The following section deals with the elevated temperature plasticity behaviour.

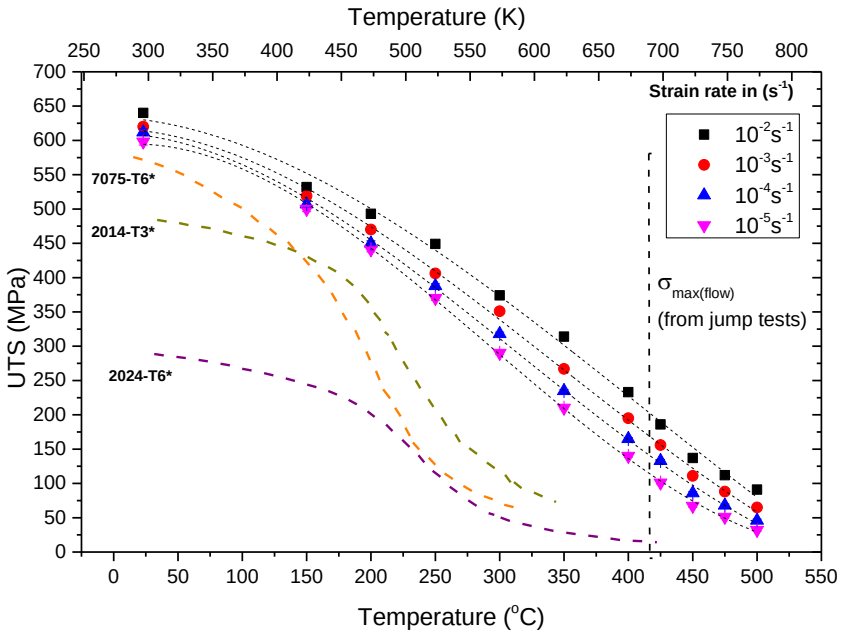

Figure 8.4 UTS of the NQX alloy at various temperatures and strain rates. Strength behaviour for three conventional Al alloys is also shown from literature (ASM, 1990, Rice, 2003).

8.3.2 Elevated temperature plasticity (250-500°C)

Rate dependent plastic mechanisms in the NQX alloy can be investigated using data from the flow curves. In section 7.4.3 the strain rate sensitivity (m) and stress exponent (n_{se}) were calculated at a fixed strain in order to consistently include the tests having low ductility. The region from ~150-250°C displayed dynamic strain ageing behaviour and mostly caused early fractures well before the steady state was achieved and this is discussed seperately in section 8.3.3.

In chapter 7 it was also observed that a steady state stress level were achieved in 300°C and 350°C tests and also a quasi steady state for most tests at 250°C (section 7.2), and all samples up to 350°C tests contain the I-phase (section 7.2.1). An I-phase transformation takes place during the 400°C tests[I] and all the jump tests (425, 450, 475 and 500°C) have an I-phase tranformed microstructure (section 7.2.1). To analyse the elevated temperature plasticity more accurately, steady state stress values have been used in this section for all temperatures[J].

In the following sections an attempt has been made to explain the elevated temperature plasticity behaviour of the NQX alloy in two regions

(i) 425-500°C[K] (I-phase transformed) region. (ii) 250-350°C[L] (I-phase containing) region.

[I] 400°C behaviour has been shown in graphs for the continuity but not included in any discussion as it contains a significantly changing microstructure during the tests.

[J] 250C tests were found reaching a quasi-steady state, so their maximum stress values have been used

[K] 425-500°C region (i) I-phase has been transformed, (ii) a steady state is achieved, (iii) power law creep is present. Further, 400°C tests were not included as a phase transformation occurred during those tests.

[L] 250-350°C region (i) contains stable I-phase (ii) a steady state flow stress is achieved for most tests, (iii) it is present in both power law breakdown and power law creep regions (see section 8.3.2.2), and (iv) it is the extreme upper end of any Al based application.

8.3.2.1 Application of Zener-Hollomon model

The requirement to predict the mechanical behaviour necessitates data fitting in a mechanical model. A phenomenological model, presented by Zener and Hollomon (1944), has been extensively used in literature to explain the elevated temperature plastic flow behaviour, and it can be applied to a wide range of stresses. Sellars and McTegart (1966) modified the model in the form of Eqn. 8.9 which equates the strain rate ($\dot{\varepsilon}$), stress (σ) and temperature (T) in a single relation.

$$\dot{\varepsilon} = A_{zh} F(\sigma) e^{\left(-\frac{Q}{RT}\right)} \qquad \textbf{Eqn. 8.9}$$

Where A_{zh} is a constant and $F(\sigma)$ is a function of applied stress with the following possibilities (Lin and Chen, 2011) :

(i) $F(\sigma) = \sigma^{n_{se}}$, if $\alpha\sigma < 0.8$ (low stresses)

(ii) $F(\sigma) = e^{(\beta\sigma)}$, if $\alpha\sigma > 1.2$ (high stresses)

(iii) $F(\sigma) = [\sinh(\alpha\sigma)]^{n_{zh}}$, for all stress ranges of $\alpha\sigma$ such that

$$\alpha \approx \frac{\beta}{n'} \approx \frac{\beta}{n_{zh}} \qquad \textbf{Eqn. 8.10}$$

The activation energy Q for the plastic flow can be found by

$$Q_{app} = R\left[\frac{\delta \ln\{Sinh(\alpha\sigma)\}}{\delta(1/T)}\right]\left[\frac{\delta \ln(\dot{\varepsilon})}{\delta \ln\{Sinh(\alpha\sigma)\}}\right] \qquad \textbf{Eqn. 8.11}$$

Zener-Hollomon parameter (Z) is then calculated as

$$Z = \dot{\varepsilon} e^{\left(\frac{Q}{RT}\right)} = A_{zh}[\text{Sin h}(\alpha\sigma)]^{n_{zh}} \qquad \textbf{Eqn. 8.12}$$

The slope of the Z vs Sinh(ασ) plot on a log-log scale provides the stress exponent for ZH model (n_{zh}) and intercept provides the constant ln(A_{zh}). Where α, β, A_{zh} are the constants, n', n_{zh} are the stress exponents, Q is the activation energy. n' is the average slope of the log- log plot of $\dot{\varepsilon}$ vs σ_{ss} in a given temperature range and β is the average slope of semi-log plot of $\dot{\varepsilon}$ vs σ_{ss} in a given temperature range. α is an adjustable parameter, and its average value is found for the temperature range using Eqn. 8.10.

The model was applied separately to both the temperature regions, and the detail of the plots is provided in appendix 4. The final graphs, containing plots of Z vs Sinh(ασ), have been provided with all calculated parameters[M] for 300-350°C region (Figure 8.6) and 425-500°C (Figure 8.5).

The Q_{app} in section 7.4.4 for 250-350°C region was from ~225-305kJ/mol, which is close to the Q found by the Zener-Hollomon model (324kJ /mol). n_{zh} has been found having a higher value (~18) for this temperature region similar to those found in section 7.4.3 (~45-17), indicating a higher flow stress values.

n_{zh} and Q values in 425-500°C region are ~6 and 489kJ/mol respectively, which are comparable to the values calculated in section 7.4.4 for the same temperature region (n~10.6 to 6.3, and Q~405±77kJ/mol). A value of stress exponent value close to ~5 indicates a climb controlled mechanism (Tjong and Mai, 2003).

[M] 'Pearson's correlation coefficient' or 'Pearson's r' is mentioned in the graphs and text. It provides the information about the linear dependence of two variables. A value of 1.0000 means a total positive correlation and '0.0000' means no correlation between variables.

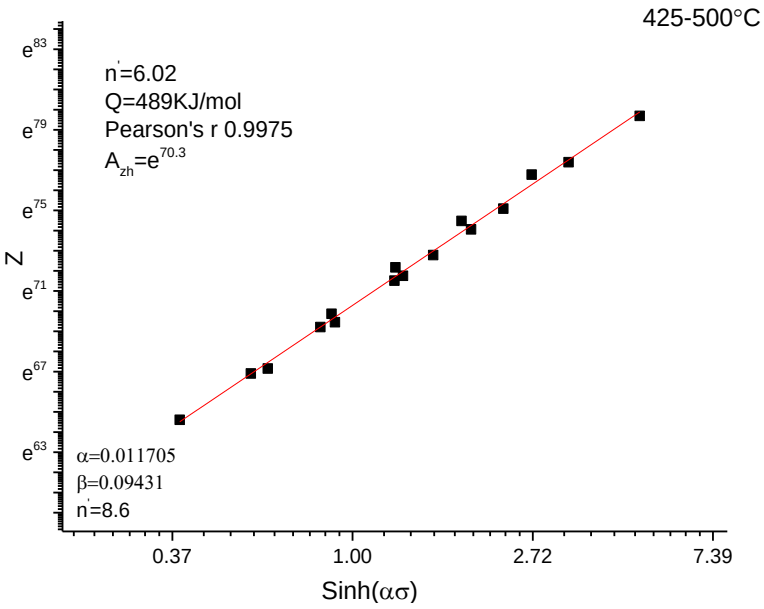

Figure 8.5 Z vs Sinh(ασ) on a log-log scale in 425-500°C region, a summary of all parameters is provided. n_{zh} value is ~6.0.

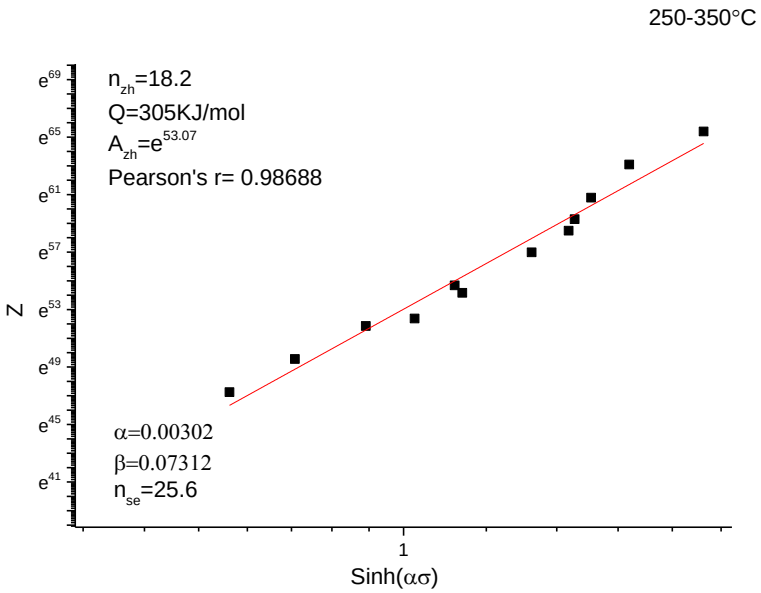

Figure 8.6 Z vs Sinh(ασ) on a log-log scale in 250-350°C region, a summary of all parameters is provided. n_{zh} value is ~18.2.

8.3.2.2 Power law creep and power law breakdown

At elevated temperature materials show a rate dependent plasticity behavior such that $\dot{\varepsilon} \propto (\sigma)^{n_{se}}$, which is known as power law creep (see section 2.7). Figure 8.7 shows the plot of lattice diffusion (D) compensated strain rates vs modulus compensated steady state stresses for the NQX alloy data which results in straight line at each temperature whose slope provides the n_{se}.

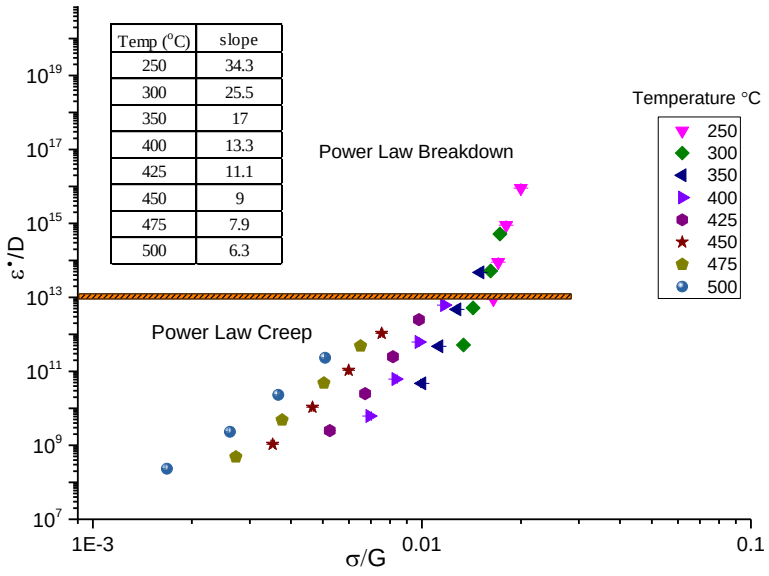

Figure 8.7 Normalised strain rate plotted against normalised stress for the NQX alloy. PLB can be coarsely assumed to occur above ε̇/D=10^{-13} m^{-2} after Mishra (1992).

Frost and Ashby (1982) constructed deformation mechanism maps for various materials and showed that the power law creep occurs in a certain temperature and strain rate regime. At higher stressess, the mechanisms change from dislocation climb to dislocation glide such that stress has an exponetial relationship with strain rate ($\dot{\varepsilon} \propto \exp^{\alpha\sigma}$), and power law creep equation does not hold, this is called 'power law breakdown' (PLB). In pure metals, the PLB occurs around σ/G ~10^{-4}-10^{-3} (Frost and

Ashby, 1982). Arieli and Mukherjee considered the PLB to occur if $\dot{\varepsilon} / D \geq 10^{-13} m^{-2}$ (Mishra, 1992); whereas Lesuer et al. (2000) use an effective diffusion coefficient[N] (D_{eff}) instead and maintained the same criteria (provided in appendix 4).

A straight line at $\dot{\varepsilon}/D=10^{-13}m^{-2}$ was also used to coarsely indicate the start of the PLB as mentioned above, although in reality the boundaries of PLB and power law creep may be diffused and both mechanisms might have been operative simultaneously in that region. Thus, all 250°C-350°C tests are divided in both power law creep and PLB regions whereas all the tests in 425-500°C temperature range are in power law creep region.

The simple power law creep relation (Figure 8.7) failed to get the data converged on a single line which necessitates the requirement of the application of further advanced models and this is deliberated in the following section.

8.3.2.3 Application of threshold stress model

High values of stress exponent and activation energies present in dispersion strengthened alloys are generally rationalised using the concept of threshold stress (σ_{th}). Lund and Nix (1976) explained that the total applied stress should exceed a threshold value in order to produce creep in a dispersion strengthened alloy and below this threshold stress (σ_{th}) the creep was assumed to be absent. The original creep equation (Eqn. 8.13) can be re-written such that applied stress (σ) is replaced by the effective stress (σ-σ_{th}) as seen in Eqn. 8.14 (Mukherjee, 2002).

$$\dot{\varepsilon} = C_3 \frac{Gb}{kT} D_o \left(\frac{\sigma}{G} \right)^{n_{se}} e^{\left(-\frac{Q}{RT} \right)} \qquad \textbf{Eqn. 8.13}$$

[N] Diffusion coefficient is $D = D_o e^{\left(-\frac{Q}{RT}\right)}$, and $D_{effective} = f_{pipe} D_{pipe} + f_{lattice} D_{lattice}$, , where f_{pipe} is fraction of pipe diffusion which equals ~$50(\sigma/E)^2$. Also for Al, $D_{o,pipe}=2.8x10^6$ m^2/s, and $Q_{pipe}=82kJ/mol$, $D_{o,lattice}=1.7x10^4$ m^2/s, and $Q_{pipe}=142kJ/mol$. At elevated temperatures $f_{lattice}$~1. The plot using $D_{effective}$ is shown in appendix 4, and it is similar to Figure 8.7.

$$\dot{\varepsilon} = C_3 \frac{Gb}{kT} D_o \left(\frac{\sigma - \sigma_{th}}{G} \right)^{n_{se}} e^{\left(-\frac{Q}{RT}\right)}$$ **Eqn. 8.14**

Where $\dot{\varepsilon}$ is the steady state strain rate in steady state creep, n_{se} is the stress exponent, Q is the activation energy, T is the temperature (in K), σ_{th} is the threshold stress, C_3 is a constant, D is diffusion coefficient such that $D = D_o e^{\left(-\frac{Q}{RT}\right)}$ where D_o is the frequency factor, G is the shear modulus, k is the Boltzmann constant, b is the Burgers vector.

The threshold stress model was applied to explain the high n_{se} and Q of the NQX alloy. The σ_{th} was found by assuming the values of n_{se} having some physical sense (e.g. n~ 3, to 8) (Peng et al., 1999). $\dot{\varepsilon}^{1/n}$ is then plotted against σ_{ss} (Lagneborg and Bergman, 1976) for various values of n_{se}(3, 5, 6, 7, 8) for both temperature regions (e.g 250-350°C and 425-500°C). Straight lines are obtained whose x-intercept yields the threshold stress value for the particular temperature (graphs in appendix 4), the values are provided in Table 8.11. Pearson's correlation coefficients of these straight lines are provided in Table 8.12. Finally, to plot Eqn. 8.13, modulus normalised effective stress $(\sigma-\sigma_{th})/G$ was calculated and plotted on x-axis vs the normalised strain rate term $\dot{\varepsilon}/(DGb/kT)$ on y-axis at various temperatures (Figure 8.8 to Figure 8.10).

Table 8.11 Values of threshold stress found by assuming various values of n_{se} (graphs in appendix 4)

Temp (°C)	n_{se} =8	n_{se} =7	n_{se} =6	n_{se} =5	n_{se} =3
250	315	326	339	350	294
300	231	244	257	270	210
350	136	152	167	182	141
400	74	88	102	115	105
425	42	55	68	81	105
450	13	24	35	46	67
475	0	10	20	30	49
500	-10	-2	6	14	30

Table 8.12 Pearson's coefficient for various values of n_{se}, from plot of $\dot{\varepsilon}^{1/n}$ vs σ_{ss} (graphs in appendix 4)

Temp (^oC)	n_{se} =8	n_{se} =7	n_{se} =6	n_{se} =5	n_{se} =3
250	0.98951	0.99186	0.98079	0.99727	0.99909
300	0.9863	0.98414	0.99921	0.97528	0.94609
350	0.99974	0.99971	0.9958	0.99769	0.98403
400	0.9986	0.99759	0.98998	0.99251	0.97252
425	0.99483	0.99293	0.99523	0.98511	0.95946
450	0.99837	0.99721	0.99583	0.99167	0.97048
475	0.99871	0.99767	0.99911	0.99247	0.97195
500	1.000	0.99981	0.98079	0.99728	0.98237

8.3.2.3.1 425-500°C region

The values of the Pearson's correlation coefficients suggested that higher n_{se} values (7 and 8) have a better fit. However, it can be observed in Table 8.11 that the threshold stress values were negative for n_{se}=7 or 8 at 500°C, which has no physical meaning; therefore, corresponding σ_{th} were discarded. In this n~6 provided a best compromise without any negative σ_{th} and resulted in fairly high values of Pearson's coefficient. As seen in normalised strain vs normalised effective stress plots in Figure 8.8 and Figure 8.9, the data for 425-500°C region converges on a single line which has a resulting slope of ~5.7 (Figure 8.8 and Figure 8.9). Effective stress values for n_{se}=6 are provided in Table 8.13.

Table 8.13 Effective stress (σ-σ_0) at n_{se}=6.

$\dot{\varepsilon}$ (s^{-1})	10^{-2}	10^{-3}	10^{-4}	10^{-5}
Temperature (^oC)	**σ-σ_{th}**	**σ-σ_{th}**	**σ-σ_{th}**	**σ-σ_{th}**
250	68	45	36	19
300	61	28	35	25
350	82	57	34	25
400	122	77	54	41
425	127	102	61	40
450	155	107	75	47
475	138	99	69	41
500	128	95	66	37

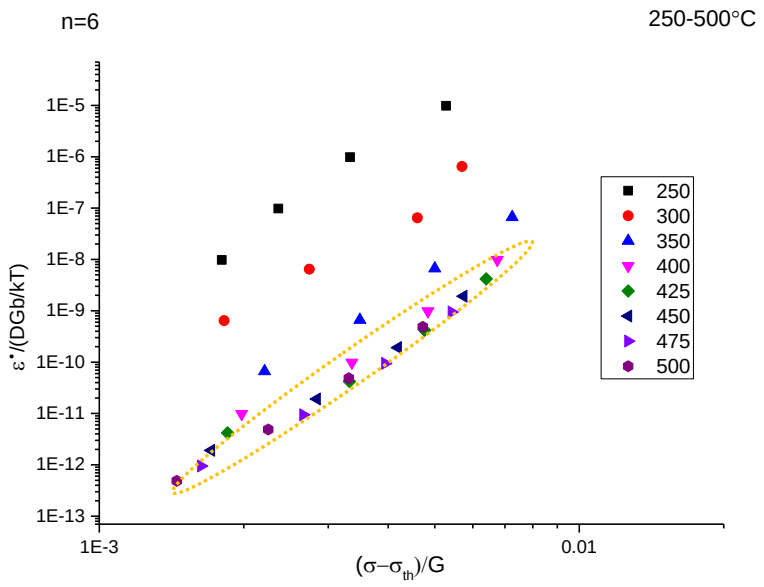

Figure 8.8 Normalised strain rate vs normalised effective stress after applying threshold stress model (n_{se}=6) for 250-500°C containing both temperature regions. A straight line can be fitted for the data in 425-500°C region (inside a dotted elipse) whereas 250-350°C data does not converge on a single line.

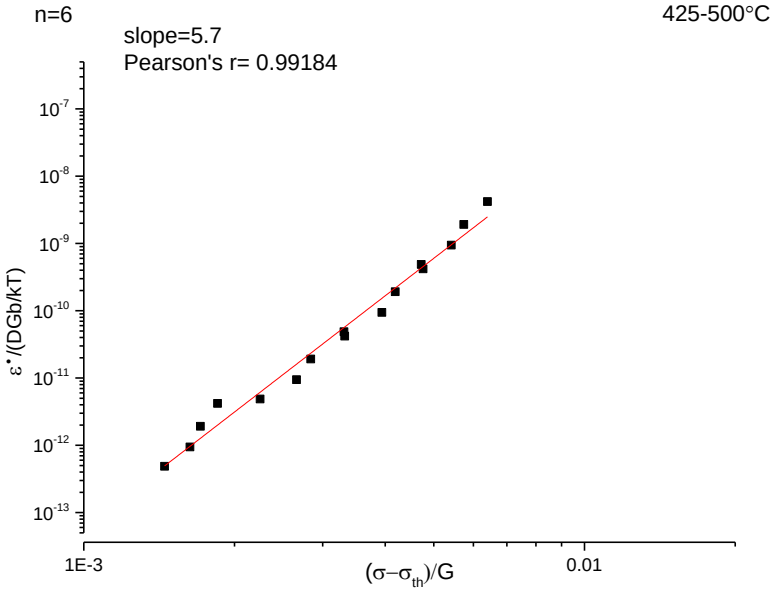

Figure 8.9 Normalised strain rate vs normalised effective stress at various temperatures after applying threshold stress model for both 425-500°C. Straight line has a slope of ~5.7.

8.3.2.3.2 250-350°C region

n_{se} values were used in a wide range n_{se}(3, 5, 6, 7, 8) and threshold stress values were obtained. In the normalised effective stress vs normalised strain rate plots the data for 250°C-350°C region does not converge on a single line for any value of n_{se}, although it remains close. This further confirms that this region is not fully governed by the power law creep equations, a condition already established from PLB criteria in Figure 8.7. However, an attempt was made to find some explanation of the mechanisms involved. (Galano et al., 2009a) had obtained n_{se}~7 while working on melt spun Al-Fe-Cr-X (X = V, Ta, Ti,) ribbons in the temperature range of 300-350°C. A value of n_{se}=7 was; therefore, used and threshold stress model was applied in the temperature range of 250-350°C as seen in Figure 8.10; additionally 400°C point was also added to make comparisons.

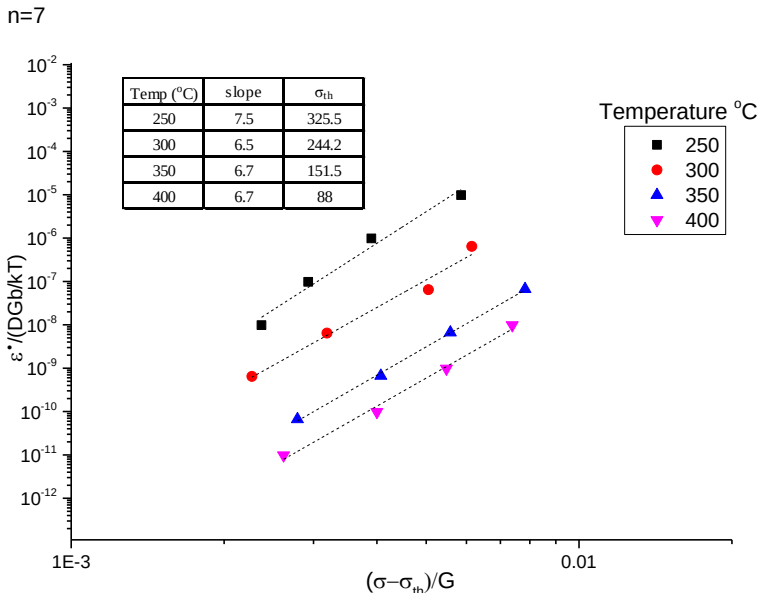

Figure 8.10 Normalised strain rate vs normalised effective stress after applying threshold stress model (n_{se}=7) for 250-400°C region. Data does not converge on a single line. However several separate straight lines were obtained.

Table 8.14 Effect of temperature on E_{Al} , σ_{th} and σ_{orowan}.

Temperature		Modulus of Al Matrix	Threshold Stress for n_{se}=7	Orowan's Stress at Temperature
T(°C)	T(K)	E_{Al} (GPa)	σ_{th} (MPa)	σ_{orowan} (MPa)
250	523	61.3	325	194
300	573	59.5	244	187
350	623	57.7	151	180
400	673	55.6	88	172

If the threshold stress model is assumed to be applicable in the 250-350°C region, then it can be seen in Table 8.14 that the associated threshold stress is related to temperature and also to the elastic modulus given as Eqn. 8.15 and Eqn. 8.16 respectively[O] (graph in appendix 4).

$$\sigma_{th} = 1237.4 - 1.74T \qquad \textbf{Eqn. 8.15}$$

$$\sigma_{th} = -2714.5 + 0.04961E \qquad \textbf{Eqn. 8.16}$$

A minimum stress is required for the dislocation glide, and in the presence of obstacles it is the Orowan's stress which is also modulus (and temperature) dependent (Table 8.14) similar to the σ_{th} behaviour. Thus, the σ_{th} can be considered to be related to the Orowan's stress. Higher values of σ_{th} (at 250-300°C) than the Orowan's stress are perhaps due to the presence of other obstacles to the dislocation glide such a grain boundaries and solute-dislocation locking. Lower values of σ_{th} (at 350-400°C) than the Orowan's stress probably mean that diffusion and subsequently, dislocation climb are becoming relevant which circumvents the need to bypass the particles by Orowan's mechanism.

8.3.2.4 Elevated temperature plasticity mechanisms in the NQX alloy

In order to improve creep performance and to produce alloys having a higher thermal stability and strength Knipling et al. (2006) stated the following criteria for the

[O] Increase in temperature results a decrease in elastic moduli, Orowan's stress as well the threshold stress.

constituents alloying elements in Al alloys: (i) the alloying elements must form strengthening phases, (ii) show low solid solubility in Al, and (iii) have a low diffusivity in Al. Mukherjee (2002) also noted that the addition of fine size, finely dispersed, high modulus, non-coherent (with the matrix) reinforced particles reduces the creep rates by several orders of magnitude. The NQX alloy containing ~44% volume fraction of the nano size, hard, icosahedral particles fulfill all these criteria. The alloy displays a superior elevated temperatures performance in comparison to conventional alloys (see Figure 8.4). Higher values of n_{se} and Q_{app} are associated with the dispersion strengthened (DS) metallic materials than the pure metals (Tjong and Mai, 2003).

At low temperatures and/or high stresses, dislocation glide is the main plastic deformation mechanism (Kuhn and Medlin, 2000). According to Mughrabi (1993), Orowan's bowing is the major mechanism during low temperature plasticity in the presence of hard dispersoids. At low temperature, a threshold stress (or yield limit) is introduced due to these hard dispersiods by the Orowan's mechanism, and below this threshold stress no dislocation glide occurs (Brown and Ham, 1971). Since bulk diffusion requires a higher activation energy so pipe diffusion and vacancy assisted diffusion (both having low activation energies) play an important role in deformation at low to intermediate temperature region (Hall, 1970). At elevated temperatures the dislocations have an extra degree of freedom and they can climb out of plane (over the obstacles) under the thermal activation. Similar to the concept of (yield stress), at intermediate stress/ high temperature regime the concept of threshold stress was postulated such that below this stress, creep should not theoretically occur for dispersion strengthened materials (Lund and Nix, 1976).

In this study the case of 425-500°C is relatively simple where the stress exponent values from both Zener-Hollomon and threshold stress models were found of the similar order,

~6. This indicates that that the 'dislocations climb' is the most likely the rate controlling mechanism in this high temperature region. It is consistent with the general observations in the dispersion strength alloys where n_{se} is ~6-8 and bulk diffusion takes place by vacancy exchange for the dislocation climb (Mukherjee, 2002). This must be kept in mind that the material in this region has transformed I-phase and it should be considered a different material than the I-phase containing alloy. At elevated temperatures, according to Arzt and Ashby (1982), the resistance to climb is proportional to volume fraction of second phase and the climb can be of two types. (i) At relatively higher stresses, a local climb (over individual obstacles) occurs, and the threshold stress is estimated to be higher (σ_{th}~$0.4\sigma_{orowan}$). (ii) For smaller stress and higher temperatures, the dislocation climb is of the order of interparticle spacing and the threshold stress value is small (σ_{th} ~$0.04\sigma_{orowan}$). In NQX alloy the ratio σ_{th} /σ_{Orowan} was calculated to be from 0.41-0.04 in 425-500°C region. It was also noted that Arzt and Ashby (1982) made the observations while working on the alloys with smaller volume fractions (up to 10%). The NQX alloy even in the I-phase transformed condition has a very high volume fraction (~42%) of the reinforcing particles and since threshold stress is considered to be volume fraction dependent, the NQX alloy has a higher Orowan's stress as well as high values of threshold stress, and subsequently a higher climb (or creep) resistance.

In the intermediate-high temperature region (250-350°C) both the PLB as well as the dislocation climb mechanisms are taking place simultaneously and seamless application of threshold model is met with difficulties due to the same reason. Coming from the power law creep side onto the PLB regime, the mechanism change from diffusion-controlled climb of dislocations to obstacle-limited dislocation glide regime (Frost and Ashby, 1982). Sherby and Young (1975) consider that contributions from excess

vacancies generated during deformation and the pipe diffusion play a major role during the PLB. In order to find the actual limit of the power law creep and the start of the PLB, further testing is required over 8-10 orders of magnitude of strain rates (e.g ~10^{-2} to $10^{-10}s^{-1}$) in the 250-350°C region, backed by the characterisation work.

The σ_{th} is strongly temperature dependent (decreases with temperature increase). Due to the same reason, questions have been raised about its 'physical sense', despite the ability of the model to successfully explain the creep behaviour of dispersion strengthened materials at elevated temperatures. In order to bring in the concept of actual physical sense Rösler and Arzt (1990) postulated another creep model in which it was suggested that an attractive attachment between the gliding/climbing dislocation and the particles exists, as the dislocation core can relax at the particle interface. The detachment of dislocation from the particle interface is thermally activated and it requires higher stresses than the local climb. Using this energetic consideration for dislocation detachment, the existence of threshold type stress can be justified. However; the model is applicable to coarse grained materials and it may have a limited applicability in the NQX alloy.

8.3.3 Dynamic strain ageing in the NQX alloy (150-250°C)

In chapter 6 and 7, anomalous behaviour was observed to be caused by dynamic strain ageing (DSA). Negative strain rate sensitivity, minima in ductility as well as in the SRS exponent, high hardening rate, anomalous yield strength behaviour and serrations were observed in the NQX alloy (section 7.4.6) as the manifestations of the DSA and these are discussed alongside the DSA mechanisms in this section. DSA is a commonly observed phenomenon in alloys and it is considered to be a rule than the exception (Abbaschian and Reed-Hill, 2008).

8.3.3.1 DSA mechanisms

The explanations and models of DSA have stirred up many intellectual debates over the decades and it is hard to find a single undisputable model / mechanism explaining the phenomenon. In a pioneering work, Cotrell postulated that the DSA was due to the interaction of mobile dislocations with diffusing solute atoms, and also calculated their interaction energies by assuming all interactions as linear, isotropic and elastic (Friedel, 1964, Hall, 1970). The solute diffusion is instrumental in this interaction; however, the bulk diffusion in itself is a slow process insufficient to cause the DSA at low temperatures. It was proposed that in substitutional alloys vacancies are created during the test and after reaching a critical strain the number of vacancies becomes sufficient to cause an enhanced diffusion (Friedel, 1964). Alternatively, it was also proposed that instead of the vacancy diffusion the pipe diffusion was the main reason for enhanced solute diffusion causing the DSA (Mulford and Kocks, 1979).

According to Cottrell's theory, only the solute drag could cause DSA; however, Sleeswyk (1958) modified it by considering that the dislocations get arrested at obstacles (such as forest dislocations), and whilst they wait for the thermal activation, the solutes can diffuse and pin the dislocation (ageing) to increase their strength. The corresponding contribution to the flow stress is 'anti-thermal', which increases with high temperature and low strain rate and causes a hump or a plateau in the flow stress vs temperature curve (Bouchaud et al., 1991). In the present work, a similar plateau or the yield strength anomaly was observed in the yield strength vs temperature from 23^{o}C to 200^{o}C (see Figure 7.28).

Waiting time (t_w) is the time when dislocations are arrested at obstacles and wait for the thermal activation to overcome those, aging time (t_a) is the time required by the solute to lock the dislocations (Bouchaud et al., 1991). The dislocations finally breakaway but

get arrested at other obstacles again and the process repeats itself. The waiting time for the dislocations is small at the start of the test; however, it increases with the strain and so does the interaction of the dislocations. The number of strain induced vacancies and/or the dislocations increase with increasing strain which enhances the solute diffusion (subsequently, the solute concentration on dislocation C_s also increases) and decreases aging time (McCormick, 1972). As a result, the serrations only appear after some initial straining as observed in the present work (see Figure 7.22 and 7.23). Penning (1972) mathematically proved that negative strain rate sensitivity is a crucial condition for the DSA and it has been widely accepted. Both the solute diffusion coefficient and the waiting time affect the 'Portevin Le Chatelier effect' (PLC). In addition, the solute diffusion (and its concentration on the dislocation called C_s) decreases due to increasing strain rate. Additionally, C_s also has a negative contribution to the strain rate sensitivity (SRS), which becomes more negative with increasing strain, at one stage the result in an overall negative SRS with unstable plastic flow and serrations appear (Van den Beukel, 1975). Solute concentration on the dislocation does not instantly acquire its final critical value C_s, instead it increases in a characteristic transient time τ_t. When a negative SRS is observed (DSA in operation) the transient time is of the order of waiting time $\tau_t \approx t_w$ and when the temperature is higher the transient is a small fraction of the waiting time $\tau_t << t_w$ (Bouchaud et al., 1991). The dislocation structure formation due to a low strain rate is different than that formed at a higher strain rate, and it affects the location of ductility minima ($T_{min\ ductility}$) (Bouchaud et al., 1991). This correlates to the present study in which $T_{min\ ductility}$ was observed at 200°C for $10^{-5}s^{-1}$ and at ~250°C for 10^{-3} and $10^{-4}s^{-1}$ (Figure 7.26). Moreover, the location of minima in the SRS ($T_{min\ SRS}$) was observed at 150°C (section 7.4.5). A similar observation has been made in the work of Skinner et al. (1989) and Bouchaud et al. (1991)

where the $T_{min\ ductility}$ was found to be slightly different than the $T_{min\ SRS}$ and was dependent on strain rate. The higher end of the DSA temperature range represents the most rapid and strongest dislocation immobilization, which results in a higher rate of dislocation accumulation (Rodriguez, 1984). This results in a lower ductility. At even higher temperatures the 'cloud' of solute concentration is not stable and rather 'evaporates', this is the reason for the observation that a certain type of impurity atoms cause the DSA in a specific temperature and strain rate range (Mughrabi, 1993).

Recently Curtin et al. (2006) presented a dislocation cross core mechanism using Monte-Carlo simulation in Al-Mg alloy. The model predicts a particular concentration of solute within the tension side (high concentration) and compression side (low concentration) of a dislocation core in Al-Mg alloys. This was observed by Aboulfadl et al. (2015) using atom probe tomography, on samples prepared from inside a PLC band. Most of the theories considering DSA in Al alloys have been formulated using strain hardening Al-Mg alloys which are tested to a high strain values.

Dislocation multiplication occurs during the tensile testing and provides the basis for DSA (Friedel, 1964). Regardless of what theory is applied for the explanation of DSA (vacancy-assisted diffusion or pipe diffusion), the diffusion during DSA is significantly faster than the bulk diffusion, and the latter is a comparatively slow process. In the present study, the (atomic) percentage of alloying elements in the Al (98.2±0.4) solid solution was found to be Fe (0.35±0.1), Cr (0.4±0.1), and Ti (1.05±0.2) at room temperature in the 'as extruded' condition (see Table 8.2). The amount of elements in solid solution is less than what is observed in common dynamically strain aging Al alloys (such as Al-Mg alloys); however, the PLC (or the DSA) requires only a small concentration of solute atoms at dislocations (Van den Beukel, 1975)

8.3.3.2 Strain rate sensitivity (SRS) and ductility minima

A negative value of the SRS exponent is considered the crucial condition for the occurrence of the DSA (Van den Beukel, 1975), in the present work this condition was observed at the strain rates of 10^{-4}-$10^{-5}s^{-1}$, at 150^{o}C . The occurrence of DSA in the present study is proved by the presence of minimum in the SRS, its negative value, and a coupled ductility minimum (section 7.4.5). The decrease in ductility is a consequence of negative SRS. Strain hardening is one of the factors affecting the ductility, as necking is delayed if strain hardening exponent is high (Ma, 2006). However, once the necking starts, a high strain rate hardening becomes instrumental in increasing the ductility of the material by offering resistance to the necking (Ma, 2006). Necking is another type of plastic instability in which the strain localises (to a small 'neck' region) during a tensile test (Antolovich and Armstrong, 2014). If the SRS exponent values are very high (e.g. m>0.5 as observed in superplastic materials), whenever a neck forms the local strain rate increases and the material strain hardens owing to a high m value. As a result the neck formation is resisted (Ma, 2006). In materials with a negative SRS the situation is reversed, instead of resisting the neck formation it is promoted instead, consequently, the material fractures much earlier (Bouchaud et al., 1991). In the NQX alloy, the DSA related anomalies were not only present where the negative m value was found but also found to be spread over a range of temperature. Mulford and Kocks (1979) also noted that DSA related anomalies are present on a wider range of temperatures that include temperatures/strain rates which are not generally associated with the DSA. Similar to the present work, various researchers (Skinner et al., 1989, Bouchaud et al., 1991, Li and Bakker, 1995, Mitra, 1992) (see Table 2.5) worked on RS Al alloys and noted the DSA manifestions (e.g minima in the SRS exponent and ductility) were present over a range of temperatures.

8.3.3.3 Yield strength anomaly, and high hardening rate

As discussed above that the solute diffusion and its concentration on an arrested dislocation have an 'anti-thermal' effect on the flow stress and the reason for yield strength anomaly. According to Morris (1974), the anti-thermal increase in the flow stress is balanced by the recovery, so the final shape of the flow curve depends on the dominant mechanism (increase in the flow stress or the recovery). Robinson and Shaw (1994) are of the view that the yield strength anomaly in Al alloys becomes noticeable at room temperature In the present study, the yield strength anomaly occurred from 23^{o}C to 200^{o}C (See Figure 7.28) which is a similar temperature range observed by Skinner et al. (1989) in DSA study of an RS Al-Fe-V-Si alloy (Table 2.5).

Once DSA is operative, the hardening rate is expected to increase (Rodriguez, 1984). At the strain rate of $10^{-5}s^{-1}$, the highest value of average hardening rate was observed at 150^{o}C in the NQX alloy (see Figure 7.27). Interestingly, 150^{o}C and $10^{-5}s^{-1}$ are the temperature/strain rate values at which the crucial condition of DSA (that is the negative SRS exponent) was observed, and this further validates that DSA is operative in this alloy at this temperature.

8.3.3.4 Element responsible for DSA

In this section, an attempt is made to estimate the element responsible for the DSA observed in the present study. The semi-quantitative analysis is primarily based on Cotrell theories used from the literature (Cottrell, 1953, Friedel, 1964, Hall, 1970, McCormick, 1972) and the DSA behaviour of RS Al alloys (Skinner et al., 1989, Bouchaud et al., 1991).

The average velocity of dislocations ($\bar{v}$) can be written in terms of their distance (l) and time (t) required to cover that distance ($\bar{v}$=l/t). The velocity ($\bar{v}$) of mobile dislocations

with a density (ρ_m) and imposed strain rates ($\dot{\varepsilon}$) are related by Orowan's law as $\dot{\varepsilon} = \bar{v} b \rho_m$ (Dieter and Bacon, 1986). The average distance (l) between dislocations is estimated by $\sqrt{\rho_f}$ (ρ_f is density of forest dislocations) then a combined relation can be written as Eqn. 8.17 (Van den Beukel, 1975).

$$t = \frac{b\rho_m}{\dot{\varepsilon}\sqrt{\rho_f}} \qquad \textbf{Eqn. 8.17}$$

If the temperature is high enough and strain rate is such that ageing takes place during the test, the time t in Eqn. 8.17 then becomes the waiting time (t_w). Considering $\dot{\varepsilon}$ as $10^{-5}s^{-1}$, ρ_m from 10^{10}-$10^{11}m^{-2}$, $\rho_f = 5x10^{13}m^{-2}$, b= 0.286nm, then t_w is calculated from ~0.1 to 1.1s. The waiting time depends on strain rate and dislocation structure of the material which is of the similar order as found in various static aging experiments (Mughrabi, 1993).For small concentration the interaction energy (W) [P] is defined by following relation (Friedel, 1964)..

$$W_{\min} = kT \ln\left(\frac{c_o}{c_1}\right) \qquad \textbf{Eqn. 8.18}$$

c_1 is the steady state concentration of the impurity atom on the dislocation used as 0.5 by Friedel (1964), c_o is the concentration of impurity atoms far from dislocation (concentration of atoms in the matrix), k is the Boltzmann constant, T is the temperature. The concentration of impurity atoms will reach to its equilibrium in a transient time which equals the waiting time of dislocations during DSA. Eqn. 8.19 provides the estimation of the required ageing time (McCormick, 1972).

$$t_w \approx t_s \approx \frac{kTb^2}{3D|W_{\min}|}\left(\frac{c_1}{\alpha c_o}\right)^{\frac{3}{2}} \qquad \textbf{Eqn. 8.19}$$

[P] Free energy of the interaction between dislocation and impurity/alloying atom is the work done by the stresses due to the presence of impurity/alloying atom; it results in a force on the atoms which is equal to the negative gradient of the interaction energy, and draws them towards the dislocations. The interaction energy reaches from zero to a minimum as an impurity/alloying atom approaches from a long distance to the proximity of a dislocation

t_s is the time to saturate the dislocation (which is the transient time τ_t, and during DSA it equals the waiting time t_w. α is a geometric parameter having value ~3.57. rearranging the Eqn. 8.19, the diffusion coefficient during DSA can be obtained by Eqn. 8.20.

$$D \approx \frac{kTb^2}{3t_w |W_{\min}|}\left(\frac{c_1}{\alpha c_o}\right)^{\frac{3}{2}} \qquad \textbf{Eqn. 8.20}$$

Using Eqn. 8.17 to Eqn. 8.20, the minimum interaction energy and the diffusion coefficients of each of the three elements in the NQX matrix were calculated during the DSA. The values for W_{min} and D for each element are provided in parentheses as: Fe(0.181eV, $3.4x10^{-18}m^2/s$), Cr(0.176eV, $2.9x10^{-19}m^2/s$) and Ti(0.14eV, $8.5x10^{-19}m^2/s$). The calculations show that Fe has the highest value of interaction energy and a higher diffusion coefficient, marginally ahead of Cr. Ti has the smallest of the interaction energy, and it is the slowest diffusing element. Cottrell (1953) expected the PLC to occur in aluminium alloy(s) when the diffusion coefficient (m^2/s) is of the order of Eqn. 8.21.

$$D \approx 10^{-14}\dot{\varepsilon} \qquad \textbf{Eqn. 8.21}$$

In the present work, the DSA was prominent when the strain rates ($\dot{\varepsilon}$) were in the range of 10^{-4}-$10^{-5}s^{-1}$. This sets the estimation of D (for the DSA) of the order of~10^{-18}-10^{-19} m^2/s which is of the same order as calculated from Eqn. 8.20 for Fe and Cr, out of which Fe is faster diffusing element.

Du et al. (2003) collected the experimental volume diffusion data of various transition elements in Al (Fe, Cr, Ti inclusive) from several studies over decades and pooled it in combined plots which follow a trend line over a large temperature range for each element. Mantina et al. (2009) calculated the diffusion coefficients of 3d transition impurities in aluminium by first principles and also used the diffusion data from litera-

ture similar to Du et al. (2003) for comparison. The calculated values were slightly higher than the experimental, but the trend was similar. The calculated values for the bulk diffusion coefficients are shown in Figure 8.11, which shows that Fe is the fastest diffusion element in fcc aluminium, whereas Cr is a distant second, and Ti is the slowest of the three. These trends of the volume diffusion coefficients of the (Fe, Cr, Ti) transition metals match with the trends for the calculated diffusion coefficients during the DSA in the present work. However, normal volume diffusion is much slower and not directly responsible for the DSA.

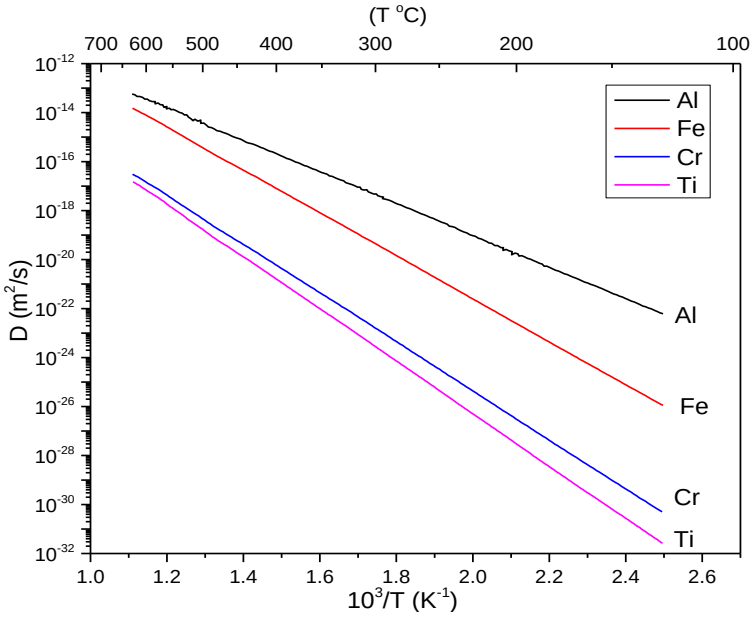

Figure 8.11 Calculated bulk diffusion coefficients of Fe ,Cr ,Ti and Al in Al (Mantina et al., 2009).

As observed in Table 2.5, Skinner et al. (1989) found Fe to be a responsible element for DSA in various RS Al alloys between temperature ranges of ~150-200^{o}C. They observed a minimum in m as well as a dip in ductility at temperatures similar to the present study. Similar observations were made by Bouchaud et al. (1991) in the study of an RS Al alloy.

The calculated diffusion coefficients using the elastic model of Cottrell, the volume diffusion behaviour of Fe, Cr, Ti solutes in aluminium and the literature studies of the DSA in RS alloys point out towards the possibility of a most likely candidate to cause the DSA. Based on the aforementioned discussion it can be deduced that Fe is the most likely cause for DSA in $Al_{93}Fe_3Cr_2Ti_2$ NQX alloy at ~150-250^oC between ~10^{-4}-$10^{-5}s^{-1}$.

It was however noted that the study uses the Cottrell theories and equations, to semi-quantitatively analyse the DSA behaviour of the alloy, which assumes an ideal (linear, elastic interaction in the isotropic material) between one type of solute and the dislocation. These do not take into account the effect of various competing solute atoms or the presence of precipitates. The various models in literature have been developed for steels or in simple Al-Mg alloys which may not be a perfect depiction of a quaternary alloy such as the NQX containing three competing solutes and a large volume fraction of 2nd phase particles, and nano-sized grains.

8.4 Fatigue of the NQX Alloy

Fatigue results were provided in sections 6.6 and 7.3. One important reason for the better fatigue performance of the NQX alloy is its inherently high tensile strength. The high strength alloys perform better in the HCF testing (Lee, 2005). In fcc metals (Al, Cu, and Austenitic Fe alloys), there is a decrease in fatigue strength in the VHCF regime (section 6.6). Resultantly, the failures are observed at a low stress amplitude, as seen in the VHCF tests of the NQX alloy. The room temperature NQX SN curves are divided into two distinct portions by drawing a vertical line at ~N_f=10^5 as seen in result section 6.6, Figure 6.11. The region to the left of the line highlights samples in which failures were initiated at the surface, whilst the region to the right has samples in which

failures were caused by the inclusions. As discussed in section 2.8, Mughrabi (2006) classified the alloys in relation to VHCF behaviour, Type I alloys are those in which the fracture is always initiated at surface whereas in Type II there are internal inhomogeneties present which cause fracture at a high number of cycles. The fatigue fracture behaviour of the NQX alloy suggests that it should be considered as a type II alloy. As confirmed by EDS analysis, the inclusions were found to have both a metallic and non-metallic nature (see Table 8.15).

The run out in the 23°C VHCF test was enforced at $1.07x10^{10}$ cycles; however, the SN curve does not show an asymptote, hinting at the absence of a fatigue limit. It has been debated by researchers that there is no infinite fatigue life in the metallic materials (Bathias, 1999). A real fatigue limit may be achieved in the absence of a corrosive environment, and in a material with no microstructural flaws or inhomogeneities, which is unlikely in engineering applications (Pyttel et al., 2011).

In the literature, the only available fatigue study of the $Al_{93}Fe_3Cr_2Ti_2$ NQX alloy was recently conducted by Chlupova et al. (2016); however, it was limited to ~10^7 cycles at room temperature (Figure 2.12).

At 300^{o}C, all the samples fractured due to some internal inhomogeneity. It was noted that at the two highest load levels (that is 350 and 325MPa), the fatigue fractures were caused by pores containing Sn traces, and this was also a common observation in most of the tensile samples at elevated temperature (section 7.2.2). It is proposed that the pore was a Sn alloy particle, which is immiscible in Al, and melted at a high temperature ($T_{m,\ Sn}$ = 232^{o}C), and this caused an accelerated fracture during cyclic loading. Further, the stress intensity range calculations (see details in section 8.4.2) were not applicable to these two samples (σ_{man}=350MPa and 325MPa at 300˚C) which also indicate towards an anomaly in these samples. Thus, it can be deduced that the presence

of the Sn contamination masked the actual high load/ low N_f fatigue behaviour of the NQX alloy in these two particular samples. The fractures in the other low stress amplitude samples solely originated from the metallic (Ti/O or Al/Ti intermetallic), or the nonmetallic (Si/O or Ca/O) inclusions, similar to the room temperature fatigue samples.

8.4.1 Fatigue crack growth

Bathias and Paris (2004) analytically calculated the number of cycles consumed during fatigue crack propagation inside the fisheye, which in itself was formed by the inclusions, using the aproximate relation Eqn. 8.22.

$$N_{Fisheye} = \frac{\pi E^2}{\Delta\sigma^2} \qquad \textbf{Eqn. 8.22}$$

Where E is Young's modulus and $\Delta\sigma$ is the range of the applied stress. Eqn. 8.22 was applied to estimate the fatigue crack growth life (in fisheyes), whereby the number of crack propagation cycles ($N_{fisheye}$) were calculated and found to be of the order of ~1 to $3x10^5$; in agreement with the work by Paris and coworkers (Marines-Garcia et al., 2007, Bathias and Paris, 2004). The calculations suggest that after crack initiation in the HCF or the VHCF regime, the NQX samples survive a small number of cycles (~10^5), which is insignificant in comparison to their total fatigue life. It re-emphasizes that the crack initiation is the critical factor in determining the total fatigue life in the VHCF study of the NQX alloy. As crack initiations are always caused by inclusions at a high number of cycles, the presence of inclusions or defects play an extremely important role in the fatigue study of the NQX alloy.

8.4.2 Inclusion size and effect

The inclusions or pores can be treated as cracks (Murakami, 2002). The stress intensity range[Q] (ΔK) due to these pre-existing cracks (inclusions in the present case) can be estimated using the inclusion area (A_{incl}) by the following equations (Murakami, 2002).

$$\Delta K = 0.5\Delta\sigma\sqrt{\pi\sqrt{Area_{inc}}} \quad \text{(Internal inclusion)} \qquad \textbf{Eqn. 8.23}$$

$$\Delta K = 0.65\Delta\sigma\sqrt{\pi\sqrt{Area_{inc}}} \quad \text{(Surface inclusion)} \qquad \textbf{Eqn. 8.24}$$

Using these equations the √(Inclusion Area) in the present fatigue study was measured to be in the range of ~59 to 6μm, whereas the corresponding ΔK was found to be in the range of 1.82 to 0.65 MPa.√m (Table 8.15). $\Delta K_{fisheye}$ was also calculated from the same equations using the area of fisheye(s). At room temperature, the comparison of the failure cycles (N_f) and the √($Area_{inclsion}$) (or ΔK) reveals that the higher N_f corresponds to a smaller √($Area_{inclsion}$) (or ΔK), meaning that the samples with smaller inclusion size have a longer fatigue life. Conversely, this also means that the larger size inclusions cause an early fatigue failure by assisting the crack initiation as suggested by Mughrabi (2006).

The control volume[R] was calculated as 32.8mm^3, 187mm^3 and 140mm^3 for 20kHz (RT), 60Hz (RT) and 60Hz (300^{o}C) samples respectively (see calculations in appendix 2). The probability of finding a defect in a smaller control volume is lower than the same probability for a larger control volume. However, it was observed that in room temperature tests below 2.2x10^5 cycles the fracture always initiated from the surface

[Q] $\Delta K = K_{max} - K_{min}$, where K is the stress intensity factor due to the presence of a crack. It is proportional to the crack growth rate (da/dN).
[R] Control volume is defined as the region in which stress amplitude is greater than 90% of σ_{max} amplitude (Murakami; 2002).

regardless of the test frequency and the control volume (disregarding Sn assisted failures). The same conclusion can be drawn from the observation that the fracture initiation is surface dominant for a lower number of cycles, and interior (inclusion) dominated for a higher number of cycles at room temperature, which is type II fatigue behaviour.

Table 8.15 A summary of NQX fatigue failures.

Test Condition	Max Load (MPa)	Cycles to Failure	Crack Initiation at	Nature of Inclusion	$\sqrt{(Area_{inc})}$ (µm)	ΔK_{inc} (MPa.m$^{0.5}$)	$\Delta K_{fisheye}$ (MPa.m$^{0.5}$)
HCF (60Hz, 23°C)	420	4986	Surface				
	390	11622	Surface				
	360	53320	Surface				
	340	220199	Subsurface (inclusion)	Ca/O/Si	24	1.82	3.9
	330	2.65E06	Inclusion	Fe/O	32.4	1.5	6.6
VHCF (20kHz, 23°C)	340	20432	Surface	-	-	-	-
	310	20738	Surface	-	-	-	-
	280	1.63E06	Inclusion	Si/O	58.8	1.71	4.5
	260	1.47E09	Subsurface (Inclusion)	Ca/O/Si	5.8	0.65	2.44
	240	2.63E08	Inclusion	Al/ Ti/O	12.7	0.68	2.9
	210	1.07E10	Run out	-	-	-	-
HCF (40Hz, 300°C)	350	9074	Internal	Sn (molten)	Invalid		
	325	4972	Internal	Sn (molten)	Invalid		
	300	1.11E6	Inclusion	Si/O	31.4	1.49	6.81
	270	2.154E6	Inclusion	Ti/O	11.2	0.80	7.11
	240	4.398E6	Inclusion	Si/O/Ca	15.2	0.83	4.79
	240	561324	Inclusion	Al/Ti/O	24.1	1.04	4.53
	210	9.264E6	Inclusion	Al/Ti	14.5	0.71	4.96

8.4.3 Comparison with conventional aluminium alloys

A comparison of the approximate fatigue strength of the NQX alloy at 10^6 and 10^7 cycles with some high strength conventional aluminium alloys is provided in Table 8.16. It can be observed that the room temperature fatigue performance of the NQX alloy is good whereas 300°C fatigue performance is excellent in comparison the other Al alloys. Only a high strength Al7075-T6 is slightly better than the NQX alloy at room temperature. However at high temperatures, the NQX alloy surpasses all conventional

Al alloys specifically designed for elevated temperatures, and at 300^{o}C the NQX alloy fatigue performance matches the performance of other conventional Al alloys at much lower temperatures 150^{o}C. It has already been shown in the NQX SN curve (Figure 7.13) that at 300^{o}C, its fatigue performance is far superior to an elevated temperature alloy 2618-T651 alloy tested at 250^{o}C.

Table 8.16 Approximate fatigue strength comparison of the NQX alloy with conventional Al alloy.

Alloy	Load Ratio (R)	Temp	Fatigue Strength (MPa)		Reference
		^{o}C	10^6 cycles	10^7 cycles	
2014-T6	0	RT	320	285	(Kaufman, 2008)
2618.AS3	0	RT	270	215	(Kaufman, 2008)
7075-T6	0.2	RT	370	330	(Kaufman, 2008)
2024-T851	0	RT	260	240	(Dragolich et al., 1994)
NQX	0.1	RT	330	~280	This work
2024-T851	0	150	285	210	(Dragolich et al., 1994)
2618.AS3	0	150	255	205	(Kaufman, 2008)
2618.AS3	0	260	175	130	(Kaufman, 2008)
NQX	0.1	300	~260	~200	This Work

8.5 Fracture Mechanisms in the NQX alloy

The fractographic analysis using SEM revealed that in the majority of the tensile samples, the fractured surface has a macroscopically flat appearance. Pronounced necking or classic cup and cone fractures are not optically visible in the samples tested below 350°C. The cup and cone shape starts to become noticeable for the samples tested at very high temperatures such as ~>400°C meaning thereby that sample becomes macroscopically ductile.

The presence of prominent dimples in all the tested samples, irrespective of the heat treatment, temperature, and/or strain rate conditions, is indicative of the fact that the void growth and coalescence mechanisms which are associated with the ductile fracture

(Callister and Rethwisch, 2007), are operative for the NQX alloy. The ductile fracture is preferred in materials in engineering applications as the failure is not catastrophic due to associated plasticity with this type of fracture; moreover, associated fracture toughness has larger values than the brittle materials.

8.5.1 Effect of 2nd phase particles in the fracture development

Hard 2nd phase particles have been known to affect the fracture mechanisms in the dispersion strengthened materials. In fact, a void is nucleated at the particle-matrix interface as a result of decohesion due to the increasing stress (Martin, 1980). According to Brown and Embury (1973), the void subsequently elongates, initially at a rate higher than the sample itself and this rate decreases as the void grows. Once the length of neighbouring voids approaches their mutual distance the ductile fracture immediately occurs as the plastic slip can now ensue locally. Large size particles cause the early cavitation of larger size voids which results an early fracture (Martin, 1980). This can be related to the tensile tests and fractography of the samples 400°C/100h and 450°C/100h in sections 6.4 and 6.5 respectively. The brittle intermetallic particles (after the I-phase transformation) in these two samples grew to comparatively large sizes, subsequently the fracture strain value was observed to be significantly lower than the other samples containing (smaller) I-phase particles.

As mentioned earlier that cavities may arise due to debonding between particle-matrix interfaces, and when such interfacial damage develops the overall matrix-particle load transfer efficiency decreases, especially at elevated temperatures (Tjong and Mai, 2003). However, in the presence of high volume fraction of the second phase particles, the high-temperature performance is still better than materials with no reinforcement particles (Tjong and Mai, 2003).

8.5.2 Effect of inclusions in the fracture development

The inclusions or defects are believed to be the nucleating sites for the ductile cracks in most of the metallic materials. The fractographic analysis revealed two types of inclusions (i) metallic inclusions, such as Sn, pure Al, or aluminium intermetallics containing Ti or Fe, and (ii) nonmetallic inclusions, such as Si/Ca/K oxides. The most abundantly found foreign inclusion in the elevated temperature tensile tests is 'Sn' (Figure 7.11 (a, b)) which causes the fracture initiation as a result of softening and melting at elevated temperatures . The crack growing under the assistance of molten Sn does not appear to grow with the void growth and coalescence mechanisms. This is the probable reason that 'Sn affected area' contains no dimples. This idea is further strengthened by the observation is that fractures due to 'Sn' are observed only at high temperature, no fracture surface from a room temperature test (fatigue or tensile) sample was ever observed to contain Sn at the origin.

8.5.3 Effect of inclusions on tensile and fatigue behaviour

Inclusions were observed to have a no clear impact on the tensile ductility of the NQX alloy. For example most of the elevated temperature failures for $10^{-2}s^{-1}$ and $10^{-4}s^{-1}$ strain rate tests are due to Sn inclusions; however, the ductility behaviour is different. The tensile ductility of the samples tested at $10^{-2}s^{-1}$ increases with temperature, whereas the ductility of the samples tested at $10^{-4}s^{-1}$ first decrease and then increase with temperature. Which shows that if inclusions have any impact on the ductility of the tensile sample, it must be very small. However, the situation changes for the fatigue tests, during which the inclusions act as a crack nucleating sites. Since most of the fatigue life in VHCF regime is spent in crack nucleation; therefore, the presence of inclusions and their role as a crack nucleating site have an instrumental effect on the total fatigue life.

8.5.4 Origin of the inclusions

The origin of the inclusions was investigated by examining the powder manufacturing methods. It is likely that inclusions formed from metallic elements such as Al intermetallics, pure metals Al/Ti/Fe and/or their oxides originated from inhomogeneities of melting and the gas atomisation processes. Other inclusions such as Si/Ca and their oxides might have originated from: (i) the contamination of master alloys and/or, (ii) from ceramic components used during melting and atomisation process and/or, (iii) contamination introduced during, handling, canning, sieving or preparing for extrusion. The possible source of Sn contamination was thought to be due to: (i) cross contamination during sieving of the alloy powders from an Al-Sn alloy present in the powder lab, and (ii) possible traces of Sn in the master alloys.

References

Abbaschian, R. and Reed-Hill, R. (2008) *Physical metallurgy principles.* Cengage Learning.

Aboulfadl, H., Deges, J., Choi, P. and Raabe, D. (2015) 'Dynamic strain aging studied at the atomic scale', *Acta Materialia*, 86, pp. 34-42.

Antolovich, S. D. and Armstrong, R. W. (2014) 'Plastic strain localization in metals: origins and consequences', *Progress in Materials Science*, 59, pp. 1-160.

Arzt, E. and Ashby, M. F. (1982) 'Threshold stresses in materials containing dispersed particles', *Scripta Metallurgica*, 16(11), pp. 1285-1290.

ASM (1990) *Nonferrous Alloys and Special-Purpose Materials, vol. 2. ASM International, Materials Handbook*: ASM International.

Audebert, F., Prima, F., Galano, M., Tomut, M., Warren, P. J., Stone, I. C. and Cantor, B. (2002) 'Structural characterisation and mechanical properties of nanocomposite Al-based alloys', *Materials transactions*, 43(8), pp. 2017-2025.

Baldwin, W. (1958) 'Yield strength of metals as a function of grain size', *Acta Metallurgica*, 6(2), pp. 139-141.

Barrales-Mora, L. A. (2008) *2D and 3D grain growth modeling and simulation.* Cuvillier Verlag.

Bathias, C. (1999) 'There is no infinite fatigue life in metallic materials', *Fatigue and Fracture of Engineering Materials and structures*, 22(7), pp. 559-566.

Bathias, C. and Paris, P. C. (2004) *Gigacycle fatigue in mechanical practice.* CRC Press.

Belov, N. A., Aksenov, A. A. and Eskin, D. G. (2002) *Iron in aluminium alloys: impurity and alloying element.* CRC Press.

Bouchaud, E., Kubin, L. and Octor, H. (1991) 'Ductility and dynamic strain aging in rapidly solidified aluminum alloys', *Metallurgical Transactions A*, 22(5), pp. 1021-1028.

Brahmi, A., Gerique, T., Torralba, M. and Lieblich, M. (1997) 'Flow stress of rapidly solidified Al-5Cr-2Zr alloy as a function of processing variables', *Scripta materialia*, 37(11), pp. 1623-1629.

Brown, L. M. and Embury, J. D., *3rd international conference on strength of metals and alloys, Institute of Metals*. London, 164.

Brown, L. M. and Ham, R. K. (1971) 'Dislocation-Particle Interactions', in Kelly, A. & Nicholson , R.B. (eds.) *Strengthening methods in crystals*: Elsevier Publishing Company.

Callister, W. D. and Rethwisch, D. G. (2007) *Materials science and engineering: an introduction.* Wiley New York.

Campbell, F. C. (2008) *Elements of metallurgy and engineering alloys.* ASM International.

Chateau, J. P. (2011) 'Basics of Mechanical Properties of Metals', in Belin-Ferré, E. (ed.) *Mechanical Properties of Complex Intermetallics Complex Metallic Alloys*: World Scientific.

Chlupova, A., Chlup, Z. and Kruml, T. (2016) 'Fatigue properties and microstructure of quasicrystalline AlFeCrTi alloy', *International Journal of Fatigue*, 91 (1), pp. 251–256.

Chlupová, A., Chlup, Z., Kruml, T., Kuběna, I. and Roupcová, P. 'Microstructure, tensile properties and fatigue behaviour of bulk nano-quasicrystalline al alloy $AL_{93}FE_3CR_2TI_2$', *Nano Con*, Brno, Czech Republic, 21-23 September 2011.

Conrad, H. (1963) 'Effect of grain size on the lower yield and flow stress of iron and steel', *Acta metallurgica*, 11(1), pp. 75-77.

Corti, C., Cotterill, P. and Fitzpatrick, G. (1974) 'The evaluation of the interparticle spacing in dispersion alloys', *International Metallurgical Reviews*, 19(1), pp. 77-88.

Cottrell, A. (1953) 'LXXXVI. A note on the Portevin-Le Chatelier effect', *The London, Edinburgh, and Dublin Philosophical Magazine and Journal of Science*, 44(355), pp. 829-832.

Curtin, W. A., Olmsted, D. L. and Hector, L. G. (2006) 'A predictive mechanism for dynamic strain ageing in aluminium–magnesium alloys', *Nature materials*, 5(11), pp. 875-880.

Dám, K., Vojtěch, D. and Průša, F. (2013) 'Powder metallurgy Al–6Cr–2Fe–1Ti alloy prepared by melt atomisation and hot ultra-high pressure compaction', *Materials Science and Engineering: A*, 560, pp. 705-710.

De Vaucorbeil, A., Poole, W. and Sinclair, C. (2013) 'The superposition of strengthening contributions in engineering alloys', *Materials Science and Engineering: A*, 582, pp. 147-154.

Dieter, G. E. and Bacon, D. (1986) *Mechanical metallurgy*. McGraw-Hill New York.

Dragolich, K. S., DiMatteo, N. D. and Henry, S. D. (1994) *Fatigue data book: light structural alloys*. ASM International.

Du, Y., Chang, Y., Huang, B., Gong, W., Jin, Z., Xu, H., Yuan, Z., Liu, Y., He, Y. and Xie, F.-Y. (2003) 'Diffusion coefficients of some solutes in fcc and liquid Al: critical evaluation and correlation', *Materials Science and Engineering: A*, 363(1), pp. 140-151.

Dubois, J.-M. and Wei, T. K. (2005) *Useful quasicrystals*. World Scientific.

Dunstan, D. and Bushby, A. (2014) 'Grain size dependence of the strength of metals: the Hall–Petch effect does not scale as the inverse square root of grain size', *International Journal of Plasticity*, 53, pp. 56-65.

Ehrström, J. and Pineau, A. (1994) 'Mechanical properties and microstructure of Al-Fe-X alloys', *Materials Science and Engineering: A*, 186(1-2), pp. 55-64.

Frazier, W. and Koczak, M. (eds.) (1988) *Grain boundary and Orowan strengthening of elevated temperature PM aluminum- titanium alloys*. Warrendale: TMS.

Friedel, J. (1964) 'Dislocations Pergamon', *New York*.

Frost, H. J. and Ashby, M. F. (1982) 'Deformation mechanism maps: the plasticity and creep of metals and ceramics'.

Galano, M., Audebert, F., Escorial, A. G., Stone, I. and Cantor, B. (2009a) 'Nanoquasicrystalline Al–Fe–Cr-based alloys. Part II: Mechanical properties', *Acta materialia*, 57(17), pp. 5120-5130.

Galano, M., Audebert, F., Stone, I. and Cantor, B. (2009b) 'Nanoquasicrystalline Al–Fe–Cr-based alloys. Part I: Phase transformations', *Acta Materialia*, 57(17), pp. 5107-5119.

Gale, W. F. and Totemeier, T. C. (eds.) (2003) *Smithells metals reference book*: Butterworth-Heinemann.

García-Escorial, A., Natale, E., Cremaschi, V. J., Todd, I. and Lieblich, M. (2015) 'Quasicrystalline Al93Fe3Cr2Ti2 alloys', *Revista de Metalurgia*, 51(4), pp. 10.3989/revmetalm. 054.

Gargarella, P., Almeida, A., Vilar, R., Afonso, C., Rios, C., Bolfarini, C., Botta, W. and Kiminami, C. (2009) 'Microstructural characterization of a laser remelted coating of Al 91 Fe 4 Cr 3 Ti 2 quasicrystalline alloy', *Scripta Materialia,* 61(7), pp. 709-712.

Hall, E. (1951) 'The deformation and ageing of mild steel: III discussion of results', *Proceedings of the Physical Society. Section B,* 64(9), pp. 747.

Hall, E. (1970) *Yield point phenomena in metals and alloys.* Plenum Press.

Hansen, N. (1977) 'The effect of grain size and strain on the tensile flow stress of aluminium at room temperature', *Acta Metallurgica,* 25(8), pp. 863-869.

Hatch, J. E. (1984) *Aluminum: properties and physical metallurgy.* ASM International.

Inoue, A. (1998) 'Amorphous, nanoquasicrystalline and nanocrystalline alloys in Al-based systems', *Progress in Materials Science,* 43(5), pp. 365-520.

Inoue, A. and Kimura, H. (1999) 'High elevated-temperature strength of Al-based nanoquasicrystalline alloys', *Nanostructured materials,* 11(2), pp. 221-231.

Inoue, A. and Kimura, H. (2000) 'High-strength aluminum alloys containing nanoquasicrystalline particles', *Materials Science and Engineering: A,* 286(1), pp. 1-10.

Inoue, A. and Kimura, H. (2001) 'Fabrications and mechanical properties of bulk amorphous, nanocrystalline, nanoquasicrystalline alloys in aluminum-based system', *Journal of light metals,* 1(1), pp. 31-41.

Joshi, S., Ramesh, K., Han, B. and Lavernia, E. (2006) 'Modeling the constitutive response of bimodal metals', *Metallurgical and Materials Transactions A,* 37(8), pp. 2397-2404.

Kang, S.-J. L. (2004) *Sintering: densification, grain growth and microstructure.* Butterworth-Heinemann.

Kaufman, J. G. (2008) *Properties of aluminum alloys: fatigue data and the effects of temperature, product form, and processing.* ASM International.

Kendig, K. and Miracle, D. (2002) 'Strengthening mechanisms of an Al-Mg-Sc-Zr alloy', *Acta Materialia,* 50(16), pp. 4165-4175.

Kim, K., Xu, W., Tomut, M., Stoica, M., Calin, M., Yi, S., Lee, W. and Eckert, J. (2007) 'Formation of icosahedral phase in an Al 93 Fe 3 Cr 2 Ti 2 bulk alloy', *Journal of alloys and compounds,* 436(1), pp. L1-L4.

Knipling, K. E., Dunand, D. C. and Seidman, D. N. (2006) 'Criteria for developing castable, creep-resistant aluminum-based alloys–A review', *Zeitschrift für Metallkunde,* 97(3), pp. 246-265.

Kocks, U. (1985) 'Kinetics of solution hardening', *Metallurgical Transactions A,* 16(12), pp. 2109-2129.

Kuhn, H. and Medlin, D. (2000) 'ASM Handbook. Volume 8: Mechanical Testing and Evaluation', *ASM International, Member/Customer Service Center, Materials Park, OH 44073-0002, USA, 2000. 998*.

L.F, M. (1976) *Aluminum alloys: structure and properties'; 1976. London-Boston: Butter Worths & Co Ltd*.

Lagneborg, R. and Bergman, B. (1976) 'The stress/creep rate behaviour of precipitation-hardened alloys', *Metal Science,* 10(1), pp. 20-28.

Lee, Y.-L. (2005) *Fatigue testing and analysis: theory and practice.* Butterworth-Heinemann.

Lesuer, D., Syn, C. and Sherby, O. 'An evaluation of power law breakdown in metals, alloys, dispersion hardened materials, and compounds', *Deformation, Processing and Properties of Structural Materials, TMS,* , Warrendale, PA, October 20, 1999: The Metals/Minerals Society, 81-194.

Lewandowska, M., Wejrzanowski, T. and Kurzydłowski, K. J. (2008) 'Grain growth in ultrafine grained aluminium processed by hydrostatic extrusion', *Journal of Materials Science,* 43(23-24), pp. 7495-7500.

Li, D. and Bakker, A. (1995) 'Temperature and strain rate dependence of the portevin-le chatelier effect in a rapidly solidified Al alloy', *Metallurgical and Materials Transactions A,* 26(11), pp. 2873-2879.

Lin, Y. and Chen, X.-M. (2011) 'A critical review of experimental results and constitutive descriptions for metals and alloys in hot working', *Materials & Design,* 32(4), pp. 1733-1759.

Lumley, R. (2010) *Fundamentals of aluminium metallurgy: Production, processing and applications.* Elsevier.

Lund, R. and Nix, W. (1976) 'High temperature creep of Ni-20Cr-2ThO 2 single crystals', *Acta Metallurgica,* 24(5), pp. 469-481.

Ma, E. (2006) 'Eight routes to improve the tensile ductility of bulk nanostructured metals and alloys', *Jom,* 58(4), pp. 49-53.

Mahon, G. and Marshall, G. (1996) 'Microstructure-property relationships in O-temper foil alloys', *JOM,* 48(6), pp. 39-42.

Mantina, M., Shang, S., Wang, Y., Chen, L. and Liu, Z. (2009) '3 d transition metal impurities in aluminum: A first-principles study', *Physical Review B,* 80(18), pp. 184111.

Marines-Garcia, I., Paris, P., Tada, H. and Bathias, C. (2007) 'Fatigue crack growth from small to long cracks in VHCF with surface initiations', *International Journal of Fatigue,* 29(9-11), pp. 2072-2078.

Martin, J. W. (1980) *Micromechanisms in particle-hardened alloys.* CUP Archive.

McCormick, P. (1972) 'A model for the Portevin-Le Chatelier effect in substitutional alloys', *Acta metallurgica,* 20(3), pp. 351-354.

Miller, A. K. (2012) *Unified constitutive equations for creep and plasticity.* Springer Science & Business Media.

Mishra, R. (1992) 'Dislocation creep mechanism map for particle strengthened materials', *Scripta metallurgica et materialia,* 26(2), pp. 309-313.

Mitra, S. (1992) 'Elevated temperature mechanical properties of a rapidly solidified Al-Fe-V-Si alloy', *Scripta metallurgica et materialia,* 27(5), pp. 521-526.

Morris, J. (1974) 'Dynamic strain aging in aluminum alloys', *Materials Science and Engineering,* 13(2), pp. 101-108.

Mughrabi, H. (1993) 'Plastic deformation and fracture of materials'.

Mughrabi, H. (2006) 'Specific features and mechanisms of fatigue in the ultrahigh-cycle regime', *International Journal of Fatigue,* 28(11), pp. 1501-1508.

Mukherjee, A. K. (2002) 'An examination of the constitutive equation for elevated temperature plasticity', *Materials Science and Engineering: A,* 322(1), pp. 1-22.

Mulford, R. and Kocks, U. (1979) 'New observations on the mechanisms of dynamic strain aging and of jerky flow', *Acta Metallurgica,* 27(7), pp. 1125-1134.

Murakami, Y. (2002) *Metal fatigue: effects of small defects and nonmetallic inclusions: effects of small defects and nonmetallic inclusions.* Elsevier.

Noble, B., Harris, S. and Dinsdale, K. (1982) 'The elastic modulus of aluminium-lithium alloys', *Journal of materials science,* 17(2), pp. 461-468.

Peng, L., Zhu, S., Ma, Z., Bi, J., Chen, H. and Wang, F. (1999) 'High temperature creep deformation of an Al–Fe–V–Si alloy', *Materials Science and Engineering: A,* 259(1), pp. 25-33.

Penning, P. (1972) 'Mathematics of the portevin-le chatelier effect', *Acta Metallurgica,* 20(10), pp. 1169-1175.

Petch, N. (1953) 'The cleavage strength of polycrystals', *J. Iron Steel Inst.,* 174, pp. 25-28.

Pineau, A., Benzerga, A. A. and Pardoen, T. (2016) 'Failure of metals III: Fracture and fatigue of nanostructured metallic materials', *Acta Materialia,* 107, pp. 508-544.

Priester, L. (2013) *Grain boundaries and crystalline plasticity.* John Wiley & Sons.

Pyttel, B., Schwerdt, D. and Berger, C. (2011) 'Very high cycle fatigue – Is there a fatigue limit?', *International Journal of Fatigue,* 33(1), pp. 49-58.

Rice, R. C. (2003) *Metallic Materials Properties Development and Standardization (MMPDS): Chapters 1-4.* National Technical Information Service.

Robinson, J. and Shaw, M. (1994) 'Microstructural and mechanical influences on dynamic strain aging phenomena', *International materials reviews,* 39(3), pp. 113-122.

Rodriguez, P. (1984) 'Serrated plastic flow', *Bulletin of Materials Science,* 6(4), pp. 653-663.

Rösler, J. and Arzt, E. (1990) 'A new model-based creep equation for dispersion strengthened materials', *Acta Metallurgica et Materialia,* 38(4), pp. 671-683.

Rounthwaite, N. J. (2012) *Development of Bulk Nanoquasicrystalline Alloys for High Strength Elevated Temperature Applications.* DPhil Thesis, University of Oxford.

Ryen, Ø., Holmedal, B., Nijs, O., Nes, E., Sjölander, E. and Ekström, H.-E. (2006) 'Strengthening mechanisms in solid solution aluminum alloys', *Metallurgical and Materials Transactions A,* 37(6), pp. 1999-2006.

Sellars, C. and McTegart, W. (1966) 'On the mechanism of hot deformation', *Acta Metallurgica,* 14(9), pp. 1136-1138.

Sherby, O. D. and Young, C. M. (1975) 'Some factors influencing the strain rate-temperature dependence of the flow stress in polycrystalline solids', in Li, J.C.M. & K., M.A. (eds.) *Rate Processes in Plastic deformation of Materials*: American Society for Metals, pp. 497-541.

Skinner, D. and Zedalis, M. (1988) 'Elastic modulus versus melting temperature in aluminum based intermetallics', *Scripta metallurgica,* 22(11), pp. 1783-1785.

Skinner, D., Zedalis, M. and Gilman, P. (1989) 'Effect of strain rate on tensile ductility for a series of dispersion-strengthened aluminum-based alloys', *Materials Science and Engineering: A,* 119, pp. 81-86.

Sleeswyk, A. (1958) 'Slow strain-hardening of ingot iron', *Acta metallurgica,* 6(9), pp. 598-603.

Smallman, R. E. and Bishop, R. J. (1999) *Modern physical metallurgy and materials engineering.* Butterworth-Heinemann.

Smith, C. S. (1948) 'Grains, phases, and interphases: an interpretation of microstructure', *Transactions of the Metallurgical Society, AIME,* 175, pp. 15-51.

Thangaraju, S., Heilmaier, M., Murty, B. S. and Vadlamani, S. S. (2012) 'On the estimation of true Hall–Petch constants and their role on the superposition law exponent in Al alloys', *Advanced Engineering Materials,* 14(10), pp. 892-897.

Tjong, S. C. and Mai, Y.-W. (2003) 'Failure of Metal-Matrix Composites', in Karihaloo, B.L. & Knauss, W.G. (eds.) *Fundamental Theories and Mechanisms of*

Failure Comprehensive structural integrity: Elsevier.

Todd, I., Chlup, Z., O'Dwyer, J., Lieblich, M. and García-Escorial, A. (2004) 'The influence of processing variables on the structure and mechanical properties of nano-quasicrystalline reinforced aluminium alloys', *Materials Science and Engineering: A,* 375, pp. 1235-1238.

Totten, G. E. and MacKenzie, D. S. (2003) *Handbook of Aluminum: Vol. 1: Physical Metallurgy and Processes.* CRC Press.

Van den Beukel, A. (1975) 'Theory of the effect of dynamic strain aging on mechanical properties', *Physica status solidi (a),* 30(1), pp. 197-206.

Vojtěch, D., Michalcová, A., Průša, F., Dám, K. and Šedá, P. (2012) 'Properties of the thermally stable Al 95 Cr 3.1 Fe 1.1 Ti 0.8 alloy prepared by cold-compression at ultra-high pressure and by hot-extrusion', *Materials Characterization,* 66, pp. 83-92.

Vojtěch, D., Verner, J., Šerák, J., Šimančík, F., Balog, M. and Nagy, J. (2007) 'Properties of thermally stable PM Al–Cr based alloy', *Materials Science and Engineering: A,* 458(1), pp. 371-380.

Yamasaki, M., Nagaishi, Y. and Kawamura, Y. (2007) 'Inhibition of Al grain coarsening by quasicrystalline icosahedral phase in the rapidly solidified powder metallurgy Al–Fe–Ti–Cr alloy', *Scripta materialia,* 56(9), pp. 785-788.

Zener, C. and Hollomon, J. (1944) 'Effect of strain rate upon plastic flow of steel', *Journal of Applied physics,* 15(1), pp. 22-32.

9. Conclusions and Future Work

9.1 Conclusions

9.1.1 Atomised powder

25-50μm $Al_{93}Fe_3Cr_2Ti_2$ alloy powder characterisation revealed that the alloy comprises the icosahedral quasicrystalline phase (I-phase) particles in α-aluminium matrix. DSC analysis showed that the onset of the I-phase transformation in the alloy powder is ~535^{o}C at a heating rate of 40°C/min.

9.1.2 Extrusion of the alloy

The extrusion pressure values were calculated to be in the range of 1000-1200MPa, and similar peak pressure values were observed during the extrusion experiments. The pressure required to extrude the alloy is strongly dependent on the friction coefficient and extrusion speed. Extrusion produces internal heating due to the conversion of mechanical energy into heat energy, and high extrusion speeds outmatch the flow of heat away from the material. This results in an internal adiabatic temperature rise, which causes an undesired phase transformation in the alloy. The extrusion parameters suitable for a successful extrusion of the 25-50μm $Al_{93}Fe_3Cr_2Ti_2$ alloy powder to produce bars preserving the microstructure without transfoming the I-phase were determined and are summarised in Table 9.1.

Table 9.1 Extrusion parameters.

Parameter	Details
Extrusion ratio	12.76:1
Extrusion Speed	1-0.8 mm/s
Extrusion temperature	400^{o}C
Die temperature	200^{o}C
Lubrication	Can, die, and container all should be well lubricated with HBN
Powder pre-heating	400^{o}C to 415^{o}C for 30 min
Can and output bar dimensions	Can (L=101mm,φ=50mm), Bar(L~800m,φ=14mm)
Peak pressure required	1015-1220MPa

An excellent repeatability was achieved with these extrusion conditions as all the extruded bars were similar in their microstructure.

9.1.3 Characterisation of the extruded alloy

9.1.3.1 Microstructure of the 'as extruded' alloy

Following the extrusion conditions described in Table 9.1, the microstructure of the extruded bars is similar to the alloy powders, consisting of I-phase particles of 151±11nm diameter from a log normal distribution. The I-phase has a volume fraction of 44%±3% in the α-aluminium matrix. The solid solution of Al contains small atomic % quantities of Fe(0.35%), Cr(0.4%) and Ti(1.05%) which are higher than the stable equilibrium concentration. No porosity was observed in the extruded alloy.

I-phase particles were aligned in the extrusion direction, and a banded structure appeared due to various sizes of I-phase particles present in the alloy. The alloy contains an Al fibre texture with <111> being the major component parallel to the extrusion direction, along with a small <100> texture component. The Al grains were slightly elongated in the longitudinal directions having the longitudinal and cross section average sizes of ~473nm and ~432nm respectively.

9.1.3.2 Microstructure of the annealed alloy

The activation energy for the transformation of the I-phase present in the extruded bars is 250±4kJ/mol. The alloy was annealed at 250, 300, 350, 400, and 450°C for 100hrs and subsequent microstructural changes were studied. Lower annealing temperatures (250^{o}C and 300^{o}C) cause no visible change to Al matrix or the I-phase particle. However, very small size Al_3Ti and Al_6Fe are occasionally found to appear next to the to the I-phase particles. After 100h at 350^{o}C crystalline intermetallic phases are identified,

whereas only some I-phase particles are also present but no changes in the Al-grains is observed.

After 100h at higher annealing temperature (400^{o}C), the I-phase transforms into crystalline intermetallics such as Al_6Fe, $Al_{13}Cr_2$, $Al_{13}Fe_4$, and Al_3Ti. These have a mean particle size of 193±5nm following a log normal distribution.

After 100h at an even higher temperature (450^{o}C), the transformation is completed, reaching the stable equilibrium phase. The metastable Al_6Fe is replaced by elongated $Al_{13}Fe_4$, also $Al_{13}Cr_2$, and Al_3Ti are observed in the sample. The mean particles size becomes 239±7nm in a log normal distribution. However, as a consequence of large diffusivity of Fe in Al, some $Al_{13}F_4$ particles grow up to a few micron length, whereas $Al_{13}Cr_2$, and Al_3Ti have smaller sizes (<~400nm). Only a small Al grain growth (~30nm to 100nm) is caused by the high annealing temperatures of 400^{o}C and 450^{o}C.

9.1.4 Physical properties of the alloy (from appendix 5)

The alloy density is 2.949±0.003g/cm^3, which is 9% higher in comparison with pure Aluminium. Coefficient of thermal expansion (CTE) is 19 to 21.6μ/^{o}C in 150-450°C temperature range Pure Al has ~33-60% higher CTE values in the same temperature range. Thermal conductivity was calculated to be on the lower side 45-73W/(m.°C) in 23-400°C temperature range, whereas most Al alloys have a value of 100-200W/(m.°C) in the same temperature range.

9.1.5 Mechanical behaviour of the alloy

9.1.5.1 Elastic constants

The Young's and shear moduli of the alloy in the 'as extruded' condition were measured as 92.3±0.4GPa and 34.5±0.2GPa respectively, which are ~31% higher in comparison with aluminium, and most conventional alloys (ASM, 1990). After 100hrs

of annealing at 450^{o}C the I-phase is transformed into crystalline phases and the room temperature Young's modulus of the alloy increases by ~7%. On the other hand heat treatments have very little effect on the value of Young's modulus in almost all the conventional Al alloys (ASM, 1990). In comparison with the pure aluminium, the elastic constants also fare better at all test temperatures (up to 350^{o}C); the Young's modulus at 350^{o}C is 74GPa which is even higher than the Young's modulus of Al or alloys at room temperature (70GPa).

9.1.5.2 Strength at room temperature

The NQX alloy in the 'as extruded' condition has a room temperature strength of 598-640MPa which is ~>5% higher than that of the high strength Al alloys (e.g 7075-T6, 7178-T6). However, the genuine superiority of the NQX alloy is in resisting the strength degradation caused by the elevated temperature annealing as compared to any high-performance conventional Al alloy. The strength of the NQX alloy is retained even after 100 hours exposure to 300^{o}C; whereas 7075-T6 and 2024-T3 lose their strengths by 58% and 46% after the same heat treatment (Rice, 2003, ASM, 1990). Even after the I-phase transformation and heating to further high temperatures (400°C and 450°C for 100hrs) the strength drop is only ~10 to 16%.

The alloy exhibits a low strain hardening and strain rate hardening behaviour.

9.1.5.3 Strength at elevated temperatures

In comparison with the high-performance Al alloys (7075, 2014, and 2024), the elevated temperature strength of the NQX alloy is higher at all testing temperatures up to 500˚C. The decreasing rate of the strength with the temperature increase is slow, and does not strongly drop as reported for the conventional alloys. The NQX alloy also shows a lower strain hardening and a low strain rate hardening behaviour at all tempera-

tures with respect to the conventional Al alloys. Testing temperatures higher than 400^{o}C result in the I-phase transformation; however, the volume fraction of resulting intermetallics is almost similar and the strength of the alloy even without quasicrystals is still much higher than any conventional Al alloys.

9.1.5.4 Fracture behaviour

A ductile fracture mechanism consisting of void growth and coalescence operates at all temperatures (23˚C to 500˚C) and strain rates (10^{-2} to $10^{-5}s^{-1}$). 2nd Phase particles have an effect on the fracture behaviour as larger size particles cause and early fracture. The fracture origin mostly points towards small (φ<50μm) inclusions of a metallic and non-metallic nature. Sn inclusions are the most frequently observed entity at the fracture origin of the high-temperature tensile tests. Overall, the alloy has fair values of elongation to failure (~2-17%) at all temperatures, and the inclusions do not seem to cause a detrimental effect to tensile ductility.

9.1.5.5 Strengthening mechanisms at room temperature

The grain boundary and the Orowan's strengthening mechanisms are the major (>89%) contributors to the strength of the total alloy strength at room temperature. The grain boundary strengthening in the annealed samples remains almost unaffected regardless of annealing temperatures, but the relative particle strengthening contribution significantly decreases for the samples annealed at a higher temperature (400^{o}C/100h or 450^{o}C /100h). In these samples, the transformation of the I-phase and the growth of the crystalline intermetallic phases causes ~10-16% drop in the strength of the alloy.

9.1.5.6 Dynamic strain ageing

Dynamic strain ageing takes place in the NQX alloy in the ~150-250°C and 10^{-4}-$10^{-5}s^{-1}$ temperature/strain rate range, which is likely caused by Fe atoms in the Al solid solution. The manifestations of the phenomenon in the form of anomalous mechanical behaviour include: negative strain rate sensitivity, strain rate sensitivity reduction with temperature, ductility reduction with temperature, yield strength anomaly, a high hardening rate, and serrated flow.

9.1.5.7 Elevated temperature plasticity mechanisms

The analysis of high temperature plasticity mechanisms yields high values of the apparent stress exponent and the apparent activation energy which are associated with (creep resistant) dispersion strengthened alloys. The power law breakdown was identified at all tests below 250˚C and lower temperatures in the given strain rate (10^{-2} to $10^{-5}s^{-1}$) range. At a higher temperature range (250-350^{o}C), both dislocation controlled glide (power law break down), and dislocation controlled climb (power law creep) occur. At very high temperatures (425-500^{o}C), for the alloy containing no I-phase particles, a climb controlled mechanism drives the plastic flow.

9.1.5.8 Fatigue bevaiour

Room temperature fatigue performance of the NQX alloy is similar to high strength Al7075-T6 alloy, whereas 300°C fatigue performance is much superior to any conventional Al alloy including 2618-T651alloy having a high strength at temperature (Kaufman, 2008). Generally, the fracture is initiated: (i) from the surface for high stresses/low N_f, and (ii) from inclusion at low stresses/high N_f (>~10^5) failure cycles. Thus, the NQX alloy behaves as a type II material in fatigue, as classified by Mughrabi (2006).

The number of cycles spent in the crack growth is estimated to be in the order of ~10^5, which is a fraction of its total life in very high cycle fatigue testing. Large inclusion sizes (or nature of the inclusions) result in an early fatigue fracture of the NQX alloy. Sn inclusions have a detrimental effect on the fatigue performance at elevated temperatures.

9.2 Future work

- All the uniaxial tensile tests were performed such that the extrusion direction was parallel to the applied load, sample testing in lateral and slanted direction can further improve the understanding of the NQX alloy behaviour.
- Strain-controlled laser or video extensometers may be used for attaining better accuracy.
- The alloy has a reasonable plasticity almost at all temperatures; the claims of tension-compression yield strength asymmetry on the similar alloy by Luo et al. (2005) may be verified by performing tensile and compression tests at a range of temperatures.
- This work was confined to temperature regimes from room temperature to 500^{o}C, a low temperature (below 0˚C) and low strain rates for inquiring the deformation mechanisms are still needed, and it will also help to determine the lower limit of yield strength anomaly during the DSA.
- Standard creep tests may be conducted at a strain rate range over nine orders of magnitude, from 10^{-10} to $10^{-2}s^{-1}$. Standard jump creep test at intermediate temperatures (150˚C-400˚C) will help to determine the plastic flow control mechanism in the NQX alloy containing quasicrystals. A detailed TEM characterisation work on the tested samples will help to find the evidence and further

explain the plastic deformation models discussed in the present work. Post failure SEM analysis of the samples can also be carried out to study the role of second phase particles (before and after the I-phase transformation) in the cavitation and subsequent fracture.

- Also, standard jump creep test at high temperatures (400˚C-600˚C) followed by a detailed microstructure characterisation will help to refine the model of the plastic flow mechanism at high temperature in the NQX alloy without quasicrystals.
- The number of fatigue samples in each test may be increased to ~30 or higher for a reliable statistical analysis and before commissioning the alloy for the design phase in an application (Lee, 2005). Low cycle fatigue (LCF) and thermomechanical fatigue (TMF) performance may also be assessed, prior to considering the alloy usage in some practical engineering application. 'Plane strain fracture toughness' study should be carried out and compared with other alloys. Crack growth studies can also follow provided the material is available in the required quantity and dimensions.
- Internal friction studies can be carried out utilising the current data and further into higher temperature regimes to probe the anelastic relaxation mechanisms to further understand the behaviour of the alloy.
- An attempt to model the dislocation behaviour by a dislocation dynamics simulation may be useful for the understanding of dislocation interactions in the alloy.

References

ASM (1990) *Nonferrous Alloys and Special-Purpose Materials, vol. 2. ASM International, Materials Handbook*: ASM International.

Kaufman, J. G. (2008) *Properties of aluminum alloys: fatigue data and the effects of temperature, product form, and processing.* ASM International.

Lee, Y.-L. (2005) *Fatigue testing and analysis: theory and practice.* Butterworth-Heinemann.

Luo, H., Shaw, L., Zhang, L. and Miracle, D. (2005) 'On tension/compression asymmetry of an extruded nanocrystalline Al–Fe–Cr–Ti alloy', *Materials Science and Engineering: A,* 409(1), pp. 249-256.

Mughrabi, H. (2006) 'Specific features and mechanisms of fatigue in the ultrahigh-cycle regime', *International Journal of Fatigue,* 28(11), pp. 1501-1508.

Rice, R. C. (2003) *Metallic Materials Properties Development and Standardization (MMPDS): Chapters 1-4.* National Technical Information Service.

Appendix 1. Calculations for the Estimation of Extrusion Pressure

Extrusion is a mechanical forming process in which a metal piece is forced to flow through a die opening to produce a desired cross-sectional shape. Based on the direction of load application relative to the extrudate, the extrusion can be categorised as direct extrusion (RAM and extrudate move in the same direction), or indirect extrusion (RAM and extrudate move in opposite directions) (ASM-Handbook, 2006). A schematic of direct extrusion is provided in Figure A.1.1 (a). A Ram pushes the billet into the die opening and extra energy has to be expended against friction. Consequently, a higher pressure is required for the direct extrusion in comparison with the indirect extrusion, as seen in the Figure A.1.1 (b).

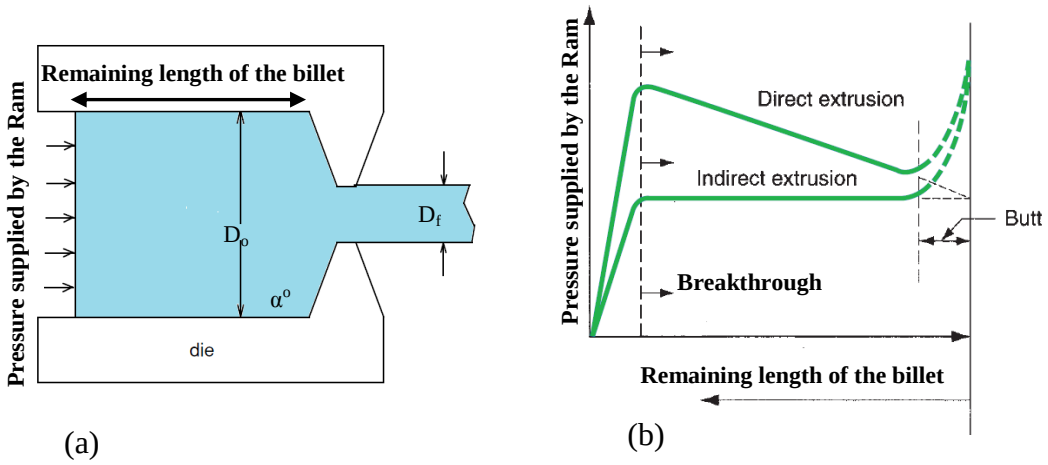

Figure A.1.1 (a) A schematic of extrusion of billet in a die, billet with an initial dia (D_o) is extruded (directly), through a die with angle α_o, and reduced to final dia (D_f), resulting in a desired cross section shape after (Hosford and Caddell, 2011), (b) ram pressures for direct and indirect extrusions, adapted from Groover (2010).

'Breakthrough' pressure is the maximum pressure corresponding to the point where the actual extrusion begins. As the billet begins to extrude the remaining length starts decreasing, and so does the force/pressure required to extrude that length. A small

amount of metal at the end of billet, called as 'Butt' cannot be extruded even with higher pressures, as shown in Figure A.1.1(b) (Groover, 2010).

1.1 Important Parameters for Extrusion

Several material parameters are required for the extrusion pressure calculation such as true strain (ε)[1] strength coefficient (K), strain rate hardening coefficient (n_{sh}) (section 7.4.2) and strain rate sensitivity (m) (section 7.4.3), which can be acquired from the flow curves. These parameters were initially acquired from the work of Rounthwaite (2012) in our group as he performed tensile tests for the same alloy at 23^{o}C and 250^{o}C at a strain rate of $10^{-3}s^{-1}$. Values for these variables were then linearly extrapolated 400°C to be initially used for the calculations of the extrusion parameters. Later, in the present work the values of the mechanical constants/properties were obtained (section 7.4) at a wide temperature and strain rate ranges (23-500^{o}C and 10^{-5}-$10^{-2}s^{-1}$). These values were used for the final calculations.

1.1.1 Temperature

Temperature can be considered as the most important parameter as mostly the values of other parameters constants are a function of temperature. The extrusion can be named cold (~0.3T_m), warm (~0.4T_m-0.5T_m) or hot extrusion (~0.5-0.75T_m) based on the temperature where T_m is the absolute melting temperature (Groover, 2010). In order to increase ductility and to reduce the amount of work required for extrusion (Groover, 2010), high strength Al alloys are generally extruded in the 375-475^{o}C temperature range (Kalpakjian, 2001). In the present study, the available extrusion press had the maximum temperature limit of 500^{o}C. A higher temperature is favoured for easy extrusion; however, since the quasicrystalline phase is a metastable phase so a lower

[1] $\varepsilon = \ln(A_o/A_f)$, where A_o and A_f are cross-sectional areas for billet and extruded bar respectively,

temperature was preferred. The extrusion temperature was chosen as 400^{o}C, which is ~100-130^{o}C lower than the onset of decomposition temperature for the quasicrystalline phase in the alloy powder but still high enough to carry out extrusion safely.

1.1.2 Strain rate

In strain rate, sensitive materials a change of strain rate may vary the values of many mechanical related parameters such as σ_{yeild}, K, n_{sh} especially at high temperatures. During the extrusion, the cross section area of the billet changes in the conical die and the average true strain rate ($\dot{\varepsilon}$) can be estimated using the following relation (Dieter and Bacon, 1986).

$$\dot{\varepsilon} = \frac{6vD_0^2 \ln(\frac{A_o}{A_f}) \tan\alpha^o}{D_0^3 - D_f^3} = \frac{6vD_0^2 \varepsilon \tan\alpha^o}{D_0^3 - D_f^3}$$

Eqn. A.1.1

Where v is the average extrusion speed (~ 0.9±0.1mm/s), α° is the die angle (21.8^{o}), D_o is the billet diameter (50mm with 2.5mm wall) and A_o is the corresponding area, D_f is the diameter of the extruded bar (14mm) and A_f the corresponding area. Average strain rate was calculated as ~ 0.1s^{-1}. The values of the other parameters (K, n_{sh}, and m) were calculated at the strain rate of 0.1s^{-1} and used in this work.

1.1.3 Lubrication

The coefficient of friction (μ) is a crucial parameter for 'direct extrusion' process as its values between billet-die and billet-container affects the total extrusion pressure. The choice and use of the lubricant is pertinent, especially for extrusion of high strength materials, as it reduces the tool wear and the heat generation due to the extrusion process (Altan et al., 2005). Hexagonal boron nitride (HBN) is a solid lubricant having an excellent thermal and chemical stability up to 1000^{o}C. The values of μ for HBN have

been reported to be ~0.1-0.2 (Martin et al., 1992). In the present study, HBN was used as a lubricant and μ values are assumed between 0.16-0.1.

1.1.4 Components of the work for extrusion

The energy required per unit volume (MJ/m^3), or the specific work (MN/m^2) has the same units as pressure (MPa= MN/m^2= MJ/m^3); therefore, the 'specific work required for the extrusion' or 'pressure required for the extrusion' have been used interchangeably. The following different types of work has been identified for the process of extrusion (Lange, 1985)

(i) Ideal work (w_{ideal})

(ii) Redundant work (w_{red})

(iii) Work done against friction in

(a) Container wall ($w_{F,w}$), and (b) Die shoulder ($w_{F,sh}$)

The total work per unit volume of extrudate is the sum of all works combined (Hosford and Caddell, 2011).

$$w_{total} = (w_{idea}) + (w_{red}) + (w_{F,sh}) + (w_{Fr,w}) \qquad \textbf{Eqn. A.1.2}$$

The fraction of ideal to total work is called the efficiency of extrusion which shows that how much additional work has to be done, over and above ideal work required for extrusion. (Hosford and Caddell, 2011)

$$\eta = w_{ideal} / w_{total} \qquad \textbf{Eqn. A.1.3}$$

1.1.4.1 Ideal work (w_{ideal})

The minimum work required per unit volume for extrusion (in the absence of redundant work and friction) is called the ideal work, and it can be calculated using following relation (Kalpakjian, 2001).

$$p = w_{ideal} = \int_{\varepsilon_1}^{\varepsilon_2} \sigma d\varepsilon = K \int_{\varepsilon_1}^{\varepsilon_2} \varepsilon^{n_{sh}} \, d\varepsilon$$ **Eqn. A.1.4**

The initial small elastic strain is neglected, so the lower limit becomes zero. And the relation can be written as following (Groover, 2010)

$$p = w_i = K \int_0^{\varepsilon} \varepsilon^{n_{sh}} d\varepsilon \Rightarrow K \frac{\varepsilon^{n_{sh}+1}}{n_{sh}+1}$$ **Eqn. A.1.5**

Where σ is the flow stress, K is the strength coefficient, ε is the true strain, n_{sh} is the strain hardening coefficient.

The alloy powder was encapsulated in a 'can' having a wall thickness of 2.5mm where-as the outer diameter was 50mm. The actual alloy powder occupies an initial diameter of 45mm which was used in measuring the strain (ε).

1.1.4.2 Redundant work (w_{red})

The redundant work is the energy expended in plastic straining (which otherwise is not required) as the deformation of material from larger to smaller diameter is not homogeneous. In the extruded component the central portion of material 'flows' more than the surface material and this relative shearing increases with the die angle α^o (Hosford and Caddell, 2011). For small die angles the approximate redundant work is given by following relation (Lange, 1985).

$$w_{red} = \frac{2}{3} \tan\alpha K \frac{\varepsilon^{n_{sh}}}{n_{sh}+1}$$ **Eqn. A.1.6**

Where σ is the flow stress, K is the strength coefficient, ε is the true strain, n_{sh} is the strain hardening coefficient, α^o is the die angle.

1.1.4.3 Work done against friction (w_F)

During the direct extrusion, there is relative movement and a contact between the container wall and the billet and energy has to be expended to overcome the friction. The coefficient of friction plays an instrumental role to determine the specific work required against friction.

The work done against friction between container wall/billet ($W_{F,w}$) depends on the coefficient of friction (μ), initial length (L_o) of solid billet, and initial outer diameter (D_o) of the can used, and the yield strength (σ_{yield}). It can be estimated from following relation (Lange, 1985).

$$w_{F,w} = \frac{4\mu L_0 \sigma_{yield}}{D_0} \qquad \textbf{Eqn. A.1.7}$$

As the material is forced through the die opening the work needs to be performed against the frictional force in the die shoulder ($W_{F,\ sh}$) region magnitude of which depends on the ideal work, the die angle (α) and the coefficient of friction (μ) (Lange, 1985).

$$w_{F,sh} = \frac{2w_{ideal}\mu}{\mathrm{Sin}2\alpha} \qquad \textbf{Eqn. A.1.8}$$

1.2 Calculation of Total Specific Work (Pressure) for the Extrusion

Table A.1.1 summarises the contributions by the individual works in mathematical expressions.

Table A.1.1 Various components of the work required for extrusion.

Ideal Work	Redundant Work	Work against friction (in die shoulder)	Work against friction (in container wall)	Total Work	Efficiency
w_{ideal}	w_{red}	$w_{F,sh}$	$w_{F,w}$	W_{total}	η
$K\frac{\varepsilon^{n_{sh}+1}}{n_{sh}+1}$	$\frac{2}{3}\tan\alpha\ K\frac{\varepsilon^{n_{sh}}}{n_{sh}+1}$	$\frac{2w_{ideal}\mu}{\mathrm{Sin}2\alpha}$	$\frac{4\mu L_0\sigma_{yeild}}{D_0}$	Σw	$w_{ideal}/\Sigma w$

The expression and variables in Table A.1.1 have already been defined in the above discussion. Using the values of these parameters the contribution of the each component of the work required to perform the extrusion was calculated and provided in Table A.1.2. The total work or pressure required for extrusion is calculated as 1015 and 1200MPa at 400^{o}C using μ values of 0.1 and 0.16 respectively. The estimated values of the peak extrusion pressure provide a guide for performing a safe extrusion.

Table A.1.2 Calculations of estimated extrusion pressures at various temperatures.

$\dot{\varepsilon}$	T	L_o	μ	σ_{Yield}	K	n_{sh}	W_{ideal}	W_{red}	$W_{F,sh}$	$W_{F,wall}$	Total Work	Efficiency
s^{-1}	^{o}C	mm		MPa	MPa		MPa					
0.1	23	65	0.15	551	800	0.05	1856	212	861	458	3388	0.55
0.1	350	65	0.15	304	390	0.03	907	104	421	253	1684	0.54
0.1	400	65	0.16	213	280	0.05	650	74	301	177	1202	0.54
0.1	400	65	0.1	197	280	0.05	650	74	188	102	1015	0.64

References

Altan, T., Ngaile, G. and Shen, G. (2005) *Cold and hot forging: fundamentals and applications.* ASM international.

ASM-Handbook (2006) *Metalworking: Bulk Forming.* ASM International.

Dieter, G. E. and Bacon, D. (1986) *Mechanical metallurgy.* McGraw-Hill New York.

Groover, M. P. (2010) *Fundamentals of modern manufacturing: materials processes, and systems.* John Wiley & Sons.

Hosford, W. F. and Caddell, R. M. (2011) *Metal forming: mechanics and metallurgy.* Cambridge University Press.

Kalpakjian, S. (2001) *Manufacturing engineering and technology.* Pearson Education India.

Lange, K. (1985) *Handbook of metal forming. McGraw-Hill Book Company, 1985*.

Martin, J., Le Mogne, T., Chassagnette, C. and Gardos, M. N. (1992) 'Friction of hexagonal boron nitride in various environments', *Tribology transactions*, 35(3), pp. 462-472.

Rounthwaite, N. J. (2012) *Development of Bulk Nanoquasicrystalline Alloys for High Strength Elevated Temperature Applications.* DPhil Thesis, University of Oxford.

Appendix 2. Fatigue

The fatigue can be either called: (i) high cycle fatigue (HCF, N_f ~>10^6), (ii) low cycle fatigue (LCF, N_f ~10^3-10^5), (iii) thermo- mechanical fatigue (TMF, variable σ and T) or (iv) corrosion fatigue depending upon number of failure cycles (N_f), applied load, temperature or environmental condition. In HCF, the high cyclic frequency is coupled with small loads (or small elastic strains) and nucleation of fatigue crack is extremely important in limiting the fatigue life since the defects act as crack nucleation sites (Tjong and Mai, 2003).

2.1 Fatigue Crack Growth Calculations

When fatigue fracture takes place at an internal inhomogeneity in type II alloys (steels and few Al alloys) it generally has a 'fisheye' appearance (Höppel et al., 2011). The number of cycles in the fisheye can be estimated by combining Paris-Hertzberg-McClintock relation for the crack growth rate (Eqn. A.2.1) and the stress intensity factor of a circular crack (Eqn. A.2.2).

$$\frac{da}{dN} = b\left(\frac{\Delta K_{Eff}}{E\sqrt{b}}\right)^3 \qquad \textbf{Eqn. A.2.1}$$

$$\Delta K = \frac{2\Delta\sigma\sqrt{\pi a}}{\pi} \qquad \textbf{Eqn. A.2.2}$$

Where ΔK_{eff} denotes stress intensity range, E is Young's modulus, da/dN is crack growth per cycle, b is Burgers vector and Δσ is stress range. Using the said relations Bathias and Paris (2004) came up with a predictive equation to estimate the number of cycles in a fisheye ($N_{fisheye}$), from threshold corner to brittle fracture.

$$N_{Fisheye} = \frac{\pi E^2}{\Delta\sigma^2} \qquad \textbf{Eqn. A.2.3}$$

Eqn. A.2.3 in present work (section 8.4.1) was used to show that the number of cycles spent in crack initiation is very large as compared to the number of cycles spent in crack growth in the fisheye.

2.2 Control Volume Calculations

The maximum stress occurs at the minimum cross section of the sample area. By definition, the control volume is enclosed inside the boundary (cross section area) experiencing 90% of the maximum stress, and this cross section area is; therefore, equal to the minimum cross-sectional area times $(0.9)^{-1}$. Figure A.2.1 is the schematic of the curved portion of a fatigue sample for the calculations of the control volume. Where R_o is the length of minimum radius (which corresponds to a point in the cross section area having the maximum stress), $R_{con.vol}$ is the radius of the cross section with 90% stress value (corresponding to the boundary of the control volume), and L is the horizontal distance between R_o and $R_{con.vol}$. The radius of curvature is the minimum radius of the curve joining the R_o and R_{cv} with a centre point C(0,0), P(x,y) is any point on the radius of curvature whereas B is the intersection point of the boundary of control volume and radius of curvature as shown in the Figure A.2.1.

The curvature (of the circle) joining the R_o and $R_{con.vol}$ has a radius R, and the equation of the circle in cartesian coordinates is of the following form.

$$\left(x - x_1\right)^2 + \left(y - y_1\right)^2 = R^2$$

Eqn. A.2.4

Eqn. A.2.4 can be solved for the curves in values of R_0 and $R_{con.vol}$ are known, it can be then written in terms of the value of y and the volume of revolution inscribed by the curve around the x-axis can then written as the following.

$$\text{Volume of revolution} = \int_{-L}^{L} Area(x).dx \qquad \textbf{Eqn. A.2.5}$$

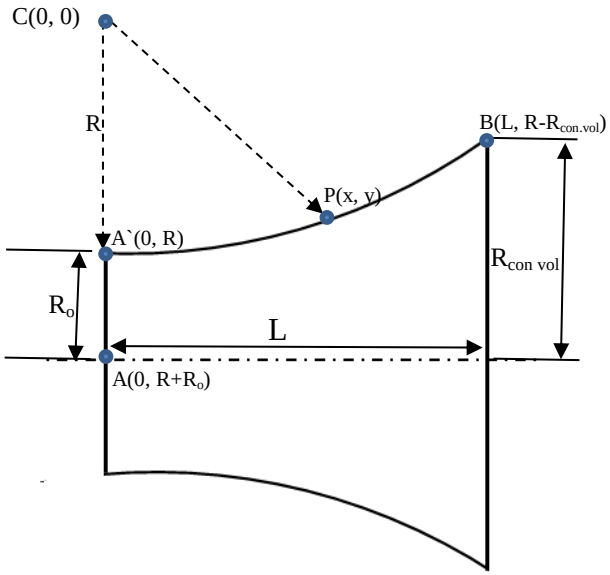

Figure A.2.1 Side view of the curved portion of a fatigue sample corresponding to half of control volume.

The schematic for all fatigue samples is shown in chapter 3 Figure 3.5. The control volume calculations for all three samples are given below.

2.2.1 60Hz HCF, 23°C sample

Control volume= $V_{control} = \pi r^2 L_{Gauge}$ + curved portion volume

radius in gauge section = r =2.15mm,

Gauge Length = L_{Gauge} =12mm

$V_{control}$ =174.26mm^3 + curved portion

radius of curvature = 8mm

R_o =2.15mm

$R_{con.vol}$ =2.2663

as

$(x-0)^2-(y-10.15)^2=8^2$

$at\ y = 2.2663 \Rightarrow x = 1.3591$

$$y = f(x) = \left(10.15 - \sqrt{8^2 - x^2}\right)$$

volume of revolution= $\int_{-1.3591}^{1.3591}$ Area(x).dx

Cross-sectional area=πy^2

Volume of curve= $\int_{-1.3591}^{1.3591} \pi\left(10.15-\sqrt{8^2-x^2}\right)^2 .dx$

$=40.896mm^3$

Control Volume=174.26+40.896=$215.16mm^3$

2.2.2 20kHz VHCF, 23°C sample

There is no gauge section in samples (ii) and (iii) so the control volume is only calculated using the curved portion.

radius of curvature = 31mm

$R_o = 1.5mm$, $R_{con.vol} = ?$

$as \;\; A_o = \frac{\pi(1.5)^2}{0.9} = 7.068mm^2$

$A_{con.vol} = 7.854mm^2$

$R_{con.vol} = 1.5811mm$

equation of the center portion of fatigue sample can be written as

$(x-0)^2 - (y-32.5)^2 = 31^2$

at y=1.5811mm $\Rightarrow$ x= 2.2413

rearranging

$y = f(x) = \left(32.5 - \sqrt{31^2 - x^2}\right)$

volume of revolution= $\int_{-2.2413}^{2.2413} Area(x).dx$

$cross\,\text{sec}\, Area = \pi y^2$

Control Volume $= \pi \int_{-2.2413}^{2.2413} \left(32.5 - \sqrt{31^2 - x^2}\right)^2 .dx$

$= 32.846mm^3$

2.2.3 40Hz HCF, 300°C sample

Radius of curvature = 40.64mm

$R_o = 2.54mm$, $R_{con.vol} = ?$

$as\ A_{con.vol} = \frac{\pi(2.54)^2}{0.9} = 22.5203mm^2$

$R_{con.vol} = 2.6774mm$

equation of the center portion of fatigue sample can be written as

$(x\text{-}0)^2 - (y - 43.18)^2 = 40.64^2$

at y=2.6774mm $\Rightarrow$ x= 3.33895

rearranging

$y = f(x) = \left(43.18 - \sqrt{40.64^2 - x^2}\right)$

volume of revolution= $\int_{-3.33895}^{3.33895} Area(x).dx$

$cross\,\sec Area = \pi y^2$

Control Volume= $\int_{-3.33895}^{3.33895} \pi\left(43.18\text{-}\sqrt{40.64^2\text{-}x^2}\right)^2 .dx$

=140.234mm^3

References

Bathias, C. and Paris, P. C. (2004) *Gigacycle fatigue in mechanical practice.* CRC Press.

Höppel, H. W., May, L., Prell, M. and Göken, M. (2011) 'Influence of grain size and precipitation state on the fatigue lives and deformation mechanisms of CP aluminium and AA6082 in the VHCF-regime', *International Journal of Fatigue,* 33(1), pp. 10-18.

Tjong, S. C. and Mai, Y.-W. (2003) 'Failure of Metal-Matrix Composites', in Karihaloo, B.L. & Knauss, W.G. (eds.) *Fundamental Theories and Mechanisms of Failure Comprehensive structural integrity*: Elsevier.

Appendix 3. Grains in the EBSD

To define a grain the TSL OIM[A] (EBSD) software uses an algorithm which is based on the value of the 'grain tolerance angle'. Two neighbouring scan points are considered to be from the same grain if their misorientation is less than the (user defined) grain tolerance angle (15° in the present case). Use of the 'unique grain colour maps' is the best way to show how the points are grouped to form the individual grains by the software. Each neighbour of a grain is assigned a different colour to generate a 'unique grain colour map'. The grain size histogram in the EBSD images in section 4.3.5 and 5.2.5 represent the grain sizes from the 'unique grain colour map'. The minimum number of points required to decide whether a given group of points is to be counted as a 'grain' can be specified by the user (200nm in the present case).

Grain size is specified by the area which can be calculated by using the number of points in a grain and the step size. The grains are considered to be circular and their diameter is calculated/reported form the respective grain area.

Unique grain colour maps are provided in this section for the grain size distribution results used in section 4.3.5 and 5.2.5.

[A] Help file of the TSL OIM software has been used for writing up of this section.

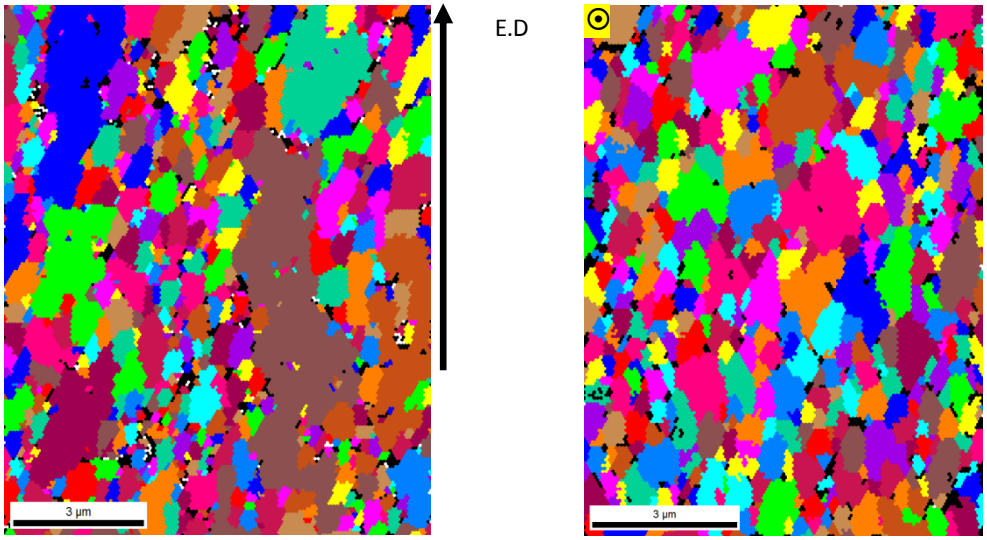

(a) 'as extruded', longitudinal section (b) 'as extruded', cross section

Figure A.3.1 EBSD 'unique grain colour map' for the 'as extruded' samples (a) longitudinal sample (b) cross section sample.

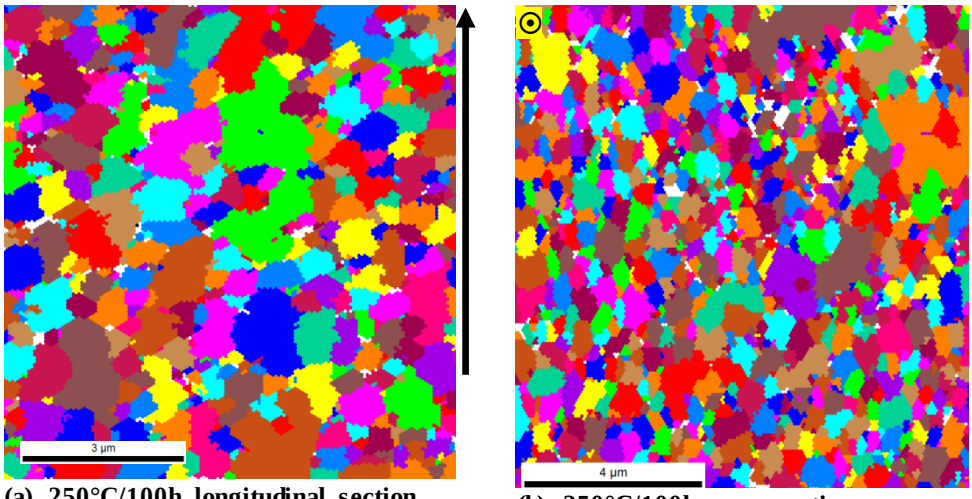

(a) 250°C/100h, longitudinal section (b) 250°C/100h, cross section

Figure A.3.2 EBSD 'unique grain colour map' for the 250°C/100h samples (a) longitudinal sample (b) cross section sample.

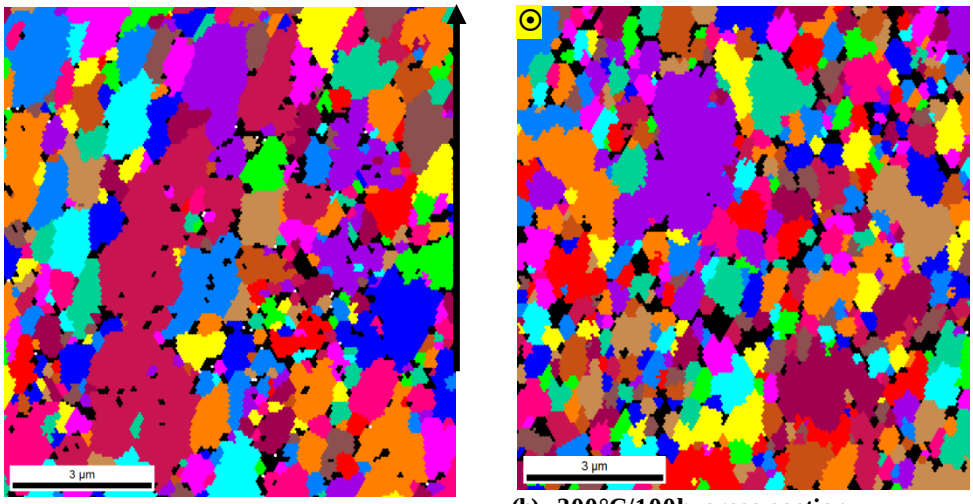

(a) 300°C/100h, longitudinal section (b) 300°C/100h, cross section

Figure A.3.3 EBSD 'unique grain colour map' for the 300°C/100h samples (a) longitudinal sample (b) cross section sample.

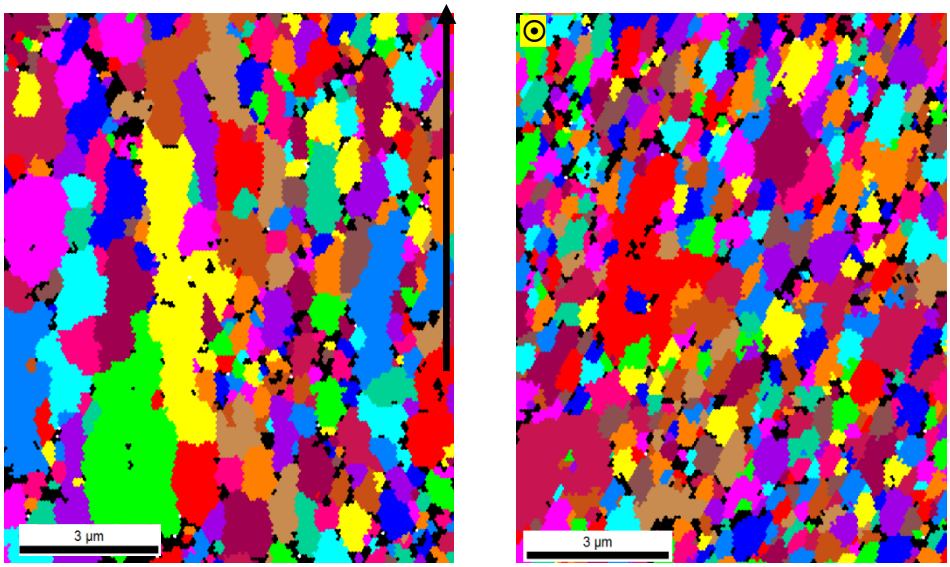

(a) 350°C/100h, longitudinal section (b) 350°C/100h, longitudinal section

Figure A.3.4 EBSD 'unique grain colour map' for the 350°C/100h samples (a) longitudinal sample (b) cross section sample.

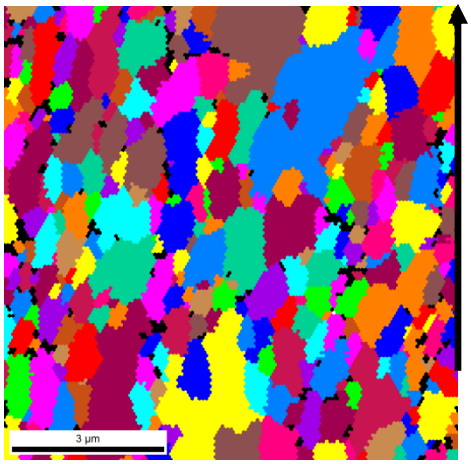

(a) 400°C/100h, longitudinal section

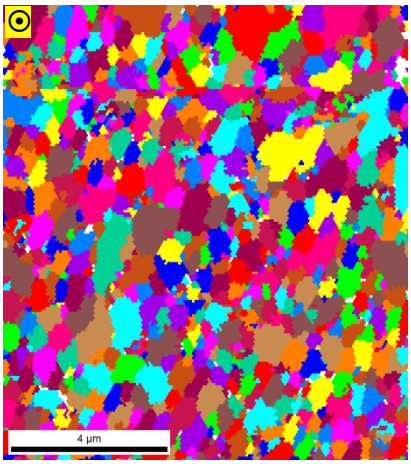

(b) 400°C/100h, cross section

Figure A.3.5 EBSD 'unique grain colour map' for the 400°C/100h samples (a) longitudinal sample (b) cross section sample.

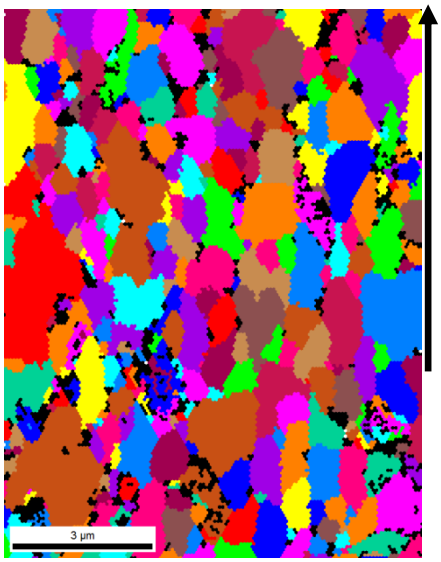

(a) 450°C/100h, cross section

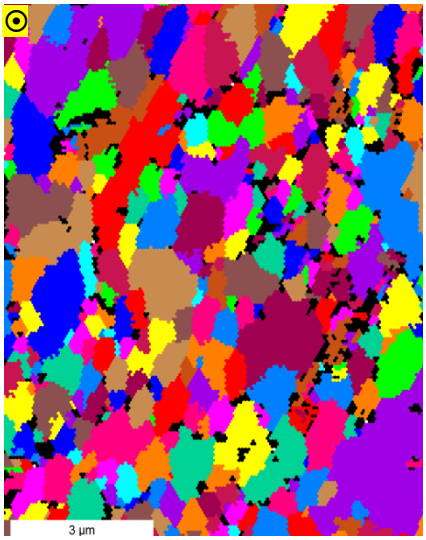

(b) 450°C/100h, cross section

Figure A.3.6 EBSD 'unique grain colour map' for the 450°C/100h samples (a) longitudinal sample (b) cross section sample.

Appendix 4. Engineering Stress - Engineering Strain and True Stress - True Strain Relations

True stress – true strain curves were shown in chapter 6 and 7. The engineering stress-engineering strain and the corresponding true stress or true strain can be obtained using the following relations[A].

if

Engineering stress = S , Engineering strain= e

True stress= σ, True strain=ε

Load=F,

Initial Area= A_o, Area= A

Initial Length=L_o, Length=L

Constancy of volume implies that

$$A_o L_o = AL \qquad \textbf{Eqn. A 4.1}$$

$$e = \left(\frac{L - L_o}{L_o} \right) = \left(\frac{A_o - A}{A} \right) \qquad \textbf{Eqn.A 4.2}$$

$$\varepsilon = \ln\left(\frac{L}{L_o} \right) = \ln(1+e) \qquad \textbf{Eqn.A 4.3}$$

$$S = \frac{F}{A_o} \qquad \textbf{Eqn.A 4.4}$$

$$\sigma = \frac{F}{A} = S(1+e) \qquad \textbf{Eqn.A 4.5}$$

[A] Dieter, G. E. and Bacon, D. (1986) *Mechanical metallurgy.* McGraw-Hill New York.

Appendix 5. Elevated Temperature Plasticity

The elevated temperature plasticity behaviour was analysed in two regions (i) 425-500°C region (I-phase transformed) (ii) 250-350°C region (I-phase containing).

5.1 Finding parameters of the Zener-Hollomon model

The model was explained in section 8.3.2.1. n_{se} was calculated by plotting $\dot{\varepsilon}$ vs σ_{ss} on a log-log scale (Figure A.5.1) , β was calculated from a semi log plot of $\dot{\varepsilon}$ vs σ_{ss} (Figure A.5.2). In both temperature regions, average values of n_{se} (called n`) and β were used to find the value of constant α using Eqn. A.5.1.

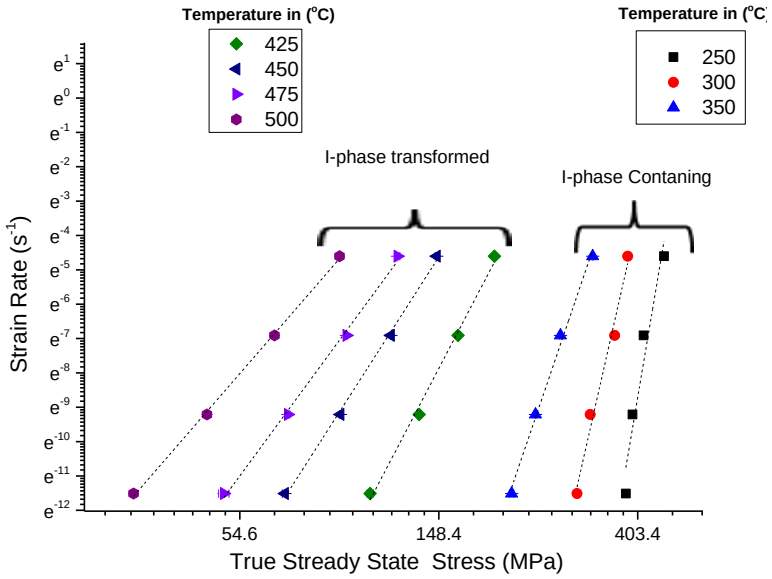

Figure A.5.1 Stress exponent (n_{se}) values were obtained from the slope of the straight lines for two temperature regions.

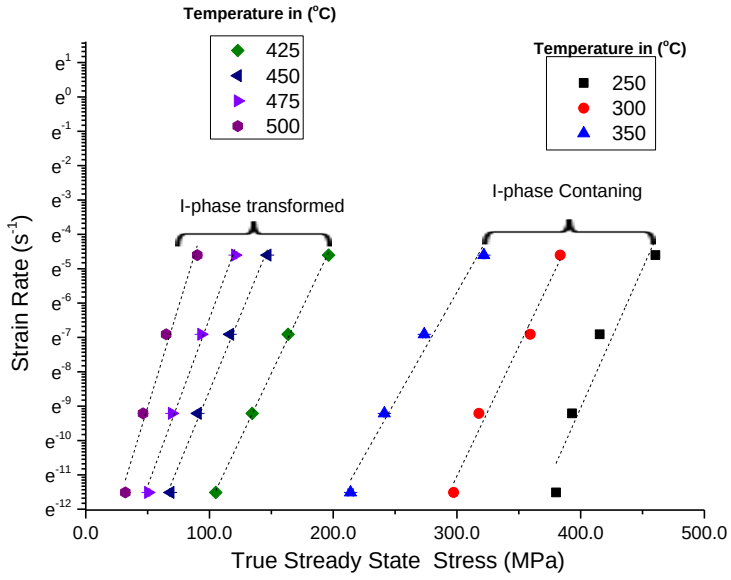

Figure A.5.2 β values were obtained from the slope of the straight lines two temperature regions.

$$\alpha \approx \frac{\beta}{n'} \approx \frac{\beta}{n_{zh}} \qquad \textbf{Eqn. A.5.1}$$

Activation energy can be calculated using the equation below, which contains two terms S1 and S2 (marked with the brackets).

$$Q_{app} = R\underbrace{\left[\frac{\delta \ln\{Sinh(\alpha\sigma)\}}{\delta(1/T)}\right]}_{S1}\underbrace{\left[\frac{\delta \ln(\dot{\varepsilon})}{\delta \ln\{Sinh(\alpha\sigma)\}}\right]}_{S2} \qquad \textbf{Eqn. A.5.2}$$

S1 is the average slope found by plotting Sinh(ασ) vs 1/T on a semi log-log scale (Figure A.5.6and Figure A.5.3); whereas S2 is the average slope found by plotting $\dot{\varepsilon}$ vs Sinh(ασ) on a log-log scale (Figure A.5.7and Figure A.5.4). Q_{app} is found using Eqn. A.5.2.

Zener-Hollomon parameter (Z) is then calculated using Eqn. A.5.3 (Figure A.5.8 and Figure A.5.5).

$$Z = \dot{\varepsilon} e^{\left(\frac{Q}{RT}\right)} = A_{zh}[\sinh(\alpha\sigma)]^{n_{zh}} \qquad \textbf{Eqn. A.5.3}$$

5.1.1 425-500°C region

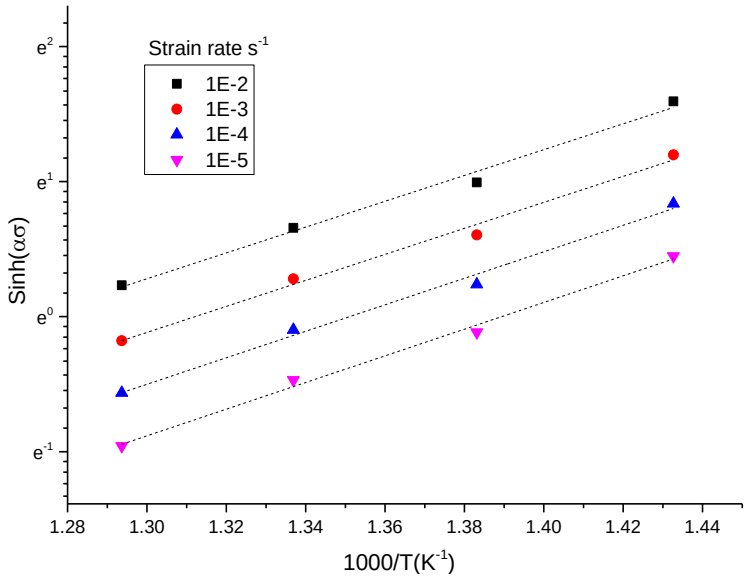

Figure A.5.3 S1 values are calculated from the average slopes of ln Sinh(ασ) vs 1/T plot.

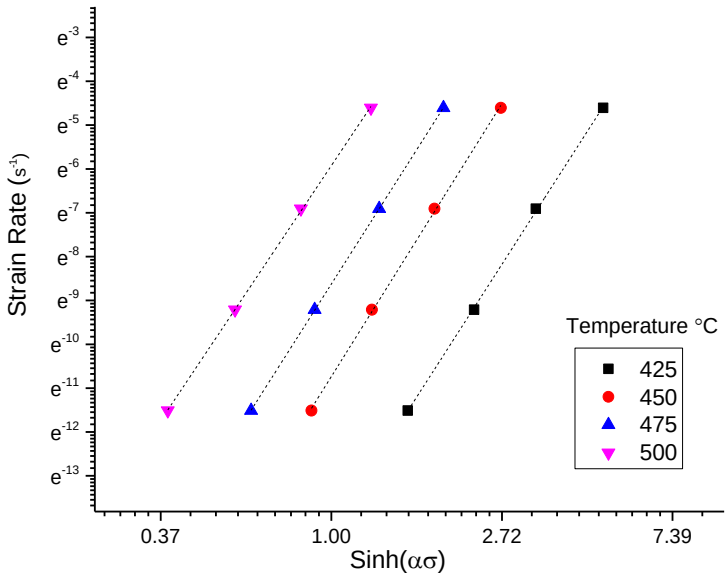

Figure A.5.4 S2 values are calculated from the average slopes of the plot ln$\dot{\varepsilon}$ vs ln(Sinh(ασ)).

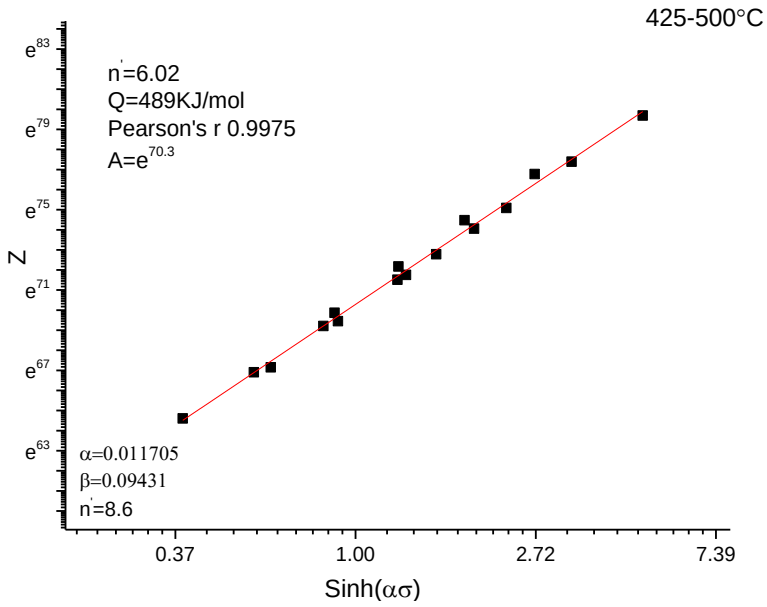

Figure A.5.5 Z vs Sinh(ασ) on a log-log scale in 425-500°C region, a summary of all parameters is provided. n_{zh} value is ~6.0.

5.1.2 250-350°C region

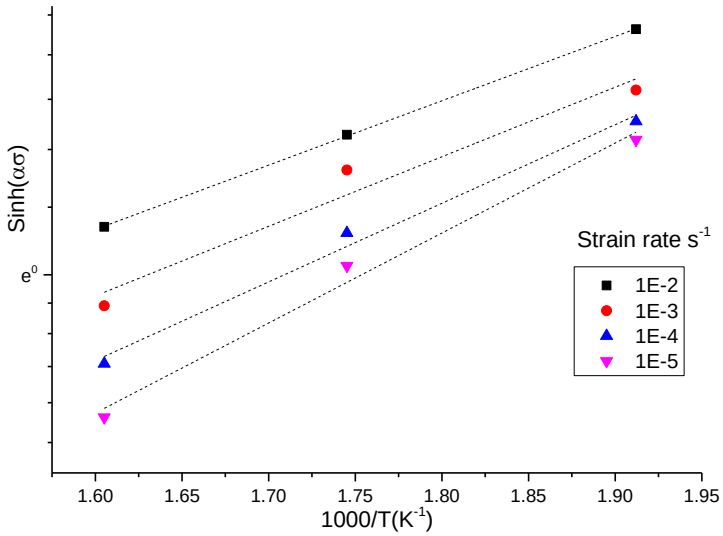

Figure A.5.6 S1 values are calculated from the average slopes of ln Sinh(ασ) vs 1/T plot.

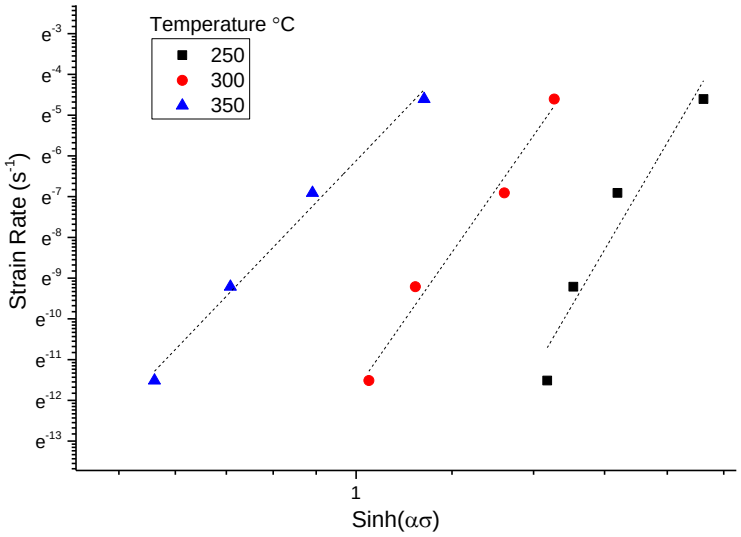

Figure A.5.7 S2 values are calculated from the average slopes of the plot lnε̇ vs ln(Sinh(ασ)).

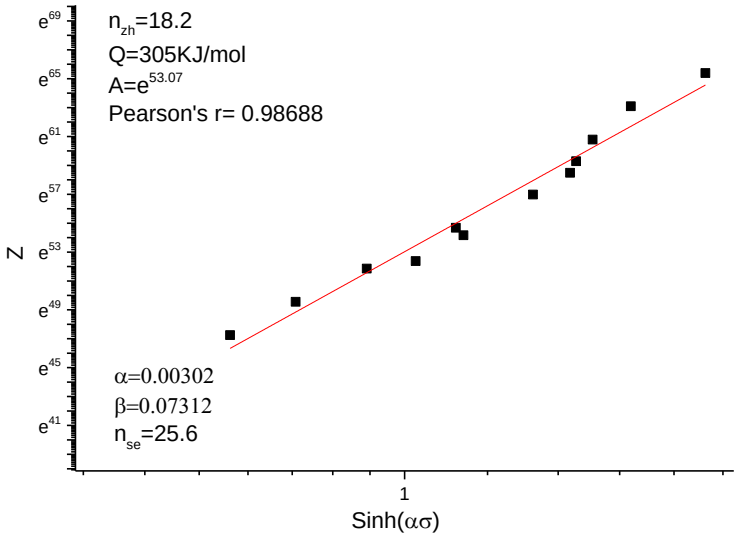

Figure A.5.8 Z vs Sinh(ασ) on a log-log scale in 300-350°C region, a summary of all parameters is provided. n_{zh} value is ~15.6.

5.2 Power Law Creep and Power Law Breakdown

The power law creep plot between $\dot{\varepsilon}/D_{effcetive}$ vs σ/G are provided in Figure A5.9. $\dot{\varepsilon}/D_{eff}=10^{-13}$ m^2/s is a criteria used for the start of power law break down by Lesuer et al. (2000).

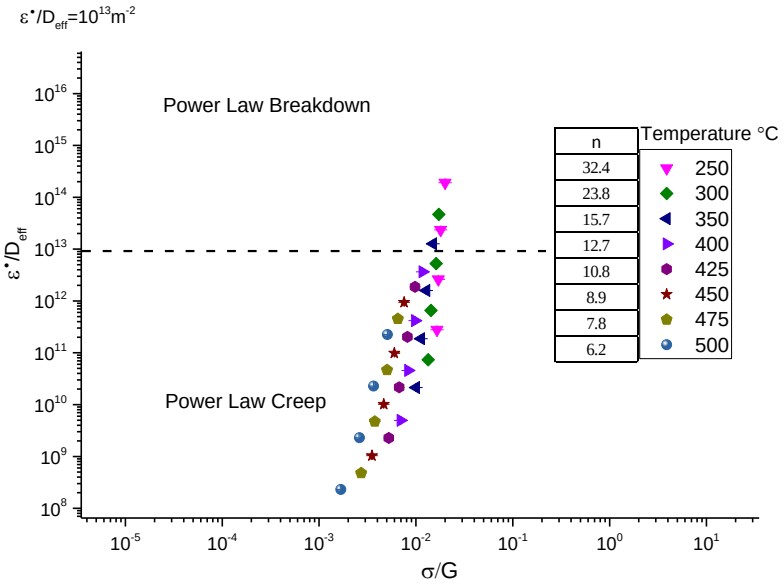

Figure A5.9 Normalised strain rate plotted against normalised stress for the NQX alloy. PLB can be assumed to occur above $\dot{\varepsilon}/D_{eff}=10^{-13}$ m^{-2} after Lesuer et al. (2000).

$$D_{effective} = f_{pipe}D_{Pipe} + f_{Lattice}D_{Lattice} \qquad \textbf{Eqn. A5.4}$$

Where D is diffusion coefficient and f is volume fraction such that

$$f_{pipe} + f_{lattice} = 1 \qquad \textbf{Eqn. A5.5}$$

$$f_{pipe} \sim 50\left(\frac{\sigma}{\mathrm{E}}\right)^2 \qquad \textbf{(Brahmi et al., 1998)} \qquad \textbf{Eqn. A5.6}$$

$$D = D_o e^{\left(-\frac{Q}{RT}\right)} \qquad \textbf{Eqn. A5.7}$$

Also for Al, $D_{o,pipe}=2.8x10^{6}$ m^2/s, $Q_{pipe}=82kJ/mol$, $D_{o,lattice}=1.7x10^{4}$ m^2/s, and $Q_{pipe}=142kJ/mol$.

5.3 Finding the Values of Threshold Stress

The threshold stress (σ_{th}) was found by assuming different values of n_{se} (3, 5, 7, 8). $\dot{\varepsilon}^{1/n}$ is plotted against σ_{ss} (Lagneborg and Bergman, 1976), for both temperature regions; straight lines are fitted whose x-intercept gives the threshold stress value for the particular temperature the plots are shown for n (8, 7, 6, 5, and 3) from Figure A.5.11 to Figure A.5.14 respectively.

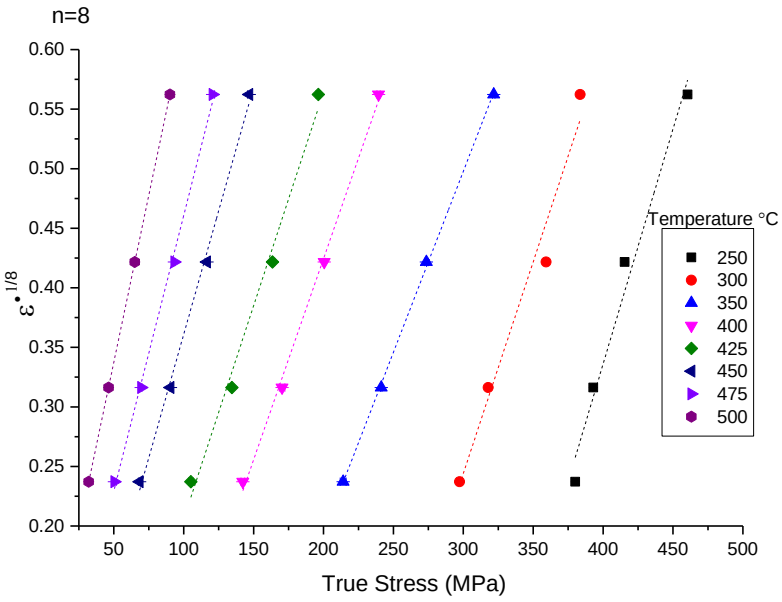

Figure A.5.10 Plot of $\dot{\varepsilon}^{1/8}$ vs σ_{ss}, the x-intercepts gives the threshold stress.

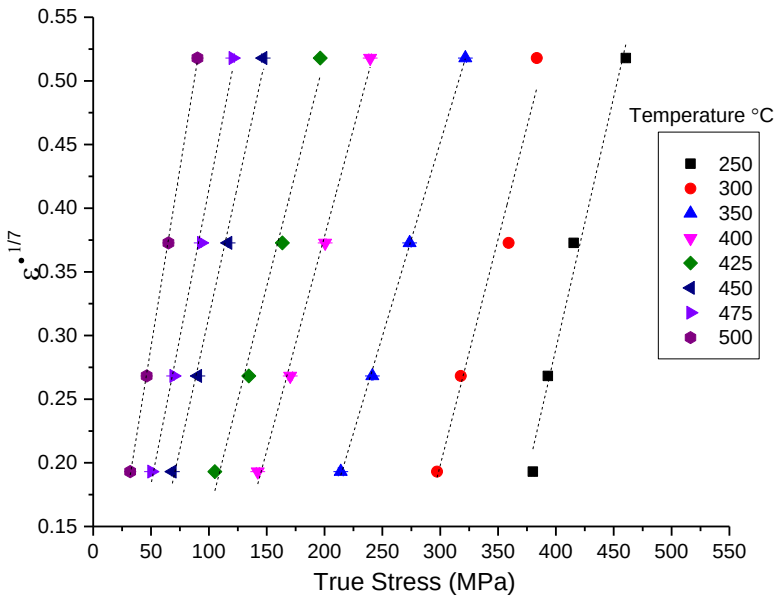

Figure A.5.11 Plot of $\dot{\varepsilon}^{1/7}$ vs σ_{ss}, the x-intercepts gives the threshold stress.

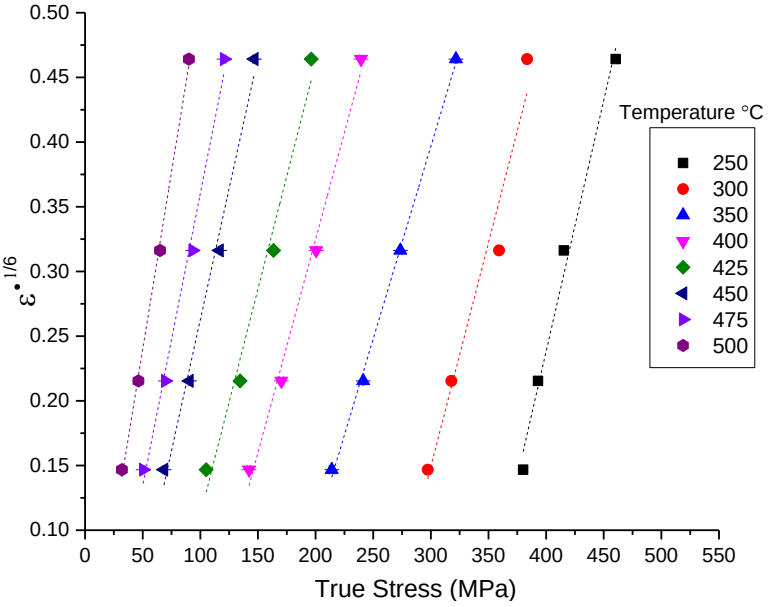

Figure A.5.12 Plot of $\dot{\varepsilon}^{1/6}$ vs σ_{ss}, the x-intercepts gives the threshold stress.

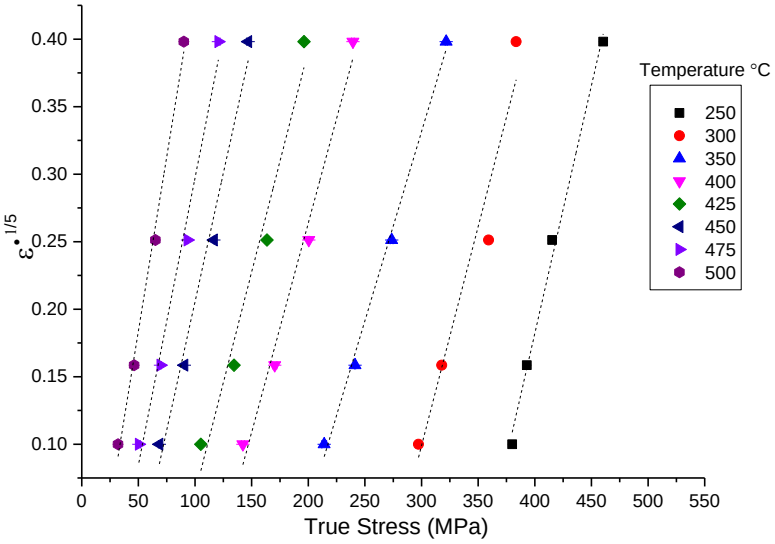

Figure A.5.13 Plot of $\dot{\varepsilon}^{1/5}$ vs σ_{ss}, the x-intercepts gives the threshold stress.

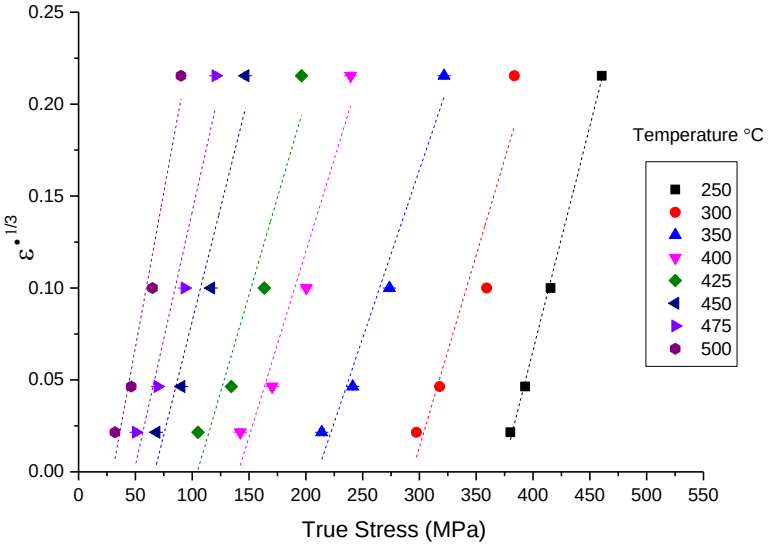

Figure A.5.14 Plot of $\dot{\varepsilon}^{1/3}$ vs σ_{ss}, the x-intercepts gives the threshold stress.

5.4 Threshold stress vs Temperature and Modulus

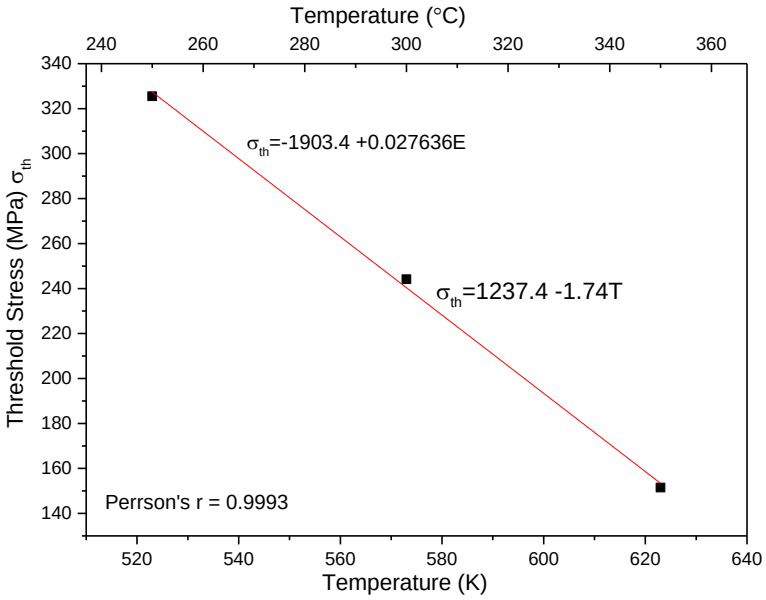

Figure A5.15 Threshold stress (n=7) vs Temperature for 250-350°C region.

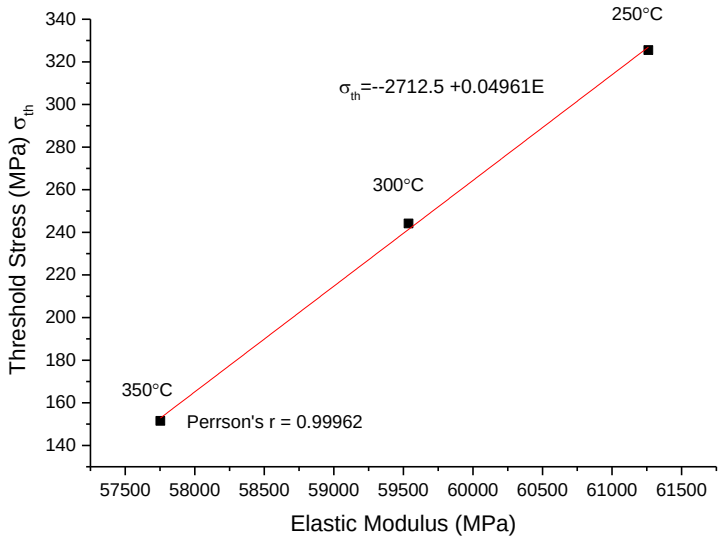

Figure A5.16 Threshold stress (n=7) vs Al Young's modulus for 250-350°C region.

References

Brahmi, A., Gerique, T., Torralba, M. and Lieblich, M. (1998) 'The threshold stress in a rapidly solidified Al–5Cr–2Zr alloy', *Materials Science and Engineering: A*, 246(1), pp. 55-60.

Lagneborg, R. and Bergman, B. (1976) 'The stress/creep rate behaviour of precipitation-hardened alloys', *Metal Science*, 10(1), pp. 20-28.

Lesuer, D., Syn, C. and Sherby, O. 'An evaluation of power law breakdown in metals, alloys, dispersion hardened materials, and compounds', *Deformation, Processing and Properties of Structural Materials, TMS,* , Warrendale, PA, October 20, 1999: The Metals/Minerals Society, 81-194.

Appendix 6. Thermo-Physical Properties of the NQX Alloy

Thermo-physical properties such as coefficient of thermal expansion, thermal diffusivity and thermal conductivity are important for alloys used in engineering applications at the elevated temperatures such as pistons. These physical properties are unknown for the NQX alloy. This appendix reports the experimental methods and the measurements of some thermo-physical properties of the $Al_{93}Fe_3Cr_2Ti_2$ NQX alloy.

6.1 Experimental Methods

The measurements were subcontracted to National Physical Laboratory. Thermal expansion measurements were made in a Linseis twin apparatus system testing the two test-pieces simultaneously by measuring the change in length of each sample. Three thermal cycles were performed to 450 °C at a heating/cooling rate of 2 °C/min with a 10-minute hold at the maximum temperature in accordance with the European standard CEN EN 821-1 (CEN, 1995).

Thermal diffusivity measurements were made using the laser flash method. In this method, a single thermal laser light is pulsed onto one side of a plane parallel sample, and the temperature response on the other side of the sample is measured. From this response, the thermal diffusivity of the sample can be calculated (Parker et al., 1961), (Cowan, 1963). The laser flash thermal diffusivity apparatus was designed and built by Netzsch (model LFA427). The disc-shaped samples for solid measurements, approximately 10 mm (diameter) x 2.5 mm (thick), were heated (or cooled) to the measurement temperature in a graphite element furnace, under an atmosphere of argon, and stabilised with respect to temperature for at least 10 minutes prior to making a thermal diffusivity measurement. Samples were tested uncoated, but with a grit-blasted surface to improve laser absorbance. For the present tests on solid samples, the apparatus was heated to

400°C with measurements taken at 50°C steps. At least five laser pulses were applied at each temperature step to provide a check on repeatability and an average value. The uncertainties associated with the derived thermal diffusivity values were considered to be approximately ±4%.

6.2 Results and Discussion

The coefficient of thermal expansion (CTE) for the extruded alloy was measured at various temperatures from 150 to 450^{o}C as shown in Figure A.6.1**,** considering the length at room temperature as the reference. The CTE values were found to be in the range of 19 to 21.6μ/^{o}C. The CTE values of 99.99% pure aluminium have also been provided from literature (Hatch, 1984). The average value of the CTE for most Al alloys is ~23-30 μ/^{o}C in the temperature range of 20-400^{o}C (ASM, 1990, Lundberg, 1994). A low CTE is generally desirable in high-temperature automotive applications such as pistons (Hillier and Coombes, 2004), where small or large CTE values could be the difference between smooth running and engine seizure.

The room temperature densities of all the bars were measured to be ~2.95g/cm^3 (or 10^3.kg/m^3) as mentioned in section 6.1. The CTE is considered an isotropic property, and if its value is known at higher temperatures, the density of the material can be calculated at that temperature using Eqn. A 6.1 (Morrell et al., 2015).

$$\rho_T = \frac{\rho_o}{(1+CTE_T.\Delta T)^3} \qquad \textbf{Eqn. A 6.1}$$

Where ρ_T is the density at a certain temperature, ρ_o is the density at a reference temperature (room temperature in this case), CTE_T is the coefficient of thermal expansion at a certain temperature, and ΔT is the temperature difference. The density decreases as the material expands at higher temperatures, thus, assuming an isotropic material, the

values for elevated temperature density can be calculated using Eqn. A 6.1. The results are shown in Figure A.6.2 (b).

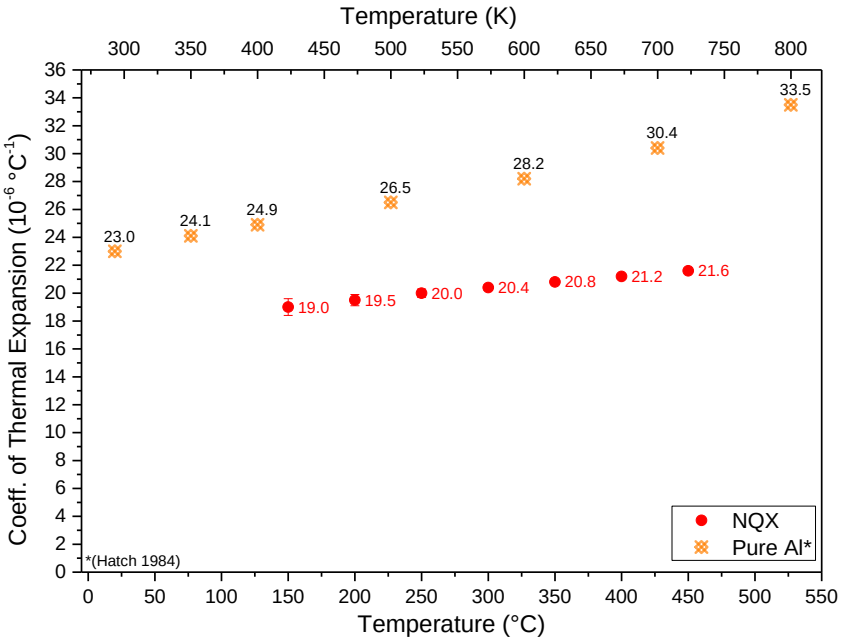

Figure A.6.1 Coefficient of thermal expansion for the 'as extruded' NQX alloy (this work), and pure aluminium (Hatch, 1984) at various temperatures.

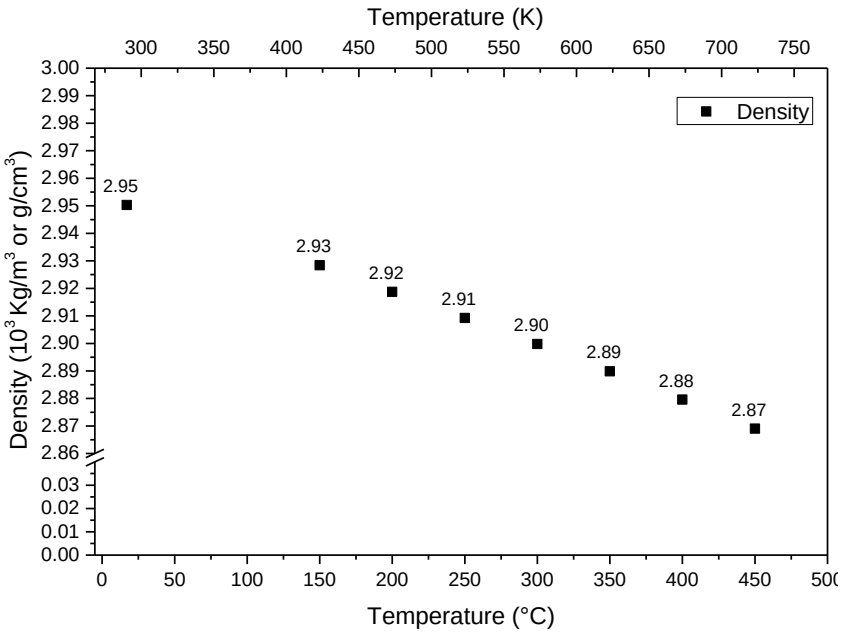

Figure A.6.2 Average measured density at room temperature and calculated density values at various elevated temperatures for the NQX alloy.

Accurate measurement of specific heat (C_p) of materials is difficult, and the values for the alloys are generally calculated (Hatch, 1984). Software (MTDATA) based calculation of the specific heat (C_p) of the alloy was performed, using the nominal at% composition of each of the major elements present in the alloy (Al, Fe, Cr, and Ti). Cr was not available in the software database; however, its room temperature C_p value equals that of Fe. Therefore, Fe was used instead of Cr for the C_p calculations of the alloy (Morrell et al., 2015). The graph for the specific heat calculation of the NQX alloy is shown in Figure A.6.3. The value of the specific heat increases almost linearly up to higher temperatures (Hatch, 1984). Aluminium has a relatively high specific heat (900J/kg.^{o}C) in comparison with other metals, and it increases almost linearly up to the melting point. The room temperature specific heat value for the NQX alloy is 839J/kg.^{o}C, which is ~7% less than pure Al. This is due to the presence of low specific heat capacity elements such as Fe (440J/kg.^{o}C), Cr (450J/kg.^{o}C), and Ti (540J/kg.^{o}C).

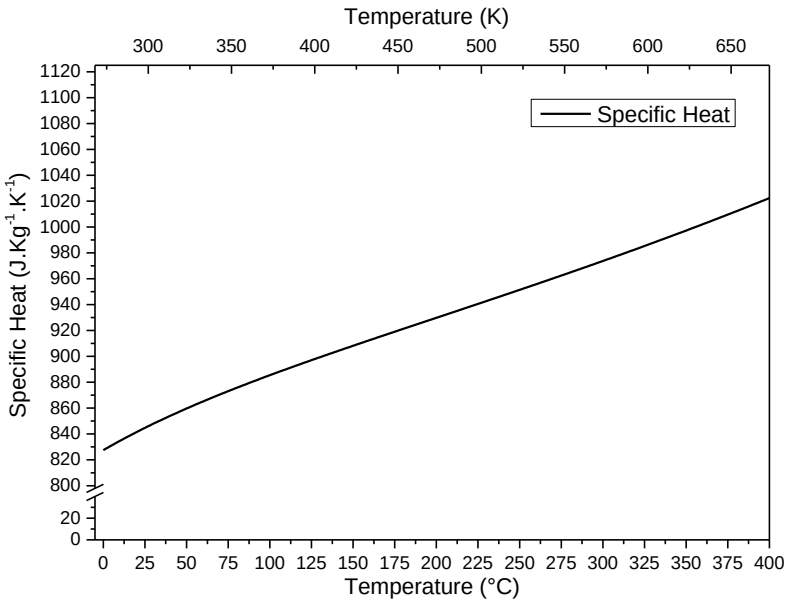

Figure A.6.3 Specific heat calculations for the NQX alloy (using MTDATA software).

The thermal conductivity (κ_{th} in W/m.^{o}C) at various temperatures can be calculated using Eqn. A.6.2 (Dubois and Wei, 2005), which includes a measured value of the

thermal diffusivity (λ_{diff} in m^2/s), the calculated values of the specific heat (C_p in J/kg.^oC), and the measured or calculated density at corresponding temperatures (ρ_T, kg/m^3).

$$\kappa_{th} = C_p \lambda_{diff} \rho_T \qquad \textbf{Eqn. A.6.2}$$

Figure A.6.4 shows the graphs for the thermal diffusivity (right scale) and the thermal conductivity (left scale) between 23^{o}C to 400^{o}C. The thermal diffusivity of the alloy has been found to be in the range of 18 to 24.9 ($10^{-6}m^2/s$). The typical value for the room temperature diffusivity of aluminium is ~$90x10^{-6}m^2/s$ (Dubois and Wei, 2005), which is five times higher than the one for the NQX alloy.

The thermal conductivity for the alloy was calculated to be between 44.3-73.3 W/m.^{o}C in the temperature range 23^{o}C-400^{o}C with values steadily rising with an increase in temperature. The thermal conductivity values of 99.9% aluminium by Hatch (1984) are also shown.

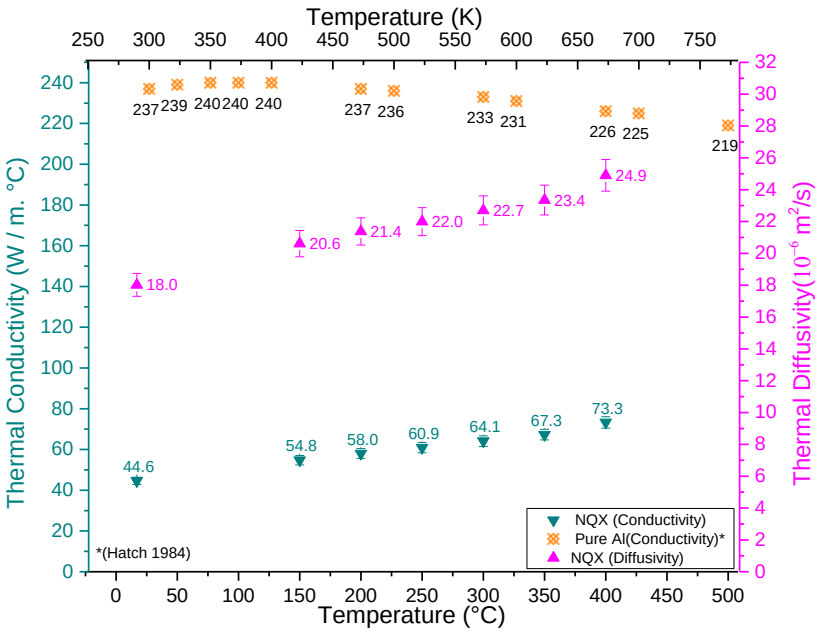

Figure A.6.4 The thermal diffusivity (right) and thermal conductivity(left) for the extruded alloy bar (this work) in comparison with pure Al (Hatch, 1984).

Both lattice vibrational waves (phonons) and free electrons are responsible for heat transport in materials. In pure metals, the thermal transport by free electrons is more efficient as compared to phonons (Campbell, 2008). The addition of alloying elements (solutes) reduces the thermal transport as these act as the scattering centres and reduce the efficiency of the motion of free electrons (Campbell, 2008). Temperature has a major influence on the thermal transport properties, and additionally, lattice defects (e.g. dislocations, grain boundaries), precipitates, and elastic/plastic strains also increase the resistance to thermal conduction. Thermal conductivity of 99.99% pure Al is ~230W/m.°C, whereas its value for the conventional Al alloys is found to be between 110-190W/m.°C, e.g 2024-O (193W/m.°C), 6061-T6 (167 W/m.°C), and 7075-T6 (130 W/m.°C) (ASM, 1990). Thermal conductivity increases almost linearly with the increase in temperature, and it can be ~200 W/m.°C at 400°C for several 2xxx, 4xxx and 7xxx series Al alloys (Lundberg 1994). The thermal conductivity of the NQX alloy ranged from 44.3 to 73.3 W/m.°C in the temperature range 23-400°C. Thermal conductivity has been measured in $Al_{62}Cu_{35.5}Fe_{12.5}$ (stable) quasicrystals between ~2-5 W/m.°C. Since a large volume fraction, the alloy contains the I-phase particles which have an inherently low thermal conductivity so the NQX alloy has an overall lower value of thermal conductivity in comparison with the other aluminium alloys.

A high thermal conductivity is generally desirable in Al alloys for automotive engine application (e.g. pistons), (i) to avoid temperature build up in a specific area (Hillier and Coombes 2004), and (ii) to promote a uniform temperature distribution throughout the component (Mahle 2012). However, a contrasting approach utilises low thermal conductivity of the piston face using the ‘low heat rejection engine’ concept. A thermal barrier coating is applied on the piston face which helps retain more heat in the combustion chamber to increase thermal efficiency (Azadi, Baloo et al. 2013). Thus, a

relatively low value of thermal conductivity can be beneficial depending on the usage or the application.A summary of all the measured or calculated properties discussed above is provided in Table A.6.1.

Table A.6.1 Values for the density and thermal properties[1] for the alloy at various temperatures.

Temperature	CTE	Density	Specific heat	Thermal diffusivity	Thermal conductivity
°C	10^{-6}/ °C	kg/m^3	J/(kg. °C)	10^{-6} m^2 /s	W/(m. °C)
17	-	2950±3	839	18.0±0.7	44.6±1.8
150	19.0±0.6	2928±3	907	20.6±0.8	54.8±2.2
200	19.5±0.4	2919±3	930	21.4±0.8	58±2.3
250	20±0.3	2909±3	952	22±0.9	60.9±2.4
300	20.4±0.2	2900±3	974	22.7±0.9	64.1±2.6
350	20.8±0.1	2890±3	997	23.4±0.9	67.3±2.7
400	21.2±0.1	2880±3	1022	24.9±1.0	73.3±2.9
450	21.6±0.1	2869±3			

References

ASM (1990) *Nonferrous Alloys and Special-Purpose Materials, vol. 2. ASM International, Materials Handbook*: ASM International.

Campbell, F. C. (2008) *Elements of metallurgy and engineering alloys.* ASM International.

Author (1995)*: BS EN 821-1 Advanced technical ceramics. Monolithic ceramics. Thermo-physical properties. Determination of thermal expansion*.

Cowan, R. D. (1963) 'Pulse method of measuring thermal diffusivity at high temperatures', *Journal of Applied Physics*, 34(4), pp. 926-927.

Dubois, J.-M. and Wei, T. K. (2005) *Useful quasicrystals.* World Scientific.

Hatch, J. E. (1984) *Aluminum: properties and physical metallurgy.* ASM International.

Hillier, V. A. W. and Coombes, P. (2004) *Hillier's fundamentals of motor vehicle technology*. Nelson Thornes.

Lundberg, S. (1994) *Material aspect of fire design*.

Morrell, R., Mildeova, P., Chapman, L., P N Quested and Gisby, J. (2015) *Thermal Expansion, Specific Heat, Thermal Diffusivity and Thermal Conductivity Estimation of an Aluminium Alloy,* Teddington, UK: National Physical Laboratory2015090077/1).

Parker, W., Jenkins, R., Butler, C. and Abbott, G. (1961) 'Flash method of determining thermal diffusivity, heat capacity, and thermal conductivity', *Journal of applied physics*, 32(9), pp. 1679-1684.

[1] The overall uncertainty in the thermal diffusivity can be up to 4%; actual data scatter is much smaller ~ 0.1x10^{-6}m^2 /s. Similar errors are propagated in the thermal conductivity calculations. Specific heat data was obtained from the line graph with an R^2 value of 0.999.